"A river cuts through rock, not because of its power, but because of its persistence" - Jim Watkins

Members of the Examination Committee

prof. dr. ir. Bernard De Baets, UGent, Chairman

prof. dr. ir. Kathy Steppe, UGent, Secretary

prof. dr. ir. Abdul Mouazen, UGent

prof. dr. Hans W. Griepentrog, University of Hohenheim

prof. dr. Spyros Fountas, Agricultural University of Athens

Promotors

prof. dr. ir. Jan Pieters, Department of Biosystems Engineering, UGent

dr, ir. Koen Mertens, Technology and Food Science Unit, ILVO

dr. ir. Jürgen Vangeyte, Technology and Food Science Unit, ILVO

Dean

prof. dr. ir. Marc Van Meirvenne

Rector

prof. dr. ir. Rik Van de Walle

DEVELOPMENT OF AN IMAGE BASED 3D TECHNIQUE TO DETERMINE SPREAD PATTERNS OF CENTRIFUGAL FERTILIZER SPREADERS

ir. Simon Cool

Thesis submitted in fulfilment of the requirements for the degree of Doctor (PhD) of Applied Biological Sciences: Agricultural Sciences

December 2017

Dutch translation of the title

Ontwikkeling van een op beeldverwerking gebaseerde 3D techniek om strooibeelden van centrifugaalstrooiers te bepalen

WOORD VOORAF

Een doctoraat doen, nooit gedacht dat het iets voor mij zou zijn. Veel te theoretisch, ik ben niemand om ganse tijd achter een bureau te zitten, zo dacht ik vroeger. Ik was van kleins af aan gefascineerd door landbouw, tractoren en landbouwmachines. Boer of loonwerker worden, dát was mijn jongensdroom. Toen ik ging verder studeren en tegen mijn ouders zei dat ik bij de Bio-ingenieurs landbouwkunde wilde studeren, kwam dat dan ook niet als grote verrassing. Tijdens mijn voorlaatste jaar kwam de interesse voor landbouwtechniek bovendrijven en ben ik voor mijn thesis bij de vakgroep Biosysteemtechniek gaan aankloppen. Via Jan Pieters ben ik op het ILVO terechtgekomen en een jaar later had ik, voor ik het goed en wel besefte, zonder twijfelen toegezegd om een doctoraat te beginnen. Het zijn vier hele leuke jaren geweest, waarin ik de kans heb gekregen om enorm veel bij te leren. Een doctoraat maak je echter niet alleen, daarom wil ik dan ook een aantal mensen bedanken die elk op hun manier een steentje hebben bijgedragen.

In de eerste plaats een woord van dank aan mijn promotor Jan Pieters. Bedankt, Jan, voor alle kansen die je me hebt gegeven, voor je wijze raad en om telkens weer teksten van mij na te lezen en te verbeteren. Ik heb veel van je bijgeleerd en sta nog altijd in bewondering voor je enorme kennis en inzicht. Ik kan in alle eerlijkheid zeggen dat ik geen betere promotor had kunnen treffen.

Dank ook aan jou, Jürgen, voor het vertrouwen in mij en om tijd voor me vrij te maken. Jouw managementkwaliteiten en expertise hebben mij sterk vooruit geholpen. David, je bent pas op het eind met mijn onderzoek betrokken geraakt, maar toch zeker bedankt voor alle hulp.

I would also like to thank the members of the examination committee for reviewing my manuscript: Prof. Bernard De Baets, prof. Kathy Steppe, prof. Abdul Mouazen, prof. Griepentrog and prof. Fountas. Your remarks and suggestions have certainly lifted this work to a higher level.

Koen, merci voor de leuke tijden op de bureau, om altijd tijd voor me te maken, het zeveren tussen het werken door, je goede raad. Ik heb me meer dan geamuseerd in onze bureau, ook al was het in het begin wat zoeken om een evenwicht te vinden tussen ruit open en chauffage aan, zeker in de winter.

Merci aan alle collega's op het werk, in het bijzonder de mensen van Agrotechniek voor de leuke sfeer tijdens de middagpauze, maar ook gewoon tijdens het werken of bij bedrijfsuitstappen of feestjes. De laatste maanden had ik door mijn doctoraat wat minder tijd, maar dat maken we hierna zeker goed. Tim en Dieter, tijd om nog eens te gáán op een goede plaat op weg naar Delhaize! Marleen, bedankt om mijn rommel op te kuisen en mij niet teveel onder mijn voeten te geven, ook al was het vaak wel eens nodig. Stephanie, merci voor de interessante discussies over statistiek. Bedankt, Elsy en Sofie omdat ik altijd bij jullie terechtkon voor vanalles en nog wat en er een glimlach bij cadeau kreeg. Dank aan het ganse team van techniekers op TV115 en in het bijzonder de mensen die aan mijn opstelling meegeholpen hebben: Brecht, Bart Lannau en Tim De Bock. Ook aan Bart Eloot voor het bestellen van kunstmest en aan Bernard en Filip om me snel verder te helpen als ik weer maar eens een tractor nodig had om strooitesten te doen.

Tim, nu is het jouw beurt. Ik herinner me nog ons eerste gesprek aan de keukentafel op ILVO. Het was direct duidelijk dat we veel gemeenschappelijke interesses hadden, maar wie had op dat moment gedacht dat we zo'n goeie maten zouden worden. Dat er nog mensen zoals ik rondlopen, het is niet te geloven, en dan nog niet eens uit West-Vlaanderen komen! Merci voor de raad als het eens wat lastiger ging en je hulp tijdens de strooitesten, het ontwerpen van de opstelling, het programmeren van code, etc. Ik kijk er enorm naar uit om samen aan nieuwe projecten te werken in de toekomst.

Verder wil ik ook nog Tom van Looveren van Hilaire Van der Haeghe NV en Jan Provoost van Kverneland group bedanken om strooiers voor mij beschikbaar te stellen om testen mee te doen. Dank aan prof. Jan Van den Bulcke en prof. Joris Van Acker voor hun hulp en om gebruik te maken van hun indrukwekkende micro-CT installatie. Dank aan Mathias Van De Gucht voor zijn hulp bij de strooitesten. Ook een woordje van dank aan mijn thesisstudenten Gunter, Joachim, Jonas, Joris, Arjen, Matthijs, Jason, Jens, Hendrik, Giel, Mathieu en Aaron en ook Jordi en Kevin. Merci voor jullie motivatie, het was een plezier om met jullie samen te werken. Sergio, thank you for the good times during your stay here in Belgium, playing the guitar however will never become one of my strengths. I am very curious if you still can talk "e bitje west vlams", we should meet up soon! Thanks, Frédéric and Julien, for your help with the strobe and the interesting discussions. I hope that we keep in contact and that we can work together again in the future.

I also want to thank some people I got to know during my internship in Switzerland. Dejan, thank you for the opportunity, the interesting discussions and your professional

advice. Also thanks to Leandro for helping me out and for the fun moments in Winterthur. If you are ever in Belgium, we will have a Belgian beer you enjoy so much instead of a glühwein.

De boog kon natuurlijk niet altijd gespannen staan. Graag wil dan ook mijn vrienden uit mijn studententijd bedanken. Wat een goeie tijd was dat als je eraan terugdenkt. Wat hebben we gelachen in de les, op feestjes, tijdens het lopen rond de watersportbaan, in de Limiet, op Steam of tijdens het gamen!

Een grote dankjewel aan mijn familie: papa, mama, Heleen en Mathijs, om gewoon de beste familie ooit te zijn. Papa en mama, een heel dikke merci voor alles wat jullie voor mij gedaan hebben en nu nog doen, veel teveel om op te noemen. Jullie hebben me mee gevormd tot de persoon die ik nu ben en ik ben jullie hiervoor ontzettend dankbaar. Ook dank aan mijn grootouders, oma en opa Cool, oma Agnes en opa Gerard. Merci aan nonkel Toon en opa Gerard om mij de liefde voor de landbouw bij te brengen. Vaak denk ik nog terug aan die goeie tijd op de boerderij waarbij ik samen met opa op de tractor zat, op de courgettemachine of op de hooizolder, weidedraden installeerde, aardbeien plantte of ze bovenop de kipkar uit hun plasticzakken trok in de zomerzon. Als ik hieraan terugdenk besef ik pas wat een voorbeeld je voor mij was, opa, en wat je voor mij betekende. Merci, oma Agnes om mij op te vangen tijdens mijn herexamens het eerste jaar, het was zeker niet makkelijk om op die zonnige dagen binnen te zitten studeren maar dankzij jouw aanmoedigingen is het gelukt, en zie waar het mij heeft gebracht hé! Merci, opa en oma Cool om voor papa en mij de Ferguson aan de kant te zetten. Sleutelen aan die oude tractor heeft bij mij zeker de interesse voor landbouwtechniek aangewakkerd. Zo kom ik ook bij jou terecht, Benedict, niets is leuker dan samen aan machines werken en ik moet toegeven, jouw spaghetti op kot in Gent met Top-Gear op de achtergrond blijft gewoon de beste.

Tot slot de meest belangrijke persoon voor mij, mijn vriendin Catya, de liefde van mijn leven en mijn fitnessmaatje. Na drie maandjes al gingen we samen een grote uitdaging aan, drie maanden alleen in Zwitserland en sindsdien zijn we onafscheidelijk. Ik heb nooit gedacht dat ik iemand zou vinden die zo goed bij mij past als jij. Bedankt voor al je hulp, vooral ook tijdens de laatste maanden van mijn doctoraat. Ik apprecieer heel hard wat je allemaal voor mij gedaan hebt en doet. Als iemand hier de grootste pluim hier verdient, dan ben jij dat zeker!

Simon Cool, december 2017

SUMMARY

Optimizing fertilizer inputs in agricultural production systems is an important strategy to reduce their large environmental impact while answering the world's increasing need for food. Centrifugal fertilizer spreaders are by far the most commonly used granular fertilizer spreaders due to their large working width, small size, low price and their simple and robust design. Although the simple working principle, the spreading process of this type of spreaders is difficult to control because it depends on various parameters such as the physical properties of the fertilizer particles, spreader settings, wind conditions, etc. Therefore, deviations between the desired and the actual spread pattern may occur in practice, leading to local under- and over-applications. In order to assess the spreader performance and perform corrections if necessary to avoid this uneven application, their spread pattern must be determined. Because existing methods to measure the spread pattern are labour intensive and time-consuming or require large indoor test facilities, performing these tests is rarely done in practice. In literature, different "predict rather than collect" methods have been developed, determining the spread pattern by simulating individual particle trajectories and calculating their subsequent landing positions. Until now however, none of these approaches could predict the spread pattern in an accurate way. Furthermore, no test results were reported on real, commercially available spreaders.

The aim of this PhD research is to design and evaluate an automated system capable of determining spread patterns of commercial centrifugal spreaders in a fast, accurate, cost- and space-efficient way. Based on a literature review, the most promising method to fulfil these requirements was to predict the spread pattern using the hybrid approach, i.e. by simulating the spread pattern based on measurements of particle parameters after leaving the discs and then predicting their trajectories and subsequent landing positions using a ballistic model. From all hybrid techniques, image processing approaches are most promising because they allow to determine the parameters of multiple particles without interfering with the fertilizer flow. To avoid the use of expensive high speed cameras to retrieve three-dimensional information, stereovision with multi-exposure is used to determine the particle positions and the velocities in three dimensions and the particle sizes. With the multi-exposure technique, multiple flashes of light are applied within the same camera exposure to visualise multiple positions of moving particles on one image.

In chapter 2, a three-dimensional ballistic model was developed. The model incorporated the effect of gravitation and drag but also wind. The drag coefficient was

calculated based on the Reynolds number, which changes during the trajectory and the particle sphericity. Because there was no analytical solution, the model was solved numerically using a numerical solver. By performing simulations, the effect of different step sizes was investigated. It was found that a step size of 1e-3 s was sufficient for this application. Eight commonly used fertilizer types were selected and their physical properties were determined in laboratory conditions, including the particle size distribution, the bulk density, the true density, the angle of repose and the 3D particle shape. The latter was determined using X-ray micro-CT and was used to determine the sphericity distribution. Based on the obtained results, single-particle simulations were performed to determine the travelled distance for the different fertilizer types. Different cases were considered: particles leaving a flat and a conical disc with a low, medium and high velocity. The travelled distance between different particle types was clearly different. The difference between particle types was generally higher for the conical compared to the flat disc case and increased clearly with the particle velocity. Subsequently, simulations were performed to determine the effect of particle- and environmental parameters on the landing position. These parameters were: the horizontal and vertical velocity of the particles, the particle size, sphericity, true density, initial height, and also the density of air. Finally, also the effect of wind was determined, both in the longitudinal and transverse direction. The absolute sensitivity was calculated to quantify the effect of these parameters for the different cases mentioned above. The perturbation factors for the analysis were based on realistic measurement errors. Results indicated that an increase in particle velocity, vertical outlet angle, initial height, tail wind, particle size, true density and sphericity increased the travelled distance, while for increasing the air density and head-wind, the opposite was true. The sensitivity to the different parameters was clearly affected by the particle type, velocity and vertical outlet angle. To compare the effect of the different parameters, the relative sensitivity was calculated. Generally, it was found that the landing position was most sensitive for the vertical velocity and particle diameter and least for the initial height and the density of air. The effect of wind on the individual particle trajectories was relatively large. Based on these findings, it can be concluded that hybrid methods should measure particle velocity in three spatial dimensions and also, the particle size should be determined accurately.

In chapter 3, a specific high power LED illumination system was developed for multi-exposure image acquisition of fertilizer particles. To achieve a high accuracy for measuring the particle parameters from the images, a high irradiance level was necessary without compromising the uniformity of light distribution. In a first step, the optimal LED was selected from a range of commercially available high power LEDs taking into account the camera sensitivity. Next, the optimal configuration of LEDs was

determined using a multiple objective genetic algorithm. Both the irradiance level and homogeneity of the light distribution were considered, in contrast to other approaches in literature. The angular distribution pattern from the manufacturer was used to simulate light distribution patterns for multiple LEDs. Comparing simulation results for three types of LED-lenses, the narrow angle lens was found optimal for this application. Multiple Pareto optimal solutions were found for different numbers of LEDs and from this set, the best configuration was selected. The optimal configuration had a high intensity and high uniformity, the Coefficient of Variation (CV) of the simulated light distribution was below 2%.

In chapter 4, a multi-camera system was developed to predict the spread pattern of commercial centrifugal spreaders in a fast, accurate, cost- and space-efficient way. Using a first set of two cameras and corresponding image processing algorithms, the positions and velocities (particle dynamics) of the particles being ejected by the spreader were determined in three spatial dimensions. The illumination system developed before was implemented for multi-exposure to achieve high speed information and high resolution images at a relative low cost. Next to the particle dynamics, also the size of the individual particles was determined using image processing. The particle dynamics were expressed relative to a coordinate system associated with the spreader, which was automatically determined using a second set of two cameras. By using this information as input for the ballistic model developed in chapter 2, landing positions of individual fertilizer particles can be simulated and the spread pattern can be determined.

Experiments were conducted with a commercially available spreader in combination with a commonly used fertilizer type. Two spreader configurations, each with two replicates, were evaluated, corresponding to a lower and higher disc rotational velocity. The measurement system showed a high repeatability and accuracy in determination of the particle size distribution, as the results were similar between all experiments and the particle size distributions corresponded well with sieve test results. The predicted particle velocities and resulting two-dimensional spread patterns were highly repeatable between replicates. The two-dimensional spread patterns were transformed to transverse spread patterns to compare the results with spread patterns obtained in the field using a transverse row of collection trays. The predicted spread patterns showed a good correlation (97.5% to 98.5% over all experiments) with the results obtained in the field. The calculated homogeneity of distribution, quantified by the CV after overlapping subsequent swaths was also similar. The average difference between the CV obtained with both approaches was 0.75% for the first spreader configuration and 3.77% for the second spreader configuration. Based on these

findings, it could be concluded that the predicted spread patterns were comparable with spread patterns obtained in the field.

Because spread patterns are predicted by simulating individual particle trajectories based on particle parameters that are measured after ejection by the spreader, simulations can be performed to study the effect of different parameters on the spread pattern without having to perform extra measurements. The effect of for example wind can be easily determined, which is very difficult using traditional approaches. By using the data from the spread tests above, the effect of tractor velocity, spreader height and wind on the spread pattern was determined for both spreader configurations. Wind had a relatively larger impact compared to an increase in tractor velocity and spreader height, especially for the case of side wind. Side wind increased the CV from 7.36% and 4.42% in the base case (no wind) to 17.27% and 17.24% (for the highest wind velocity considered) for both spreader configurations respectively, above the acceptable limit of 15%. The results indicate that wind is an important parameter to consider when spreading fertilizer with a centrifugal fertilizer spreader, especially in case of boundary spreading. More research will be necessary to evaluate the effect of wind for other settings, particle types and spreaders.

Compared to previous approaches to predict spread patterns, significant improvements were made in this work. By using multi-camera stereovision, the 3D position and 3D velocity of the particles relative to the spreader were determined. Furthermore, also the size of the particles was determined using image processing. By implementing the multi-exposure technique, high resolution images were obtained at a relative low cost. Compared to traditional approaches using collection trays, the measurement system is much more space-efficient. The developed system can be used for assessment of spreader performance in practice and to calibrate spreaders, e.g. by service providers or control bodies. The system can be of interest for spreader manufacturers to design spreading charts without the need for large, expensive spread halls while offering more insight in the spreading process compared to traditional approaches. Simulations can be performed to quantify the effect of different parameters such as wind, spreader height and tractor velocity on the spread pattern, without having to perform extra experiments. By fertilizer producers, the system can be used for performing experiments and simulations, e.g. to improve the spreadability of their product.

SAMENVATTING

Het optimaliseren van het gebruik van kunstmest in landbouwkundige productiesystemen wordt gezien als een belangrijke strategie om de negatieve milieukundige effecten te minimaliseren en tegelijk de groeiende wereldbevolking te blijven voeden. Om korrelvormige kunstmest te strooien worden voornamelijk centrifugaalstrooiers gebruikt omwille van hun grote werkbreedte, beperkte grootte, lage prijs en robuuste bouw. Ondanks hun relatief eenvoudig werkingsprincipe is het strooiproces van dit type strooiers moeilijk te controleren omdat het afhangt van verschillende factoren zoals de fysische eigenschappen van de kunstmestkorrels, de instellingen van de strooier, wind, enz. Daardoor kan er in de praktijk een afwijking optreden tussen het werkelijke en het gewenste strooibeeld wat kan leiden tot lokale onder- of overdoseringen op het veld.

Om de prestatie van de strooier te beoordelen en correcties uit te voeren indien nodig, moet het strooibeeld bepaald worden. Omdat de gangbare methoden om strooibeelden op te meten arbeidsintensief en tijdrovend zijn of veel ruimte vereisen, wordt dit zelden gedaan in de praktijk. In de literatuur zijn er daarom verschillende methoden ontwikkeld om strooibeelden te voorspellen in plaats van ze op te meten, waarbij het strooibeeld bepaald wordt door individuele korrelbanen te simuleren en hun corresponderende landingsposities te berekenen. Geen enkele van deze methoden is er echter in geslaagd om strooibeelden op een nauwkeurige manier te voorspellen. Bovendien werd tot op heden enkel gebruik gemaakt van teststrooiers en niet van commercieel beschikbare strooiers.

De doelstelling van dit doctoraatsonderzoek was een automatisch systeem te ontwerpen en evalueren om op een snelle, nauwkeurige en kost- en ruimte-efficiënte manier strooibeelden van centrifugaalstrooiers te bepalen. Uit de literatuurstudie bleek dat het voorspellen van strooibeelden het best gebeurt via de hybride methode. Bij deze methode wordt het strooibeeld voorspeld op basis van metingen van korrelparameters nadat ze de strooischijven verlaten hebben, waarna hun individuele korrelbanen gesimuleerd worden via een ballistisch model en de landingsposities berekend worden. Van alle hybridemethoden zijn de methoden die gebruik maken van beeldverwerking het meest veelbelovend, omdat ze de parameters van verschillende korrels kunnen bepalen zonder interferentie in het strooiproces te veroorzaken. Om het gebruik van dure *high speed* camera's te vermijden, werd in dit werk gebruik gemaakt van stereovisie in combinatie met de multi-exposure techniek om de 3D posities, 3D snelheidsvectoren en korrelgroottes te bepalen. Bij multi-exposure worden

meerdere lichtflitsen toegepast binnen dezelfde sluitertijd van de camera om opeenvolgende posities van bewegende korrels op één beeld weer te geven.

In hoofdstuk 2 werd een driedimensionaal ballistisch model ontwikkeld. Het model houdt rekening met het effect van zwaartekracht en luchtweerstand, maar ook met wind. De luchtweerstandscoëfficiënt werd bepaald via het Reynoldsgetal en de sfericiteit van de korrels. Omdat er geen analytische oplossing voor het model was, werden de vergelijkingen op een numerieke manier opgelost. Simulaties werden uitgevoerd om het effect van verschillende stapgroottes te bepalen. Uit de resultaten bleek dat een stapgrootte van 1e-3 s voldoende nauwkeurig was voor deze toepassing. Acht verschillende kunstmestsoorten werden geselecteerd en hun fysische eigenschappen werden bepaald in laboratoriumomstandigheden. De grootteverdeling, bulkdichtheid, werkelijke dichtheid, storthoek en 3D vorm werden bepaald. Deze laatste werd bepaald via X-ray micro-CT en werd gebruikt om de sfericiteit van de korrels te bepalen. Op basis van de meetresultaten werden individuele korrelbanen gesimuleerd voor de verschillende korrelsoorten. Verschillende gevallen werden beschouwd: een platte en een conische strooischijf, korrels met een lage, medium en hoge snelheid. De afgelegde afstand was duidelijk verschillend voor de verschillende korrelsoorten. Het verschil tussen de korrelsoorten was groter voor de conische schijf in vergelijking met de platte en werd groter met een toenemende korrelsnelheid. Vervolgens werden simulaties uitgevoerd om het effect van korrel- en omgevingsfactoren op de afgelegde afstand na te gaan. Volgende parameters werden onderzocht: de horizontale en verticale snelheid van de korrels, de sfericiteit, de echte dichtheid, de korrelgrootte, de beginhoogte en de dichtheid van lucht. Verder werd ook het effect van wind nagegaan, zowel in de longitudinale als in de transverse richting. De absolute sensitiviteit werd berekend om het effect van bovenstaande parameters te bepalen. De perturbatiefactoren hiervoor waren gebaseerd op realistische meetfouten. Voor alle factoren, behalve de luchtdichtheid en tegenwind, resulteerde een grotere waarde in een toename van de afgelegde afstand. De sensitiviteit voor de verschillende parameters was duidelijk afhankelijk van de korrelsoort, de snelheid en de verticale vertrekhoek. Om het effect van de verschillende parameters te vergelijken werd de relatieve sensitiviteit berekend. De afgelegde afstand was het meest gevoelig voor de verticale snelheidsvector en de korrelgrootte en het minst voor de beginhoogte en de luchtdichtheid. Ook het effect van wind op de individuele korrelbanen was relatief groot. Op basis van deze resultaten kan geconcludeerd worden dat bij hybride methoden, waarbij het strooibeeld wordt voorspeld aan de hand van individuele korrelbanen, de snelheidsvectoren in drie dimensies moeten bepaald worden en dat ook de korrelgroottes nauwkeurig bepaald moeten worden.

In hoofdstuk 3 werd een specifiek power LED belichtingssysteem ontwikkeld om multi-exposure beelden te nemen van kunstmestkorrels. Om de korrelparameters met een grote nauwkeurigheid te bepalen is een hoge belichtingsintensiteit en -homogeniteit noodzakelijk. Eerst werd de optimale LED-soort geselecteerd uit een assortiment van commercieel beschikbare power LEDs. Hiervoor werd rekening gehouden met de spectrale output van de LEDs en de gevoeligheid van de camera's. De optimale configuratie van de LEDs werd bepaald via een *multi-objective* genetisch algoritme. In tegenstelling tot andere methoden in de literatuur werd hierbij rekening gehouden met zowel de intensiteit als de uniformiteit van de lichtverdeling. De spatiale output per LED werd bepaald om de lichtverdeling van een combinatie van LEDs te berekenen. Simulaties werden uitgevoerd voor verschillende LED-lenzen en de smalle-hoek lens bleek optimaal voor deze toepassing. Meerdere Pareto-optimale oplossingen werden gevonden voor een verschillend aantal LEDs en op basis van deze set werd de beste configuratie gekozen. Deze resulteerde in een hoge intensiteit en uniformiteit. De variatiecoëfficiënt van de gesimuleerde lichtverdeling was lager dan 2%.

In hoofdstuk 4 werd een multi-camera systeem ontwikkeld om strooibeelden van centrifugaalstrooiers te bepalen op een snelle, nauwkeurige, kost- en ruimte-efficiënte manier. Via een eerste set van twee camera's en bijbehorende beeldverwerkingsalgoritmes werden de posities en snelheden van korrels die door de strooier werden uitgeworpen, bepaald in drie spatiale dimensies. Het belichtingssysteem dat in vorig hoofdstuk werd ontwikkeld, werd hierbij gebruikt om *high speed* informatie (via multi-exposure) en beelden op hoge resolutie te bekomen aan een relatief lage kost. Naast de snelheid en positie van de korrels werden ook de groottes van de korrels bepaald via beeldverwerking. De positie en snelheid van de korrels werd uitgedrukt in het coördinatenstelsel van de strooier, dat automatisch bepaald werd via een tweede set van twee camera's. Door deze informatie te gebruiken in het ballistisch model uit hoofdstuk 2, kunnen landingsposities van individuele korrels voorspeld worden en kan het strooibeeld voorspeld worden.

Strooitesten werden uitgevoerd met een commercieel beschikbare strooier en een veelgebruikte kunstmeststof. Twee strooierconfiguraties werden getest, waarbij telkens twee strooitesten werden uitgevoerd. Een hoge herhaalbaarheid en nauwkeurigheid voor de voorspelde korrelgrootteverdeling werd aangetoond, aangezien de resultaten voor alle experimenten vergelijkbaar waren en de grootteverdeling overeen kwam met de verdeling die opgemeten werd via zeven. Ook de voorspelde snelheden en tweedimensionale strooibeelden waren vergelijkbaar tussen de corresponderende strooitesten. Het tweedimensionaal strooibeeld werd omgerekend naar een transvers strooibeeld om resultaten te vergelijken met

strooibeelden die opgemeten werden in het veld via een rij met collectiebakken. Een hoge correlatie werd gevonden (97.5% tot 98.5%) tussen de voorspelde en de opgemeten strooibeelden. De homogeniteit van het strooibeeld na overlap van opeenvolgende strooigangen (gekwantificeerd door de CV) was eveneens gelijkaardig. Het gemiddelde verschil in CV tussen beide technieken was 0.75% voor de eerste strooierconfiguratie en 3.77% voor de tweede. Gebaseerd op de resultaten kon geconcludeerd worden dat de voorspelde strooibeelden vergelijkbaar waren met de strooibeelden die opgemeten werden op het veld.

Met het ontwikkelde meetsysteem kunnen strooibeelden voorspeld worden door middel van simulatie van individuele korrelbanen, die berekend worden aan de hand van parameters van korrels die opgemeten worden na het verlaten van de strooischijven. Hierdoor kunnen simulaties uitgevoerd worden om het effect van een aantal parameters na te gaan waarvoor in andere gevallen nieuwe strooitesten uitgevoerd zouden moeten worden. Het effect van wind kan op die manier, in tegenstelling tot meettechnieken die gebruik maken van collectiebakken, op een eenvoudige manier bepaald worden. Gebaseerd op de data van de hierboven vermelde strooitesten werd het effect van tractorsnelheid, strooierhoogte en wind op het strooibeeld nagegaan. Het effect van wind was groter dan de tractorsnelheid of de strooierhoogte, zeker in het geval van zijwind. Zijwind zorgde ervoor dat de CV toenam van 7.36% en 4.42% tot 17.27% en 17.24% (voor de hoogste windsnelheid die beschouwd werd) voor beide strooierconfiguraties, boven de toegelaten limiet van 15%. De resultaten tonen aan dat wind een belangrijke parameter is om rekening mee te houden tijdens het strooien van kunstmest met een centrifugaal strooier, zeker ook in het geval van kantstrooien. Bijkomend onderzoek is echter nodig om het effect van wind na te gaan voor andere strooier-instellingen, korrelsoorten en strooiers.

Vergeleken met andere methoden om strooibeelden te voorspellen, werd in dit onderzoek significante vooruitgang geboekt. Via stereovisie werd niet alleen de 3D positie en 3D snelheid van de korrels relatief tegenover de strooier, maar ook de korrelgrootte bepaald. Door gebruik te maken van de multi-exposure techniek konden beelden op hoge resolutie bekomen worden aan een relatief lage kost. In vergelijking met traditionele technieken waarbij gebruik gemaakt wordt van collectiebakken, is heel wat minder ruimte nodig om het strooibeeld te bepalen. Het ontwikkelde meetsysteem kan gebruikt worden om de prestatie van strooiers in de praktijk te beoordelen en om strooiers af te stellen. Testen kunnen uitgevoerd worden door specifieke bedrijven maar ook door controle- of overheidsinstanties. Voor fabrikanten van strooiers kan het systeem interessant zijn om strooitabellen op te stellen zonder nood aan grote en dure strooihallen. Het systeem biedt bovendien meer inzicht in het strooiproces en

simulaties kunnen uitgevoerd worden om het effect van parameters zoals wind na te gaan zonder hiervoor extra strooitesten te moeten uitvoeren. Ook voor producenten van kunstmest kan het systeem interessant zijn, zowel om experimenten uit te voeren maar ook voor simulaties, bijvoorbeeld om de strooibaarheid van hun product te verbeteren.

LIST OF ABBREVIATIONS

Abbreviation	Explanation	Unit
a_x, a_y, a_z	Acceleration	m/s²
A	Projected area	m²
A_{hull}	Area of convex hull	pixels
A_p	Area of particle	pixels
BMP	Best management practices	
CYAN	Cyanamide fertilizer	
C_d	Drag coefficient	
Cd	Candela	
CEMIB	Cemagref Mineral Bench	
Cov	Covariance	
CPU	Central Processing Unit	
CV	Coefficient of variation	%
D	Diameter	m
DEM	Discrete element method	
DEMs	Digital elevation models	
D_{eq}	Diameter of equivalent sphere	pixels
DGPS	Differential global positioning system	
D_{trav}	Travelled distance	m
E	Irradiance	W/m²
ENTEC	ENTEC fertilizer	
EP	Eutrophication potential	
f_x, f_y	Focal length of camera model	pixels
F	Force	N
F_d	Drag force	N
F_g	Gravitational force	N
FPS	Frames per second	
FWHM	Full width at half maximum	°
g	Gravitational acceleration	m/s²
GWP	Global warming potential	
h	Particle height	m
HCSM	Hybrid centrifugal spreading model	
He	Helium	
Hz	Hertz	
I	Luminous intensity	Cd
IMU	Inertial Measurement Unit	

I_0	Luminous intensity in the normal direction	Cd
k_1, k_2, k_3	Radial distortion coefficients	-
K	Camera matrix	pixels
KCL	KCL fertilizer	
k_w	Weighting factor	-
L	Landing position	m
LED	Light Emitting Diode	
lm	Lumen	
LS	Least Squares	
lx	Lux	
m	Mass of fertilizer particle	kg
MRF	Markov Random Fields	
NPK15	NPK15-15-15 fertilizer	
NPK18	NPK18-6-5 fertilizer	
NUE	Nitrogen use efficiency	
O_C	Optical centre	m
$p_{c,x}, p_{c,y}$	Position of principal point in camera matrix	pixels
P_C	Principal point	pixels
PK	Patentkali fertilizer	
P_p	Perimeter of a contour	pixels
PTO	Power take-off	
p_1, p_2	Tangential distortion coefficents	-
q	Projection point	pixels
Q	Object point	m
Q_m	Mass flow rate	kg/s
R	Rotation matrix	
RAM	Random-access memory	
Re	Reynolds number	-
RMS	Root mean square	
RTK	Real time kinematic	
s	Scale factor for camera model	m
SCS	Spreader coordinate system	
sr	Sterradian	
t	Time	s
t	Translation matrix	
t_{delay}	Delay time between flashes of the illumination system	μs
t_0	Initial time	s

t_{end}	End time	s
TROP	Tropicote fertilizer	
v	Particle velocity	m/s
V	Volume of scanned particle	voxels
v_{hor}	Horizontal velocity	m/s
VRA	Variable rate applications	
VRT	Variable rate technology	
$v_{tractor}$	Tractor velocity	m/s
v_{ver}	Vertical velocity	m/s
v_{wind}	Wind velocity	m/s
W	Working width	m
α	Vertical angle	°
α_{wind}	Wind angle	°
β	Horizontal outlet angle	°
γ	Convexity	-
δ	Epipolar distance	pixels
Δr	Segment radius of orifice	m
Δt	Time step	s
Δφ	Segment angle of orifice	°
ε_{stereo}	Stereo matching coefficient	-
ε_{time}	Time matching coefficient	-
ζ	Angular outlet position	°
η	Circularity	-
$\theta_{1/2}$	Half width view angle	°
μ_{air}	Dynamic viscosity of air	kg/m s
ρ	Particle true density	kg/m³
ρ_{air}	Density of air	kg/m³
ρ_p	Pearson coefficient of correlation	-
σ	Standard deviation	
φ	Sphericity	-
ω	Rotational velocity	rev/s

TABLE OF CONTENTS

OUTLINE

In this thesis, a system for determining the spread pattern of centrifugal fertilizer spreaders is developed and evaluated. The first chapter is the general introduction. In this chapter, the economic and ecological aspects related to fertilizer spreading and the equipment used for this is discussed with a focus on the centrifugal spreader. The parameters influencing the spreading process and the methods for determining the spread pattern are addressed.

In chapter 2, a ballistic model is developed. This model will be used later in this work to predict the spread pattern based on the simulation of individual particle trajectories. Physical properties of eight commonly used fertilizer types are determined and based on the results, simulations are performed to quantify the effect of different parameters on the travelled distance of individual particles.

In chapter 3, a custom designed illumination system is developed using high power LEDs. This illumination system will be used later on in this work for multi-exposure image acquisition of fast-moving fertilizer particles.

In chapter 4, a multi-camera system is developed for predicting spread patterns of centrifugal fertilizer spreaders. Using a first set of cameras and the illumination system from previous chapter, the position, velocity and size of the particles being ejected by the spreader are determined using image processing. The particle dynamics are expressed relative to a coordinate system associated with the spreader, which is automatically determined using a second set of cameras. By using these parameters as input for the ballistic model developed in chapter 2, the spread pattern can be determined by calculating the landing position of the individual particles. Spreading experiments are conducted with a commercially available fertilizer spreader to evaluate the system and compare the results with field tests. Based on these results, simulations are performed to evaluate the effect of wind, spreader height and tractor speed on the spread pattern.

In chapter 5, the general conclusions and the future perspectives of this research are given.

CHAPTER

1

INTRODUCTION

1.1. Background

A growing world population and an increasing consumption of calorie- and meat-intensive diets are expected to roughly double global crop demand by 2050 (Tiltman et al., 2011). Because the amount of arable land is limited, these needs will require an intensified primary production. To account for these needs, fertilizer use is expected to increase globally (Snyder et al., 2009). According to a recent report (FAO, 2017), the global demand for fertilizer nutrients (N, P and K) is expected to increase from 184 million tons in 2015 to more than 201 million tons in 2020. The use of fertilizer however has some ecological side-effects. A recent study by Goucher et al. (2017) illustrates the large environmental impact of fertilizer in a wheat-to-bread supply chain. The use of ammonium nitrate fertilizer alone accounted for 43.4% of the overall Global Warming Potential (GWP) and 34.1% of the Eutrophication Potential (EP) in the production of a loaf of bread. The production of fertilizers causes emissions of carbon dioxide because of energy consumption during production or solidification processes (Yara, 2014), but also of nitrous oxide, for example during the production of nitric acid for producing ammonium nitrate (Snyder et al., 2009). Nitrogen fertilizers cause direct nitrous oxide emissions from soils, emanating from microbial soil processes and indirect emissions due to volatilization of ammonia, which also contributes to acidification of ecosystems, and leaching of nitrate (Flysio et al., 2011). Over-application of N-fertilizer can result in large amounts of residual nitrogen, which can migrate to ground and surface water (Tissot et al., 2002; Reumers et al., 2003), resulting in eutrophication. This affects the water quality and the biodiversity of aquatic ecosystems (Moshou et al., 2004; Withers & Haygarth, 2007).

The need for optimizing fertilizer inputs is widely accepted as an important strategy to reduce greenhouse gas emissions in the food chain (Zhang et al., 2010). Increasing nutrient use efficiency (NUE) while maintaining a high yield is seen as one of the most immediate solutions (Tiltman et al., 2011; Goucher et al., 2017). Best Management Practices (BMP), based on the principles of using the right source, at the right rate, at the right time on the right place (Roberts, 2007; Virk et al., 2013), play a large role in minimizing soil residual nitrogen lowering the risk for increased nitrous oxide emissions (Snyder et al., 2009) and leaching of nutrients to ground water (Tissot et al., 2002). Amongst others, the use of precision agriculture techniques can help mitigate negative environmental impacts of intensive agriculture (Mueller et al., 2012). Detailed soil and crop information can be used to improve nutrient efficiency using site specific, variable rate application of fertilizers for fine-tuning fertilizer rates to actual crop demands (Griepentrog & Kyhn, 2000; Isherwood, 2000).

Centrifugal fertilizer spreaders are most commonly used for spreading granular mineral fertilizers, particularly because of their relative low cost and large working widths (Olieslagers et al., 1996; Vangeyte, 2013; Hijazi et al., 2014; Villette et al., 2017). Because the spread pattern is very sensitive to errors, deviations can occur between the actual and the desired application on the field, leading to local under- and over-applications in the field, which result in yield losses for the farmer (Sogaard & Kierkegaard, 1994). In some cases, the effects of uneven fertilization are visible as streaks in the fields (Scharf, 2010). This is illustrated in Figure 1.1.

Figure 1.1. Streaks of higher and lower nitrogen application in grassland. Scharf (2010)

In order to assess the performance of spreaders and perform corrections if necessary to avoid this uneven application, their spread pattern and the resulting distribution of fertilizer in the field must be determined. Because existing methods to measure the spread pattern are labour intensive and time-consuming or require large indoor test facilities, performing these tests is rarely done in practice. Alternative methods to determine spread patterns in an accurate way are currently lacking.

In this chapter, the general background of fertilizer spreading using centrifugal spreaders is discussed. The working principle and design of the centrifugal fertilizer is explained in more detail (section 1.2). The resulting spread patterns and the different parameters influencing this distribution are explained. Section 1.3 deals with different methods to determine the spread pattern. Both the traditional way of measuring the spread pattern and recent developments to predict this distribution are discussed. Finally, the objectives of this thesis are described in section 1.4.

1.2. Centrifugal fertilizer spreader

1.2.1. Granular fertilizer spreaders

Different types of machines are used for spreading granular fertilizers in the field. The first category of machines has a spreading width similar to the width of the machine. Band fertilizer spreaders are similar to seeding machines and can be used to apply fertilizer particles in rows. The working width is very limited, however the equipment can be combined with other field actions like seeding or drilling to place fertilizer particles close to the crop row (Van Liedekerke et al., 2006a). Pneumatic spreaders distribute particles using a boom comparable to field sprayers. Instead of liquid however, granular particles are distributed through a forced airstream. Pneumatic spreaders are very accurate and not sensitive to wind. Their spread pattern is steep at the edges which is ideal for border spreading, however also results in a higher sensitivity for driving errors (Hofstee et al., 1999). Pneumatic spreaders are very expensive and therefore rarely used in practice. The second category are broadcast spreaders, having a mechanism for throwing particles into the air to increase the spreading width and accordingly the working width of the spreader. With these spreaders, fertilizer particles describe a considerable trajectory in the air before impacting the ground. The first type of broadcast spreader is the pendulum spreader, using a horizontally oscillating pendulum to accelerate the fertilizer particles. This type of spreader was widely used in the past but its use has declined due to the limited working width. The second type is the spinner spreader, disc spreader or centrifugal fertilizer spreader which is by far the most commonly used in practice because of their large working width, small size, low price (Olieslagers et al., 1996; Villette et al., 2017) and their simple, and robust design requiring little maintenance (Kweon & Grift, 2006). Therefore, in this thesis, the focus lies on centrifugal fertilizer spreaders.

1.2.2. Spreading process of centrifugal fertilizer spreader

Centrifugal spreaders (see Figure 1.2) use spreading discs equipped with vanes for accelerating the fertilizer particles before throwing them into the air. Particles are stored in a hopper and are gravimetrically delivered to the spreading discs through orifices with an adjustable size. To increase the capacity and the working width, in most cases two discs are used, spinning in opposite directions. Generally, two different types of spreaders can be identified, depending on the rotational direction of the discs. With in-centric spreaders (e.g. Bogballe), fertilizer is thrown towards the longitudinal centreline of the spreader, generating more overlap of the spread pattern of each disc. Off-centric spreaders (e.g. Amazone, Rauch, Vicon) on the other hand throw particles away from

the centreline of the spreader. Because less overlap is generated, this type of spreader is more suitable for border spreading or Variable Rate Applications (VRA).

Figure 1.2. Centrifugal fertilizer spreader (Amazone ZAM). The spreader uses spinning discs equipped with vanes to throw fertilizer particles in the field. A closer view from one of the spreading discs is shown at the bottom right

The discs are mechanically (through Power take-off, PTO), hydraulically or electrically (less common) driven with a rotational velocity, depending on the fertilizer type and desired working width, of 500 to 1000 rpm. The particles are ejected with a velocity normally ranging between 15 and 50 m/s (Hofstee et al., 1999). To increase the working width, some manufacturers recommend tilting the spreader or use conical spreading discs or inclined vanes to give the particles an upwards velocity component to increase their travelled distance. The spreading process for a single spreading disc is illustrated in Figure 1.3.

Although the spreading process is simple in its nature, it is difficult to control because it is strongly dependent on the physical properties of the fertilizer particles. To account for these varying properties, different parameters of the spreader can be adjusted to assure a homogeneous distribution on the field. This can be the position of the vanes on the disc, the rotational velocity of the disc or the position of the orifice relative to the disc, etc. Spreader manufacturers design spreading charts by performing numerous spreading experiments with different types of fertilizer. These tables must be used by

the farmer to determine which settings, working width and tractor velocity to use for a certain application rate of his specific type of fertilizer.
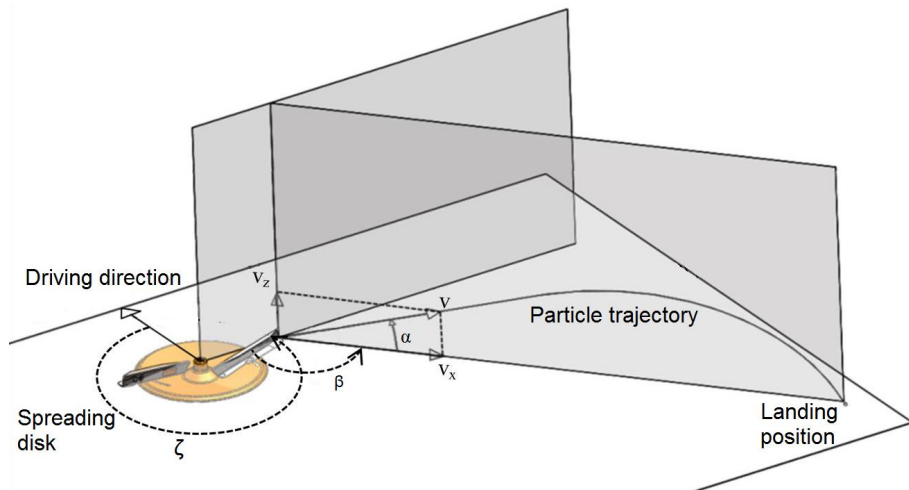

Figure 1.3. Schematic overview of a fertilizer particle being ejected from a centrifugal spreader, describing a trajectory through the air and landing on the ground. The particle leaves the spreader at angular outlet position ζ, with horizontal outlet angle β and vertical outlet angle α (modified from: Vangeyte, 2013))

Centrifugal spreaders can be equipped with two types of sensor technology providing feedback on the spreading process. First of all, sensors can be used to determine the mass flow rate to the discs in real time to ensure that the correct dosage of fertilizer is applied. This is done using load cells (often used in combination with a tilt sensor), pressure- (in the case of hydraulically driven spreading discs) or torque sensors. The latter two systems have the advantage that the mass flow rate of both discs can be independently controlled. These systems assure that on average the correct amount of fertilizer is applied on the field, however they do not provide information about its distribution over the application area (Hensel, 2003). For this, a second type of technology is used. Sulky developed the "Justax" system, consisting of two aluminium rails equipped with piezoelectric sensors (transducing mechanical impacts into a voltage) on a rotating arm that was swept through the fertilizer flow. The system provided general information about the main angular distribution of particles around the disc. The system had to be frequently renewed due to corrosion (Cointault et al., 2008). Amazone developed the "Argus" system, which consisted of a camera system with pulsated IR-illumination to reduce ambient light interference. The system

compared measured distributions with databases stored in the on-board computer and performed online corrections. Rauch together with MSO GmbH developed the "Axmat Plus" system, consisting of 27 radar sensors mounted around one of the spreading discs. They measure the position and expansion of the particle flow. The system is also available for both spreading discs ("Axmat Duo"). Amazone recently offers the possibility to add a similar system, named "Argus Twin" to their spreaders. Both manufacturers offer their radar sensor as feedback sensor for automatically controlling the position of the orifice. These systems however are black-box and measure only a limited amount of parameters related to the spreading process. Therefore, they cannot directly predict the spread pattern of a centrifugal fertilizer spreader.

For spreading at the borders of the field, specific equipment such as deflector plates is used to limit the number of particles being spread outside the field (see Figure 1.4).

Figure 1.4. Deflector plates (the "Limiter" system of Amazone) mounted before the spreading disc for spreading towards the boundary of the field (from: Amazone)

1.2.3. Spread pattern
1.2.3.1. General

The mass distribution pattern of fertilizer on the ground, generated by a fertilizer spreader is generally called a spread pattern and can be expressed in one or two spatial dimensions (Dintwa et al., 2004b). Spread patterns are measured to assess spreader performance on farm-level and by spreader manufacturers to design spreading charts for different fertilizer types (Van Liedekerke et al., 2009a). The one-dimensional spread pattern, perpendicular to the direction of travel is called the transverse spread pattern. Because of their working principle, centrifugal fertilizer

spreaders generate Gaussian, triangular or trapezoid shaped transverse spread patterns (Olieslagers et al., 1996; Grift, 2000). Because of this, overlap is necessary between subsequent swaths to achieve a homogeneous distribution (see Figure 1.5).
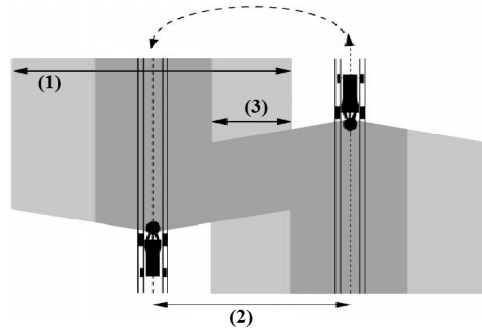

Figure 1.5. Overlap of spread patterns between two subsequent swaths. Terminology: (1) spreading width, (2) working width, (3) overlap (modified from: Tissot et al., 1999)

Most often, a back-and-forth trajectory is used on the field, meaning that successive swaths have opposite driving directions (Vangeyte, 2013). The shape of the transverse spread pattern has an effect on the overall spreading uniformity. "M"- and "W"- shaped patterns should be avoided (Fulton et al., 2001). The spread pattern must be symmetrical around the spreader centre to assure a uniform distribution with fixed working widths. Furthermore, the ends of the spread pattern should not be too steep because this increases the variability of the overlapped distribution in case of small deviations from the pre-set working width (Olieslagers et al., 1996). Figure 1.6 illustrates the transverse spread pattern generated by a centrifugal spreader in practice.
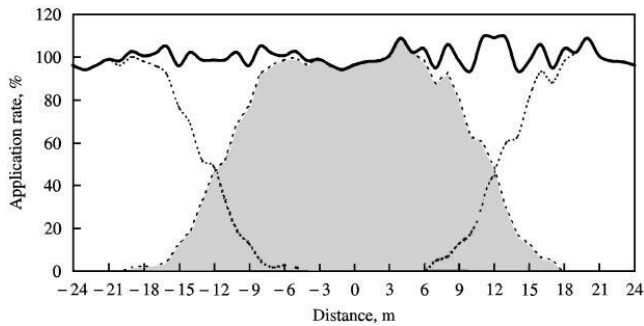
Figure 1.6. Transverse spread pattern for single swaths (dotted lines) and after overlapping subsequent swaths with a working width of 24 m (solid line). (from: Tissot et al., 1999)

The coefficient of variation (CV), determined as by the ratio of the standard deviation and the mean of the application rate after overlap, is often used to quantify the homogeneity of the transverse distribution after overlap. According to the European standard EN13739 (2011), this value should not exceed 15%. Quality assurance programs throughout the world use other tolerance levels, for example the New Zealand Spread mark certification employs limits of 15% for nitrogen fertilizers and 25% for other fertilizers and lime (Grafton et al., 2016).

Because the transverse spread pattern is not steep at the edges, the centrifugal spreader is generally less suited for boundary or border spreading compared to e.g. pneumatic spreaders. However, as mentioned in section 1.2.2, specific equipment can be used to limit the amount of particles being spread over the field edge (economically but also ecologically important, especially in case the field is next to a watercourse) while still maintaining an accurate application rate at the border zone of the field (important from an economical point of view). Generally, there are two ways for spreading the field borders using a centrifugal spreader. The first way is by spreading from a distance (often half the working width) towards the border (see Figure 1.7.a) and using special equipment (e.g. border spreading vanes, tilt systems, deflection systems) or spreader settings (e.g. disc rotational velocity in case of a hydraulic spreader) to limit the spreading width of the spreading disc at the side of the border. The second way is by spreading from the border (see Figure 1.7.b) by using only one spreading disc (the orifice of the disc at the side of the border is closed). This is only possible with off-centric spreaders and in most cases, it is still necessary to use specific deflection plates.
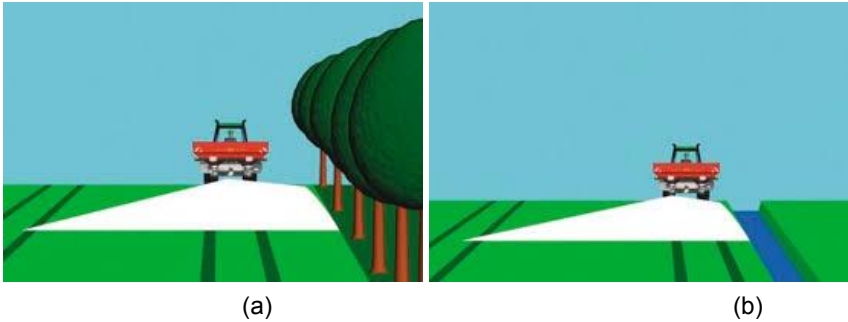
<center>(a)   (b)</center>

Figure 1.7. Spreading towards (a) and away from (b) the border (from: Kverneland)

The two-dimensional spread pattern from a stationary spreader is called a static spread pattern (see Figure 1.8). It shows that the distribution is not line-shaped and has two spatial dimensions. From the static spread pattern, the transverse spread pattern can be calculated by summing the values in the driving (longitudinal) direction and taking into account the time of spreading and the tractor velocity.
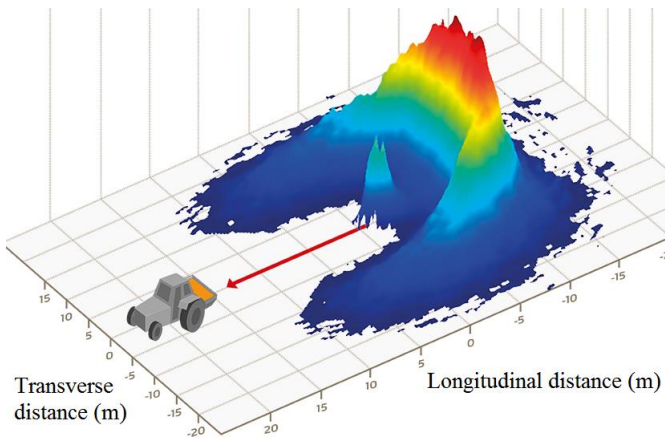

Figure 1.8. Static 2D spread pattern (from: Piron and Miclet, 2011)

1.2.3.2. Parameters influencing the spread pattern

General

The main factors influencing the spread pattern of centrifugal fertilizer spreaders can be categorized in different groups: the spreader settings, the physical properties of the fertilizer particles, the operator behaviour and external factors such as wind or slope (Olieslagers et al., 1996; Yule & Grafton, 2013).

Spreader settings

From a research point of view, the centrifugal spreader has the advantage that many parameters can be set (see Table 1.1). This however involves that these parameters must be precisely controlled (Hofstee 1995). Many parameters are manufacturer-specific and must be correctly set according to the spreading charts provided by the spreader manufacturer.

Table 1.1. Overview of different spreader parameters influencing the spread pattern of centrifugal fertilizer spreaders. The parameters adaptable during spreading are indicated by (*), this may not be true for all spreaders (based on Hofstee, 1995; Olieslagers et al., 1996; Yildirim, 2006, 2008)

Disc	Radius
	Cone angle
	Distance between disc centres
	Angular velocity (*)
	Rotation direction
	Height above ground (*)
	Tilt
Vane	Shape
	Position
	Amount
	Height
Orifice	Shape (*)
	Position (*)
Hopper	Fill level

Important design factors of spinning discs are the radius and the cone angle. Conical discs are used to discharge fertilizer particles with a vertically directed velocity component to increase the spreading width. For this purpose, also higher angular velocities of the disc can be used (Yildirim, 2006a), although the resulting higher impact can increase the number of broken particles. Other design parameters are the number of vanes (Yildirim, 2006b), their shape (Hofstee, 1995), height (Yildirim & Kara, 2003) and position (Hofstee, 1995; Villette et al., 2005). The tilt angle of the discs is also important as it affects the vertical angle of the fertilizer particles and it can change the drop point of fertilizer particles on the disc. Parish (2003) investigated the effect of inclining or declining the spreader (front-to-rear out of level). Experiments were conducted with walk-behind spreaders at two angles (5° and 10°). The resulting spread patterns were highly distorted in some cases with CV values ranging from 10% to 48%. The effect of side-to-side out of level, for example caused by the three-point hitch or the inflation level of the tires, was investigated by Yildirim (2008) for two different fertilizer spreaders at two angles (5° and 10°) and showed severe distortions of the transverse spread pattern, indicating the importance of a correctly levelled fertilizer spreader.

The size of the orifice determines the mass flow rate of fertilizer particles to the spreading discs and therefore affects the general application rate. Many different orifice shapes are used in practice and their shape has a large influence on the motion of particles on the disc (Olieslagers et al., 1996). Parish (2002) found that rate adjustments that simultaneously shift the position of the drop point relative to the spreading disc can distort the spread pattern. Simulation results by Olieslagers et al. (1996) and Kweon and Grift (2006) and experimental results by Reumers et al. (2003) and Yildirim & Kara (2003) show that changing the mass flow rate by increasing the size of the orifice also affects the shape of the spread pattern. This is illustrated in Figure 1.9: changing the size of the orifice by increasing the segment angle of the orifice clearly altered the shape of the transverse spread pattern from triangular to an undesired M-shape. Changing the dimensions of the orifice alters the initial drop point of the particles on the disc which therefore changes the trajectory of the particles on the disc and their velocity and outlet angle after being ejected.
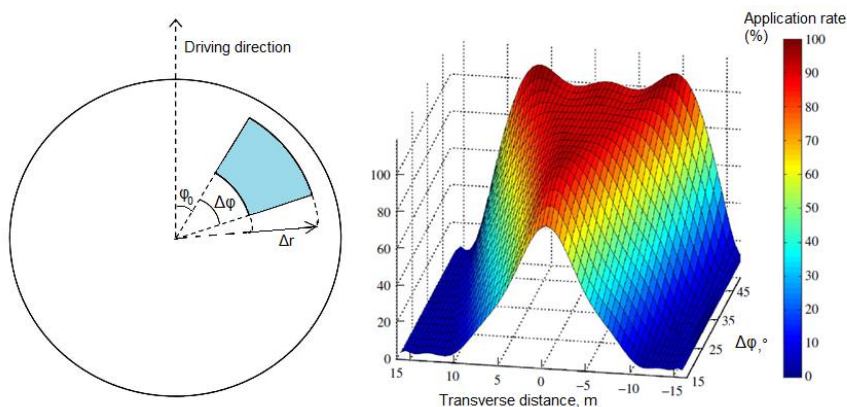
Figure 1.9. Simulated effect of different orifice sizes on the transverse spread pattern. The orifice has a segment radius (Δr) and a segment angle (Δφ). Increasing one or both will increase the flowrate. In this case, the segment radius was kept constant while the segment angle was varied (from: Kweon & Grift, 2006)

This is especially important for VRA, because this implies that not only the mass flow rate but also other adjustments are necessary to adjust the shape of the spread pattern (Hofstee et al., 1995; Olieslagers et al., 1996; Fulton et al., 2001; Kweon and Grift, 2006; Yule & Grafton, 2013).

Parish (1999) showed that the spreader fill level had an effect on the mass flow rate from the hopper. At 10% fill level, the flow rate was 45% lower compared to the flowrate at 50% fill level. The effect on the shape of the spread pattern was not investigated.

<u>Fertilizer physical properties</u>

According to Hofstee & Huisman (1990), the performance of a spreader and the shape and quality of the spread pattern is largely dependent on the physical characteristics of the fertilizer particles. Cool et al. (2016b) conducted experiments with different fertilizer types with identical spreader settings. The resulting spread patterns were clearly different (see Figure 1.10).
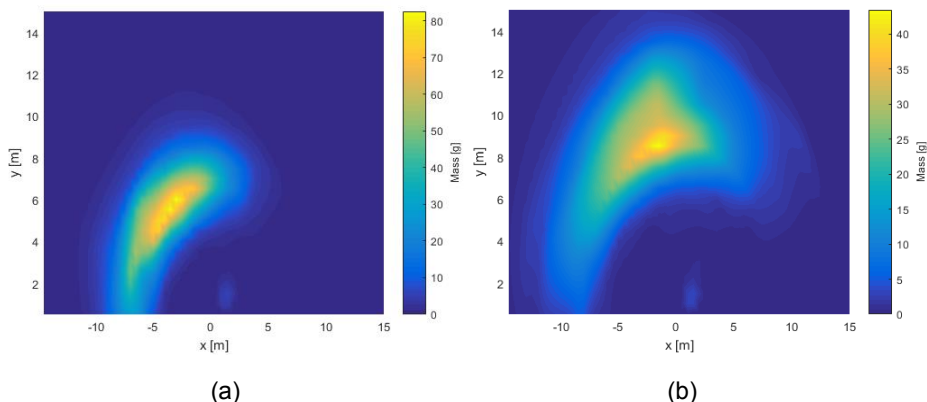
Figure 1.10. Static spread pattern obtained for two different fertilizer types: CAN (a) and KCL (b) at the same spreader settings (from: Cool et al., 2016b)

The most important physical properties of fertilizer particles influencing their motion on the disc and motion in the air are their size distribution, density, particle shape, particle strength, coefficient of restitution and drag coefficient (Hofstee & Huisman, 1990; Hofstee, 1992; Aphale et al., 2003). Particle size has a large influence on the particle motion through the air (Hofstee & Huisman, 1990). Together with the true particle density, it determines the mass of the particle. Generally, particles with a higher mass will travel further compared to lighter particles (Parkin et al., 2005; Yule & Grafton, 2013). The particle size distribution, generally measured by sieving, describes the within-product variation in particle size which can be very different between different fertilizer types (Hofstee, 1992; Aphale et al., 2003; Lawrence et al., 2007). Spreading experiments by Parkin et al. (2005) showed a significant effect of particle size distribution on the spreading width. Differences in particle size can cause segregation during handling and transport (Tissot et al., 1999; Miserque & Pirard, 2004). Particle size also effects the mass flowrate. At the same hopper settings, smaller fertilizer particles flow faster than larger ones. This indicates the importance of a correct orifice setting (Padfield, 2011).

The friction of the particles with the spreading vanes and the spreading disc affects their motion on the disc (Hofstee & Huisman, 1990; Olieslagers et al., 1996), which determines the outlet velocity of the particles, the outlet angle and the outlet position (or duration of stay on the disc). Different methods have been developed to measure this parameter, both by determining the static coefficient of friction (Hofstee & Huisman, 1990; Aphale et al., 2003) and by determining the apparent coefficient of friction (Grift

et al., 2006; Kweon et al., 2007; Villette et al., 2010), which accounts also for side effects such as rolling of particles, aerodynamic behaviour by the rotational movement of the disc and interactions between particles. Differences in friction coefficient can be found between different fertilizer types but also between similar fertilizer types from different manufacturers (Hofstee, 1992). Van Liedekerke et al. (2009b) performed spread pattern simulations and considered also friction between fertilizer particles. The particle-particle (internal) coefficient of friction however is very difficult to measure and the authors indicated that no accurate data was available for this. Simulations indicated that increasing this parameter slightly reduced the outlet speed and outlet angle of the particles, however to a more limited extent than friction between particles and the spreading vanes. According to the authors, this can be caused by the fact that normal forces for particle-particle contact act more randomly, therefore partially cancelling each other out.

The coefficient of restitution (calculated as the ratio of the rebound velocity to the impact velocity) determines the elasticity of fertilizer particles (Inns & Reece, 1962; Hofstee & Huisman, 1990). The breaking force has an indirect effect on the particle motion. When exceeded, particles are fragmented into smaller pieces, reducing their size and severely affecting their aerodynamic behaviour. Hofstee (1992) found an increase in breaking force for larger particles.

The drag coefficient C_d has an influence on the aerodynamic behaviour of the particles and their travelled distance. It is related to the shape of the particles, their size and velocity and also depends on the medium the particle is travelling in (therefore often expressed in function of the Reynolds number). Some authors (Olieslagers et al., 1996; Reumers et al., 2003b; Vangeyte, 2013) assumed fertilizer particles to be spherical and therefore use well-established empirical equations for calculating the drag coefficient. Others use experimental methods to calculate this parameter. In most cases, this is done by measuring the terminal velocity of fertilizer particle in a fluid (Aphale et al., 2003; Gindert-Kele, 2005) or in a vertical wind tunnel or elutriator (Hofstee & Huisman, 1990; Hofstee 1992). Alternatively, calibration methods are used based on movement of particles in fall tests (Grift & Hofstee., 1997b; Walker et al., 1997; Hofstee et al., 2002). Hofstee (1992) compared results obtained with an elutriator and a fall test. Relatively large differences between both measurement methods were found and were attributed to measurement errors of the elutriator. Grift & Hofstee (1997b) performed fall tests to determine the drag coefficient of different fertilizer particles. They introduced an aerodynamic resistance parameter, named the q-factor, to relate the fall time of fertilizer particles to the fall time of perfectly spherical particles. The factor was used to correct the drag coefficient of fertilizer particles for their irregular

shape. Walker et al. (1997) designed a rotating platform on which fertilizer particles (one at a time) could be placed in the field of view of a camera and two images were taken. They calculated a shape factor, based on the difference between the particle shape on the images and the best fitting circle and correlated this with experimental fall times of particles. An equation was proposed linking the shape factor to the drag coefficient.

Blending different types of fertilizers offers an increased flexibility to the farmer in providing the required nutrients for his crops. However, because each fertilizer type has specific physical properties, particle segregation can occur during the various operations such as filling or emptying a container (Miserque & Pirard, 2004) or during the spreading process (Tissot et al., 1999; Yule et al., 2011). The latter can be caused by a difference in particle motion on the disc, but also during the ballistic flight. According to Grafton et al. (2015b), ballistic separation increases exponentially with particle speed. The segregation effect can cause, even though the blend is distributed homogeneously in the field, a non-uniform chemical distribution. Spreading experiments by Tissot et al. (1999) with two different blends at different rates indicated that the application rate of some components can vary by more than 40%. The authors suggested a double coverage (divide the flowrate and working width by two) to counter this effect.

Operator

The operator is responsible for setting the parameters of the spreader according to the spreading charts provided by the manufacturer. In practice, spreading charts however are not always followed correctly (Vangeyte 2013) causing deviations between the actual and the desired distribution on the field. The tractor velocity has a direct effect on the amount of fertilizer spread. For a given application rate, the mass flow rate must be changed accordingly when changing the tractor velocity. Furthermore, it is important that a constant working width is maintained. Changing the working width will cause local under- or over-applications. The steepness of the spread pattern at the ends determines the sensitivity of the spread pattern to errors in the used working width (Olieslagers et al., 1996). Overlaps can occur at field ends (start and stops) and starting and stopping the spreader at an optimal position can improve the in-field variability (Grafton et al., 2011). Lawrence (2007) and Lawrence et al. (2007) used transverse spread pattern test results and vehicle tracking data to measure and compare the effect of driving accuracy, driving method and field shape on the distribution of fertilizer on the field. The in-field variability was determined using the CV, which was calculated in

two spatial dimensions. Their results indicate that these parameters have a large effect. The biggest gain could be achieved from the driver accuracy and the driving method. Results from Grafton et al. (2011) show that implementation of a differential GPS system (DGPS), can significantly improve the in-field CV. Care however must be taken to account for the positional offset between the GPS antenna and the centre of the spread pattern (see Figure 1.8) and the offset due to system latency while the tractor moves. The total offset depends on many parameters like the machine design, fertilizer type, the working width and the tractor speed (Griepentrog & Persson, 2001).

External factors

Generally, spread tests executed in the field can give different results compared to tests executed under ideal conditions in test halls because of external factors (Parish, 1991; Fulton et al., 2003; Yule & Grafton, 2013; Grafton et al., 2016). These factors can also be responsible for variations in the application rate of fertilizer and the resulting yield losses (Sogaard & Kierkegaard, 1994).

Wind speed and wind direction are important external parameters directly influencing the path of fertilizer particles from disc to the ground of the field (Sogaard & Kierkegaard, 1994). According to Yule (2011), an excessive amount of small particles will cause dust problems and could lead to drift and off-site application in the presence of wind. The effect of wind is difficult to measure in controlled conditions. A field experiment by Grafton et al. (2015a; 2015b) illustrated that there was a large overall effect of crosswind (6 m/s) on the transverse spread pattern, the CV increased from 15% to more than 30%. Although the effect is large, little research has been done on this topic.

The mass flow rate of fertilizer is largely affected by the friction between fertilizer particles (Hofstee, 1995). The friction between particles however depends on the air moisture content and the hygroscopic properties of the fertilizer (Van Liedekerke et al., 2006b). Traditionally, spreaders are tested on flat level sites (Yule and Grafton, 2013). Abbou-ou-Cherrif et al. (2017) simulated spread patterns on non-flat fields (side and longitudinal slopes). Local under-and over-applications of 25 and 45% were respectively found for irregular fields (slope changes in the field). On regular fields (constant slope), application errors were found between ±10°%. Results from an experiment by Grafton et al. (2016) show the effect of spreading on a slope of 10-12° on the transverse spread pattern. Severe distortions of the spread pattern and skewing to one side were observed. Due to slopes, the drop-point where the particles reach the

disc, may change (Yule and Grafton, 2013). Another external factor having an effect on the spread pattern is the fact that surface irregularities are present on the field. An experiment was conducted by Parish (1991b) to determine this effect. The surface roughness caused erratic bouncing of the particles on the disc, resulting in a significant change of the spread pattern. Their results showed that larger and spherical particles were less affected than smaller, irregular particles.

1.3. Determining the spread pattern of a centrifugal fertilizer spreader
1.3.1. General

Spread patterns can be measured for multiple reasons. Spreader manufacturers determine spread patterns to design spreaders and create spreading tables (Piron et al., 2010). Taking into account the fertilizer type, these tables define the settings of the spreader for a given working width and driving speed to achieve an acceptable distribution of fertilizer at the desired application rate. The spread pattern is also determined at farm level. This can be done for a general assessment of the performance of the spreader for a specific type of fertilizer, but also to calibrate the spreader if the distribution homogeneity is found insufficient or when yield decreases due to uneven application of fertilizer on the field are visible (e.g. streaking or lodging of grain). Various parameters influence the spreading process, as described in previous section. Deviations between the desired and the actual spread pattern can have various reasons: different physical properties between the used fertilizer and the ones in the spreading tables, poor fertilizer quality, the change of physical properties of the fertilizer due to storage and transport, wear on the spreader, a lack of correct spreading charts or misinterpretation leading to an erroneous configuration for the spreader. Depending on the purpose and the stakeholders involved, the spread pattern can be determined in different ways. The traditional approach is by measuring the distribution of particles after they land using collection trays. The spread pattern can also be predicted, by taking into account the physical properties of the particles and simulating their individual trajectories using a ballistic flight model.

1.3.2. Measuring the spread pattern
1.3.2.1. Farm level

At farm level, the transverse spread pattern is determined by placing a row of collection trays perpendicular to the driving direction during spreading on the field (see Figure 1.11). A few trays must to be removed around the centre point to allow the tractor to pass. Because the spread pattern is not line-shaped, the spreader must be activated

and deactivated at sufficient distance from the row of trays to assure that the full distribution is measured. To decrease the amount of particles ricocheting out of the trays, the trays are often internally subdivided into different compartments using plastic grids.

Figure 1.11. Measuring the transverse spread pattern using collection trays on the field. This test was executed to recalibrate the spreader of a farmer since striping in the field was observed

After spreading, the contents of the individual trays must be emptied and their contents weighed (see Figure 1.12) to determine the transverse distribution. Because fertilizer particles can bounce in or out of the collection trays, despite the trays being subdivided (Parish, 1991a), only the relative spatial distribution can be evaluated and not the actual application rate (ASAE 341.2, 1988). The latter must be determined by measuring the mass flow rate from the hopper. By simulating the distribution after overlapping subsequent swaths, the variability of the distribution can be assessed by calculating the CV. When the CV is lower than a specific level (often 15%, see section 1.3.1), the spreader must be recalibrated, meaning that other settings must be found (trial and error) to ensure a more homogeneous distribution on the field. Tissot et al. (2002) reported CV values ranging from 5% to more than 50% for more than 300 spreaders used by farmers in practice. On average, a CV of 25% was found during the tests. After recalibration, the CV was generally reduced with more than 10%. Next to the standard transverse spread pattern, also the case of border spreading should be considered. This is important from an economical point of view, but can be important also for ecological reasons for example when the field is adjacent to a water course.

Figure 1.12. The amount of fertilizer in each collection tray must be collected and weighed

Some manufacturers provide guidelines in their operational manuals to execute transverse spread pattern experiments. Also, more standardized protocols can be followed, e.g. ASAE 341.2 (1988), ISO 5690/1 (1985), EN13739 (2011). These differ in number and size of the trays, the distance between the trays, the number of rows and the number of passes required (Lawrence et al., 2007; Jones et al., 2008). Parish (1986) compared twelve different protocols for a manually operated spreader and two granular materials. Lawrence et al. (2005, 2006), Yule & Lawrence (2008) and Jones et al. (2008) compared different protocols for conventional spreaders. In these studies, significant differences were found between the resulting measured spread patterns. The authors concluded that direct comparisons between different methods must be avoided. Yule & Lawrence (2008) found that removing trays around the centre line of the spreader had a large effect on accuracy, while reducing the number of trays further out had less effect. For large, pulled spreaders with double or even triple tires, this can cause a problem because in those cases a lot of trays have to be removed from the centre region in order to allow the spreader to pass (Yule, 2011). Jones et al. (2008) argued that multiple rows of trays, multiple passes of the spreader and longer trays can improve the accuracy of the transverse spread tests.

Due to the large spreading widths, performing transverse spread pattern tests is a very laborious and time-consuming process. Because they are executed on the field, the experiments are strongly weather dependent. Furthermore, repetitions cannot be performed without exceeding the application rate at the place of measurement, since

fertilizer is applied on the field during each experiment. Farmers often do not have the required equipment or operational knowledge to perform these experiments or to interpret the results and because these tests are time-consuming and labour-intensive, they are expensive to outsource. Therefore, these experiments are often only executed when yield differences due to uneven application of fertilizer are visible in the field. At the moment, there is no mandatory spreader inspection in Europe. A crucial factor for implementing this policy is to have a measurement technique to determine the spread pattern in a faster and less labour-intensive way.

To speed up transverse spread pattern experiments in the field, Lawrence et al. (2003) and Lawrence (2007) proposed a tool to determine the mass in each tray using image processing. A camera was mounted on a tripod at 0.9 m distance from the collection trays. Image processing algorithms were implemented for segmenting the particles from the background and calculating particle parameters (area, minor axis, major axis). Results indicated a strong relationship between the two-dimensional particle area and particle mass measured under laboratory conditions. Laboratory experiments showed a good correlation between the particle mass and the measured size. Results from field tests however indicated an increased level of error as the amount of fertilizer collected increased. According to the authors, this can be caused to the fact that small particles (generally found closer to the spreader, where the application rate is higher for a standard transverse spread pattern) were filtered out by the algorithms. From their experiments, it was seen that post-spreading particle size was smaller than before the spreading process, indicating mechanical breakage of the particles during the spreading process. The accuracy of the method however was insufficient and after each spread test, the collection trays must be emptied manually, the method remains relatively labour intensive. Although their method allows to determine additional information regarding the particle size distribution after spreading and the spatial distribution of the different particle sizes, the inaccuracy in the predicted amount of fertilizer limits further use of this method without combining it with a weighing system.

Hensel (2003) developed a completely different approach. He used a camera system to determine the amount of particles lying directly on the ground after spreading, thus without using collection trays. Pictures of the soil surface were taken at 0.5 m height using a standard digital camera and a flash-light. Image processing algorithms were implemented to segment particles from the background by differences in colour, shape and size. Experiments with three types of fertilizer were performed in laboratory conditions (see Figure 1.13).

Figure 1.13. Fertilizer particles on soil covered with barley detected with image processing (Hensel, 2003)

The number of particles detected by the measurement system was compared with the applied amount. No attempt was made to determine the size of the fertilizer particles, although the images could provide this information. On freshly cultivated soils, the detection rate was 100%, however when crops were introduced, the detection rate decreased significantly because some particles were partially covered by plant parts. Furthermore, also the fertilizer type, soil characteristics and light conditions had an effect. These are important drawbacks of the technique limiting the applicability in practice.

1.3.2.2. Spread halls

Instead of measuring spread patterns on the field, they can also be determined in large spread halls, like in the Faculty of Agricultural Sciences in Denmark (see Figure 1.14). Because external factors are excluded, more accurate and repeatable results are found compared to the field tests mentioned above (Reumers et al., 2003b; Padfield, 2011).

Figure 1.14. Measuring the spread pattern in large spread halls (from: Reumers et al., 2003b)

Through controlling the temperature and humidity of the building, standardized conditions of fertilizer particles are guaranteed. Because measurements are automated, the process of determining the spread pattern is less labour intensive. This can be done by continuously weighing individual trays or by transporting their contents to a weighing system using conveyor belts. In these spread halls, transverse spread patterns are measured. To obtain the static, two-dimensional distribution, multiple transverse measurements must be conducted while simultaneously changing the position of the spreader relative to the row of trays (Vangeyte, 2013). Performing these tests however requires large amounts of fertilizer, causing additional costs. After testing, the market value of the fertilizer is very low, due to damage and mixing of different products (Reumers et al., 2003b). Piron & Miclet (2006) developed an innovative measurement system (Cemagref Mineral Bench, CEMIB), consisting of a single row of collection trays and a rotating frame. The system measures the static spread pattern by rotating the spreader around the radially placed row of trays which are continuously weighed. Compared to the standard spread halls, considerably less space is required (40 m x 10 m). The two dimensional spread patterns offer much more insight in the spreading process compared to one-dimensional transverse spread patterns (Piron et al., 2010, 2011). Therefore, and because of the fact that they are measured in an automated and time-efficient way, the system has been implemented by several manufacturers for designing spreaders and to develop spreading charts (see Figure 1.15).

Figure 1.15. Measuring setup for determining the static spread pattern of the spreader used by Kverneland (from: www.vicon.eu)

The main drawbacks of these measurement systems is that they still require a lot of space, which makes building and maintaining these spread halls very expensive (Van Liedekerke et al., 2009a) . Because only a few of these test facilities exist in Europe, it is difficult to use them for calibration of spreaders of farmers, because this would require long distance machinery transport (Vangeyte, 2013). Although the mass distribution can be measured in an accurate way, the system does not measure the particle size distribution. The system offers little insight in the spreading process and the influence of physical parameters of particles on the spread pattern.

1.3.3. Predicting the spread pattern
1.3.3.1. General

Measuring spread patterns using collection trays to assess the performance of spreaders at farm level remains a very time-consuming and laborious process. Performing experiments in test halls using automated weighing systems improves the accuracy and repeatability of the experiments, however they require large, expensive test facilities. Therefore, alternative techniques have been developed in literature to determine the spread pattern using a 'predict rather than collect' approach. These techniques should allow a more affordable assessment of spreader performance at farm level (Grift & Hofstee, 1997b) or in controlled environments (Reumers et al., 2003b) and can provide more insight in the parameters involved in the spreading process compared to the collection methods mentioned above. Furthermore, they can be used to design control systems for variable rate-applications (Olieslagers et al., 1996; Kweon & Grift, 2006), because changing the application rate also affects the shape of the spread pattern (see section 1.3.2.2).

Two different approaches can be identified to predict spread patterns of centrifugal fertilizer spreaders: the modelling approach (1.3.3.2), where the behaviour of particles on the disc and subsequently in the air is modelled. And secondly, the hybrid approach (1.3.3.3), where specific parameters of particles after leaving the spreader are measured and combined with a ballistic flight model to predict the landing positions of the particles.

1.3.3.2. Modelling approach

Many authors determined sets of differential equations with analytical or numerical solutions to describe motion of individual particles along the spreading vanes, starting with geometrical and physical properties of the spreader and fertilizer particles (Patterson and Reece, 1962; Inns and Reece, 1962; Cunningham, 1963; Cunningham and Chao, 1967; Hofstee, 1995; Olieslagers et al., 1996; Aphale et al., 2003; Dintwa et al., 2004a; Villette et al., 2005; Cool et al., 2014). The models illustrate that the particle dynamics depend on fertilizer physical properties and spreader parameters and provide a better general understanding of the spreading process. Some authors have implemented these equations in simulation models that predict spread patterns of fertilizer spreaders (Griffis et al., 1983; Olieslagers et al., 1996; Dintwa et al., 2004b) using ballistic flight models to simulate trajectories of individual particles and their subsequent landing positions. The simulated spread patterns however show large differences with experimentally measured distribution patterns. According to Tissot (1995), this is caused by the fact that these models do not consider particle interactions, the impact between particles and vanes, the changing particle characteristics and the fact that an unpredictable amount of particles is not taken up by the vanes. Therefore, these models cannot be used for accurately predicting spread patterns in practice (Tissot, 1995). Olieslagers et al. (1996) and Dintwa et al. (2004b) assumed that discrepancies between simulated and measured spread patterns were mostly owing to particle interactions and suggested to adjust simulation input parameters (calibration factors) to fit experimental data. Olieslagers et al. (1996) modified the orifice dimensions, while Dintwa et al. (2004b) used the landing area of the particles on the disc as calibration factor.

Tijskens et al. (2005) and Van Liedekerke et al. (2005; 2006b; 2009a; 2009b) modelled an interactive particle flow on a centrifugal fertilizer spreader using Discrete Element Method (DEM) simulations. The drawback of the DEM approach is that they require input parameters that are difficult to obtain to characterize the physical behaviour of fertilizer particles (Villette et al., 2017). At reduced disc speeds resulting in small

spreading widths, they showed promising results, however increasing deviations were found at higher and more realistic disc speeds (Van Liedekerke et al., 2008; 2009a).

1.3.3.3. Hybrid approach

Because fertilizer particle motion on the disc proves difficult to predict, hybrid approaches have been developed, combining the measurement of initial parameters of particles close to the disc with the use of a ballistic model to determine the landing positions of the individual particles (Figure 1.16).
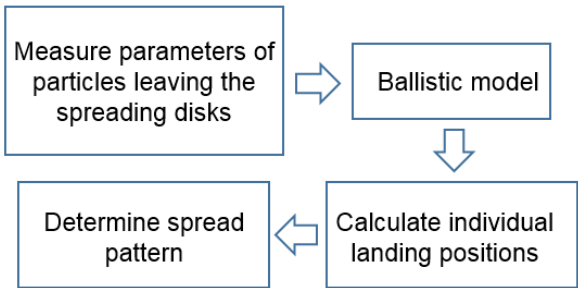

Figure 1.16. General overview of the different steps of hybrid approaches to determine spread patterns of centrifugal fertilizer spreaders

Hofstee (1994) measured three-dimensional particle velocities in a 20 mm x 20 mm area by using a technique based on the ultrasonic Doppler frequency shift using one transmitter and three receivers. Samples were taken in a grid around and just behind the spreader. The technique was also used to determine particle diameters, however proved less accurate. Furthermore, extensive data processing was required. The measurement system was used by Hofstee (1995) to determine the effect of different particle- and spreader related parameters. Grift and Hofstee (1997) developed an optical sensor using two photosensitive arrays, a light source and a converging and diverging lens to determine the radial velocity and the diameter of particle passing through a 30 mm orifice. Particle velocity and diameter were respectively estimated with 5% and 2% accuracy. Grift and Hofstee (2002) fitted the sensor to a rotating arm with encoder to scan the area around the spreading disc. The mounting configuration implied however that only the radial velocity component could be measured, which was according to the authors the reason for the under-estimation of the spreading width. Grift & Kweon (2006) and Kweon & Grift (2006) mounted the optical sensor on a spreader with one flat spreading disc as feedback sensor for variable rate application

of fertilizer for spreaders. The drawback of this technique is that only the radial velocity component is measured and only for one fertilizer particle at a time.

Reumers et al. (2003a, 2003b) developed an experimental setup allowing the measurement of cylindrical distribution patterns, describing the tangential and vertical mass distribution of the granular flow after leaving the discs (see Figure 1.17). The horizontal outlet angles of the particles were manually determined on photographic images of the particle flow. A relatively long camera exposure time was used for this, causing the particle trajectories to appear as straight lines on the images due to motion blur. Reumers et al. (2003a) studied the influence of fertilizer and spreader properties on the tangential and cylindrical distribution patterns. Reumers et al. (2003b) used measured cylindrical and tangential distribution patterns as input for simulations of the spread pattern. Based on the dimensions and the rotational speed of the spreading disc and the horizontal outlet angle, they determined the horizontal velocity of the particles. The vertical velocity vectors were determined based on the measured vertical mass distribution. By using this information and the pre-determined particle size distribution, landing positions were calculated using a ballistic model. When comparing the predicted spread pattern with measurement results obtained in a spread hall using collection trays, relatively large differences were found.
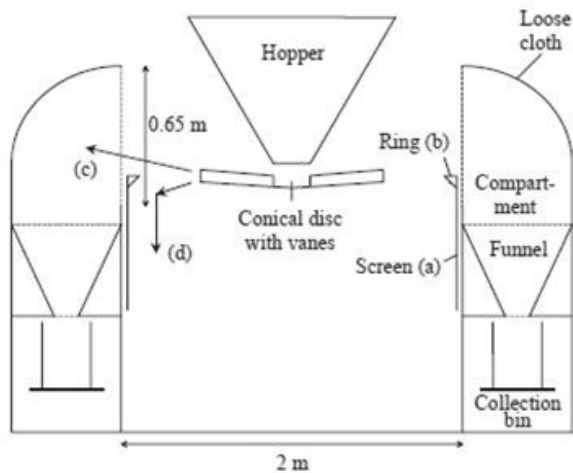

Figure 1.17. Vertical cross-section of experimental setup used by Reumers et al. (2003a; 2003b). The cylindrical distribution pattern of a custom-designed experimental spreader was measured. A vertical adjustable screen (a) was fitted to a ring (b). The upper flow of particles (c) ended up in the compartments, while the lower flow (d) was blocked. By increasing the screen height and subsequently calculating the mass in the collection bins, the cylindrical distribution was determined

Cointault et al. (2003) used a high resolution digital camera, mounted 890 mm above the granule flow, to visualize fertilizer particles leaving a designed-made experimental spreader in a field of view of approximately 1 m² (see Figure 1.18). The multi-exposure technique was used as low cost alternative for high speed cameras: a specifically designed flashing unit provided multiple (8 in total) flashes within the exposure time of the camera. This resulted in multiple projections of each fertilizer particle on the images (see Figure 1.19). The illumination system had a relatively long recycle time (1 s) and was therefore synchronized with the spreading process. Image processing algorithms were implemented to determine the velocity and horizontal outlet angles from the multi-exposure images. Motion estimation was performed using a theoretical model of particle trajectories and Markov Random Fields method (MRF). This method was however very time consuming and sensitive to illumination invariance between subsequent flashes (Hijazi et al., 2009). Furthermore, accurate initialization parameters were required which were difficult to obtain.
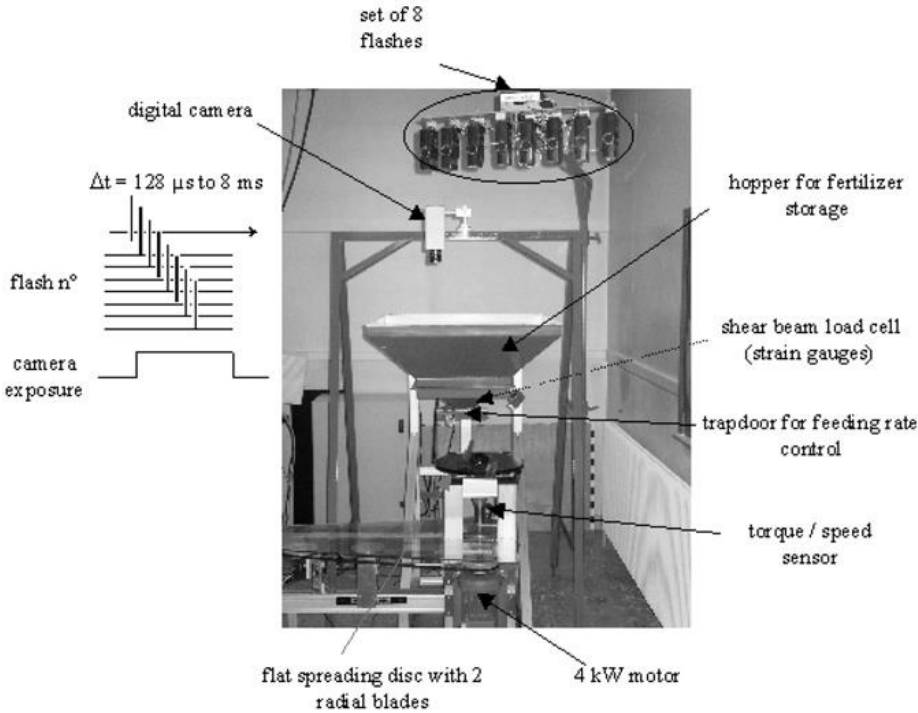

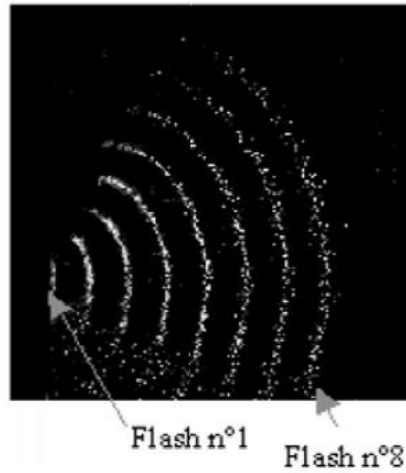**Figure 1.18.** Measurement setup with experimental test spreader (Cointault et al., 2003)

Figure 1.19. Multi exposure image created by flashing eight times during one camera exposure (Cointault et al., 2003)

Hijazi et al. (2008) evaluated two alternative methods for motion estimation: block matching and Gabor filters. They also presented an improved illumination system based on LEDs (Hijazi et al., 2013). However neither proved superior to the previous approach. A new motion estimation algorithm was developed by Hijazi et al. (2010) based on cross-correlation. Algorithms based on cross-correlation are generally based on a single stage algorithm: for each pattern in the image taken at one time step, the position in a second image taken at a second time step is found by searching for the highest correlation value. However, because particles are similar in shape, these algorithms were not giving the expected results (Hijazi et al., 2009). Therefore, a two-step algorithm was developed. Firstly, global velocity vectors were calculated based on the shape of the throw in its two subsequent positions. Secondly, the results were refined by estimating the local motion for each pixel of the particles using cross-correlation. Correlation peaks were interpolated to obtain sub-pixel accuracy. The specific parameters of the algorithm are discussed in detail by Hijazi et al. (2011). To validate the results of the algorithm, simulated images of fertilizer throws were generated (see Figure 1.20).
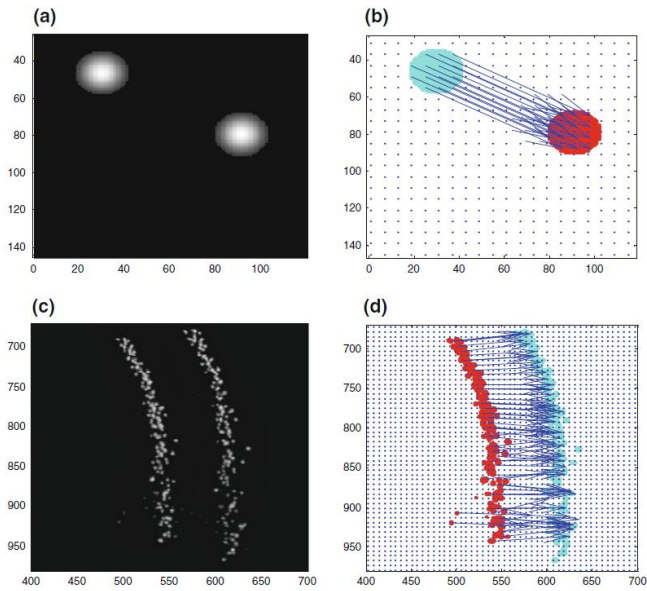
Figure 1.20. Simulated image of two fertilizer particles (a), corresponding velocity vectors obtained with the cross-correlation algorithm (b), real image of two fertilizer throws (c), corresponding velocity vectors obtained with the cross-correlation algorithm (d)

The results revealed a more accurate matching of particles compared to the MRF method of Cointault et al. (2003). Furthermore, only two successive projections were necessary for each particle instead of eight. According to the authors, the obtained sub-pixel accuracy makes it possible to use lower resolution cameras which are more affordable to implement directly on the spreader.

The measurement technique developed by Vangeyte and Sonck (2005) and Vangeyte (2013) is similar to that of Cointault et al. (2003). The field of view however was much smaller, thus yielding a higher particle resolution. Fertilizer particles are however ejected in a much wider spreading area. Therefore, the camera was mounted on a rotating arm, pivoting around the centre of an experimental test spreader (see Figure 1.21).
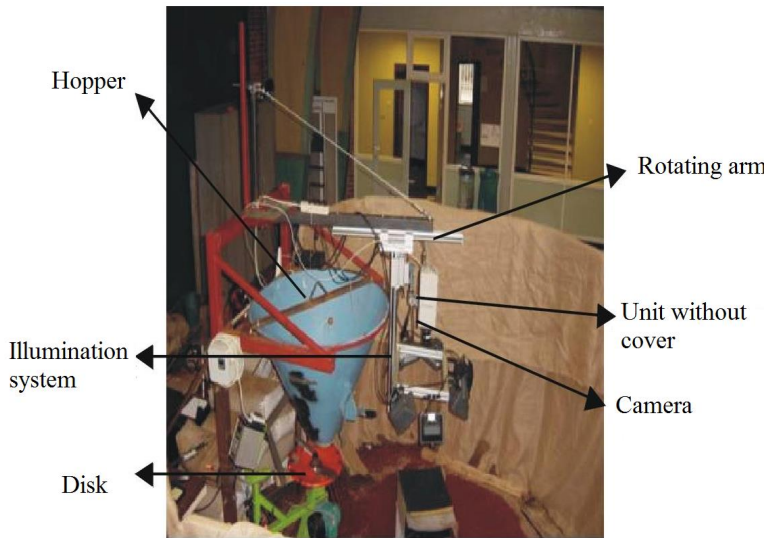
Figure 1.21. Measurement setup with experimental test spreader (Vangeyte, 2013). The camera was attached to an arm which was rotated around the measurement zone

Two different measurement techniques were evaluated: a high speed camera and a standard digital camera combined with the multi-exposure technique using a LED stroboscope. Image processing algorithms were implemented to determine the two-dimensional velocity and horizontal outlet angle of the particles. Small differences were found between both measurement approaches were found. It was shown that errors in the estimated horizontal outlet angle occur due to the fact that trajectories are not perfectly parallel to the camera plane. To predict the spread pattern, an approach similar to Reumers et al. (2003) was used: the vertical outlet angle was determined based on the measured horizontal outlet angles and the distribution pattern measured with a cylindrical collector. This was identified as an important drawback of the technique. Furthermore, the measurement system was only capable of determining the spread pattern of a single-disc experimental spreader.

Villette et al. (2006) developed an imaging technique (Figure 1.22) to derive the horizontal velocity and outlet angle based on motion blurred images (Figure 1.23). Experiments were performed using an experimental spreader. A relatively large field of view was used and image exposure was synchronized with the spreading disc. A method based on an optimized Hough transform was developed to automatically identify a large number of particle trajectories and determine their velocity based on

the measured horizontal outlet angle. Due to the fact that only two-dimensional information was obtained, the technique was applicable only in the case of flat spreading discs, assuming that particle trajectories were parallel to the image plane. And even in that case, particles leave the spreader with a vertical angle (Villette et al., 2010), causing errors in the calculated velocity vectors.
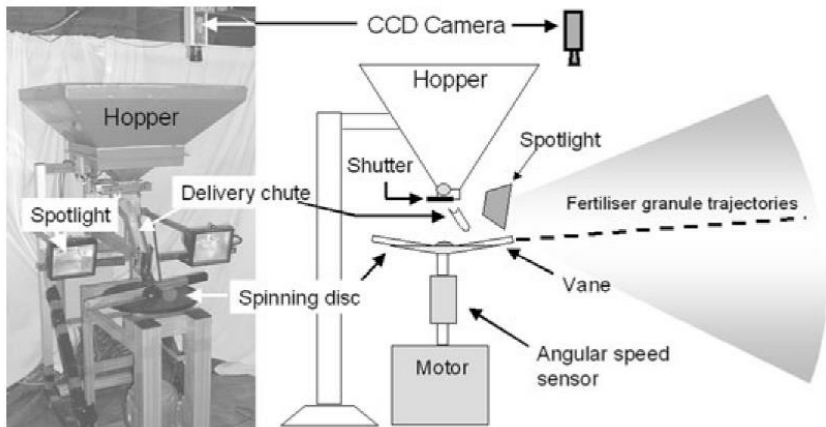

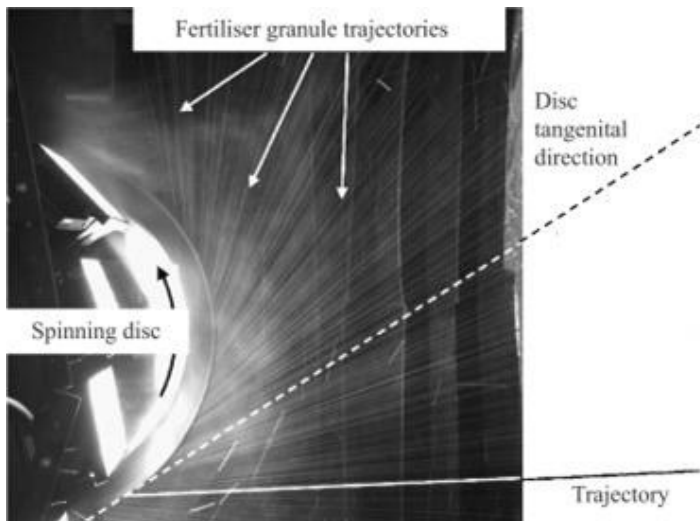**Figure 1.22.** Measurement setup with experimental test spreader (Villette et al., 2010)

Figure 1.23. Motion-blurred images used for determining the horizontal outlet angle of fertilizer particles (Villette et al., 2010)

The motion blurring technique was extended in Villette et al. (2008) to determine three dimensional velocity components of particles based on spreader configuration parameters and the measured horizontal outlet angle. The system however depends on a kinematic relationship between firstly the particle velocity on the disc and secondly the spreader configuration (disc parameters) and horizontal outlet angle (Villette et al., 2005) ignoring particle interactions. The particle size is difficult to obtain using this technique, because moving particles appear as blurred lines on the images. Furthermore, when particles move in a non-parallel way with respect to the camera sensor, the line will vary also in thickness, depending on the distance to the camera. Recently, Villette et al. (2017) developed the Hybrid Centrifugal Spreading Model (HCSM). The model combines theoretical motion models with experimental data obtained at different steps in the spreading process. Experimental data was obtained using a single-disc experimental spreader. Using the image processing technique described above, they determined the horizontal outlet angles of particles leaving the discs. To determine the vertical distribution, they used a method to record particle impacts on a vertical screen, placed close to the disc in the stream of particles (modified technique by Villette et al., 2013). The angular mass flow distribution was deduced from the static spread pattern obtained with the CEMIB measurement system (see section 1.4.2) and the measured horizontal outlet angles. The particle density and size distribution were determined before spreading. Monte-carlo simulations were computed to determine the static spread pattern. Using simulations, they demonstrated that the variability of the CV measurements increased when the application rate or the length of the collection trays decreased.

Research started by Cointaul et al. (2008) and continued by Hijazi et al. (2014) focused on using a stereo-configuration of two high speed cameras to determine the position and velocity of particles in three dimensions (Figure 1.24). The shared field of view for both cameras was large: approximately 1 m². A stereo-matching algorithm was created to find for each particle in the images of the first camera, the corresponding position in the other camera image. Images were transformed to a common plane (stereo-rectification) to simplify the matching process. Based on the position of the particle on the left and right image, the three-dimensional position of the particles was determined. Two subsequent image sets were taken and subsequent positions were matched by using the two-step cross-correlation algorithm by Hijazi et al. (2010, 2011) mentioned above (see Figure 1.20). This way, the three-dimensional velocity of the particles could be determined. The cylindrical distribution pattern of an experimental spreader was measured using a cylindrical collector (see also Figure 1.24) for validation purposes. When comparing the simulated with the measured distribution pattern, a relatively large deviation (relative error of 27%) was found. This could be caused by the low

particle resolution and the limited distance between the cameras, resulting in a high uncertainty for the three-dimensional positions and subsequently the three-dimensional velocities. Because of the low particle resolution, it was not possible to measure the size of the individual particles. Furthermore, the illumination system produced too much heat, the intensity and homogeneity of the generated light was found insufficient and the pose (position and orientation) of the camera with respect to the spreader needed to be manually determined before each experiment, leading to measurement errors.
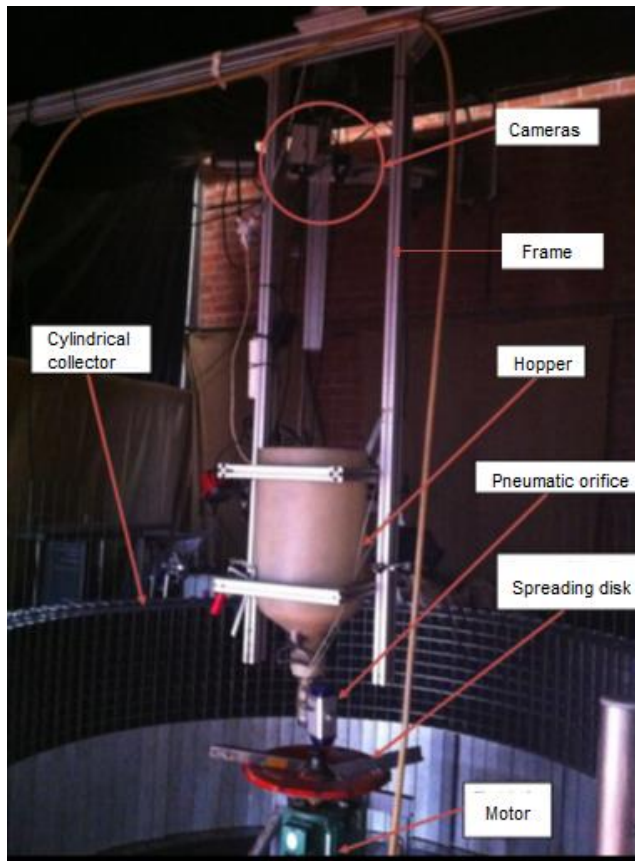

Figure 1.24. Stereovision setup mounted above an experimental spreader. Around the spreader, a cylindrical collector was mounted for validation purposes (Hijazi et al., 2014)

Many of these hybrid approaches seem promising because they can determine spread patterns in a much faster and more space-efficient way compared to the traditional measurement techniques. Because particle parameters are measured, they also provide more insight in the spreading process. Generally, to simulate particle trajectories, the position, velocity, size and drag coefficient of the particles should be known. However little is known about the quantitative effect of these parameters on the predicted landing positions. None of the approaches were able to measure all these parameters in a direct way. Most studies were able to determine the horizontal velocity of the particles. However, particles also have a vertical velocity component, especially in the case of conical spreading discs. Only in the stereovision approach of Villette et al. (2008) and Hijazi et al. (2014), the velocity could be determined in three spatial dimensions. In most studies, the particle size distribution was determined before spreading using sieve tests. Only the optical measurement technique of Grift & Hofstee (1997b) was able to determine the size of the individual particles being spread. Some authors assumed the particles to be perfect spheres and calculated the drag coefficient accordingly while others used experimental methods to determine this parameter. In all cases, simplifications and assumptions were necessary to simulate particle trajectories and calculate spread patterns from this. Until now, none of these techniques succeeded in predicting the spread pattern in an accurate way. Also, because custom-designed experimental spreaders were used for testing, their applicability for fertilizer spreaders in practice remains unclear.

1.4. Objectives

To assess and improve the performance of spreaders, the spread pattern must be determined. Because existing methods to measure the spread pattern are labour intensive and time-consuming or require large indoor test facilities, performing these tests is rarely done in practice. Alternative techniques to determine spread patterns in an accurate way are currently lacking.

The **aim of this research** was to develop and evaluate an automated system, capable of determining spread patterns of commercial centrifugal spreaders in a fast, accurate, cost- and space-efficient way.

Based on a literature review (section 1.3), the most promising approach to fulfil these requirements was to predict the spread pattern using the hybrid approach (section 1.3.3.3), i.e. simulating the spread pattern based on measurements of particle parameters after leaving the discs and then predicting their trajectories and subsequent landing positions using a ballistic model. To avoid the use of expensive high speed cameras to retrieve three-dimensional information, stereovision with multi-exposure was used to determine the particle positions and velocities in three dimensions and to determine their particle size.

The main **objectives** of this thesis are:

Objective 1: Develop a three dimensional ballistic model capable of calculating the trajectories of fertilizer particles and their subsequent landing positions

Objective 2: Determine the physical properties of different fertilizer types and use these in preliminary simulations to quantify their effect

Objective 3: Develop an illumination system for acquiring multi-exposure images of fast-moving fertilizer particles

Objective 4: Design of a system for predicting spread patterns based on individual particle trajectories.

Objective 5: Evaluate the system by performing experiments with a commercially available fertilizer spreader at realistic settings and comparing the resulting spread patterns with results of experiments executed in the field using collection trays

CHAPTER

2

FERTILIZER PARTICLES AND AIRBORNE TRAJECTORY ANALYSIS

2.1. Introduction

Measuring spread patterns using collection trays to assess the performance of centrifugal spreaders at farm level remains a very time-consuming and laborious process (Grift & Hofstee, 1997b). Performing experiments in test halls using automated weighing systems improves the accuracy and repeatability of the experiments, however they require large, expensive test facilities (Reumers et al., 2003b). Using a 'predict rather than collect' approach to determine spread patterns is generally much faster and requires less space compared to the traditional approach. Generally, these techniques use a two-dimensional ballistic flight model to simulate individual particle trajectories in the air and subsequently, the landing positions of the particles. To simulate the trajectories, different input parameters must be known: the position, velocity and size of the particles and their shape or their drag coefficient. Until now, none of the techniques was able to predict the spread pattern in an accurate way (Tissot, 1995; Vangeyte, 2013).

Besides predicting spread patterns, some authors used ballistic models to pre-assess the spreading performance of granular fertilizers. Parkin et al (2005) and Antille et al. (2013a, 2015) performed simulations to determine the size range of particles to enable broadcast application with centrifugal spreaders at certain working widths. Grafton et al. (2015a) suggested the use of ballistic modelling to identify fertilizer types having incompatible ballistic properties to prevent ballistic segregation of fertilizer blends and to determine the effect of different environmental factors such as wind. Except for particle size however, little is known about the quantitative effect of the different parameters involved in predicting the landing position of individual fertilizer particles

Therefore, the aim of this chapter is to (1) design a three-dimensional ballistic model, incorporating the effect of gravity and aerodynamic drag, but also wind. (2) Determine the physical properties of eight different types of fertilizer with varying physical properties. (3) Using these results, perform single-particle simulations to determine the effect of the different parameters on the landing position of fertilizer particles.

2.2. Materials and methods

2.2.1. Ballistic model

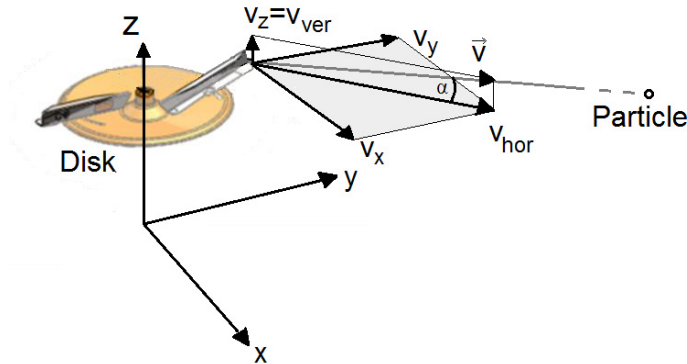Figure 2.1 gives a schematic overview of a fertilizer particle after being ejected by the spreader vanes.

Figure 2.1. Schematic overview of fertilizer trajectory being ejected by the vane. The particle leaves the spreader having a velocity vector $\vec{v}$ and a vertical angle α. The velocity can be decomposed into a horizontal and vertical component (v_{hor}, v_{ver} resp.) or into components relative to a Cartesian coordinate system (v_x, v_y, v_z)

The motion of the particle, moving in stagnant air can be described using Newton's second law:

$$m\frac{d\vec{v}}{dt} = \vec{F_d} + \vec{F_g}$$

(2.1)

with: m and v resp. the particle mass (kg) and the velocity (m/s) of the particle, F_g the gravitational force and F_d the drag force (N)

In these calculations, particles are assumed not to spin, thus the Magnus force, emanating from this was not considered here. Theoretically, fertilizer particles can obtain spin due to friction with the spreading vanes (Cool et al., 2014). Tests with high speed cameras however showed that particles at realistic mass flow rates move as group and exert too much friction on each other to achieve spin at high enough rotational velocity (data not shown).

The particle mass can be measured but in most cases it is more convenient to determine the mass using the equivalent diameter D (m), i.e. the diameter of the

equivalent sphere with the same volume, and the particle true density ρ (kg/m³). In contrast to the bulk density, the true density excludes intra-particular voids.

$$m = \rho \frac{4}{3}\pi \left(\frac{D}{2}\right)^3 \qquad (2.2)$$

The drag force (air resistance force) can be calculated as follows:

$$\vec{F}_d = -C_d \frac{A\,\rho_{air}}{2}|\vec{v}|\,\vec{v} \qquad (2.3)$$

with: C_d the drag coefficient (-), A the projected surface area of the equivalent sphere (m²), ρ_{air} the air density (kg m⁻³)

The negative sign indicates that the direction of the force is opposite to the vector of motion. The drag coefficient depends on fluid and particle properties which are expressed in the dimensionless Reynolds number.

$$Re = \frac{D\,|\vec{v}|\,\rho_{air}}{\mu_{air}} \qquad (2.4)$$

with: μ_{air} the dynamic viscosity (kg/m s)

As mentioned in section 1.2.3.2, some authors in literature regard fertiliser particles as ideal spheres (Aphale et al., 2003; Parkin et al., 2005; Cool et al., 2014; Antille et al., 2013a; 2015) and therefore used well-established equations for the drag coefficient in relation to the Reynolds number. Others determined the drag coefficient experimentally using a horizontal (Parkin et al., 2005) or vertical wind tunnel or fall tests (Hofstee, 1992; Grift & Hofstee, 1997b; Walker et al., 1997; Kweon & Grift, 2006). The main drawback of these techniques is that the terminal velocity is used to determine the drag coefficient which, for most particles, is smaller than the velocity of fertilizer particles reached during the spreading process. While some fertiliser types can have a spherical shape, most particles deviate from this and have a rather irregular shape. In this research, the following equation was used to determine the drag coefficient as a function of the Reynolds number and the particle sphericity (Chien, 1994):

$$C_d = \frac{30}{Re} + 67.289e^{-5.03\phi} \qquad (2.5)$$

with: ϕ the sphericity (-), calculated as the ratio of the surface area of the equivalent sphere and the surface area of the particle.

According to the author, Equation 2.5 is valid for particles with sphericity between 0.2 and 1. From this equation, it can be seen that the drag coefficient depends on the Reynolds number, which depends on the velocity of the particle that changes during

the trajectory. Olieslagers et al. (1996), Grift and Hofstee (2002), Aphale et al. (2003), Vangeyte (2013) considered a constant drag coefficient, indicating that this is a fair assumption given the range of Reynolds numbers typically found in the spreading process of centrifugal fertilizer spreaders. Grift & Hofstee (1997b) considered the drag coefficient as constant for small intervals in the trajectory. Antille et al. (2013a) calculated a new value for the drag coefficient at every numerical integration time-step. Similarly to Antille et al. (2013a), the Reynolds number in this work was recalculated during the trajectory. At each time step during integration, the Reynolds number was recalculated based on the actual resulting velocity at that moment.

To model the effect of a horizontal wind flow, the drag force should be calculated based on the relative motion of the particle to the air.

$$\vec{v}_{rel} = \vec{v} - \vec{v}_{wind}$$

(2.6)

with: v_{rel} the velocity of the particle relative to the air (m/s) and v_{wind} the wind velocity (m/s)

Based on previous equations, the following set of differential equations can be derived, describing motion of a particle in a three-dimensional Cartesian coordinate system (*x,y,z*) with z-axis perpendicular to the ground surface (Figure 2.1).

$$\begin{cases} a_x = \dfrac{d^2x}{dt^2} = -C_d \dfrac{A_{proj}\,\rho_{air}}{2m} v_{rel} \left(\dfrac{dx}{dt} - v_{wind,x} \right) \\ a_y = \dfrac{d^2y}{dt^2} = -C_d \dfrac{A_{proj}\,\rho_{air}}{2m} v_{rel} \left(\dfrac{dy}{dt} - v_{wind,y} \right) \\ a_z = \dfrac{d^2z}{dt^2} = -C_d \dfrac{A_{proj}\,\rho_{air}}{2m} v_{rel} \left(\dfrac{dz}{dt} - v_{wind,z} \right) - g \\ C_d = f(Re, \Phi) \\ Re = f(v_{rel}) \end{cases}$$

(2.7)

with:

$$v_{rel} = \sqrt{\left(\frac{dx}{dt} - v_{wind,x} \right)^2 + \left(\frac{dy}{dt} - v_{wind,y} \right)^2 + \left(\frac{dz}{dt} - v_{wind,z} \right)^2}$$

(2.8)

And: g the gravitational acceleration (m/s²)

The set of differential equations given in Equation 2.7 are non-linear and of second order and must therefore be solved numerically. The forward Euler method was chosen for its simplicity and short processing time (for a given step size). Choosing the step size is a trade-off between accuracy and processing time (Press et al., 1992). In preliminary research, results were compared with the Runge Kutta (RK4) method (data

not shown). Although with the RK4 method, less steps were necessary for a comparable accuracy, there was little gain in processing time for the cases considered.

The initial conditions for solving the equations are: $x(t_0)$, $y(t_0)$, $z(t_0)$, $v_x(t_0)$, $v_y(t_0)$, $v_z(t_0)$. The initial height ($z(t_0)$) is also indicated as h. The initial vertical angle (α, see Figure 2.1) is calculated as:

$$\alpha = \tan^{-1} \frac{v_z(t_0)}{\sqrt{v_x(t_0)^2 + v_y(t_0)^2}} \tag{2.9}$$

Generally, landing positions of fertilizer particles are determined at the time-step where the height (h) of the particle above ground (in Equation 2.7, the z-value) becomes negative. This however causes an over-estimation of the landing position and errors are expected to increase with the step size. Based on the position at the last and the second last time-step, the true landing position, i.e. the point at which the particle centre intersects the ground plane, can be more accurately calculated using interpolation (see Figure 2.2).
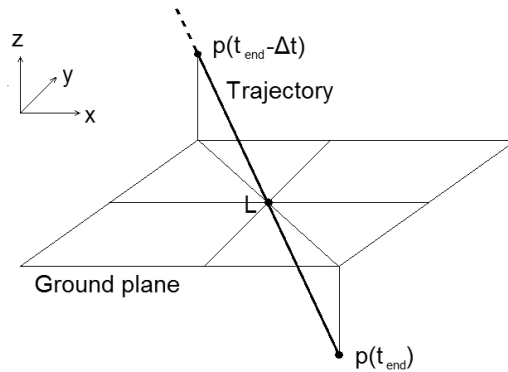

Figure 2.2. Landing position refinement. The actual landing position **L** is calculated by interpolating the position at the last time step t_{end} and the position one time step (Δt) before

Assuming that the particle follows a straight line at constant velocity between the two last time-steps (small time-interval), the landing position **L** in coordinate system x,y,z (Figure 2.2) can be determined as:

$$L$$

$$= \begin{bmatrix} x(t_{end} - \Delta t) + v_x(t_{end} - \Delta t)\dfrac{z(t_{end} - \Delta t)}{-z(t_{end}) + z(t_{end} - \Delta t)}\Delta t \\ y(t_{end} - \Delta t) + v_y(t_{end} - \Delta t)\dfrac{z(t_{end} - \Delta t)}{-z(t_{end}) + z(t_{end} - \Delta t)}\Delta t \\ 0 \end{bmatrix} \qquad (2.10)$$

With: t_{end} the last time-step after which the z-value became negative (s), Δt the step size of the solver (s).

Simulations were performed to determine the effect of step size on the accuracy of the predicted landing position. Step sizes of 1e-2, 1e-3, 1e-4 s were used and the resulting travelled distance was compared to the travelled distance calculated with a step size of 1e-5, since preliminary simulations indicated a high accuracy for this step size (compared to the RK4 method). Different cases were investigated, particles were ejected at low (10 m/s), medium (25 m/s) and at high speed (40 m/s) with vertical angle 0° and 10° (corresponding to a flat and conical disc resp.). The simulation parameters are given in Table 2.1. Landing positions were simulated with and without the refinement step mentioned above.

Table 2.1. Model parameters used for simulating the effect of different step sizes with the numerical solver. Values for particle height (h), sphericity (ϕ), true density (ρ), diameter (D), density of air (ρ_{air}), dynamic viscosity of air (μ_{air}) were based on previous research (Cool et al., 2014). The velocity of wind (v_{wind}) was assumed zero

Parameter	Value	Unit
h	0.750	m
ϕ	0.97	-
ρ	1785	kg/m³
D	3.7	mm
ρ_{air}	1.225	kg/m³
μ_{air}	1.8*1e-5	kg/s m
v_{wind}	0	m/s

2.2.2. Physical properties of fertilizer particles

2.2.2.1. General

Eight different types of fertilizer were selected for this study, see Table 2.2 and Figure 2.3. The fertiliser types are commonly used by farmers in Belgium and were selected based on their different physical properties.

Table 2.2. Different types of fertilizer used in this research (supplier: Aveve Notebaert, Scheldewindeke, Belgium)

Abbreviation	Fertilizer type	Manufacturer
TROP	Tropicote 15.5%N	Yara
NPK18	NPK 18-6-5	Scoriethom
ENTEC	Entec 26% N	Eurochem
KCL	Potassium Chloride 60% K	Scoriethom
PK	PatentKali 30% K	Scoriethom
CAN	Ammoniumnitrate 27% N	Scoriethom
NPK15	NPK 15-15-15	Scoriethom
CYAN	Calcium Cyanamide	Alzchem

Figure 2.3. Different types of fertilizer that were analysed in this study

The general physical properties that are important for the particle dynamics in the air were determined in laboratory conditions. The particle size distribution was determined by sieving using experiments performed according to the standard EN1235/A1 (2003).

The sieves (see Figure 2.4.a) had following mesh sizes: 1.40, 2.00, 2.50, 3.15, 3.55, 4 and 4.50 mm. Both the loose and the tapped bulk density were determined. The loose bulk density was determined as follows (according to EN1236, 1992): fertilizer flows from a funnel into a cylinder with known volume (see Figure 2.4.b), letting it overflow. The surplus was removed using a spatula and the mass was determined. Based on this mass and the volume of the cylinder, the density was calculated.
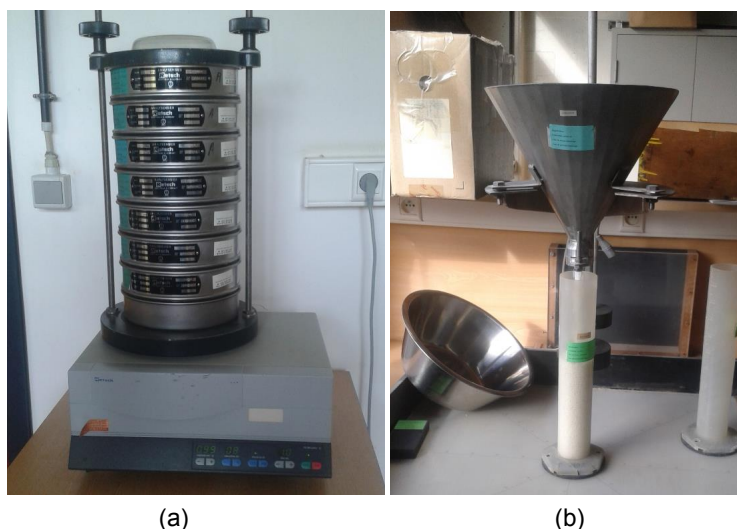

(a)   (b)

Figure 2.4. Sieving device for determining the particle size distribution (a) and equipment used to determine the bulk density (b)

The tapped bulk density was determined in a similar way (according to EN1237, 1992). After introducing the cylinder with particles to vibrations, the surplus was removed and the mass was determined, from which the density was calculated. For both the bulk density and tapped bulk density, two replicates were performed. The particle true density was determined using gas (He) pycnometry, (executed by Quantachrome GmbH & Co; Germany), in contrast to most authors in literature using liquid pycnometry (Aphale et al., 2003; Miserque et al., 2008; Grafton et al., 2015b). Therefore, errors due to dissolved particles and trapped air bubbles were avoided. For all experiments above, representative samples of batches (bags of 50 kg) were taken using specific equipment (Miserque & Pirard, 2004).

The results from the sieve test were used to determine the cumulative distribution function for the particle size. The following s-shaped function was fitted to the data:

$$f(x) = \frac{1}{a_1 + a_2 * e^{-a_3 x}}$$

<div align="right">(2.11)</div>

With: a_1, a_2, a_3 regression parameters (-)

2.2.2.2. Particle shape

The static angle of repose can be used to obtain indications about the shape of particles (Miserque et al., 2001). The angle of repose is the natural angle with the ground that forms a heap of any granular material after having flown freely (Miserque et al., 2008). Measurements were performed in laboratory conditions and according to EN12047 (1995). The procedure for determining this parameter is explained in detail by Miserque & Pirard (2004).

To determine the shape of the particles more accurately and in 3D, X-ray micro-CT was used. This non-destructive scanning technique enables the reconstruction of a virtual model of the object under study allowing visualisation of both the internal and external structures of objects. The Nanowood scanner used at Woodlab-Ugent was used here which is a setup developed at UGCT (Dierick et al. 2014), the Ghent University Centre for X-ray Tomography, in collaboration with XRE (X-Ray Engineering bvba, Ghent, Belgium; www.xre.be). Figure 2.5 shows the scanner being used for a sample of fertilizer.
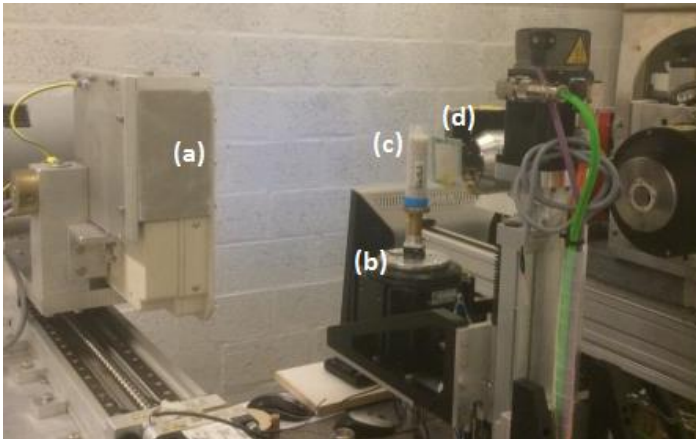

Figure 2.5. Nanowood scanner used for scanning samples of fertilizer in this research: detector (a), platform (b), sample (c), source (d)

The samples were scanned with standard cone-beam X-ray micro CT with a scan time of approximately 20 min per sample. Reconstruction was performed with Octopus (Vlassenbroeck et al. 2007, licensed by InsideMatters: Inside Matters NV, Ghent, Belgium, www.insidematters.eu), a tomography reconstruction package for parallel, cone-beam and helical geometry as well as phase correction and retrieval. Beam hardening correction was applied, both by hard- as well as software filtering. The obtained approximate voxel (the three-dimensional equivalent of a pixel) size was 40 µm. The used scanner has a stationary X-ray source and detector and a rotatable platform on which the fertiliser samples were placed (see Figure 2.5). X-rays travel from the source (cone shaped beam) through the sample to the detector and, depending on the density of the material, are absorbed to a certain extent. By rotating the platform, different 2D projections are obtained on the detector from which a 3D model is finally determined (Figure 2.6). This volume can be represented as different transversal slices.
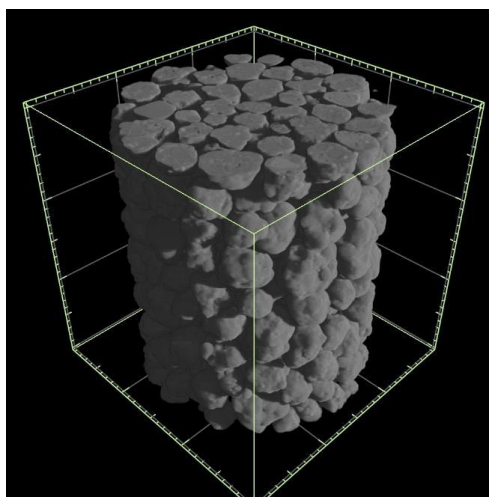

Figure 2.6. 3D model of fertilizer particles obtained after scanning

The measured volumes were further processed using the Octopus Analysis software (v.1.1.1.10), formerly known as Morpho+ (Brabant et al. 2011) and also licensed by InsideMatters, to segment individual particles in the scanned volume. The steps of the procedure are illustrated in Figure 2.7. The data was filtered first using a bilateral filter to decrease noise and preserve the particle edges. Next, a global threshold (manually set for each fertiliser type based on histogram readings) was applied and the resulting values were inverted. To segment individual particles, a distance transform was

applied, followed by a watershed transformation. Incomplete particles lying at the upper or lower border of the scanned volume were removed. Because in some cases over- (individual particles were split) or under-segmentation (multiple particles segmented as one) appeared, the segmentation process was manually corrected.
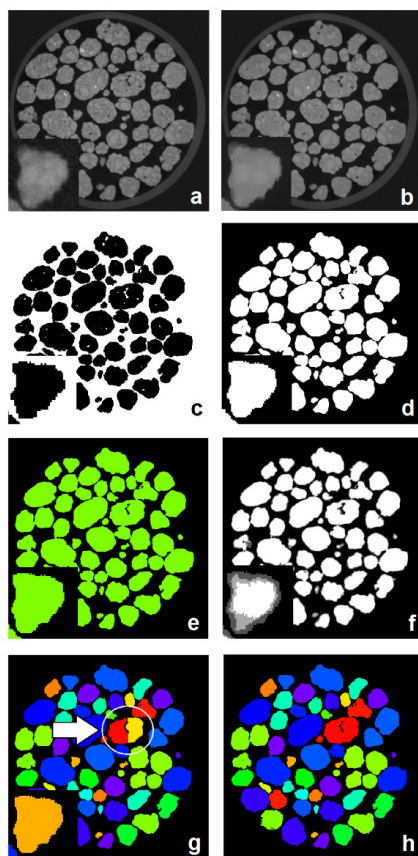

Figure 2.7. Different steps of the image processing algorithms to segment individual fertilizer particles, illustrated for CAN fertiliser (a) Raw, (b) After filtering, (c) Binary, (d) Inverted, (e) Labelled, (f) After distance transform, (g) After particle labelling, (h) Manually corrected. Colours indicate individually segmented particles. The smaller picture in the left bottom of the images (a-g) represents one fertilizer particle

The segmented images were transformed to grayscale and exported for further processing with Matlab (v.2015a, Mathworks Inc, Natic, USA). All transversal images were uploaded in a 3D matrix. After labelling the segmented particles, the volume of

each particle was calculated as the number of connected voxels. The diameter of the equivalent sphere was calculated as:

$$D_{eq} = 2\sqrt[3]{\frac{3}{4\pi}V}$$ (2.12)

With: D_{eq} the diameter of the equivalent sphere (pixels), V the volume of the particle (voxels)

From this, the surface area of the equivalent sphere A_{eq} (pixels) was calculated:

$$A_{eq} = 4\pi D_{eq}^2$$ (2.13)

To remove the voxelisation effect (the edges appear like a stairway), the data was filtered with a low pass filter. From this smoothed object, the surface area $A_{particle}$ (pixels) was determined with the *isosurface* function in Matlab by summing the area of all triangular faces which were generated using this function.

From Eqs. 2.12 and 2.13, the sphericity factor was determined as:

$$\phi = \frac{A_{eq}}{A_{particle}}$$ (2.14)

Residual noise was deleted by specifying a minimum diameter for each particle to comply. For fertiliser particles, this parameter was based on the particle size distribution determined using sieving.

To check the validity of the sphericity calculations, 3D matrices with perfect spheres with sizes similar to fertiliser particles (1, 2, 3 and 4 mm) were generated and the sphericity of these particles was determined. Values between 0.9960 and 0.9997 were found (results not shown). For the experiments with fertiliser, representative samples of 50 g were taken for each fertilizer type and stored in an air-sealed plastic container in which they were scanned. Due to the limited field of view, only the centre part of the container was scanned. Also, similar samples of plastic spheres (diameter 5.96 mm) were analysed to verify the results. Two different samples of fertilizer were taken to have two replicates for each particle type.

2.2.3. Simulations

2.2.3.1. General

The parameters of the ballistic model (section 2.2.1) can be divided in two main groups: particle parameters and environmental parameters, see Figure 2.8. Simulations were performed to determine the effect of these parameters on the landing position. Preliminary results showed very little effect of the dynamic viscosity of air on the travelled distance and therefore, this parameter was not considered here. Ultimately, the effect of the parameters on the spread pattern is important. For this however, the initial parameters (position, velocity, diameter, etc.) of particles leaving a spreader should be known. Until now, no model has succeeded in predicting accurately the motion of fertilizer particles on the disc at realistic settings (see 1.3.3.2) and accurate data from hybrid measurement techniques is lacking (see 1.3.3.3). Therefore, for these simulations, only single-particle trajectories were considered. The effect of the parameters was determined for different fertilizer types. The physical properties of the particle types determined in section 2.2.2 were used for this, as well as general values for the particle velocity and vertical angle, which were based on previous research and literature.
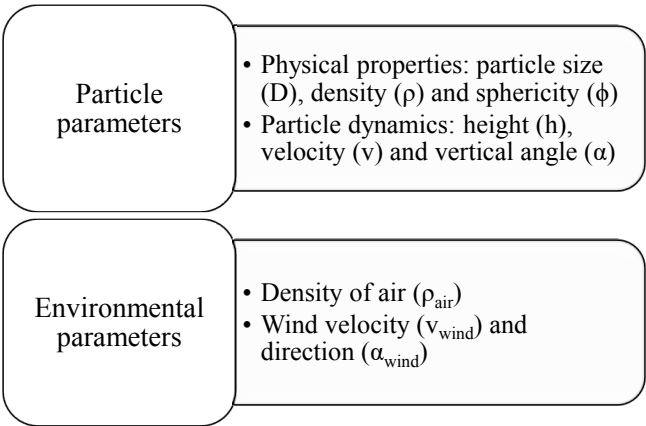

Figure 2.8. Parameters influencing the landing position of the fertilizer particle

Because the particle trajectory lies in a vertical plane (except for crosswind), see Figure 1.3, the effect on the landing position could be represented by effect on the travelled distance. In all cases, particles were ejected in the positive x-direction (see Figure 2.1),

making x the longitudinal direction and y the transverse direction. In all cases, except when crosswind occurs, particles will describe a trajectory in the xz-plane.

2.2.3.2. Effect of particle type

To determine the effect of the particle type on the travelled distance, simulations of particle trajectories for different fertilizer types were performed assuming the same initial conditions. The physical properties for the different fertilizer types were determined in section 2.2.2. For the particle size and the sphericity, the median values determined in sections 2.2.3.1 and 2.2.3.2 were used. Both the case of a flat disc and a conical disc was investigated by assuming a vertical angle of 0° and 10° respectively. Three different velocity cases were investigated: slow (10 m/s), medium (25 m/s) and fast (40 m/s) moving particles. The latter were used to represent particles ejected from a flat and a conical disc respectively. An initial height (h) of 0.75 m, air density (ρ_{air}) of 1.225 kg/m³ and air dynamic viscosity (μ_{air}) of 1.8*1e-5 kg/(m s) was assumed.

2.2.3.2. Effect of individual parameters

The effect of particle type on the travelled distance is a combination of different physical properties (particle size, true density and sphericity). Therefore, simulations were performed to determine the effect of all parameters involved in the ballistic flight (Figure 2.8) individually. The travelled distance was calculated for a range of values for each parameter (Table 2.3), assuming a constant value for the other parameters (Table 2.4). Similarly to section 2.2.3.2, trajectories were simulated for three different velocities: 10 m/s, 25 m/s and 40 m/s and two different vertical angles: 0° (flat disc) and 10° (conical disc). For the particle velocity and vertical angle, trajectories were simulated for particle velocities from 10 to 45 m/s and vertical angles from -5 to 15°. For the effect of wind, both the case of tailwind (negative values indicated headwind) and crosswind was considered. These respectively assume wind in the longitudinal direction (parallel to the particle initial direction of motion) and transverse direction. For crosswind, both the travelled distance in the longitudinal and the transverse direction was determined.

Table 2.3. Range (min and max value) of values for each parameter to determine the effect of the individual parameters

Parameter	Min	Max	Unit
v	10	45	m/s
α	-5	15	°
ϕ	0.8	1	-
h	0.4	1.4	m
ρ	1500	2200	kg/m³
D	1.0	5.5	mm
ρ_{air}	1.15	1.30	kg/m³
v_{wind} (tail)	-10	10	m/s
v_{wind} (cross)	0	10	m/s

Table 2.4. Simulation values for the initial height (h), the sphericity (ϕ), the particle true density (ρ), the particle diameter (D), the density and dynamic viscosity of air (ρ_{air} and μ_{air} resp.). No wind was assumed. Particle parameters were based on results from section 2.2.2). A median sized CAN particle was assumed

Parameter	Value	Unit
h	0.75	m
ϕ	0.97	-
ρ	1785	kg/m³
D	3.7	mm
ρ_{air}	1.225	kg/m³
μ_{air}	1.8*1e-5	kg/(m s)

For each case in section 2.2.3.2, the absolute sensitivity was calculated to quantify the effect of the individual parameters on the travelled distance for the different fertilizer types.

The sensitivity was calculated using the forward difference:

$$\frac{\delta D_{trav}}{\delta \theta_i} = \frac{D_{trav}(\theta_i + \Delta\theta_i) - D_{trav}(\theta_i)}{\Delta\theta_i} \tag{2.14}$$

with: D_{trav} the travelled distance (m), $\Delta\theta_i$ the perturbation factor for parameter θ_i

The perturbation factors are given in Table 2.5. The values for the perturbation factors were chosen because they reflect realistic measurement errors. Instead of using the

particle velocity and the vertical angle, the horizontal and vertical velocity component was used for this analysis.

Table 2.5. Perturbation factors for calculating the absolute sensitivity

Parameter	Value	Unit
D	0.5	mm
ρ	50	kg/m³
ϕ	0.01	-
h	10	mm
V_{hor}, V_{ver}	1	m/s
α	1	°
ρ_{air}	0.01	kg/m³
V_{wind}	1	m/s

By multiplying a measurement error of a parameter with its absolute sensitivity (Equation 2.14), the expected error in the travelled distance can be found, assuming a linear effect for the parameter on the sensitivity.

2.2.3.3. Relative sensitivity

To determine for which parameter the landing position is most sensitive, the relative sensitivity was calculated. To compute the relative sensitivity for a specific parameter, the absolute sensitivity for this parameter was divided by the maximal absolute sensitivity over all parameters and particle types for a specific case (flat or conical disc and low, medium or high particle velocity).

2.3. Results and discussion

2.3.1. Accuracy of the ballistic model

In Tables 2.6 and 2.7, the simulation results are given for vertical angles of respectively 0° and 10°. It can be seen that the step size has a large effect on the accuracy of the predicted landing positions. The results also show that the landing position can be calculated more accurately using landing position refinement, especially for the larger step sizes. In almost all cases, increasing the step size caused an overestimation of the travelled distance. Overall, a step size of 1e-3 s, in combination with the landing position refinement resulted in absolute differences below 9 mm which was considered accurate enough for this application.

Table 2.6. Simulation results for different step sizes (Δt). Three cases were investigated: slow (v=10 m/s), medium (v=25 m/s) and fast (v=40 m/s) moving particles. A vertical angle (α) of 0° was assumed. The landing positions (L) were calculated with and without landing position refinement. The absolute and relative difference (D_{abs} and D_{rel} resp.) was calculated compared to the reference case with time step of 1e-5 s (with refinement of the landing position)

Case	Δt (s)	Without refinement			With refinement		
		L (m)	D_{abs} (mm)	D_{rel} (%)	L (m)	D_{abs} (mm)	D_{rel} (%)
Slow	1e-2	3,6661	97,4	2,73	3,6111	42,5	1,19
	1e-3	3,5739	5,2	0,15	3,5729	4,2	0,12
	1e-4	3,5692	0,5	0,02	3,5690	0,4	0,01
Medium	1e-2	8,1226	194,4	2,45	8,0070	78,8	0,99
	1e-3	7,9447	16,5	0,21	7,9360	7,8	0,10
	1e-4	7,9297	1,5	0,02	7,9289	0,7	0,01
Fast	1e-2	11,5842	150,2	1,31	11,5200	86,0	0,75
	1e-3	11,4502	16,1	0,14	11,4428	8,7	0,08
	1e-4	11,4349	0,9	0,01	11,4348	0,8	0,01

Table 2.7. Simulation results for different step sizes (Δt). Three cases were investigated: slow (v=10 m/s), medium (v=25 m/s) and fast (v=40 m/s) moving particles. A vertical angle (α) of 10° was assumed. The landing positions (L) were calculated with and without landing position refinement. The absolute and relative difference (Dabs and Drel resp.) were calculated compared to the reference case with time step of 1e-5 s (with refinement of the landing position)

Case	Δt (s)	Without refinement			With refinement		
		L (m)	D_{abs} (mm)	D_{rel} (%)	L (m)	D_{abs} (mm)	D_{rel} (%)
Slow	1e-2	5,0474	64,8	1,30	5,0323	49,8	1,00
	1e-3	4,9908	8,2	0,16	4,9875	5,0	0,10
	1e-4	4,9831	0,5	0,01	4,9830	0,5	0,01
Medium	1e-2	13,4863	85,6	0,60	13,4524	51,8	0,39
	1e-3	13,4100	9,4	0,1	13,4059	5,2	0,04
	1e-4	13,4014	0,8	0,0	13,4011	0,5	0,00
Fast	1e-2	20,0268	52,9	0,3	19,9636	-10,4	-0,05
	1e-3	19,9807	6,8	0,0	19,9731	-0,8	0,00
	1e-4	19,9741	0,2	0,0	19,9739	-0,1	0,00

2.3.2. Physical properties of fertilizer particles

Particle size distribution, bulk density (loose and tapped), true density and angle of repose for the eight different fertiliser types are given in Table 2.8. It can be seen that CYAN fertiliser particles were much smaller than other particle types while particles of NPK15 and CAN have the largest size distribution. The bulk density after tapping is between 41 and 85 kg/m³ larger than the loose bulk density. Clearly, the bulk density clearly differs from the true particle density indicating that inter-particle voids are present in a volume filled with fertilizer particles. In most cases, a higher bulk density corresponds to a higher true density, however the relation is not absolute. Although a relatively low bulk density, CYAN particles have a large true density. The true density is smallest for ENTEC and largest for CYAN and PK particles. The angle of repose is largest for KCL indicating a more irregular shape, compared to NPK15 having the smallest value for this parameter.

Table 2.8. Physical properties of fertilizer particles. For the bulk density and true density, two replicates were analysed (1 and 2)

Parameter	Fertilizer type							
	TROP	NPK18	ENTEC	KCL	PK	CAN	NPK15	CYAN
Sieve fraction (%)								
0 - 1.4 mm	0,76	0,08	0,48	2,13	0,87	0,16	0,03	20,52
1.4 - 2 mm	5,83	0,61	4,08	5,42	8,62	0,21	0,14	38,67
2 - 2.5 mm	23,09	2,18	8,63	17,33	21,34	1,33	2,41	23,05
2.5 - 3.15 mm	47,64	23,18	42,22	32,11	35,63	15,98	16,39	15,13
3.15 - 3.55 mm	15,06	24,15	20,24	14,23	12,71	21,96	19,38	2,17
3.55 - 4 mm	7,18	23,58	14,70	13,74	10,23	30,8	43,17	0,40
4 - 4.5 mm	0,44	18,20	7,88	10,76	7,22	18,23	16,32	0,06
>4.5 mm	0	8,03	1,77	4,27	3,37	11,33	2,17	0
D50 (mm)	2,78	3,55	3,07	3,01	2,85	3,7	3,67	1,86
Angle of repose (°)	37,58	38,14	36,18	39,19	36,34	32,36	31,94	32,23
Bulk density[a] (kg/m³) 1	1106	1012	956	1060	1197	1035	1120	1020
Bulk density[a] (kg/m³) 2	1102	1012	956	1061	1194	1033	1115	1014
Bulk density[b] (kg/m³) 1	1179	1065	1015	1149	1283	1074	1178	1097
Bulk density[b] (kg/m³) 2	1181	1061	1019	1142	1276	1075	1176	1101
True density[c] (kg/m³) 1	2020	1830	1690	1970	2220	1780	1910	2220
True density[c] (kg/m³) 2	2010	1850	1690	1970	2220	1790	1910	2210

[a] Loose, [b] Tapped

[c] Determined on three significant numbers in g/cm³

Figure 2.9 shows the best fitting functions for the cumulative size distribution based on the sieving results.
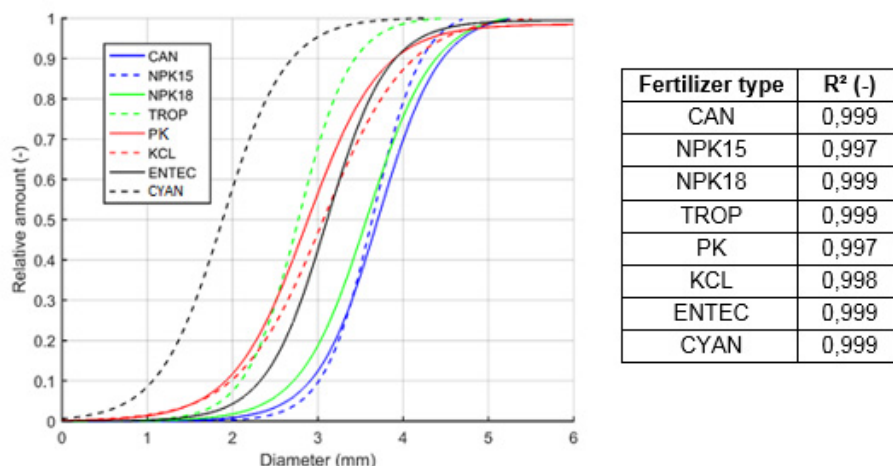

Figure 2.9. Cumulative size distribution for different fertilizer types, best fit to the distribution measured by sieving. The goodness of fit is given as well

Figure 2.10 illustrates the three-dimensional shapes for a plastic sphere, a CAN particle and a KCL particle that were scanned using micro-CT. Very small imperfections on the surface of the ideal sphere can be seen, which are probably caused by the image segmentation process. The KCL particle has a much more irregular shape compared to the CAN particle, which can also be seen by the lower sphericity value.
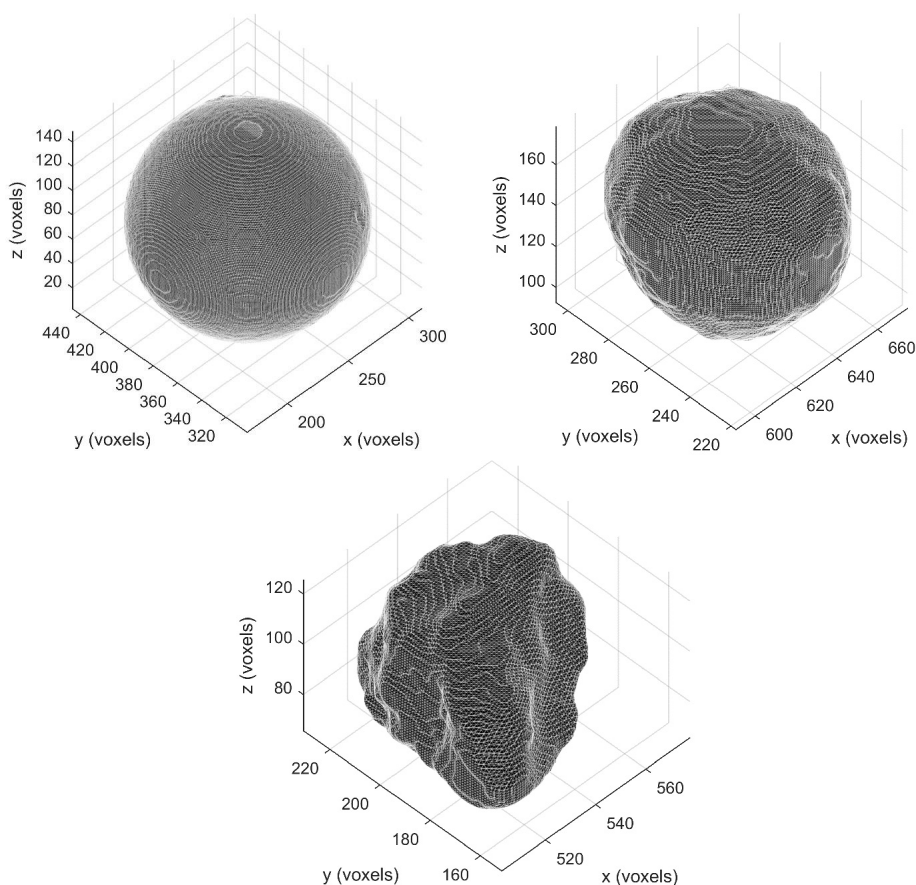
Figure 2.10. Three dimensional shape of three objects scanned with micro-CT: (a) plastic sphere (D_{eq}=5.9 mm, ϕ = 0.99), (b) CAN (D_{eq}=3.5 mm, ϕ =0.97), (c) KCL (D_{eq}=2.6 mm, ϕ = 0.83)

Table 2.9 gives the size and sphericity distribution for the two replicates of the scanned spheres and fertilizer particles. The number of individual objects is given as well. Because of the fixed volume that was scanned, more individual particles were detected for the smaller particle types such as TROP, PK and CYAN. Regarding the size and sphericity values, small differences between replicates were found, illustrating the repeatability of the experiments. Small differences could be caused by sample heterogeneity or by particle segregation within the plastic containers in which they were scanned, because only the middle part of the container was scanned. It can be seen that the sphericity of the plastic spheres approaches the theoretical value of 1 very

closely. Combined for both replicates of the spheres, the mean equivalent diameter was 5.77 mm (±0.01 mm) and the mean sphericity 0.992 (±0.001). The true particle diameter of the particles was 5.96 mm (±0.01 mm). The size of the plastic spheres was thus slightly underestimated (0.18 mm on average). It can be seen that CAN and NPK15 particles seemed to be most spherical in shape while KCL particles clearly had the most irregular shape. This is in agreement with the results for the angle of repose found earlier (Table 2.8). The relation between the sphericity and the angle of repose is illustrated by Figure 2.11.

Table 2.9. Particle size and sphericity of scanned particles. The 10th, 50th, and 90th percentile of the distribution are given. Two replicates per particle type were analysed. For each experiment, the number of particles is given

| Particle type	Nr (-)	D_{eq} (mm)			ϕ (-)		
		10%	50%	90%	10%	50%	90%
Plastic spheres	79	5,77	5,78	5,79	0,992	0,993	0,993
	76	5,76	5,77	5,78	0,991	0,992	0,993
CAN	352	2,66	3,48	4,15	0,919	0,967	0,976
	333	2,79	3,51	4,17	0,927	0,966	0,976
NPK15	371	2,68	3,55	4,09	0,938	0,964	0,977
	330	2,75	3,64	4,09	0,932	0,965	0,975
NPK18	291	2,93	3,57	4,31	0,835	0,892	0,927
	278	3,02	3,59	4,46	0,822	0,887	0,930
TROP	885	1,79	2,39	3,19	0,796	0,890	0,942
	830	1,83	2,47	3,27	0,800	0,884	0,943
PK	930	1,61	2,28	3,17	0,775	0,915	0,940
	731	1,74	2,46	3,56	0,765	0,913	0,938
KCL	645	1,74	2,57	3,66	0,698	0,787	0,843
	650	1,75	2,50	3,61	0,732	0,790	0,837
ENTEC	514	2,06	3,04	3,79	0,871	0,911	0,940
	485	2,12	3,00	3,81	0,867	0,906	0,937
CYAN	4228	0,78	1,34	2,13	0,822	0,933	0,974
	4522	0,77	1,31	2,07	0,820	0,931	0,976
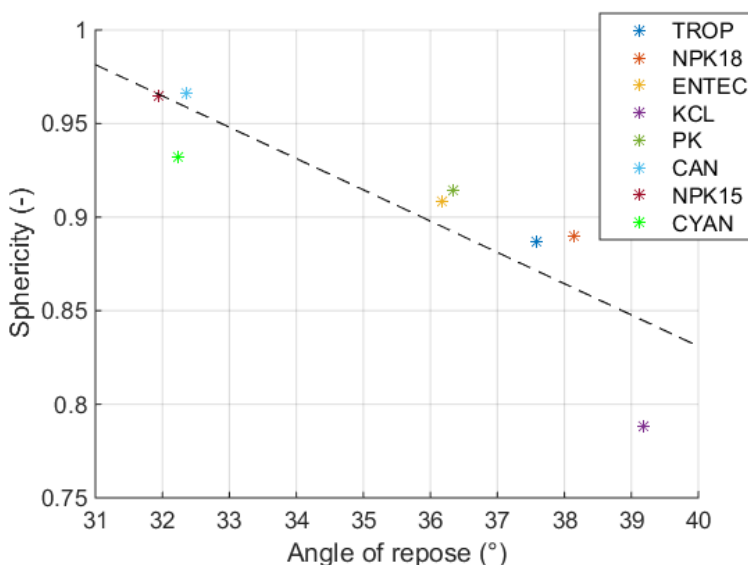
Figure 2.11. The median particle sphericity expressed relative to angle of repose for different types of fertilizer (data from both replicates combined). The best linear fit resulted in an R² of 0.7444 (-)

Based on the volume of the scanned particles, it could be possible to determine their true density by measuring their mass. However, this would imply that particles should first be correctly identified, which would be too difficult because particles were scanned in batches of several hundreds (to thousands) of particles.

The drag coefficient depends on the shape of the particles, however it is dependent on the Reynolds number (Equation 2.5), which changes during the trajectory because the velocity declines (Equation 2.4), For a given particle velocity and median sphericity, the drag coefficient of the particles is given in Table 2.10. It can be seen that the drag coefficient is very high for KCL particles and lowest for CAN and NPK15 particles which was expected due to their low and high sphericity respectively. Although TROP and NPK18 had a similar sphericity and although NPK18 particles were considerably larger (Table 2.8 and Figure 2.9), which increases their Reynolds number at the same particle velocity, they have a similar drag coefficient.

Table 2.10. Drag coefficient (C_d) of fertilizer types, calculated based on the median sphericity, a velocity of 30 m/s and the median particle size determined using sieving (ρ_{air} = 1.225 kg/m³, μ_{air} = 1.8*1e-5 kg/m s)

Particle type	C_d (-)
Perfect sphere	0,44
CAN	0,52
NPK15	0,53
NPK18	0,77
TROP	0,78
PK	0,68
KCL	1,27
ENTEC	0,70
CYAN	0,63

Grift et al. (1997) found an average q-factor of 0.87 for CAN fertilizer, 0.75 for an NPK fertilizer and 0.62 for Potassium 60 fertilizer. This factor was experimentally determined using fall-tests and relates the fall time of particles with the fall time of a perfect sphere with equivalent diameter. According to these findings, a drag coefficient of 0.51 would be found for CAN, 0.59 for NPK and 0.71 for Potassium 60. The values for CAN and NPK are comparable to the results achieved here. The drag coefficient for Potassium 60 is however smaller compared to the value of KCL found here. During fall tests, particles accelerate from standstill to terminal velocity due to gravity. Therefore, the aerodynamic behaviour they measure is therefore an "average" for the conditions during the test. Generally, the terminal velocity is lower compared to the velocities obtained in the spreading process (Hofstee & Huisman, 1990). According to Figure 2.12, their fall test method should then over-estimate the drag coefficient (lower Reynolds numbers) which is not the case here. A possible explanation for this is that the fertilizer analysed here was more irregular in shape compared to their fertilizer. Also, the sphericity of KCL particles could be under-estimated in this work, which could cause an over-estimation of the drag coefficient. Furthermore, it is possible that the relatively simple formula used to calculate the drag coefficient based on the sphericity and the Reynolds number (Equation 2.5) overestimates the drag coefficient of this type of fertilizer. Clearly, more research is necessary regarding the drag coefficient of irregular fertilizer particles.
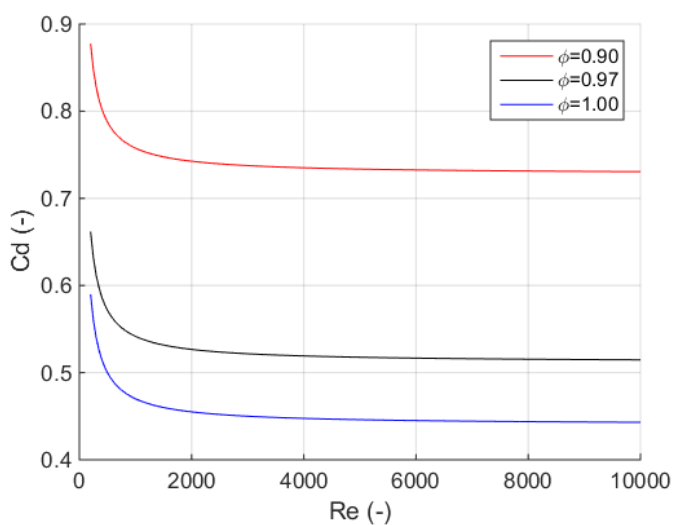
Figure 2.12. Simulation of the drag coefficient for particles with sphericity of 0.9, 0.97 and 1 (-) in function of the Reynolds number

2.3.3. Simulations

2.3.3.1. Effect of particle type

Figure 2.13 illustrates the ballistic flight for different types of fertilizer particles with similar initial conditions. Clearly, large differences between different fertilizer types are found.
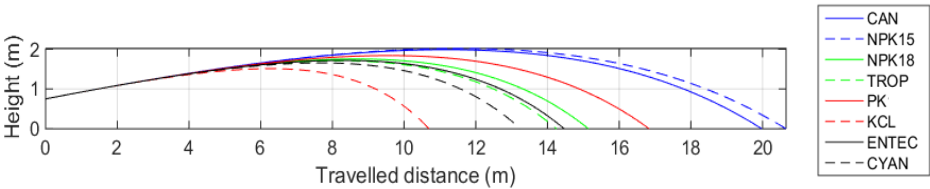

Figure 2.13. Simulated trajectories for different fertilizer types for a velocity of 40 m/s and a vertical angle of 10°

The differences are caused by the different physical parameters of the fertilizer types. Particles with higher mass (larger true density and diameter) and higher sphericity travel further than lighter, more irregular particles (Equation 2.7). CAN and NPK15 particles are generally more spherical (Table 2.9) and although they have a lower true density (Table 2.8), they travel further compared to smaller (e.g. CYAN or TROP) or more irregular particles like KCL, which have a larger drag coefficient (see Table 2.10). Table 2.11 gives the travelled distance for the different particle types for different velocities and vertical angles. The difference between the particle types clearly increases with the particle velocity and the vertical angle. This result is in accordance with findings by Grafton et al. (2015b). When some of these fertilizer types would be blended together, for example CAN and KCL, ballistic segregation would occur due to their different aerodynamic behaviour. Tissot et al (1999) determined spread patterns for two different blends, containing different ratios of three different fertilizer types, amongst which CAN and KCL fertilizer. The components were clearly segregated, resulting in an uneven chemical distribution on the field, varying by more than 40%. This can be caused by a difference in behaviour on the disc, changing the velocity and direction of motion of the particles, but also due to their aerodynamic behaviour as illustrated here.

Table 2.11. Travelled distance (m) for different fertilizer types. Three different velocities (v) and two different vertical angles (α) were considered

v (m/s)	α (°)	TROP	NPK18	ENTEC	KCL	PK	CAN	NPK15	CYAN
10	0	3,35	3,40	3,36	3,14	3,47	3,57	3,59	3,29
10	10	4,46	4,56	4,49	4,02	4,73	4,99	5,03	4,32
25	0	6,96	7,14	7,00	6,14	7,46	7,94	8,02	6,73
25	10	10,31	10,83	10,44	8,37	11,77	13,41	13,74	9,71
40	0	9,57	9,91	9,65	8,15	10,50	11,44	11,62	9,16
40	10	14,25	15,14	14,46	11,06	16,83	19,97	20,65	13,24

2.3.3.2. Effect of individual parameters

Particle velocity

The effect of the horizontal velocity and vertical angle on the travelled distance is illustrated in Figure 2.14 for CAN fertilizer.
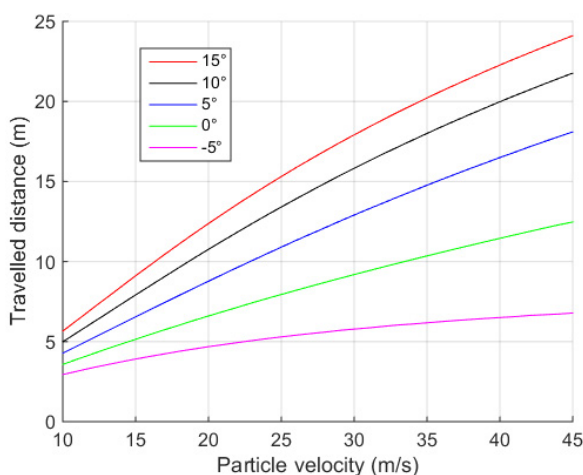
Figure 2.14. The effect of vertical angle and velocity on the travelled distance of individual fertilizer particles. Simulations were performed assuming CAN fertilizer (D=3.7 mm, ρ=1785 kg m^{-3}, ϕ = 0.97, h=0.75 m, ρ_{air} = 1.225 kg/m³, μ_{air} = 1.8*1e-5 kg/m s)

The travelled distance increases with the particle velocity, however from Figure 2.14, it can be seen that the effect is strongly dependent on the vertical angle. At a given particle velocity, the effect of vertical angle becomes smaller with increasing angles.

The first derivative of the curves in Figure 2.14 gives the absolute sensitivity of the travelled distance for the particle velocity. The sensitivity decreases with an increasing particle velocity and increases for higher vertical angles. The same can be derived from Figure 2.15, which gives the absolute sensitivity for all particle types that were analysed for three different particle velocities and two different vertical angles. Increasing the velocity of the particles with 1 m/s increased the travelled distance from 0.11 m to 0.58 m, depending on the fertilizer type and the velocity and vertical angle (for the cases considered). In all cases, the effect is smaller for CYAN and KCL fertilizer and larger for NPK15 and CAN particles.
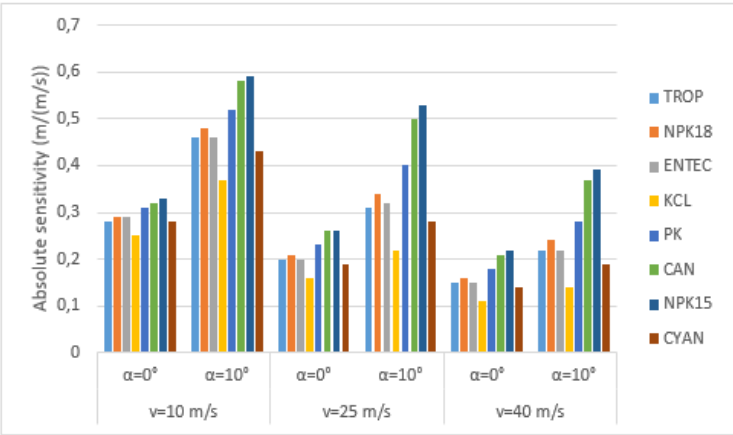
Figure 2.15. Absolute sensitivity determined as the change in travelled distance due to an increase in velocity (m/(m/s)). Different particle types were considered. For the diameter and sphericity, the median value was used.

Figure 2.16 and 2.17 illustrate the effect of the vertical angle on the travelled distance for the three different particle velocities.
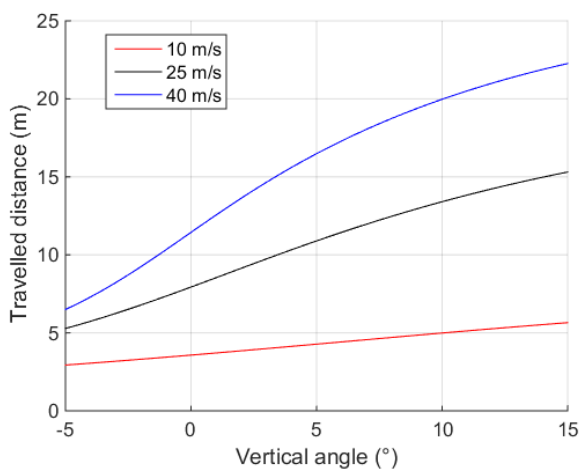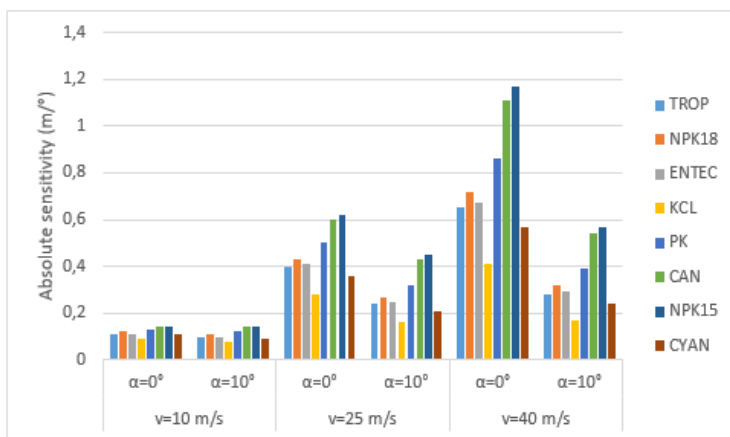
Figure 2.16. The effect of vertical angle on the travelled distance for different velocities of individual fertilizer particles. Simulations were performed assuming CAN fertilizer (D=3.7 mm, ρ=1785 kg m^{-3}, ϕ = 0.97, h=0.75 m, ρ_{air} = 1.225 kg/m^3, μ_{air} = 1.8*1e-5 kg/m s)

Figure 2.17. Absolute sensitivity determined as the change in travelled distance due to an increase in vertical angle (m/°). Different particle types were considered. For the diameter and sphericity, the median value was used

The sensitivity for the vertical angle clearly increased with the particle velocity. From Figure 2.16, it can be seen that the curve for the highest particle velocity is sigmoid-shaped, meaning that the sensitivity first increases and then decreases with the vertical angle. For medium (25 m/s) and fast (40 m/s) moving particles, the sensitivity was smaller for the conical disc case (α=10°) compared to the flat disc. Relatively large differences between fertilizer types were found. Generally, the sensitivity was highest for NPK15 and CAN particles and lowest for KCL particles.

Figures 2.18 and 2.19 give the absolute sensitivity results for the horizontal and vertical velocity component respectively. Generally, it can be seen that the sensitivity for the vertical velocity component was much higher than the sensitivity for the horizontal velocity. For the slow moving particles, there was little difference in sensitivity for the vertical velocity component. For medium and high velocity particles, the sensitivity was larger for the flat disc compared to conical discs. The sensitivity for the horizontal velocity vector was larger for the flat disc compared to the conical disc. Increasing the particle velocity decreased the sensitivity for the horizontal velocity component. The effect on the landing position is clearly different between particle types. According to our findings, an overestimation of the vertical velocity component with 1 m/s can result in 1.67 m error in the landing position for a medium sized NPK15 particle, while for KCL, a maximal error of 0.58 m was obtained at same initial conditions.
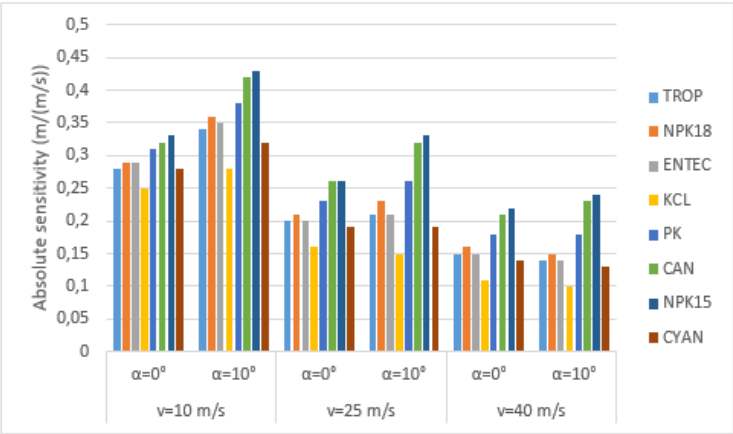

Figure 2.18. Absolute sensitivity determined as the change in travelled distance due to an increase in the horizontal velocity component (m/(m/s)). Different particle types were considered. For the diameter and sphericity, the median value was used
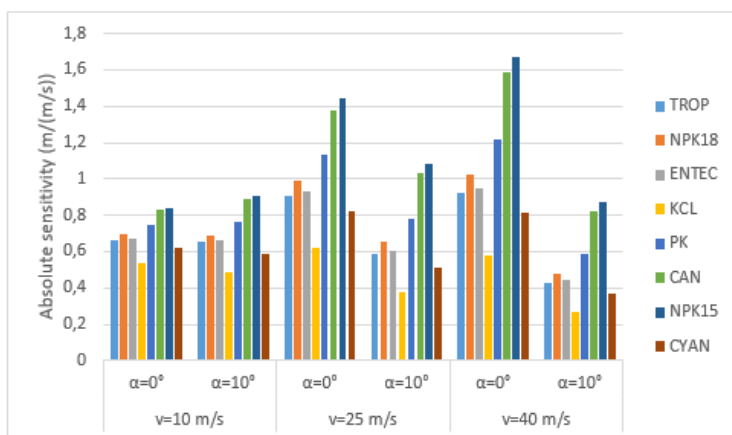
Figure 2.19. Absolute sensitivity determined as the change in travelled distance due to an increase in the vertical velocity component (m/(m/s)). Different particle types were considered. For the diameter and sphericity, the median value was used

<u>Sphericity</u>

The effect of the sphericity on the travelled distance is illustrated in Figure 2.20. Increasing the roundness of particles will clearly increase the travelled distance. This is caused by a lower drag coefficient (see Equation 2.5 and Figure 2.12). It can be seen that the sensitivity for the sphericity is generally much higher for faster particles and higher vertical angles. For slow moving particles, there is almost no effect of sphericity. The effect is clearly dependent on the velocity and the vertical angle and less on the particle type, as can be seen in Figure 2.21.
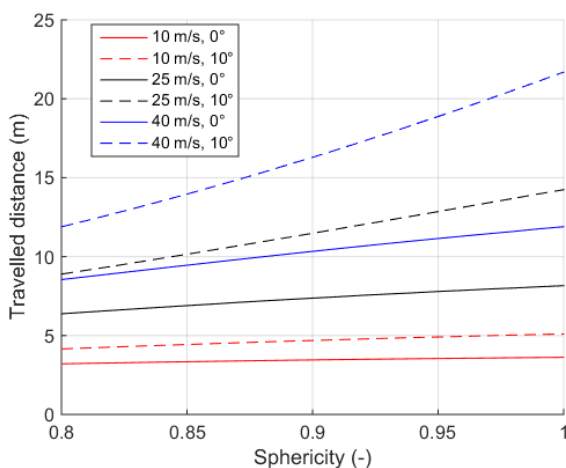
Figure 2.20. The effect of particle sphericity on the travelled distance of individual fertilizer particles. Simulations were performed assuming CAN fertilizer (D= 3.7 mm, ρ=1785 kg m^{-3}, h=0.75 m, ρ$_{air}$ = 1.225 kg/m³, μ$_{air}$ = 1.8*1e-5 kg/m s)
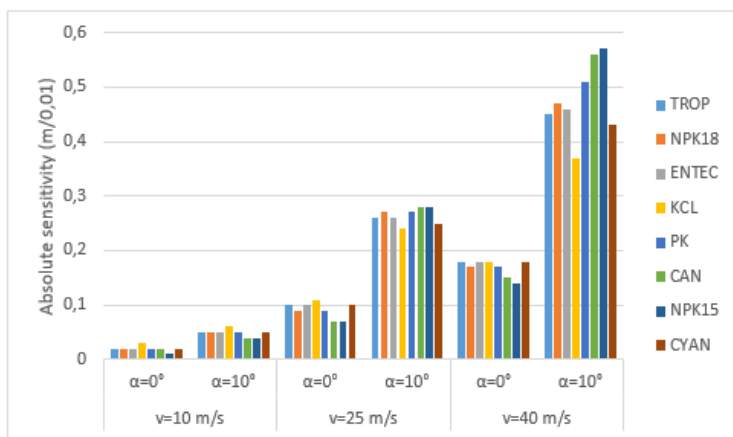

Figure 2.21. Absolute sensitivity determined as the change in travelled distance due to an increase in the particle sphericity (m/0.01). Different particle types were considered. For the diameter and sphericity, the median value was used

According to Equation 2.5, the particle sphericity, together with the Reynolds number determines the drag coefficient. Because the velocity is not constant during the trajectory, the Reynolds number and the drag coefficient vary during the trajectory.

This is illustrated on Figure 2.22 for CAN fertilizer. Assuming the drag coefficient constant during the trajectory can therefore result in errors in the calculated landing position.
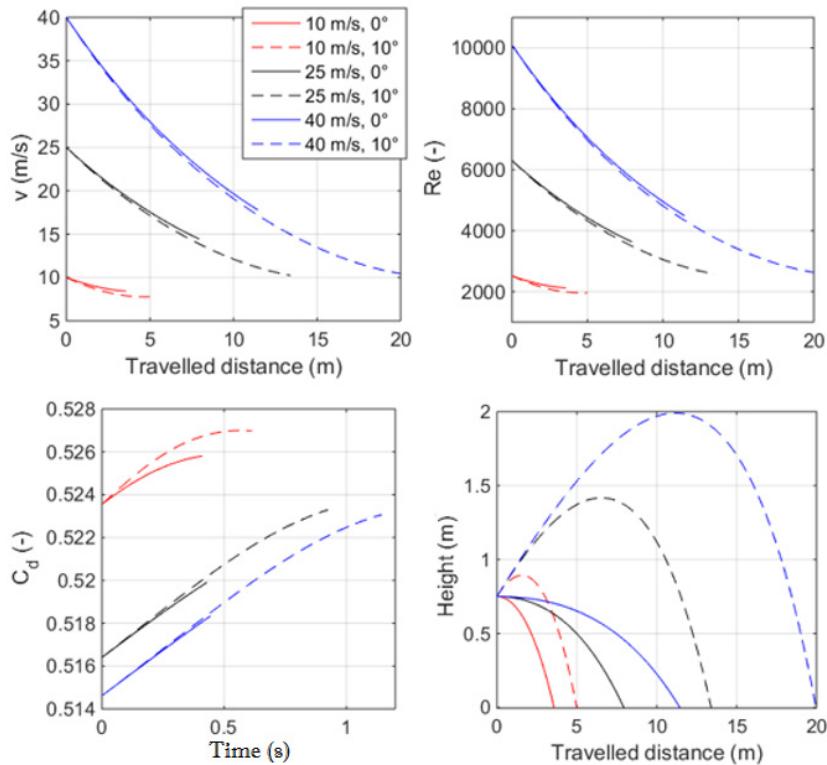

Figure 2.22. Simulation results for six different cases. The velocity, Reynolds number, C_d value and height during the trajectory are given. Simulations were performed assuming CAN fertilizer (D= 3.7 mm, ρ=1785 kg m^{-3}, ϕ = 0.97, h=0.75 m, ρ_{air} = 1.225 kg/m^3, μ_{air} = 1.8*1e-5 kg/m s)

Particle true density

Figure 2.23 gives the effect of the particle true density on the landing position for CAN fertilizer. Increasing the density, increased the mass of the particles and increased the travelled distance. The sensitivity for the particle true density (Figure 2.24) is generally higher for the conical disc compared to the flat disc case. Increasing the particle velocity and the particle velocity clearly increased the sensitivity for the true density.

The sensitivity was highest for NPK15 and CAN and slowest for KCL and CYAN particles.
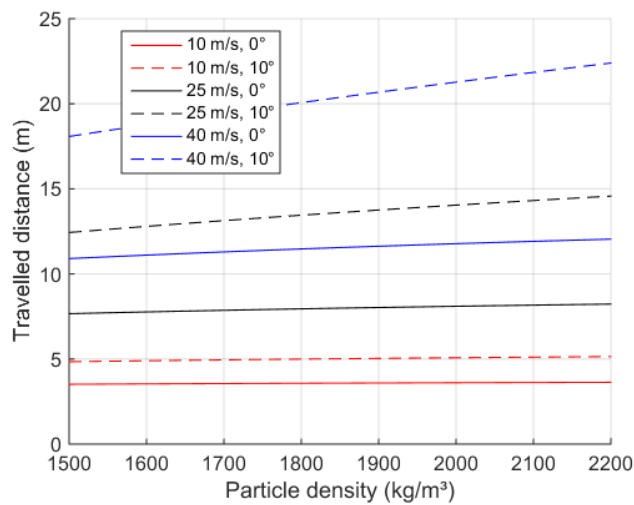

Figure 2.23. The effect of particle true density on the travelled distance of individual fertilizer particles. Simulations were performed assuming CAN fertilizer (D=3.7 mm, ϕ = 0.97, h=0.75 m, ρ_{air} = 1.225 kg/m³, μ_{air} = 1.8 1e-5 kg/m s)

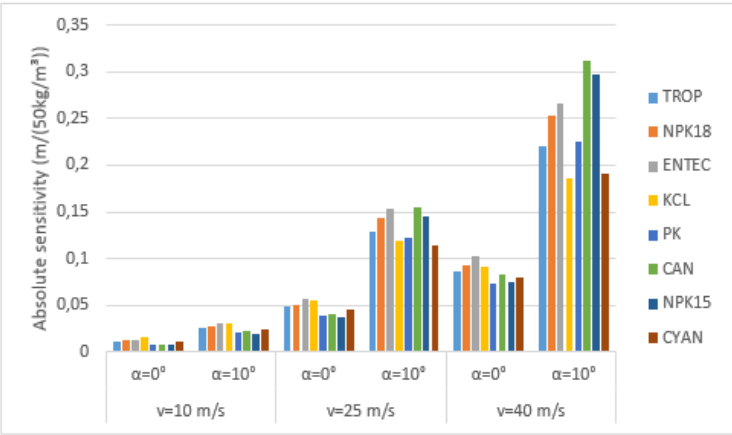**Figure 2.24.** Absolute sensitivity determined as the change in travelled distance due to an increase in the particle true density (m/(50 kg/m³)). Different particle types were considered. For the diameter and sphericity, the median value was used

Particle diameter

The sensitivity for the particle diameter is not linear, as shown in Figure 2.25. The first derivative decreases with the particle size, indicating a lower absolute sensitivity. Figure 2.26 shows that a higher sensitivity was found for conical discs and higher particle velocities. The sensitivity for the diameter was largest for CYAN, which generally have a smaller particle size. For KCL, the effect was smallest.
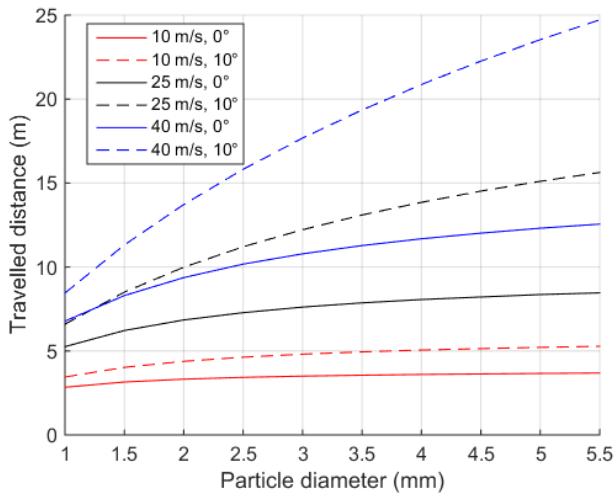

Figure 2.25. The effect of particle diameter on the travelled distance of individual fertilizer particles. Simulations were performed assuming CAN fertilizer (ρ=1785 kg m^{-3}, ϕ = 0.97, h=0.75 m, ρ_{air} = 1.225 kg/m³, μ_{air} = 1.8 1e-5 kg/m s)
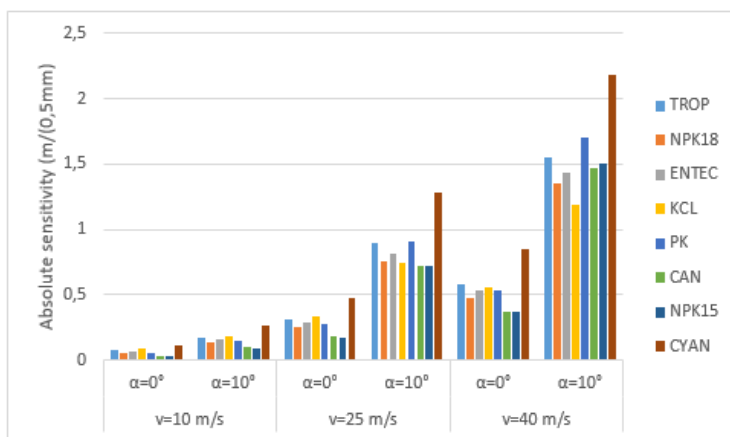
Figure 2.26. Absolute sensitivity determined as the change in travelled distance due to an increase in the particle diameter (m/0.5 mm). Different particle types were considered. For the diameter and sphericity, the median value was used

Initial height

Figure 2.27 shows that increasing the initial height increases the travelled distance. The sensitivity for the initial height (Figure 2.28) was lower for the conical disc, and was in this case relatively unaffected by the particle velocity. For flat discs, the sensitivity for the initial height increased with the particle velocity.

Figure 2.27. The effect of initial height on the travelled distance of individual fertilizer particles. Simulations were performed assuming CAN fertilizer (D= 3.7 mm, ρ=1785 kg m^{-3}, ϕ = 0.97, ρ_{air} = 1.225 kg/m³, μ_{air} = 1.8 1e-5 kg/m s)
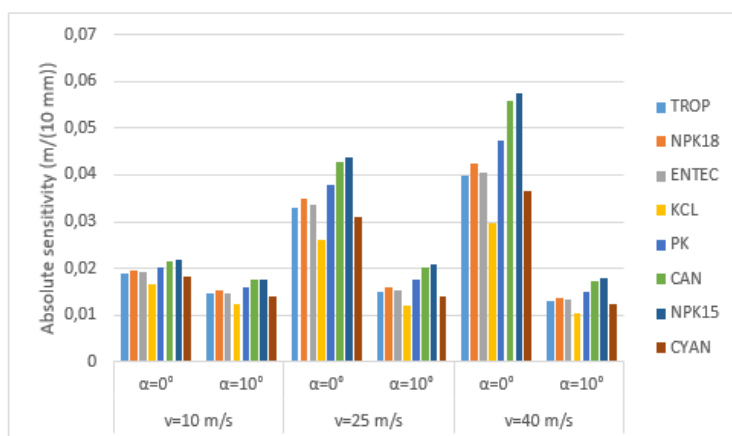
Figure 2.28. Absolute sensitivity determined as the change in travelled distance due to an increase in initial height (m/10 mm). Different particle types were considered. For the diameter and sphericity, the median value was used

Density of air

Figure 2.29 shows that the travelled distance decreases with an increase of air density. This is caused by an increase in aerodynamic drag, which can be seen in Equation 2.3. The Reynolds number is also influenced by this parameter (Equation 2.4). The sensitivity is more negative for particles with higher velocity and larger vertical angle (Figure 2.30). This means that for this case, the air density must be known more precisely to obtain the same absolute accuracy in the prediction of the landing position compared to the other cases.
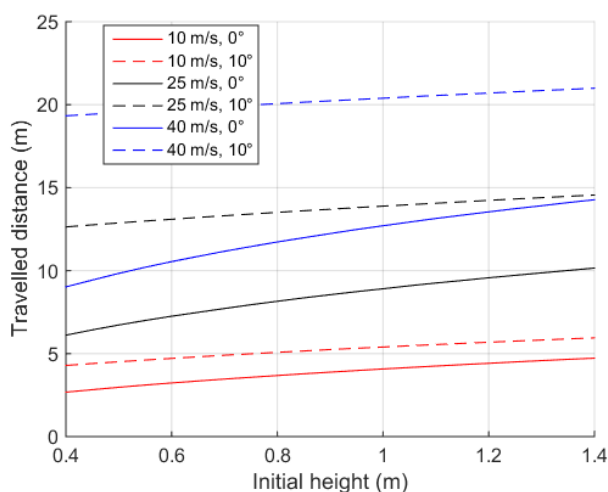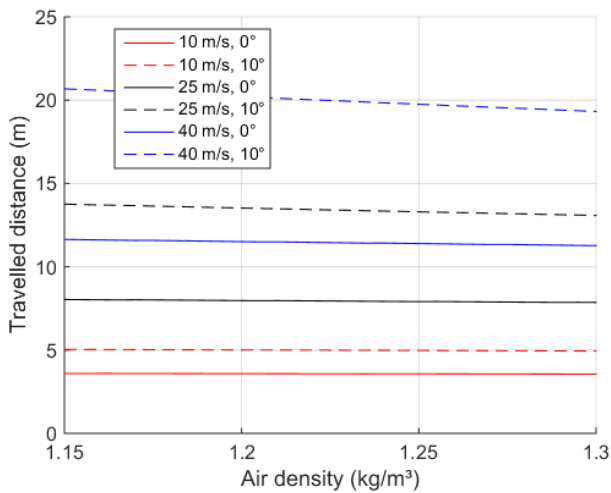

Figure 2.29. The effect of air density on the travelled distance of individual fertilizer particles. Simulations were performed assuming CAN fertilizer (D= 3.7 mm, ρ=1785 kg m^{-3}, ϕ = 0.97, h=0.75 m, μ$_{air}$ = 1.8 1e-5 kg/m s)

The air density is related to the temperature of air, but also to the pressure and the moisture content. An increase in air temperature and in relative humidity decreases the density of air while an increase in pressure increases the density. In cold or dry days the air density will thus be higher and the travelled distance will be lower compared to warmer or wet days. Thus, depending on the weather, the travelled distance may change although the initial conditions of the particles are identical.
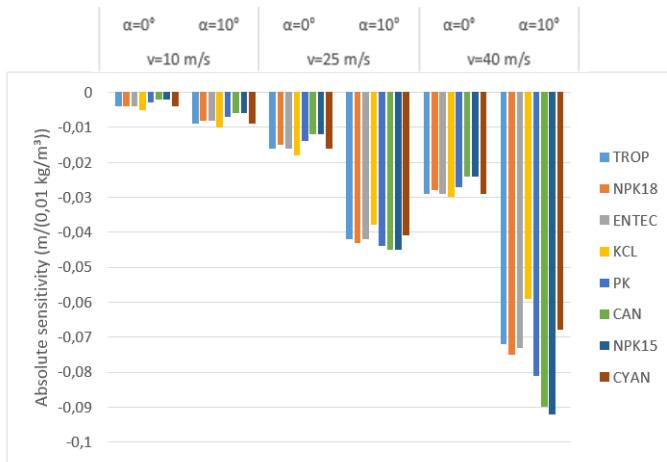
Figure 2.30. Absolute sensitivity determined as the change in travelled distance due to an increase in the density of air (m/0.01 kg/m³). Different particle types were considered. For the diameter and sphericity, the median value was used

Wind

Figure 2.31 shows clearly how wind can alter the trajectory of fertilizer particles. Both the direction and the velocity of the wind are clearly important. The travelled distance in both the transverse (perpendicular to the initial direction of motion) and longitudinal direction can be affected. Because particles are ejected in the x-direction, the travelled distance in the longitudinal and transverse direction are given by the x and the y value of the landing position respectively.
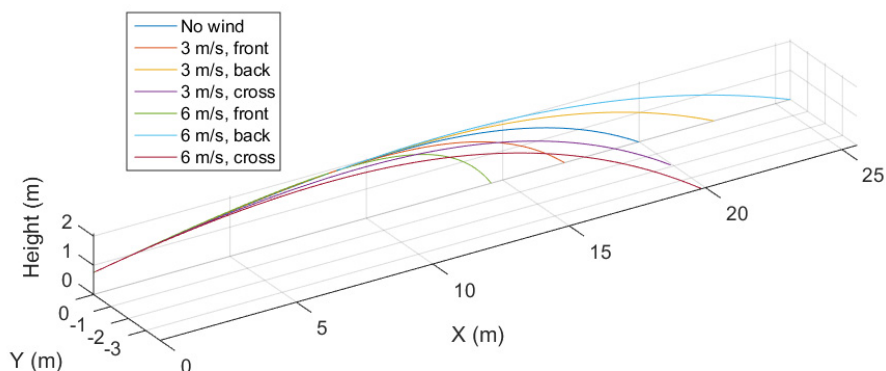
Figure 2.31. Simulated trajectories for different wind conditions. CAN fertilizer was assumed (D=3.7 mm, ρ=1785 kg m^{-3}, ɸ = 0.97, h=0.75 m, v=40 m/s, vertical angle = 10°, ρ$_{air}$ = 1.225 kg/m³, μ$_{air}$ = 1.8*1e-5 kg/ m s)

Figure 2.32 shows that the landing position increases with tailwind and decreases with headwind (negative velocity values). The absolute sensitivity increases with an increase in particle velocity, especially in the case of a conical disc (Figure 2.33). The sensitivity is very similar between particle types especially for the fast moving particles which were ejected with a vertical angle of 10°. From Figure 2.32, it can be seen that the sensitivity for tailwind is linear, also for negative velocities, i.e. headwind. This means that the magnitude of the effect of head and tailwind is similar, although the direction of the effect is opposite. A special case occurs when the velocity of the particle is the same as the velocity of wind coming from its back. In that case, the particle would not experience horizontal drag, as it is not moving relative to the air. Because the particle moves downwards due to gravitation, this means that the drag force, working in the opposite direction, will create a lift effect. This would in theory, without consideration of any other forces, result in a higher travelled distance compared to a similar situation in vacuum.
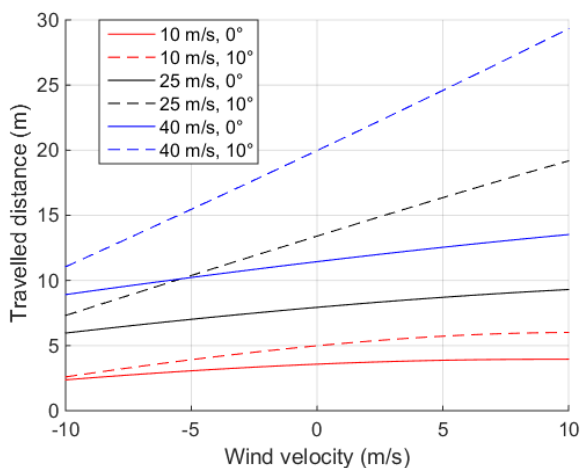
Figure 2.32. The effect of tailwind on the travelled distance of individual fertilizer particles in the longitudinal direction. Negative velocities indicate headwind. Simulations were performed assuming CAN fertilizer (D= 3.7 mm, ρ=1785 kg m^{-3}, φ = 0.97, h=0.75 m, ρ$_{air}$ = 1.225 kg/m³, μ$_{air}$ = 1.8*1e-5 kg/m s)


Figure 2.33. Absolute sensitivity determined as the change in travelled distance in the initial direction of motion (x) due to an increase in tailwind (m/(m/s)). Different particle types were considered. For the diameter and sphericity, the median value was used

Figure 2.34 shows the effect of crosswind, both in the longitudinal direction and in the transverse direction. The travelled distance in the longitudinal direction was little

affected by the wind. The travelled distance slightly decreases with the wind velocity, however the effect was very small. Due to the crosswind, the particle trajectories are bent in the direction of wind (see Figure 2.31). Similar to tailwind, the effect of crosswind was linear for the wind velocity and increased to a large extent with an increasing vertical angle. Figure 2.35 gives the sensitivity of the travelled distance in the transverse direction for crosswind. Differences between particle types can be seen. CYAN and KCL particles are more sensitive to crosswind compared to NPK15 and CAN particles. For particles ejected with high velocity using the conical disc, the difference between particle types was relatively small.

Figure 2.34. The effect of crosswind on the travelled distance (left in longitudinal direction, right in transverse direction) of individual fertilizer particles. Simulations were performed assuming CAN fertilizer (D= 3.7 mm, ρ=1785 kg m^{-3}, ϕ = 0.97, h=0.75 m, ρ_{air} = 1.225 kg/m³, μ_{air} = 1.8*1e-5 kg/m s)
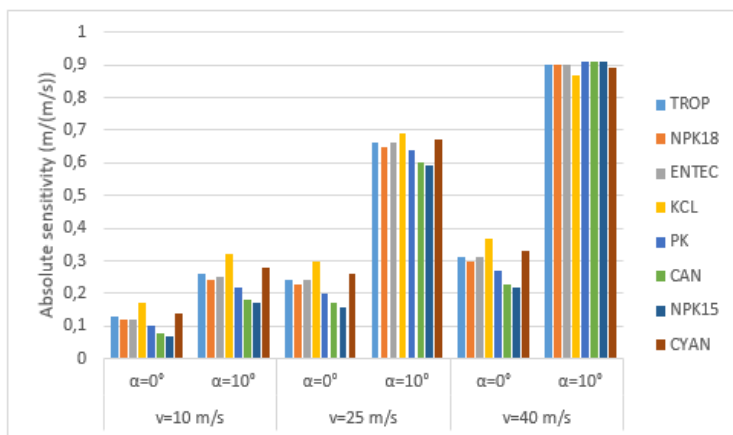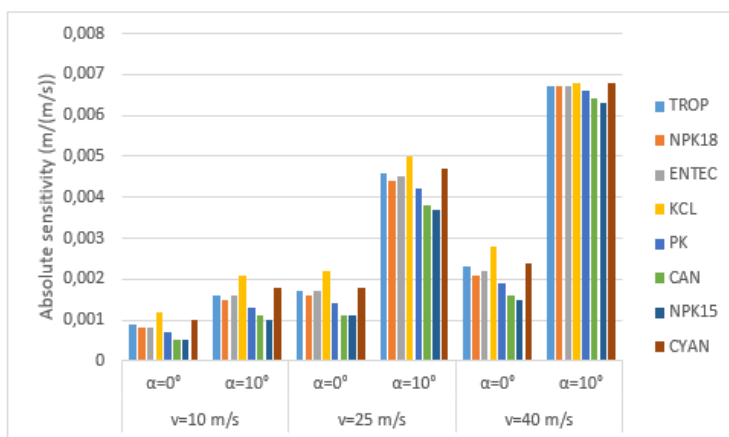
Figure 2.35. Absolute sensitivity determined as the change in travelled distance perpendicular to the initial direction of motion (y) due to an increase in crosswind (m/(m/s)). Travelled distance in the transverse direction for crosswind. Different particle types were considered. For the diameter and sphericity, the median value was used

The effect of wind direction is illustrated in Figure 2.36. The sensitivity of the travelled distance in the longitudinal direction is largest for wind directions perpendicular to the direction of motion. For the transversal distance, the opposite is true, since the sensitivity increases towards tail-or-headwind (0 and 180° resp.). It can be seen that for the lower particle velocities, the maximal deviation in the transverse direction is not at 90°, but slightly shifted towards higher angle. This indicates that the effect of crosswind is not the worst case scenario for the transversal offset due to side-wind, although this case will be close to the maximal effect. Similarly as with tail-and head-wind, the effect of crosswind will generally be a lot higher for faster moving particles and particles ejected with a larger vertical angle.
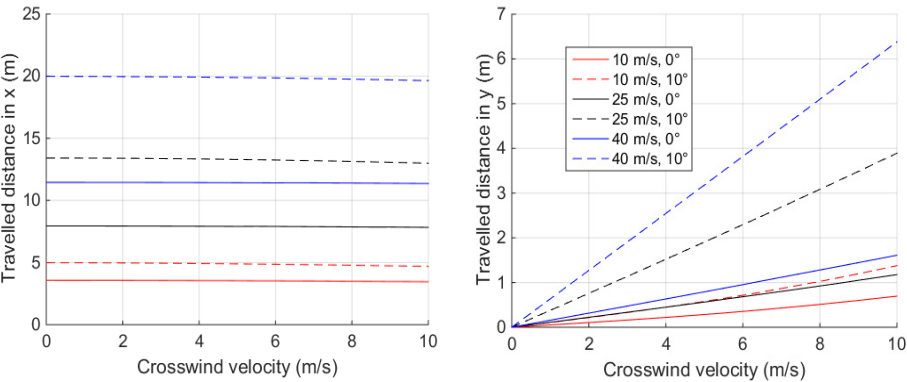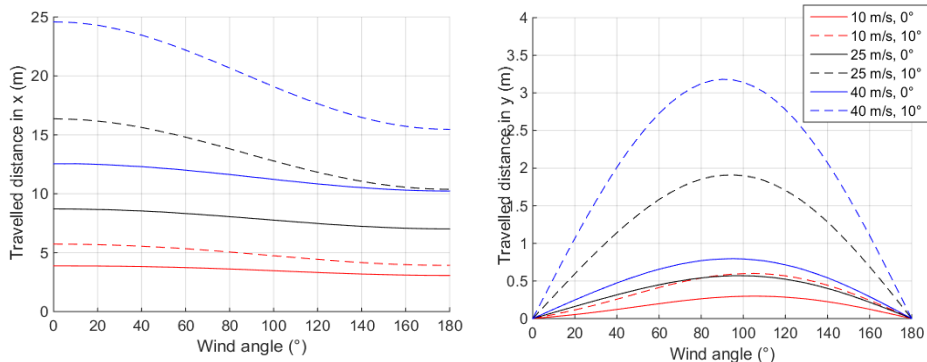
Figure 2.36. The effect of wind direction on the travelled distance (left in longitudinal direction, right in transverse direction). A wind velocity of 5 m/s was assumed. Wind angle = 0° indicates wind coming from the back, while 180° means wind coming from the front. Simulations were performed assuming CAN fertilizer (D= 3.7 mm, ρ=1785 kg m^{-3}, φ = 0.97, h=0.75 m, ρ$_{air}$ = 1.225 kg/m³, μ$_{air}$ = 1.8*1e-5 kg/m s)

Figure 2.37 also shows the effect of wind direction and wind velocity. The total travelled distance is given, as well as the angle of the landing position relative to the initial direction of motion. It can be seen that the effect of wind is mirrored with respect to the x-axis (the longitudinal direction). The total travelled distance was clearly more affected by wind in the longitudinal direction compared to wind in the transverse direction. The angular position of the landing position is affected by the wind velocity component in the x and y direction. For both cases, the effect of the transverse component of the wind velocity is clearly larger for headwind compared to tailwind.
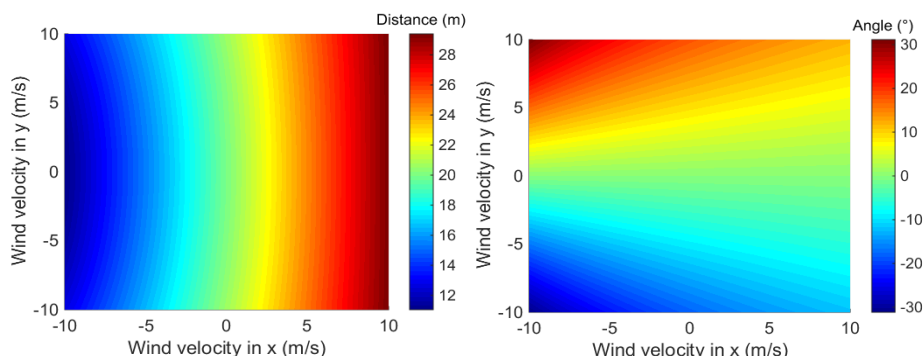
Figure 2.37. The effect of wind direction in polar coordinates. The total travelled distance and the absolute value of the angle of the landing position relative to the initial direction of motion are given. Simulations were performed assuming CAN fertilizer (v=40 m/s, α=10°,D= 3.7 mm, ρ=1785 kg m^{-3}, ϕ = 0.97, h=0.75 m, ρ$_{air}$ = 1.225 kg/m³, μ$_{air}$ = 1.8*1e-5 kg/m s)

2.3.3.3. Relative sensitivity

Based on the absolute sensitivity of the travelled distance for the different fertilizer types (section 2.3.3.2), the relative sensitivity for the different parameters was calculated for particles ejected from flat (α=0°) and conical (α=10°) discs. Figures 2.38 and 2.39 give the relative sensitivity for particles ejected with velocity of 10 m/s. The landing position was clearly most sensitive to the vertical velocity component, both for the flat and conical disc. Increasing the vertical angle from 0 to 10° increased the relative sensitivity for the horizontal velocity, diameter, sphericity and wind, both in the longitudinal direction for tailwind and in the transverse direction for crosswind. The sensitivity for the particle density, particle height and density of air was very low.

Figure 2.38. Relative sensitivity for different parameters for a flat disc (α=0°) at low velocity (10 m/s). The maximal absolute sensitivity value was 0.84 m

Figure 2.39. Relative sensitivity for different parameters for a conical disc (α=10°) at low velocity (10 m/s). The maximal absolute sensitivity value was 0.91 m.

Figures 2.40 and 2.41 give the relative sensitivity for particles ejected with a velocity of 25 m/s, for a flat and conical disc respectively. For particles ejected with a flat disc, the landing position was most sensitive to the vertical velocity component. For the conical disc, the sensitivity was highest for the particle diameter for CAN and NPK. For the other fertilizer types, the sensitivity for the particle diameter was higher, especially in the case of CYAN. Increasing the conical angle also increased the sensitivity for wind to a large extent. Also the sensitivity for the particle sphericity and density increased.

Figure 2.40. Relative sensitivity for different parameters for a flat disc (α=0°) at medium velocity (25 m/s). The maximal absolute sensitivity value was 1.44 m

Figure 2.41. Relative sensitivity for different parameters for a conical disc (α=10°) at medium velocity (25 m/s). The maximal absolute sensitivity value was 1.28 m

At high particle velocities (40 m/s) ejected with a flat disc, the landing position was most sensitive to the vertical velocity component (Figure 2.42). For the conical disc (Figure 2.43), the sensitivity was highest for the particle diameter. The relative sensitivity for the vertical velocity was much lower for the conical disc compared to the flat disc. Similarly to particles ejected with a medium velocity (25 m/s, ejecting the

particles with a conical disc increased the sensitivity for wind to a large extent. Also the sensitivity for the particle sphericity and density increased. The difference in relative sensitivity for wind between particle types was lower for the conical disc.

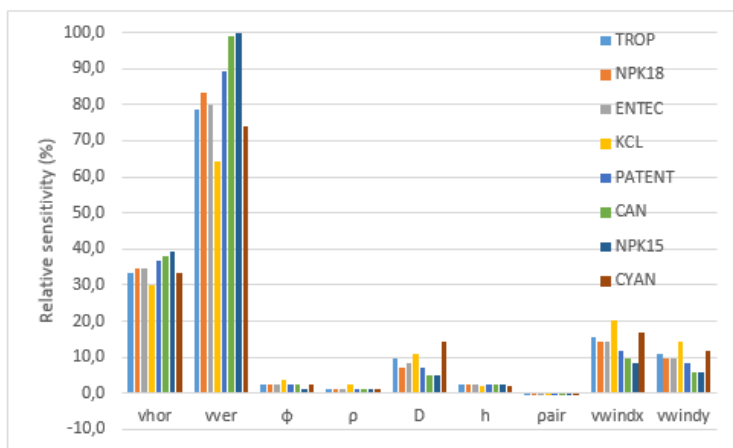**Figure 2.42.** Relative sensitivity for different parameters for a flat disc (α=0°) at high velocity (40 m/s). The maximal absolute sensitivity value was 1.67 m

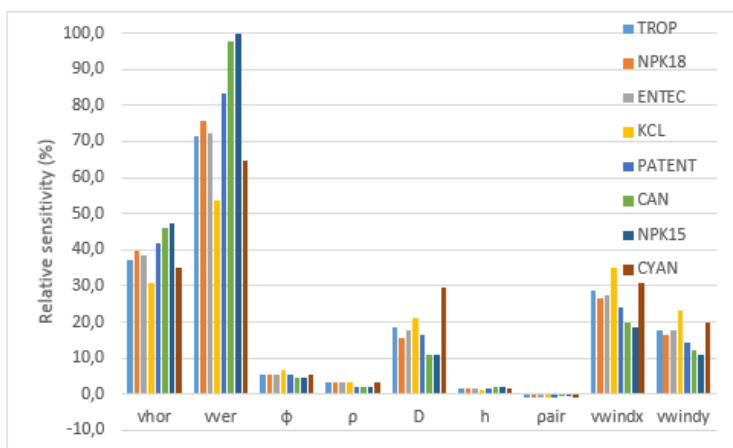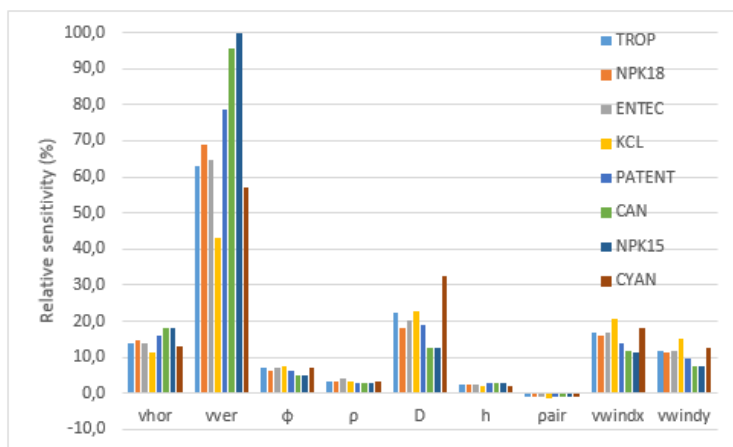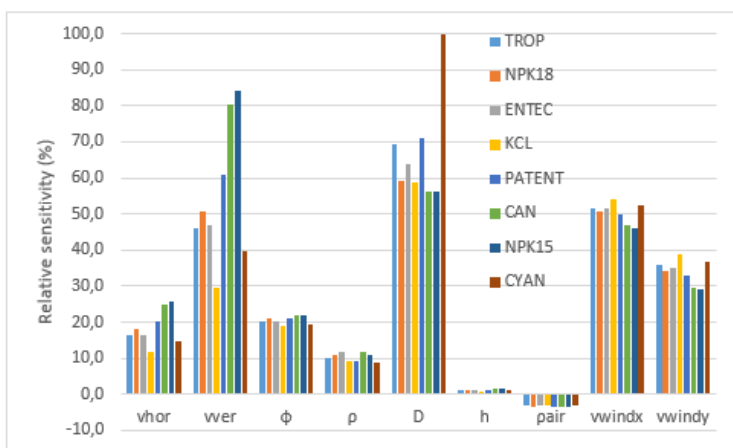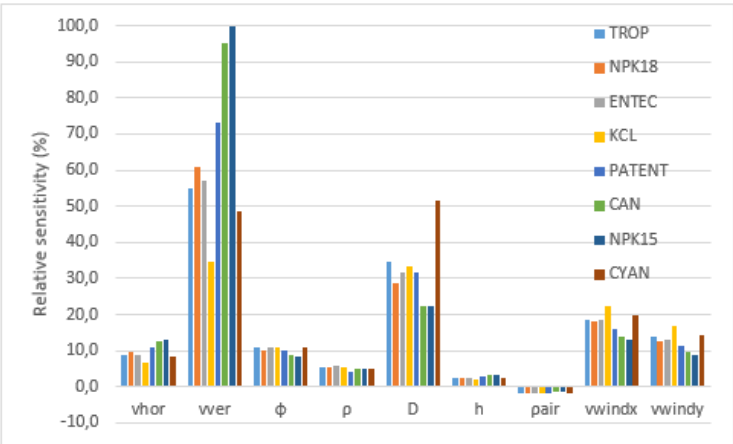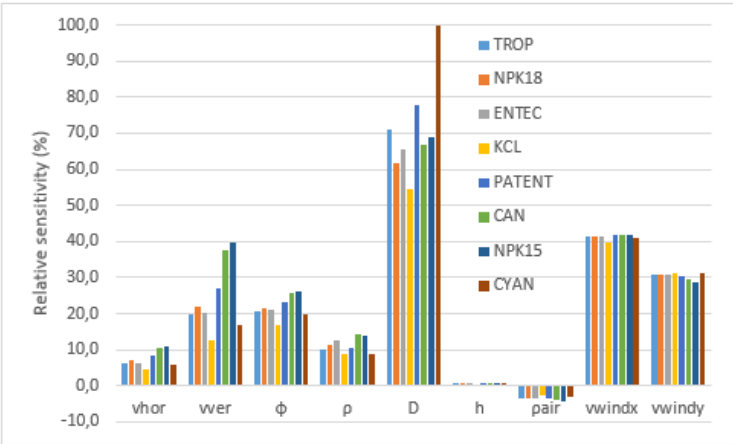**Figure 2.43.** Relative sensitivity for different parameters for a conical disc (α=10°) at high velocity (40 m/s). The maximal absolute sensitivity value was 2.18 m

Generally, the relative sensitivity for the vertical velocity component is higher than for the horizontal velocity component. Increasing the velocity of the particles decreases

the relative sensitivity for the horizontal velocity and increases the relative sensitivity for the particle diameter. Particles ejected with a conical disc are more sensitive to the particle diameter and for wind compared to particles ejected using a flat disc.

The perturbation factors that were used for this analysis were based on realistic measurement errors. Therefore, the previous results reflect the effect of these measurement errors on the predicted landing position. From the results obtained, it is clear that an accurate estimation of the particle diameter is very important. Especially for spreaders with conical discs at high rotational velocities (resulting in fast moving particles), an accurate estimation of the particle diameter is crucial to achieve a high accuracy in predicting the landing position for individual particles. This illustrates the importance of using the correct spreading table, because the particle size distribution can vary between fertilizers of similar type. Some manufacturers (e.g. Vicon) therefore recommend the farmer to measure the size distribution using a small sieving device.

Next to the particle diameter, also the vertical velocity component was clearly an important parameter. Because this parameter is related to the cone angle of the disc and the tilt angle of the spreader (see section 1.2.3.2), adding a spirit (bubble) level (in the transverse and longitudinal direction) to spreaders would be a low-cost solution to ensure a correct spreader orientation. By adding an inertial measurement unit (IMU), the orientation of the spreader can be monitored during spreading and the operator can be warned when certain limits are exceeded. Based on the large sensitivity for the vertical velocity component, it can be concluded that hybrid measurement approaches predicting the spread pattern based on measurement of particle parameters after leaving the disc thus need to determine these parameters in an accurate way. Until now, few authors measured the velocity in the vertical direction directly. Reumers et al. (2003) and Vangeyte (2013) determined the vertical angle based on horizontal outlet angles which were determined from camera images and the vertical mass distribution which was measured using a cylindrical collector. All hybrid approaches in literature used the particle size distribution determined before using sieving to simulate the trajectories of particles and calculate the spread pattern. Due to impact with the vanes however, the particle size can change because of mechanical degradation. Furthermore, these approaches assume that there is no interaction between the particle size and the particle dynamics. Experiments by Reumers et al. (2003a) indicated that larger particles achieved a higher speed on the disc, thus leaving the disc sooner and having a smaller horizontal outlet angle. Therefore, the particle size should be determined after spreading and for each particle individually. This way, the most accurate prediction of the spread pattern will be possible.

A high relative sensitivity for wind was found for conical discs, especially at medium and high particle velocities. This indicates that wind can change the trajectory of fertilizer particles to a large extent for particles ejected from spreaders with large working widths. Based on these results, especially these spreaders would benefit from an anemometer, mounted to the spreader or the tractor, to measure the wind direction and velocity. When exceeding certain limits, depending on the settings of the spreader, the operator could be warned automatically. Combined with an online (hybrid) system for determining the spread pattern, the effect on the spread pattern could be simulated in real time and correction could be performed if necessary. In this chapter, only the effect of parameters on individual particle trajectories was investigated. Ultimately, the effect of the parameters on the spread pattern is important and should be further investigated. This will be a superposition of the effect on all individual particle trajectories.

2.4. Conclusions

In this chapter, a study was performed to analyse the parameters that are involved with the prediction of the landing positions of fertilizer particles. First of all, a three-dimensional ballistic model was developed, modelling the trajectory of fertilizer particles in the air. In contrast to two-dimensional models in literature, the model allows to simulate the effect of wind on the trajectories. The model could not be solved analytically and should therefore be solved in a numerical way. The effect of different step sizes with a fixed-step solver was investigated. It was found that the step size had a large effect on the accuracy of the landing position. Generally, increasing the step size caused an over-estimation of the travelled distance. Decreasing the step size and interpolation of the landing position increased the accuracy. Simulation results indicated that a step size of 1e-3 s resulted in errors less than 10 mm for the travelled distance, which is more than sufficient for predicting fertilizer trajectories.

Eight commonly used fertilizer types were selected and their physical properties were determined in laboratory conditions, including the particle size distribution, the bulk density, the true density, the angle of repose and the 3D particle shape. The latter was determined using X-ray micro-CT. Based on this, the sphericity distribution was determined. Relatively large differences were found for the physical properties between the different particle types.

Single-trajectory simulations were performed to determine the effect of the fertilizer type on the travelled distance. The physical properties of the different fertilizer types measured above were used for this. Relative large differences between particle types were found. The difference between particle types was generally higher for the conical compared to the flat disc case and increased clearly with the particle velocity. Because of their different aerodynamic behaviour, it is clear that some fertilizer types should not be blended together to be spread simultaneously on the field.

Next, simulations were performed to determine the effect of the different parameters from the ballistic model on the landing position. These parameters were: the horizontal and vertical velocity of the particles, the sphericity, true density, initial height, and also the density of air. Finally, also the effect of wind was determined, both in the longitudinal and transverse direction. The absolute sensitivity was calculated to quantify the effect of these parameters for different cases: parameters ejected with low, medium or high velocity from a flat or conical disc and the different fertilizer types analysed above. The perturbation factors for the analysis were based on realistic

measurement errors. Results showed that increasing the particle velocity increased the travelled distance, however the extent of the effect was strongly dependent on the vertical angle. The absolute sensitivity for the vertical velocity component was clearly higher than for the horizontal velocity component. Increasing the sphericity, the particle true density and the particle diameter increased the travelled distance of the particles, especially in the case for conical discs and higher particle velocities. The effect of the sphericity and the particle true density was relatively linear, while the absolute sensitivity for the particle size decreased with an increase in the particle size. It was shown that the drag coefficient changes during the trajectory of the particles due to a change in particle velocity. The absolute sensitivity for the initial height was higher for the flat disc compared to the conical disc. An increasing air density decreased the travelled distance. The extent of the effect was higher for the conical disc and at higher particle velocities. It was shown that wind can affect both the travelled distance in the longitudinal and the transverse direction. The effect of wind was found linear with the wind velocity and was much higher for conical discs compared to flat discs. Furthermore, the effect increased with an increase in particle velocity.

To compare the effect of the different parameters, the relative sensitivity was calculated. Generally, the relative sensitivity for the vertical velocity component was much higher than for the horizontal velocity component. The relative effect of the particle density, the density of air and the initial height was very small. Increasing the velocity of the particles decreased the relative sensitivity for the horizontal velocity and increased the relative sensitivity for the particle diameter. Particles ejected with a conical disc were most sensitive to the particle diameter, especially at high particle velocities while particles ejected with a flat disc were more sensitive to the vertical velocity component. Particles ejected with a conical disc were relatively more affected by wind than particles ejected from a flat disc, especially in the case of faster moving particles. From these results, it can be concluded that the vertical velocity component and particle diameter are important parameters for accurately determining the landing position. Also the effect of wind on the individual trajectories of particles was relatively large. The effect on the spread pattern, which is generated by superimposing multiple particle trajectories however is unclear and should be further investigated.

CHAPTER

3

DEVELOPMENT OF AN ILLUMINATION SYSTEM FOR MULTI-EXPOSURE IMAGE ACQUISITION

This chapter is based on:

Cool, S., Pieters, J.G., Mertens, K.C., Mora ,S., Cointault, F., Dubois, J., Van De Gucht, T. & Vangeyte, J. (2015). Development of a high irradiance LED configuration for small field of view motion estimation of fertilizer particles. Sensors 15(11), 28627–28645.

3.1. Introduction

Different hybrid approaches have been developed in literature to predict spread patterns based on measurements of particle parameters at the beginning of their airborne trajectories. From these techniques, image processing approaches are most promising because they allow to determine the parameters of multiple particles without interfering in the fertilizer flow (Hijazi et al., 2014). Reumers et al. (2003) and Villette et al. (2006,2008) used the motion blurring technique to determine the horizontal velocity and direction of motion. By using continuous illumination and a relatively long camera exposure, the particles appeared as straight lines on the images. Vangeyte and Sonck (2005) used a high speed camera to take images of fertilizer particles at high framerate. By matching particles in subsequent images, the horizontal velocity and outlet angle was determined. Hijazi et al. (2014) used a stereovision approach of two high speed cameras to determine particle velocities in three dimensions. Although capable of high framerates, high speed cameras generally have a relatively low resolution and are very expensive (> 25 000 euro). Cointault et al. (2003) and Vangeyte and Sonck (2005) implemented the multi-exposure technique as low-cost alternative for high speed cameras. By subsequently flashing the light on and off during the exposure of the camera, fertilizer particles were captured multiple times on the same image. The imaging system by Cointault et al. (2003) had a relatively large field of view (1 m²) and used eight different flash units for this which were subsequently triggered to provide multi-exposure. The illumination system however had a relatively long recycle time (1 s) and was improved by Hijazi et al. (2008) by implementing power LEDs. The low-cost imaging system by Vangeyte and Sonck (2005) had a relative small field of view (0.3 on 0.19 m) and used a LED stroboscope for multi-exposure. The luminous intensity however was low because standard LEDs were used. Until now, none of these approaches has succeeded in predicting the spread pattern of centrifugal fertilizer spreaders in an accurate way. In this PhD research, a new measurement system is developed, combining stereovision with multi-exposure image acquisition. For this, a specific illumination system is necessary. However, no of-the-shelf commercial illumination system however meets the requirements for this.

Therefore, the aim of this chapter is to design a specific illumination system to acquire multi-exposure images of fast-moving fertilizer particles using a stereovision camera system. To minimize motion blur, the system should have a high intensity and fast switching capabilities. Furthermore, the generated light distribution in the field of view of the cameras should be highly uniform.

3.2. Theoretical background

LEDs have a number of advantages over traditional lighting sources and were therefore selected for this application. They have a relatively low energy consumption, long lifetime and small size, and moreover, various colours are available (Lei et al., 2014). Furthermore, they allow fast switching, which is important when synchronizing the illumination system with image acquisition and minimizing motion blur. LEDs are often combined in arrays for achieving a suitable light intensity and homogeneity since a single LED cannot provide sufficient illumination, and because of their lighting distribution pattern. The overall illumination pattern of an array of LEDs is obtained by superposition of the different illumination patterns of each LED (Yang et al., 2009). There are different methods for designing LED arrays for obtaining high uniform illumination patterns. Moreno et al. (2006) proposed a method to determine the optimum packaging density of square, linear, circular and hexagonal LED arrays for imperfect Lambertian sources by determining the optimum LED to LED spacing for a given distance between LED source and target. Yang et al. (2009) investigated the case of a rectangular array of LEDs. Some studies focus on the design of optical components to achieve uniform illumination from LED sources, e.g. Wang et al. (2011) designed a method to optimize the light intensity distribution curve, achieving highly uniform illumination (when the distance-height ratio is given) by designing freeform lenses. Whang et al. (2009) and Cheng et al. (2012) proposed solutions for uniform lighting with three kinds of illumination systems: circular ring arrays, linear arrays and square arrays. All the methods presented above are analytical methods, and illumination uniformity is only assessed over the central region of the target plane. For applications where uniformity is required over the whole target plane, as is the case in this situation, Lei et al. (2014) developed a local search algorithm to obtain a highly uniform illumination, considering the whole target plane. An initial random condition is iteratively improved by moving LEDs to neighbouring positions of candidate solutions. Their algorithm minimizes an objective function, being the Coefficient of Variation of the illuminance distribution in a plane perpendicular to the LED array, to obtain the highest uniformity. The algorithm does not control the illuminance level, is very sensitive to local optima and should therefore be calculated with a considerable number of initial random positions.

3.3. Materials and methods

3.3.1. General requirements

The illumination system will be designed specifically for the stereo camera system developed in chapter 4. To exclude the influence of the (varying) ambient light intensity (sunlight), the setup will be placed inside a dark environment. The camera system consists of two monochrome cameras mounted 370 mm apart. They are mounted approximately 0.6 m above the particle flow and at this distance, their shared field of view is 0.3 by 0.3 m. Because fertilizer particles move at relative high speed (15-40 m/s), the exposure time must be as small as possible to reduce motion blur. This however reduces however the amount of light reaching the camera sensor. Therefore, a high level of irradiance is necessary. Based on preliminary experiments (results not shown), it was determined that a minimum irradiance of 450 W/m² at an exposure time of 30 µs was necessary to reduce motion blur without compromising the signal-to-noise ratio of the images. Furthermore, the irradiance uniformity in the field of view of the cameras should be maximized as much as possible. The minimum Coefficient of Variation (CV) for the irradiance distribution was set at 2%. An algorithm will be used to find the optimal LED configuration to deliver a uniform irradiance on the field of view of the cameras. The distance from the illumination system to the target plane was set at 0.6 m. For practical purposes, the size of the LED system was limited to 0.5 m x 0.5 m. Furthermore, space was to be provided for the cameras. To determine the optimal number of LEDs and the individual LED positions, a multiple objective genetic algorithm was used.

3.3.2. Calculating the light distribution pattern

Generally, there are two ways to quantify optical radiation. Radiometry is the measurement of electromagnetic radiation within the frequency range 0.3 and 3000 THz, while photometry is restricted to the frequencies detectable by the human eye. General photometric and radiometric quantities and units are illustrated in Table 3.1.

Table 3.1. General photometric and radiometric quantities and units

Quantity	Photometric	Radiometric
Energy per unit time	Luminous flux (lm)	Radiant flux (W)
Power per unit area	Illuminance (lx)	Irradiance (W/m²)
Power per unit solid angle	Luminous intensity (cd)	Radiant intensity (W/sr)
Power per area solid angle	Luminance (cd/m²)	Radiance (W/m².sr)

Most authors assume that LEDs have Lambertian distribution patterns, meaning that the luminous intensity I is a cosine function of the viewing angle, being the angle off-centre (0°) (Moreno et al., 2006):

$$I(\theta) = I_0 \cos^m \theta \qquad (3.1)$$

with: I_0 the luminous intensity at the normal direction to the source surface (Cd) and θ the viewing angle (°)

Parameter m is calculated using the half width viewing angle $\theta_{1/2}$ which is the viewing angle at which the radiant intensity is half of the value at the normal direction. $\theta_{1/2}$ is calculated as half of the Full Width at Half Maximum value (FWHM) and is generally provided by the manufacturer. This parameter is calculated according to:

$$m = \frac{-\ln 2}{\ln(\cos \theta_{1/2})} \qquad (3.2)$$

In some cases, the manufacturer provides the luminous intensity distribution for a LED and LED-lens combination. This was the case for the application in this work. This photometric data was first converted to radiometric units by weighting with the standard luminosity function (see Figure 3.1). The best fitting Gaussian function (order n) was used for interpolation of the irradiance values:

$$I(\theta) = \sum_{i=1}^{n} a_i e^{-\left(\frac{\theta - b_i}{c_i}\right)^2} \qquad (3.3)$$

with: I_0 the radiant intensity at the normal direction to the source surface (W/sr), a_i, b_i and c_i are constant values depending on the function fit.
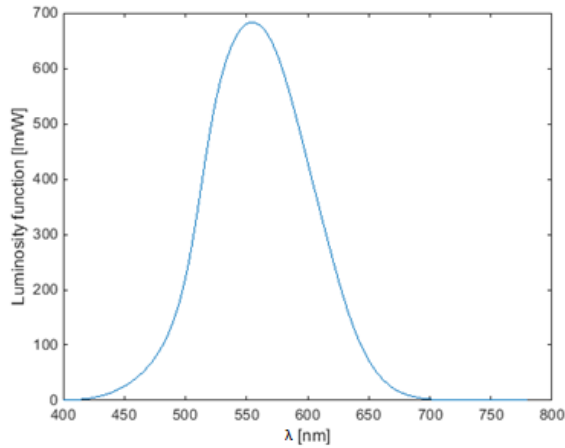
Figure 3.1. Standard luminosity function for photopic vision (Pelz, 1993)

The luminous efficacy or radiant to luminous flux conversion factor η_v (lm/W) was calculated as the ratio of the luminous flux (given by the manufacturer) to the radiant flux of the LED (calculated using the standard luminosity function).

Because the individual LEDs can have different positions with respect to the lighting source and can also be oriented in different ways, three coordinate systems can be defined. The first coordinate system is the LED coordinate system; the second is the source coordinate system, situated in the geometric centre of the LED array. The third coordinate system is the target coordinate system (x,y,z), situated in the geometric centre of the target that needs to be illuminated.
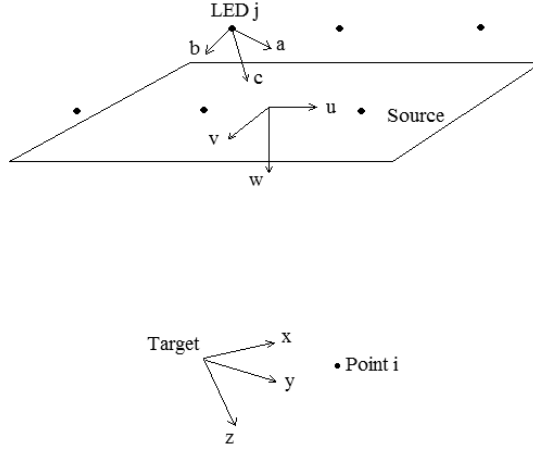
Figure 3.2. LED, source and target coordinate system

The irradiance E (W/m²) at point i, illuminated by LED j, can be calculated using the "cosine law" or "inverse square law":

$$E_{i,j} = \frac{I(\theta_{i,j})\cos\theta_{i,j}}{r_{i,j}^2}$$ (3.4)

with $r_{i,j}$ the distance between the point i and the LED j.

Let $\mathbf{P_T} = [x_i,\ y_i,\ z_{i\ 1}]^T$ be the position of point i in the target coordinate system (homogeneous coordinates), the position in the coordinate system of LED j can be calculated as:

$$\begin{bmatrix} a_{i,j} \\ b_{i,j} \\ c_{i,j} \\ 1 \end{bmatrix} = \begin{bmatrix} \mathbf{R} & \mathbf{T} \\ \mathbf{0} & 1 \end{bmatrix} \mathbf{P_T}$$ (3.5)

with:

$$\begin{bmatrix} \mathbf{R} & \mathbf{T} \\ \mathbf{0} & 1 \end{bmatrix} = \mathbf{H_{S \to L}}\, \mathbf{H_{T \to S}}$$ (3.6)

With: $\mathbf{H_{T \to S}}$ the transformation matrix from the target to the source coordinate system and $\mathbf{H_{S \to L}}$ the transformation matrix from the source to the LED coordinate system.

Since $\cos\theta_{i,j} = \frac{c_{i,j}}{r_{i,j}}$ and from Equation 3.4, the irradiance can be written as a function of the position in the target coordinate system:

$$E_{i,j} = \frac{I(\theta_{i,j})\, ([\mathbf{R_3}\ T_3]\, \mathbf{P_T})}{(([\mathbf{R_1}\ T_1]\, \mathbf{P_T})^2 + ([\mathbf{R_2}\ T_2]\, \mathbf{P_T})^2 + ([\mathbf{R_3}\ T_3]\, \mathbf{P_T})^2)^{\frac{3}{2}}}$$ (3.7)

where the subscript for **R** and **T** indicates the row of the matrix

In the case that LEDs are positioned horizontally on a source plane and the source plane is horizontally aligned with the target, $\begin{bmatrix} \mathbf{R} & \mathbf{T} \\ \mathbf{0} & 1 \end{bmatrix}$ becomes $\begin{bmatrix} 1 & 0 & 0 & -u_j \\ 0 & 1 & 0 & -v_j \\ 0 & 0 & 1 & w_i \\ 0 & 0 & 0 & 1 \end{bmatrix}$ with (u_j, v_j) the position of LED j in the source coordinate system (2D) and w_i the vertical distance of point i to the source plane

Moreno (2010) developed a simple equation to evaluate the far-field condition of a LED array in function of the LED radiation pattern, array geometry and number of LEDs. Generally, the "rule of five" can be used, stating that a LED array can be modelled as a directional point source if $\frac{r_{min}}{D}$ is larger than five, with r_{min} the minimal distance from source to target (resulting in an error of less than 1%) and D the largest dimension of the source array. When this is not the case, for example because of the considerable size of the LED array, each LED needs to be modelled separately.

When n LEDs are used, the total irradiance can be calculated as:

$$E_i = \sum_{j=1}^{n} E_{i,j} \tag{3.8}$$

Illumination uniformity can be assessed in different ways (Moreno et al. (2010). Amongst these parameters, the coefficient of variation is most widely used.

$$CV = \frac{\sigma_E}{\bar{E}} \tag{3.9}$$

with: $\bar{E}$ and σ_E the irradiance average and standard deviation in the target plane respectively

3.3.3. Multiple objective genetic algorithm

Most studies in literature seek to optimize the illuminance uniformity. The illuminance intensity is generally not considered in these studies. The purpose of this study is to find the optimal configuration of LEDs delivering a high level of irradiance in the target area. This is necessary to maximize the depth of field and minimize motion blur. However, the uniformity of the distribution is also important to reduce under-segmentation and increase the accuracy of the matching steps (Hijazi et al., 2014).

When the target area is discretized to a high level, the search space for the algorithm is very large. Especially when a high number of LEDs is used, the problem becomes very complex. Due to their broad range and efficiency (Goldberg et al., 1988), it was chosen to use a genetic algorithm for this application. This family of algorithms uses the evolution of a population over subsequent generations to search the optimal solution for a target problem. A population is defined as a set of possible solutions, i.e. individuals. Offspring is generated in two ways: cross-over recombines two parents to create a new child, while mutation introduces small random changes in the individuals creating offspring. Parents for the next generation are selected based on their fitness, which is their objective function value. Individuals with a better objective function value are given more chances to reproduce. Populations can be divided into subpopulations and migration between these subpopulations can be set. Eventually, the best individual result from the evolution process is chosen as the optimal solution (Schaffer, 1985).

The aim in this research is to find the optimal position for each LED to maximize the average irradiance (radiometric units) and homogeneity of light distribution in the target plane. Thus there are two main objectives. The most simple solution would be to combine both objectives by weighting them in a single objective function. Finding the weighting factors however is not an easy task, because the relative importance of both objectives is difficult to quantify. By performing a multi-objective optimization instead, multiple Pareto-optimal solutions can be found. This set of solutions can then be used to select the optimal solution for this specific application. In this work, the *gamultiobj* function from the Global Optimization Toolbox of Matlab 2014b (Mathworks Inc., USA) was used which uses a variant of the NSGA-II algorithm (Deb et al., 2002). The algorithm variables for which the objective functions needed to be optimized are the discrete xy positions of the LEDs. As mentioned before, the source is reduced to a plane which is horizontally aligned with the target plane. The origin of the source plane is situated at the same distance from the target plane as the camera centre at the height of the camera lens: [0 m, 0 m, 0.6 m] in the source coordinate system (see Figure 3.2). Therefore there are only two degrees of freedom for each LED: the discrete x- and y-position. To enforce symmetry into the system, the search space was reduced to one quadrant. The LEDs in the second, third and fourth quadrants take their xy position accordingly. This restricts the number of LEDs used to be a multiple of four. Furthermore, a central LED will not be approved by the algorithm. Therefore, a configuration k with n different LEDs can be represented by a matrix P_k:

$$P_k = [\mathbf{x}_k, \mathbf{y}_k] \tag{3.10}$$

With: $\mathbf{x}_k$ and $\mathbf{y}_k$ row vectors containing the x- and y-positions of the LEDs in the first quadrant.

The objective functions that must be optimized represent the radiant intensity, which should be maximized and the homogeneity, represented by the CV which should be minimized. Two-step linear objective functions were used in this study to make sure that solutions below the desired thresholds (of both irradiance and CV) were penalized to a higher degree than solutions above the thresholds were favoured:

$$f_1(\overline{E}) = \begin{cases} a_1(\overline{E}_k - \widehat{E}) + b_1, & \overline{E}_k < \widehat{E} \\ c_1(\overline{E}_k - \widehat{E}) + d_1, & \overline{E}_k \geq \widehat{E} \end{cases} \qquad (3.11)$$

With: $\widehat{E}$ the target irradiance = 450 W/m². $\overline{E}_k$ is the average irradiance in the target area reached by configuration k.

Irradiance levels below the target irradiance level are inferior while irradiance levels above this value are superior, although to a lower degree: $a_1 < c_1$. The objective function for the CV is similar:

$$f_2(CV) = \begin{cases} a_2(CV_k - \widehat{CV}) + b_2, & CV_k < \widehat{CV} \\ c_2(CV_k - \widehat{CV}) + d_2, & CV_k \geq \widehat{CV} \end{cases} \qquad (3.12)$$

With: $\widehat{CV}$ the target coefficient of variation = 2%.

Figure 3.3 illustrates the objective functions used for the simulations.
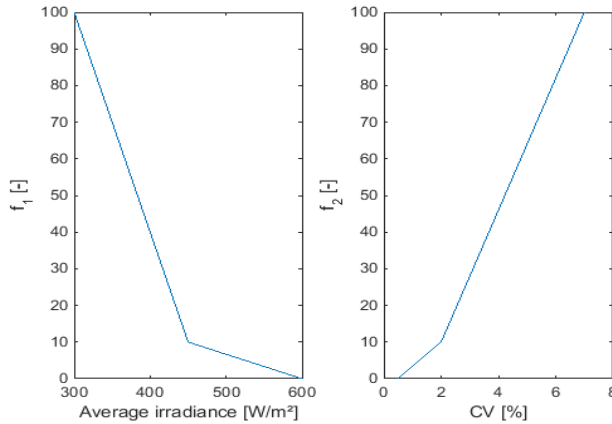
Figure 3.3. Objective functions used for the multiple objective genetic algorithm

The parameters of the optimization algorithm were determined based on exploratory simulations (results not given here): the population type was 'double vector' and a

population size of 150 individuals was used (no subpopulations). The default creation function of the toolbox was used for generating the initial population. The xy positions (algorithm variables) were restricted to set a maximum on the array size (maximally 0.25 m in x and y direction). To ensure sufficient LED spacing for thermal management and prevent LEDs from overlapping, a penalty factor of 100 was added to both objective functions in case that LED centres were closer than a 35 mm. The selection process was tournament based with a tournament size of 4, meaning that each parent was chosen by randomly selecting 4 individuals and then choosing the best one. For the reproduction, a crossover fraction of 0.8 was used and children were created using the 'intermediate' crossover function. The remaining individuals for the next generation were produced using mutation (through the 'adaptive feasible' mutation function). The default distance measure function was used and the Pareto front population fraction was taken at 0.35.

3.3.4. Simulations
3.3.4.1. LED selection

As a first step, the optimal LED was selected from a range of high power LEDs based on the spectral sensitivity of the camera. The following efficiency factor was calculated:

$$\eta_{\text{sens}} = \int_{\lambda_{\text{min}}}^{\lambda_{\text{max}}} P_{\text{led}}(\lambda)\, S_{\text{camera}}(\lambda)\, \partial\lambda \qquad (3.13)$$

with: P_{led} the normalized (area under the curve equals 1) radiant power of the LED as a function of the wavelength λ (W) and S_{camera} the relative spectral sensitivity function of the camera (-), which was provided by the manufacturer.

By multiplying η_{sens} with the radiant flux of the LED (W), the following camera spectral sensitivity factor (W) can be calculated:

$$F_{\text{camera}} = P_{\text{led}}\, \eta_{\text{sens}}\, 100 \qquad (3.14)$$

This factor represents the radiant power of the LED as perceived by the camera. The LEDs considered are given in Table 3.2.

Table 3.2. The luminous flux ϕ_v and the wavelength at peak intensity λ_{peak} are given. All values were provided by the manufacturer (Phillips Lumileds, USA)

Number	ϕ_v (lm)	λ_{peak} (nm)	Name	Part number
1	313	567.5	Lime	LXML-PX02-0000
2	122	505.0	Cyan	LXML-PE01-0070
3	161	530.0	Green	LXML-PM01-0100
4	320	-	Cool white	LXML-PWC2
5	310	-	Neutral white	LXML-PWN2
6	21	447.5	Royal blue	LXML-PR01
7	106	627.0	Red	LXM2-PD01-0050
8	140	590.0	Amber	LXML-PL01

3.3.4.2. LED configuration

Next, the optimal LED configuration was determined, minimizing the CV in the target area. The latter is defined as the field of view of the camera, which is approximately 0.30 x 0.30 m at 0.6 m distance in the z-direction. To focus the light to the target, three types of lenses were used, as given in Table 3.3.

Table 3.3. Lens specifications used for simulation (Carclo Optics, UK)

Lens	Cdlm value (Cd/lm)	FWHM (°)	Diameter (mm)	Part number
Narrow	4.60	23.0	23	10611
Medium	2.59	28.64	23	10612
Wide	1.29	44.4	23	10613

In total, 36 LEDs were used in combination with the lenses above. First of all, two traditional approaches were used: a square and circular array of LEDs was simulated for different sizes of the source plane. The empirical formula of Moreno (2006) was used to determine the optimal LED spacing in case of a square or circular array of LEDs. The multiple objective genetic algorithm was used as well to determine the optimal LED configuration and results were compared. Simulations were done for a different number of LEDs.

3.4. Results and discussion

3.4.1. LED selection

The efficiency factor η_{sens} and the camera spectral sensitivity factor F_{camera} were calculated for the different LEDs to select the most appropriate LED for this application. The results are given in Table 3.4.

Table 3.4. Radiant to luminous flux conversion factor η_v, radiant flux φ (at given forward current I_f), camera spectral efficiency factor η_{sens} and camera spectral sensitivity factor F_{camera} for different LEDs

LED number	I_f (A)	η_v (lm/W)	φ (W)	η_{sens}(%)	F_{camera} (W)
1	700 mA	461.4	0.678	80.5	54.6
2	700 mA	213.4	0.572	92.0	52.6
3	700 mA	551.9	0.292	95.6	27.9
4	1000 mA	329.6	0.971	78.1	75.8
5	1000 mA	348.4	0.890	74.6	68.5
6	700 mA	20.0	0.910	76.5	69.6
7	700 mA	97.0	1.093	56.1	61.3
8	700 mA	472.3	0.296	70.2	20.8
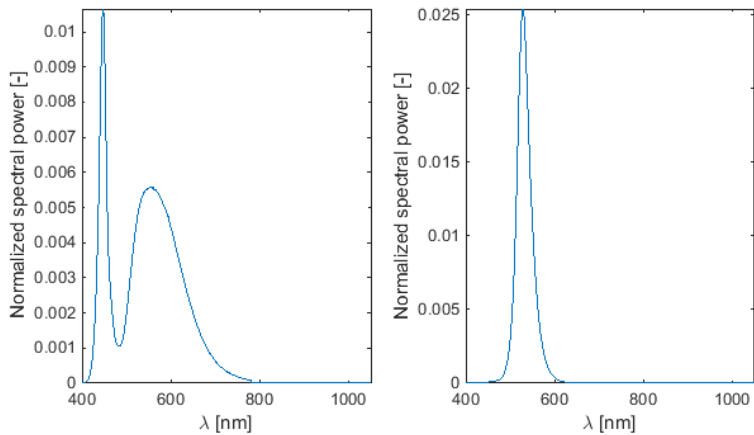
Figure 3.4. Normalized spectral power distribution for LED 4 (a) and LED 3 (b)

The selection of the LED was only based on radiant efficiency, price was similar and was not considered here. From Table 3.4, it can be seen that LED 4 and LED 7 had

the largest radiant flux. However, this does not imply that the LED will result in a higher brightness on the images of the camera sensor, because the sensitivity of the sensor needs to be considered as well. Figure 3.4 shows the normalized spectral power distribution for LEDs 3 and 4. From Table 3.4, it is clear that the efficiency factor is largest for LED 3, because the LED had a spectral power distribution very near the maximal sensitivity value of the camera. This was not the case for LED 4 and 7. However, when considering the camera spectral sensitivity factor, taking into accounts both the camera sensitivity and the LED radiant flux, the highest value was obtained for LED 4. The higher radiant flux overrules the lower camera spectral sensitivity for this LED.

3.4.2. LED configuration
3.4.2.1. Square and circular configuration

The angular luminous intensity distribution was provided by the manufacturer for the three types of lenses. Figure 3.5 illustrates the values for the narrow angle lens. The best fitting Gaussian function and the imperfect Lambertian distribution which is based on the half-angle are illustrated as well. We can see that the Lambertian distribution is not the ideal fit.
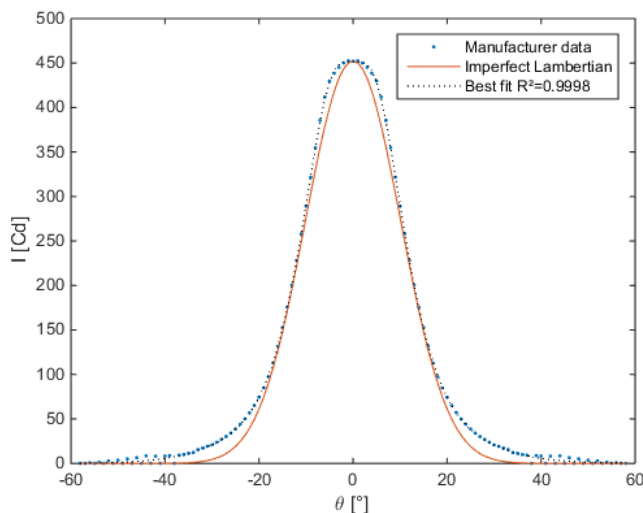
Figure 3.5 Luminous intensity distribution for narrow angle lens combined with the selected LED (data obtained at forward current of 350 mA, luminous flux of 100 lumen)

In Figure 3.6, the irradiance distribution pattern for the LED in combination with the three types of lenses simulated for a plane with size 1 m at 0.6 m distance is given.

An array of LEDs can be considered as a point source if the size of the source is small relative to the distance from source to target. Generally, the "rule of 5" applies for the ratio of this distance and the largest source dimension (r_{min}/D). This would result in an array with maximal dimension of 0.12 m, which is actually almost the smallest possible 6x6 LED array since the LEDs have a diameter of 23 mm. Moreno (2010) found for Lambertian emitters that the r_{min}/D was dependent on the number of LEDs used and the FWHM value. For Lambertian emitters, values up to 70 were necessary for the far field condition to be satisfied. This illustrates that the light source in this study could not be considered as a point source and light distribution should be modelled for each LED separately.
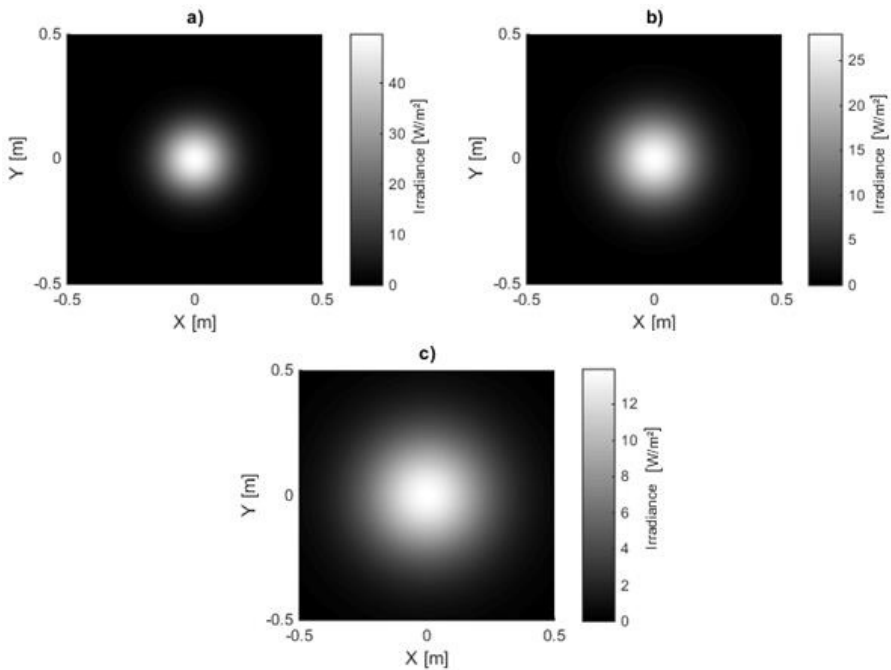
Figure 3.6. Simulated light distribution pattern at 0.6 m distance from LED 4 for (**a**) narrow; (**b**) medium; (**c**) wide angle lens

Two different popular configurations were simulated: the square and the circular array. Results for 36 LEDs are illustrated in Figures 3.7 to 3.9 for different sizes of the source plane for narrow, medium and wide angle lenses, respectively.
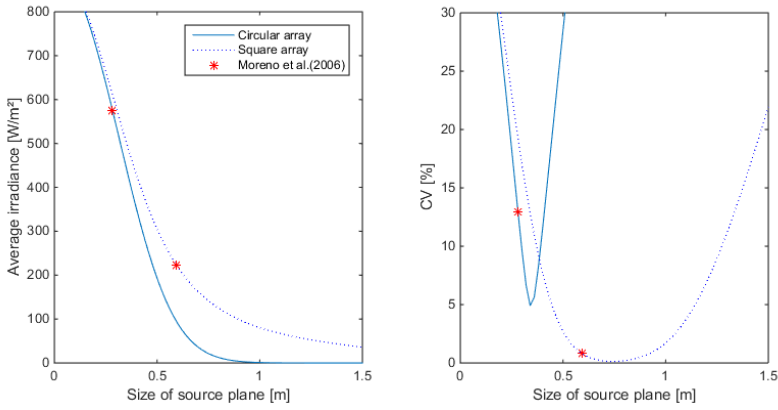
Figure 3.7. Average irradiance and CV as a function of the source plane size for square and circular arrays of 36 LEDs. Simulations are done with the narrow beam lens
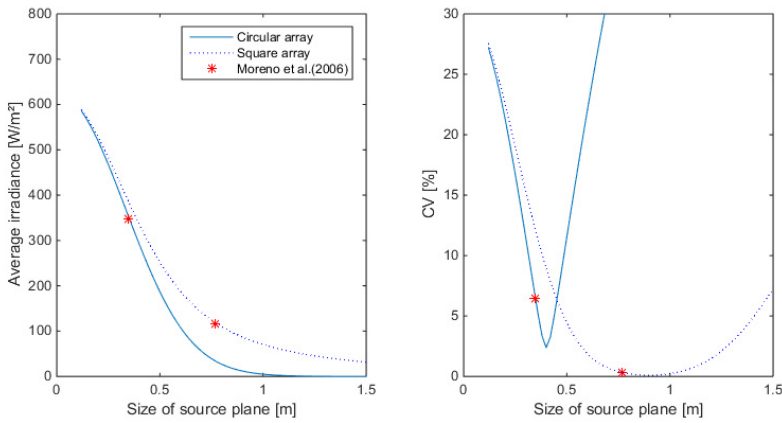
Figure 3.8. Average irradiance and CV as a function of the source plane size for square and circular arrays of 36 LEDs. Simulations are done with the medium beam lens.
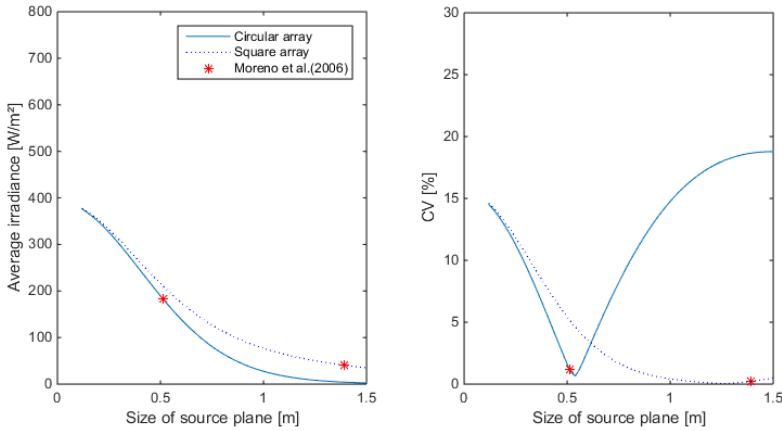
Figure 3.9. Average irradiance and CV as a function of the source plane size for square and circular arrays of 36 LEDs. Simulations are done with the wide beam lens

The size of the source plane had a large effect on the average irradiance and CV in the target area. When the source plane increased in size, the average irradiance decreased. For both the square and circular array of LEDs, the CV decreases with the size of the source plane, then reaches a minimum and then increases again. For the square array with narrow lenses, the smallest CV value was found at an array size of 0.76 m. Although the CV here was very small (0.76%), the irradiance was too low for this application, since an irradiance of 450 W/m² was required. The same was found for the medium and wide angle lens. Higher intensity values were found for a smaller source plane size, however, due to the suboptimal overlap between individual LED light distribution patterns, this resulted in a lower uniformity. With the wide angle lens, it is not possible to obtain more than 400 W/m², not even with the smallest configuration. The lowest CV for the circular array was 5% at an irradiance level of 463.8 W/m² for the narrow lens. Although the intensity was above the required level, the CV was too high, indicating a low uniformity level. For the medium and wide angle lenses, the intensity at the source plane size with lowest CV was lower than the required level. Generally, it can be seen that in case of a circular array, the intensity drops down faster with increasing source plane size compared to the square array for the same number of LEDs. On Figure 3.9, it can also be noticed that the CV as calculated by the empirical formula of Moreno et al. (2006) is not the minimum CV for a square and circular array. This can be attributed to the fact that the central region which is illuminated uniformly is different from the target area considered in this study. For 36 LEDs, the narrow angle lens seems to be the only one appropriate for this

application. The main objectives however, stated in section 3.3.1 (average irradiance > 450 W/m² and CV < 2%) cannot be reached using these configurations.

3.4.2.2. Multiple objective genetic algorithm

For the narrow lens, simulations with 36 to 52 LEDs were made in steps of four. A minimum spacing of 25 mm between LED centres was used for thermal reasons. Results are given in Figure 3.10.

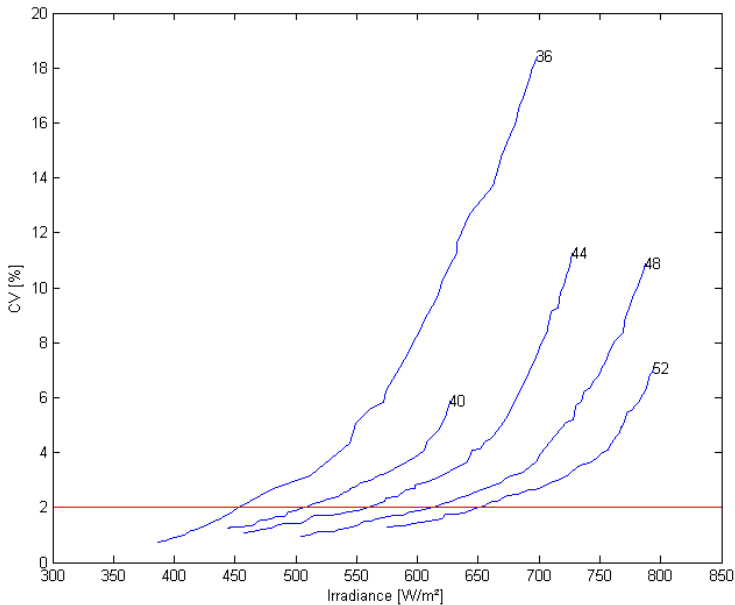**Figure 3.10.** Pareto front for 36, 40, 44, 48 and 52 LEDs. The CV limit of 2% is given by the horizontal line

From Figure 3.10, we can see that the higher the number of LEDs, the more the Pareto front moves to higher irradiance levels. Placing the upper limit for the CV at 2%, the following values were found (Table 3.5).

Table 3.5 Average irradiance at CV approximately at 2% for different number of LEDs

Number of LEDs	Average irradiance (W/m²)	CV (%)
36	452	1.98
40	504	1.97
44	558	1.99
48	616	2.05
52	648	1.95

The minimal irradiance level was set at 450 W/m² and the maximal CV at 2%. Therefore, the optimal configuration for 36 LEDs was selected for this application. By comparing the values in Table 3.5, it can be seen that the more LEDs are used, the higher the average irradiance in the target area for a similar uniformity. The selection of which configuration to choose is now based on the trade-off between price and irradiance. Higher irradiance levels are more desirable because then a smaller exposure time can be used, which can further improve the motion blur and allow a larger depth of field. However, the more LEDs used, the higher the cost of the system. Based on previous experiments it was found that 450 W/m² was necessary, therefore the configuration with 36 LEDs was chosen as the optimal configuration for this application. The LED positions for the illumination system are illustrated in Figure 3.11 and the irradiance distribution is given in Figure 3.12. The minimum irradiance in the target area was 415.8 W/m² while the maximal value was 467.1 W/m², resulting in a min to max ratio of almost 90%. It is clear that the algorithm performs better than the traditional approaches using a square or circular array of LEDs in terms of homogeneity. In contrast to the local search algorithm of Lei et al. (2014), this algorithm guarantees a symmetrical distribution of LEDs which can be important for design purposes. Furthermore, it is more flexible because it does not only optimize the uniformity of lighting in the target area, but also takes into account the required irradiance level. For thermal design, restrictions were set for the separation between LEDs and for practical purposes the size of the source plane was restricted as well. Although in this approach it was chosen to use the CV to measure the uniformity of distribution, objective functions using other variables or restrictions can be introduced into the algorithm.

(a)   (b)
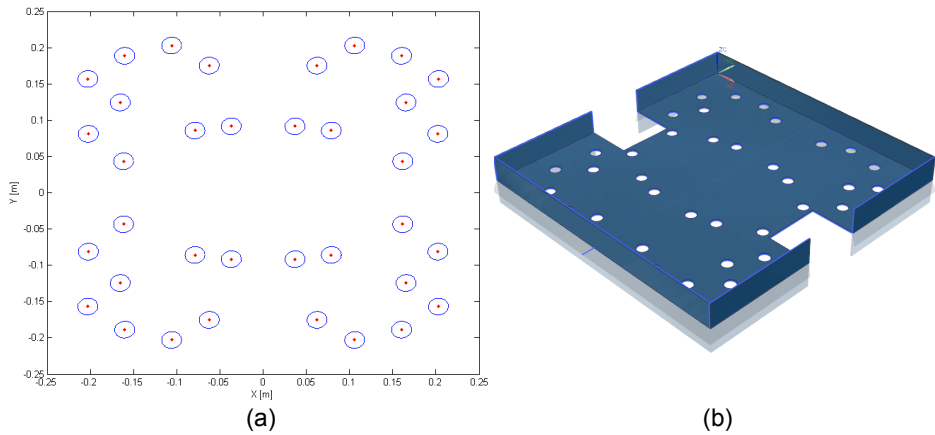
Figure 3.11. Two dimensional view (a) of the optimal LED positions calculated with the multiple objective genetics algorithm for a number of 36 LEDs. Three dimensional view of the final illumination system (b)
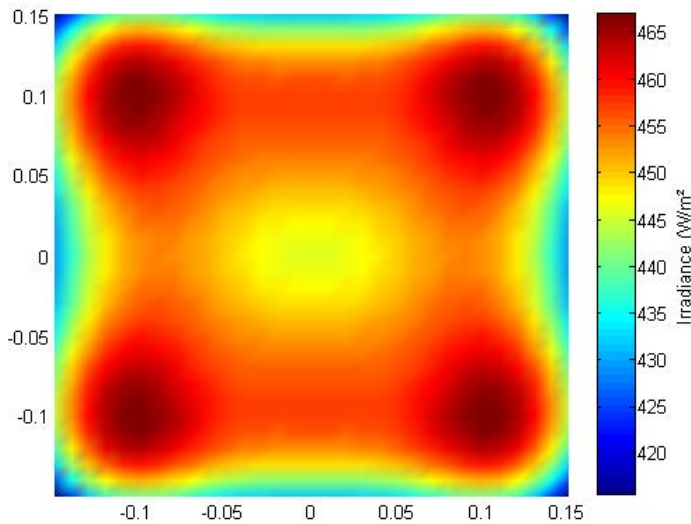
Figure 3.12. Irradiance distribution for optimal configuration obtained with a multiple objective genetic algorithm for a number of 36 LEDs

3.5. Conclusions

In this chapter, a specific high power LED illumination system was developed for multi-exposure image acquisition of fertilizer particles with a stereovision system. To achieve a high accuracy for measuring the particle parameters from the images, a high irradiance level was necessary without compromising the uniformity of light distribution. In a first step, the optimal LED was selected from a range of commercially available power LEDs by taking into account the spectral output of the LEDs and camera sensitivity. Next, the optimal configuration of LEDs was determined using a multiple objective genetic algorithm. Both the irradiance level and homogeneity of the light distribution were considered, in contrast to other approaches used in literature. The angular distribution pattern from the manufacturer was to simulate light distribution patterns for multiple LEDs. Comparing simulation results for three types of LED-lenses, the narrow angle lens was found optimal for this application. Multiple Pareto optimal solutions were simulated for different numbers of LEDs and from this set, the best configuration was selected. The optimal configuration had a high irradiance and a coefficient of variation below 2%. The illumination system will be used for multi-exposure image acquisition to determine the parameters of fertilizer particles after being ejected by the spreader using image processing.

CHAPTER

4

DEVELOPMENT AND EVALUATION OF A MEASUREMENT SYSTEM TO PREDICT SPREAD PATTERNS OF CENTRIFUGAL SPREADERS

This chapter is partially based on:

Cool, S. R., Pieters, J.G., Seatovic, D., Mertens, K.C., Nuyttens, D., Van De Gucht, T.. & Vangeyte, J. (2017). Development of a Stereovision-Based Technique to Measure the Spread Patterns of Granular Fertilizer Spreaders. Sensors 17, 1396.

4.1. Introduction

Centrifugal fertilizer spreaders are by far the most commonly used fertilizer spreader in Europe (Garcia-Ramos et al., 2012). Because their spread pattern is sensitive to errors (Villette et al., 2008), deviations can occur between the desired and the actual distribution of fertilizer on the field, leading to local under- or over-applications (Sogaard & Kierkegaard, 1994). To assess the performance of the spreading process, the spread pattern must be determined. Traditionally, this is done on the field by measuring the distribution of fertilizer using collection trays placed on the field. Due to the large working widths, this means that a lot of space is required. Furthermore, the experiments are labour intensive and time-consuming. Alternatively, the spread pattern can be predicted by using a ballistic model, calculating the trajectories and subsequent landing positions of individual fertilizer particles. This model however requires several input parameters to simulate the trajectory for each particle. Some authors used models calculating the trajectory of fertilizer particles on the spreading discs to determine the velocity and direction of motion of particles after leaving the spreading vanes (Griffis et al., 1983; Olieslagers et al., 1996; Dintwa et al., 2004b; Van Liedekerke et al., 2005). However, due to complex behaviour on the disc, these approaches were not successful in determining the spread pattern. Others used measurement systems to determine the initial conditions of the particles at the beginning of their airborne trajectory (Hofstee, 1994; Grift & Hofstee, 1997b; Cointault et al., 2003; Reumers et al., 2003a; 2003b; Vangeyte, 2013; Hijazi et al., 2014). Stereovision approaches are the most promising, because they are non-intrusive and retrieve three-dimensional information. Generally, these hybrid approaches are much faster and more space-efficient compared to the traditional approach and therefore could be used to assess the spread pattern at farm level (Grift & Hofstee, 1997b) or in controlled environments (Reumers et al., 2003). Most authors determined the velocity of the particles only in the horizontal direction and used the particle size distribution measured using sieving before spreading to simulate the individual particle trajectories. Until now, none of these approaches has succeeded in predicting the spread pattern in an accurate way, which limits their applicability in practice. Furthermore, no experimental results with real, commercially available spreaders have been reported.

The aim of this chapter was (1) to develop a measurement system to determine the size and the dynamics (position and velocity) of individual fertilizer particles leaving a centrifugal fertilizer spreader using stereovision. The illumination system developed in chapter 3 will be used for multi-exposure image acquisition. Measurement results of the system will be combined with the ballistic model developed earlier in this work (chapter 2) to simulate trajectories of particles and calculate their subsequent landing

positions. The system should enable a fast, space-efficient and accurate determination of the spread pattern for centrifugal fertilizer spreaders in practice. (2) to perform spreading experiments with a commercially available fertilizer spreader as *proof of concept* and compare results to data obtained using the traditional method.

4.2. Theoretical background

4.2.1. General

In order to obtain metrical information from cameras, the imaging process must be modelled and subsequently calibrated. The theoretical background about the camera model and stereovision is explained in the following sections.

4.2.2. Camera model

A simple way to model a camera is through the pinhole camera model. A pinhole camera can be seen as a light-proof box with a tiny hole in the front wall and a photosensitive imaging plane on the opposite side. The walls block all external rays of light except those going through the hole. Light rays moving through the hole are projected on the image plane and create an image from the three-dimensional scene. The pinhole camera model uses this exact principle, the only difference is that the imaging plane is swapped to the front (see Figure 4.1) to simplify the math (the image is no longer mirrored with respect to the scene). Images are created by intersecting rays of light, emanating from an object, with the image plane. This process can be modelled as a perspective projection (Hartley et al., 1992):

$$s \begin{bmatrix} u \\ v \\ 1 \end{bmatrix} = K \, X_c \qquad (4.1)$$

with: (u,v) the image coordinates of the projected point (pixels), s the scale factor (m), K the camera matrix and $X_c = [X_c, Y_c, Z_c]^T$: the position in the camera coordinate system (m)

The camera matrix, also called the matrix of intrinsic parameters, describes the projection from three-dimensional camera coordinates in metric units to image coordinates (pixels) and is calculated as follows:

$$K = \begin{bmatrix} f_x & 0 & p_{c,x} \\ 0 & f_y & p_{c,y} \\ 0 & 0 & 1 \end{bmatrix} \qquad (4.2)$$

with: f_x, f_y resp. the focus length[1] of the lens in the x and y direction (pixels), $p_{c,x}$ and $p_{c,y}$ the position of the principal point (projection of the optical centre on the image plane) in image coordinates (pixels)

---

[1] The focus length mentioned here is the focus length of the lens (mm) multiplied with the pixel size (pixel/mm). The focus length is a parameter that needs to be determined by calibration.

Eliminating the scale factor gives the following equation, in function of the normalized plane coordinates (x_n,y_n).

$$\begin{bmatrix} u \\ v \\ 1 \end{bmatrix} = K \begin{bmatrix} x_n \\ y_n \\ 1 \end{bmatrix}$$

(4.3)

with: $x_n=X_c/s$ and $y_n=Y_c/s$ (-)

Equation 4.3 illustrates that a scaled object will have the same projection compared to the original non-scaled object if it is placed at a proportional distance from the optical centre. Equation 4.1 is written in virtual camera coordinates and can be written in function of a world coordinate system as well:

$$s \begin{bmatrix} u \\ v \\ 1 \end{bmatrix} = K [R, t]X_w$$

(4.4)

with: [**R,t**] the extrinsic matrix, describing the transformation from a world coordinate system to the camera coordinate system in terms of rotation (rotation matrix **R**) and translation (translation matrix **t**).
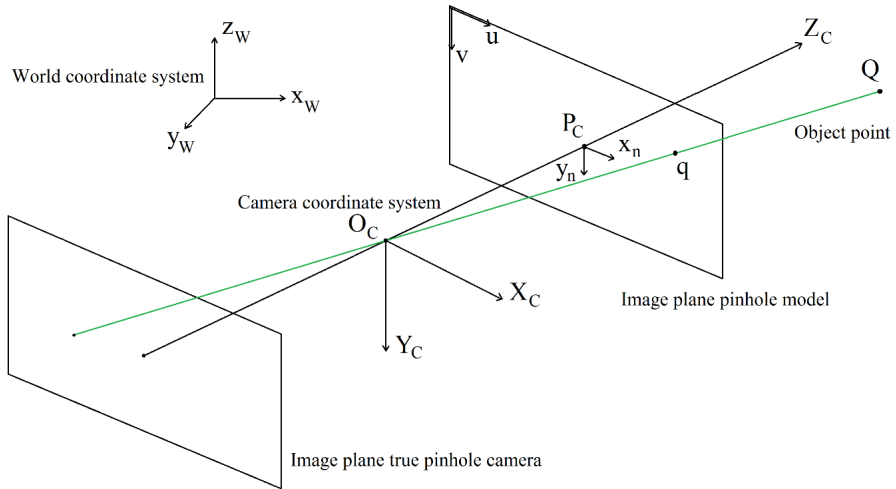
Figure 4.1. Pinhole camera model. Compared to the true pinhole camera, the image plane is swapped to the front. The original pinhole can now be seen as the optical centre (O_C). A light ray (green) originating from object point Q is projected onto the image plane (projection point q). The camera coordinate system (X_C,Y_C,Z_C) and a world coordinate system (X_W, Y_W, Z_W) are illustrated. Point q has normalized plane coordinates (x_n,y_n) and image coordinates (u,v). The principal point P_C is the projection of O_C onto the image plane

4.2.3. Lens distortion

Real pinhole cameras are not often used in practice since they do not provide enough light for the camera to allow rapid exposure. This is why lenses are used. The use of lenses however introduces distortions in the image compared to the ideal pinhole model, because lenses are not perfect and are not perfectly aligned with the camera sensor. Generally, two types of lens distortion are used to correct real lenses for their deviation from the ideal pinhole model: radial and tangential distortion.

Radial distortions arise from the shape of the lens and deviations increase towards the periphery of the image (further away from the optical centre). Radial distortion can be modelled using the following equations (Bradski and Kaehler, 2008):

$$x_{n,dist} = x_n(1 + k_1 r^2 + k_2 r^4 + k_3 r^6)$$
$$y_{n,dist} = y_n(1 + k_1 r^2 + k_2 r^4 + k_3 r^6)$$

(4.5)

with: k_1, k_2, k_3 radial distortion coefficients (-), $x_{n,dist}$, $y_{n,dist}$ the distorted normalized plane coordinates (-), x_n, y_n the distortion-corrected normalized plane coordinates (-), $r = \sqrt{x_n^2 + y_n^2}$

Tangential distortions are caused by the imperfect alignment of the camera sensor and the lens and can be modelled as follows (Bradski and Kaehler, 2008):

$$x_{dist} = x_n + (2p_1 x_n y_n + p_2(r^2 + 2x_n^2))$$
$$y_{dist} = y_n + (p_1(r^2 + 2y_n^2) + 2p_2 x_n y_n)$$

(4.6)

with: p_1, p_2 the tangential distortion coefficients (-)

The effect of radial and tangential distortion is illustrated in Figure 4.2.
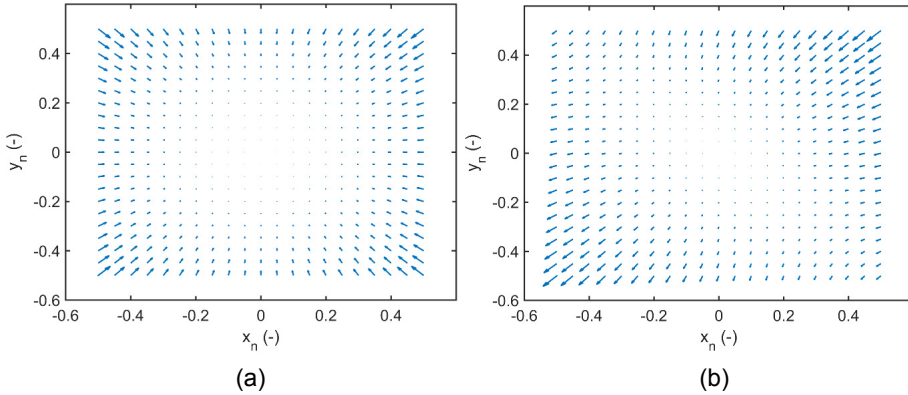
Figure 4.2. Distortion simulated for a virtual image: (a) radial distortion (k_1= -0.15, k_1= 0, k_1= 0) (b) tangential distortion (p_1= -0.0003, p_1= -0.0003)

To correct for lens distortion, Equations 4.5 and 4.6 must be solved for the distortion-corrected coordinates. Because the equations are non-linear and depend on multiple parameters, they require a non-linear solving algorithm to inverse the model and estimate the distortion-corrected from the distorted positions.

4.2.4. Stereovision and triangulation

Equation 4.1 models the transformation from object points in three-dimensional space to the two-dimensional image plane. In this case however we are interested in doing the complete opposite: calculating the three dimensional position from a two-dimensional projection. From Equation 4.1, it can be seen that this cannot be done without knowing the unknown scale factor, which is actually the z-position in the camera coordinate system[2]. By using two or more cameras, this problem can be resolved. The process of retrieving three-dimensional information using multiple cameras is called stereovision (binocular in case of two cameras).

---

[2] If the scale factor is known, the three-dimensional position can be calculated. This is used in practice to determine positions in a specified plane with a single camera.
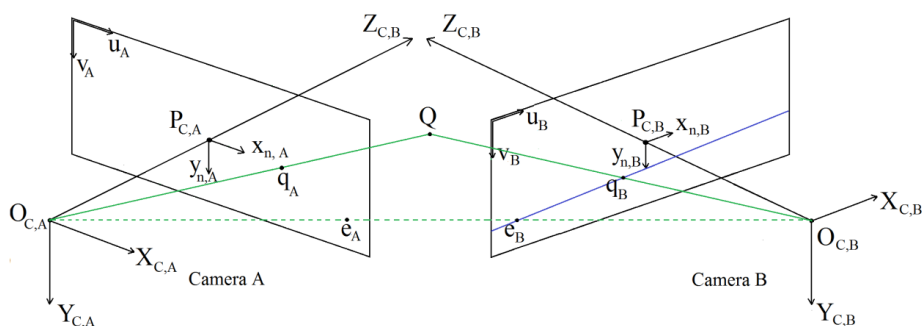
Figure 4.3. Stereovision setup of two cameras (A and B). Object point Q is projected onto the image plane of both cameras (projection points q_A, q_B). Based on these projections, the three-dimensional position can be calculated. Point Q and epipolar points e_A and e_B form the epipolar plane. The line going through e_B and q_B is the epipolar line (solid blue) for projection point q_A

In Figure 4.3, an object point Q in three-dimensional space is projected onto the image plane of two cameras A and B (projection points q_A and q_B) with optical centres $O_{C,A}$ and $O_{C,B}$ respectively. The line going through q_A and $O_{C,A}$ is seen by camera A as a single point, however the other camera sees this as a line on its image plane: the epipolar line. This is the line on which the projection point of the same object point Q must lie. If the projection point q_A and the pose (position and orientation) of both cameras relative to each other is known, then the projection of the same object point must be found on the epipolar line. The plane connecting the optical centres of both cameras and the object point is called the epipolar plane. The line connecting both optical centres intersects with the image planes at the epipolar points e_A and e_B for camera A and B cameras respectively. For each point on the image plane of camera A, there is an epipolar line on camera B.

When an object point is visible in the images of both cameras, its projection points on both images are known and the intrinsic and extrinsic (pose of the camera coordinate systems relative to each other) camera parameters known, the position of this point can be calculated (Figure 4.3). This process is called triangulation. In theory, the problem relies in finding the intersection point of the two lines (can be seen as light rays) in space, connecting the optical centres of each camera and both projection points. However, because of noise, the rays will not intersect. Different approaches can be used to solve this problem. Here, the linear Least Squares (LS) triangulation

method was used, which is often used in computer vision applications (Hartley & Sturm, 1997).

When (u_A,v_A) are the coordinates of a certain point on the image of camera A and (u_B,v_B) the coordinates of the same point on the image of camera B, then the following equations are valid (see section 4.2.2):

$$s_A \begin{bmatrix} u_A \\ v_A \\ 1 \end{bmatrix} = \boldsymbol{p}_A \begin{bmatrix} X_{C,A} \\ Y_{C,A} \\ Z_{C,A} \\ 1 \end{bmatrix} \tag{4.7}$$

$$s_B \begin{bmatrix} u_B \\ v_B \\ 1 \end{bmatrix} = \boldsymbol{p}_B \begin{bmatrix} X_{C,A} \\ Y_{C,A} \\ Z_{C,A} \\ 1 \end{bmatrix} \tag{4.8}$$

with: s_A and s_B shape factors and $\boldsymbol{X}_A = [X_{C,A}, Y_{C,A}, Y_{C,A}, 1]^T$ the position in the camera coordinate system of camera A in homogeneous coordinates.

The projection matrices ($\boldsymbol{p}_A$ and $\boldsymbol{p}_B$) for both cameras are calculated as:

$$\begin{aligned} \boldsymbol{p}_A &= \boldsymbol{K}_A \left[\boldsymbol{I}, \boldsymbol{0} \right] \\ \boldsymbol{p}_B &= \boldsymbol{K}_B \left[\boldsymbol{R}_{A-B}, \boldsymbol{t}_{A-B} \right] \end{aligned} \tag{4.9}$$

With: $\boldsymbol{R}_{A-B}$ and $\boldsymbol{t}_{A-B}$ are the rotation and translation matrix from camera A to camera B. $\boldsymbol{K}_A$ and $\boldsymbol{K}_B$ are the camera matrices for camera A and B respectively. $\boldsymbol{I}$ and $\boldsymbol{0}$ are the identity matrix and a zero array respectively.

Equation 4.6 can be rewritten as:

$$\begin{aligned} s_A u_A &= \boldsymbol{p}_{A,1}^T \boldsymbol{X}_A \\ s_A v_A &= \boldsymbol{p}_{A,2}^T \boldsymbol{X}_A \\ s_A &= \boldsymbol{p}_{A,3}^T \boldsymbol{X}_A \end{aligned} \tag{4.10}$$

with: $\boldsymbol{p}_{A,i}^T$ the i-th row of the matrix $\boldsymbol{p}_A$

Eliminating s_A results in:

$$\begin{aligned} u_A \, \boldsymbol{p}_{A,3}^T \boldsymbol{X} &= \boldsymbol{p}_{A,1}^T \boldsymbol{X}_A \\ v_A \, \boldsymbol{p}_{A,3}^T \boldsymbol{X} &= \boldsymbol{p}_{A,2}^T \boldsymbol{X}_A \end{aligned} \tag{4.11}$$

The same for camera B and Equation 5.7:

$$\begin{aligned} u_B \, \boldsymbol{p}_{B,3}^T \boldsymbol{X} &= \boldsymbol{p}_{B,1}^T \boldsymbol{X}_A \\ v_B \, \boldsymbol{p}_{B,3}^T \boldsymbol{X} &= \boldsymbol{p}_{B,2}^T \boldsymbol{X}_A \end{aligned} \tag{4.12}$$

Combining these equations, we get a system of four equations which can be solved, e.g. using singular value decomposition for matrix $\mathbf{X}_A$:

$$A\,X_A = 0 \qquad\qquad (4.13)$$

with:

$$A = \begin{bmatrix} u_A\,\boldsymbol{p}_{A,3}^T - \boldsymbol{p}_{A,1}^T \\ v_A\,\boldsymbol{p}_{A,3}^T - \boldsymbol{p}_{A,2}^T \\ u_B\,\boldsymbol{p}_{B,3}^T - \boldsymbol{p}_{B,1}^T \\ v_B\,\boldsymbol{p}_{B,3}^T - \boldsymbol{p}_{B,2}^T \end{bmatrix},\, 0 = \begin{bmatrix} 0 \\ 0 \\ 0 \\ 0 \end{bmatrix}$$

In case three or more cameras are used, the system of equations can easily be extended with more equations.

4.3. Material and methods

4.3.1. General approach

Generally, the measurement system should comply with the following requirements. The dynamics (position and velocity) of particles being ejected from the spreader must be accurately measured in three dimensions and expressed relative to a coordinate system associated with the spreader and the ground. Since individual particle trajectories are highly sensitive to the particle size (see section 2.3.3), also the size of the particles must be determined in an accurate way. The particle size can change due to mechanical impact with the vanes and during spreading because segregation can occur in the hopper (Miserque & Pirard, 2004). Therefore, the particle size must be determined after the particles have left the spreading vanes. By simultaneously measuring the size and the dynamics of the particles, possible interactions between the particle size and the particle velocity (Reumers et al., 2003) can be taken into account. No of-the-shelf stereovision camera could be used for this, therefore a custom made stereovision system was developed. To avoid the use of expensive high speed cameras for high speed stereovision, high resolution cameras were used, combined with the multi-exposure technique using the illumination system from chapter 3. By using the measured particle parameters as inputs for the ballistic model developed in section 2.2.1, the individual particle trajectories can be simulated and subsequently, also the spread pattern. This way, the spread pattern of commercially available centrifugal spreaders can be determined in a time and space efficient and labour-extensive way without compromising the accuracy of the measurement technique.

4.3.2. Measurement setup

To achieve a high accuracy, the first camera system consisting of two high resolution monochrome cameras, were placed relatively close (0.6 m) to the stream of fertilizer particles, to increase the particle resolution on the images. Because this reduces the field of view, the cameras were mounted on an arm that can be rotated to cover the wide area over which particles are dispersed (see Figure 4.4 and Figure 4.5).
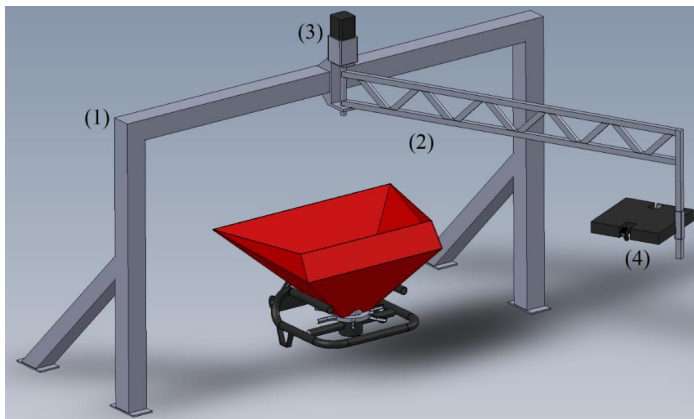
Figure 4.4. Fixed frame (1) with rotating arm (2), powered by a motor and gearbox (3). Two cameras and the illumination system (4) are attached to the rotating arm
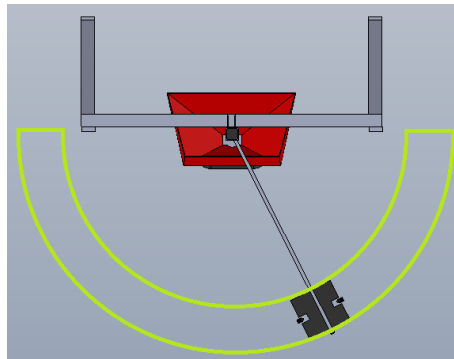
Figure 4.5. Upper view of measurement system. The measurement zone where images are taken from particles ejected by the fertilizer spreader is indicated in green

The stainless steel frame supporting the rotating arm was custom-designed. The arm was driven by a stepper motor (Nema 42, OMC Corporation Limited, Nanjing China), fitted to a reduction gearbox (1:100 reduction ratio, PE-W-084-100G, Servo2Go, GreenVille, USA). An encoder with 14 bit resolution (AS5048, AMS AG, Premstaetten, Austria) was fitted to the axle of the arm to provide the angular position. The illumination system designed in Chapter 3 and the two cameras, used to acquire high resolution images of fertilizer particles being ejected by the spreader, were attached to the end of the arm (see Figure 4.4 and 4.6). The two cameras were equipped with 16 mm lenses (for specifications, see Table 4.1) and were inclined to maximize their shared field of view. The cameras were synchronized with the illumination system to acquire multi-exposure images. On the ground underneath the measurement system, black cloths were placed, to reduce reflection of light from the background to the cameras.
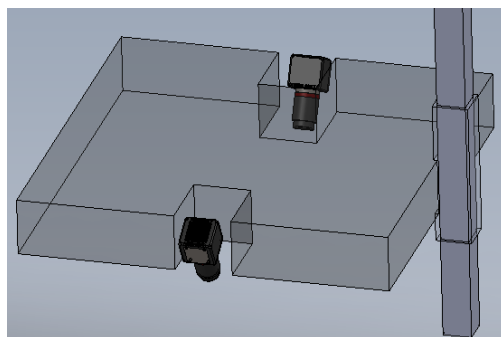
Figure 4.6. The first camera system consisting of cameras 1 and 2, used for taking images of fertilizer particles leaving the spreading disc. The illumination system is mounted in between both cameras with LEDs facing downwards

To calculate the landing position of the particles with the ballistic model and subsequently the spread pattern, the position and velocity vectors of the particles must be expressed relative to a coordinate system associated with the ground plane and the spreader. To determine the pose of the spreader and the ground plane, a second set of cameras was used (for specifications, see Table 4.1). These cameras, from hereon called the second camera system, were statically mounted to a stainless steel frame, which was fixed to the floor at the backside of the measurement setup.

Table 4.1. Camera parameters for first and second camera system (cameras: Allied Vision Technologies, Stadtroda, Germany, Lenses: Kowa Optimed Deutschland GmbH, Düsseldorf, Germany)

Parameter	Camera system 1	Camera system 2
Camera name	Manta G-419B	Mako U-503B
Lens name	LM16SC	LM6NCM
Cost (camera + lens)	1653 + 565 €	340 + 190 €
Sensor type	Mono	Mono
Interface	GigE	USB3
Resolution	2048 x 2048 pixels	2592 x 1944 pixels
Maximal framerate[*]	26 fps	14 fps
Focal length	16 mm	6 mm
Distance between cameras	370 mm	2350 mm
Angle between cameras	38.5°	23.5°

[*]At full resolution

Around the measurement system, a wooden frame (10 m x 5 m) with black plastic sheet cover was built to create a dark environment (excluding sunlight). To reduce bouncing back of particles after impacting the walls, strips of sackcloth were attached to horizontal bars attached to the frame. An overview of the full measurement setup is given in Figure 4.7.
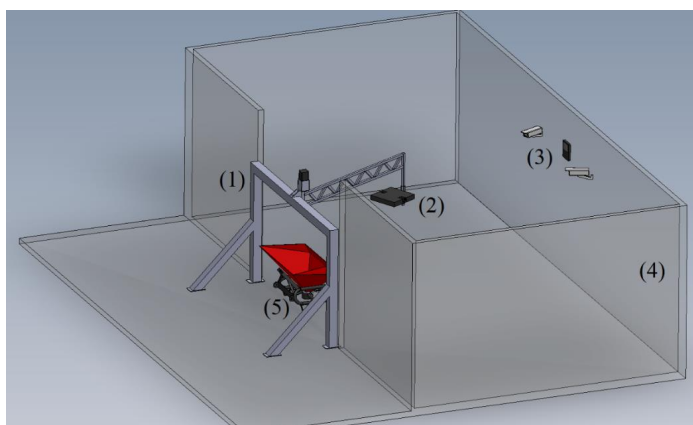
Figure 4.7. General overview of the measurement system. The following components are indicted: frame (1) the first set of cameras (2), the second set of cameras (3), the wooden frame with plastic sheet cover (4), fertilizer spreader (5)

A dedicated computer (Intel Core i5-6400 CPU, 2.70 GHz, 32 Gb RAM) was used for data acquisition and processing. The encoder, motor and illumination system were controlled using a custom-designed automation system using three Arduino (open source electronics platform, www.arduino.cc) microcontrollers in a master-slave configuration. The master controller was used for interfacing with the user and communication with the main computer while the two others respectively controlled the rotating arm and the illumination system. The software for the computer was written in Visual Studio C++. Image processing was done using the OpenCV library (Open Source Computer Vision Library, version 2.4.11). Matlab (v.2015a, Mathworks Inc, Natic, USA) was used for the graphical output.

4.3.3. Algorithms

The code for controlling the rotating arm, the illumination system and the cameras is low-level and is not explained in this work. To calibrate the cameras, a camera calibration algorithm was implemented. Image processing algorithms were written to determine the position of the spreader and the ground plane (using the second camera system) and to determine the size and the dynamics of the particles (using the first camera system) relative to a coordinate system associated with the spreader.

4.3.3.1. Camera calibration

In order to do measurements in the real, three-dimensional world where physical units (mm) matter, the cameras with their image units (pixels) need to be calibrated. Camera calibration was performed using a custom made real-time photogrammetric camera calibration application, which was based on the OpenCV library. A single-camera calibration was performed for each camera, delivering the intrinsic matrix (see Section 6.2.2) and the distortion coefficients (see Section 5.2.3). This was done by taking images from a variety of positions and angles of a reference object having different identifiable points and with known physical dimensions.

In this study, a custom designed planar symmetrical calibration patterns were used with circular markers (see Figure 4.8a). For the first camera system, a small pattern was used (circles with diameter 25 mm and distance 35 mm) because of the small field of view. The second camera system has a much larger field of view, therefore, a larger calibration pattern was used (circles with diameter 120 mm and distance 192 mm). A total number of 20 images (see Figure 4.8b) were taken for each camera at different angles from the calibration pattern to obtain a robust solution for the required parameters (intrinsic matrix, distortion coefficients).

(a)   (b)
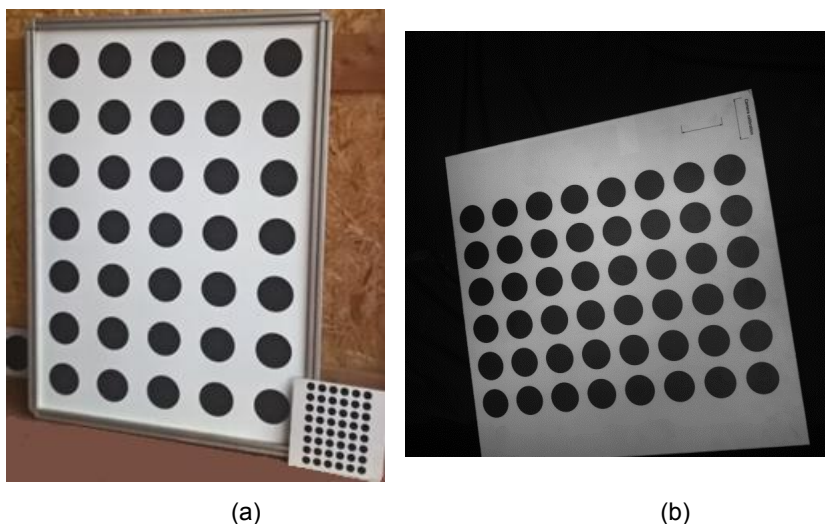
Figure 4.8. Planar symmetrical calibration patterns with circular markers used for calibrating the cameras in this work (a), example of a calibration image (acquired by the first camera system) (b)

The parameters were estimated by minimizing the reprojection error for the centre points of the circular markers based on the Levenberg-Marquardt optimization method (Bradski and Kaehler, 2008). The reprojection error for a given point can be calculated as the distance between the point and the projection of its corresponding true position, found by applying the parameters determined by calibration. To check the quality of the calibration process, the Root Mean Square (RMS) reprojection error was determined for each calibration image and the average was determined over all images. This value was generally below 0.15 pixels for the cameras of the first camera system and below 0.20 pixels for the cameras of the second camera system. Using the same approach, the extrinisics, i.e. the geometrical relationship between two cameras (with known intrinsic matrix and distortion coefficients) were determined. The following transformation matrices were determined using calibration: M_{c1-c2}, M_{c3-c4}, M_{c1-c3}. For transformation matrices we will use the following convention M_{a-b} transforms from coordinate system a to coordinate system b.

4.3.3.2. Transforming to the spreader coordinate system

The first camera system was used to determine the dynamics of the fertilizer particles leaving the spreading discs. This means that particle dynamics will be expressed relative to the first camera system (see Section 4.2.4). The spread pattern however

must be measured relative to the spreader. To achieve this, the particle dynamics need to be expressed relative to a coordinate system associated with the spreader. Furthermore, also the position of the ground must be known, because the direction of gravity is important to calculate the trajectories of the particles in the air. During experiments, the spreader remains attached to the tractor. This way, the predicted spread pattern is most representative for the true spread pattern. Because spreaders can be placed in different orientations in the measurement system, their position and orientation (azimuthal angle) must be known for each spreading experiment. Prior to each spreading experiment, the spreader coordinate system was automatically determined with stereovision using the second camera system. This coordinate system was defined as the right handed Cartesian coordinate system with origin going through the vertical projection of the spreader centre point, xy-plane coincident with the ground plane, x-axis oriented along the rear end of the spreader frame, y-axis in the negative driving direction and z-axis pointing upwards (see Figure 4.9).
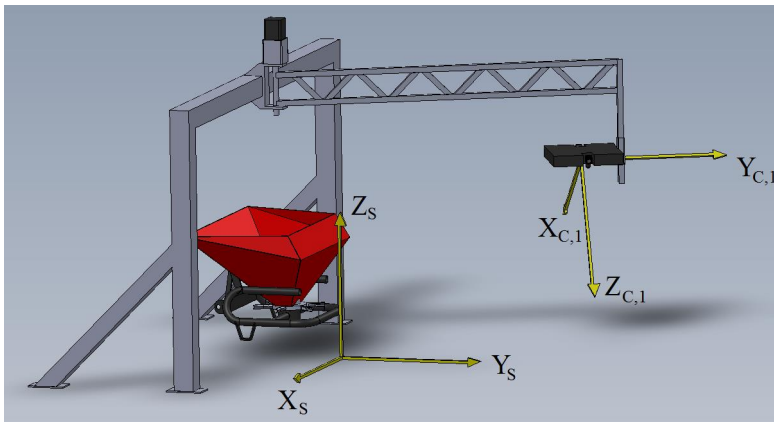
Figure 4.9. Particle dynamics are determined in the first camera coordinate system ($X_{C,1}$,$Y_{C,1}$,$Z_{C,1}$) using stereovision and must be expressed in the spreader coordinate system (X_s,Y_s,Z_s)

The spreader coordinate system was determined in different steps. First, the pose of the ground plane was determined. This must be done every time the measurement system is recalibrated. Next the spreader pose relative to the second camera system was determined. This is must be done every time when the pose of the spreader relative to the frame has changed or when another spreader is used. From these findings, the spreader coordinate system can be calculated relative to the second camera system.

The ultimate goal however is to transform particle dynamics from the first camera coordinate system to this spreader coordinate system (see Figure 4.9). As mentioned before, the field of view of the first camera system is much smaller than the zone over which particles are dispersed. Therefore, the cameras were placed on an arm which can be rotated over the measurement zone (see Figure 4.5). Because the first camera system is attached to the arm and the second camera system is fixed, the relative orientation of the camera system changes with the arm position. Coordinates are first transformed to the coordinate system of the second camera system, because the pose of the spreader relative to this camera system is known. From there, they can be transformed to the spreader coordinate system (see Figure 4.10).
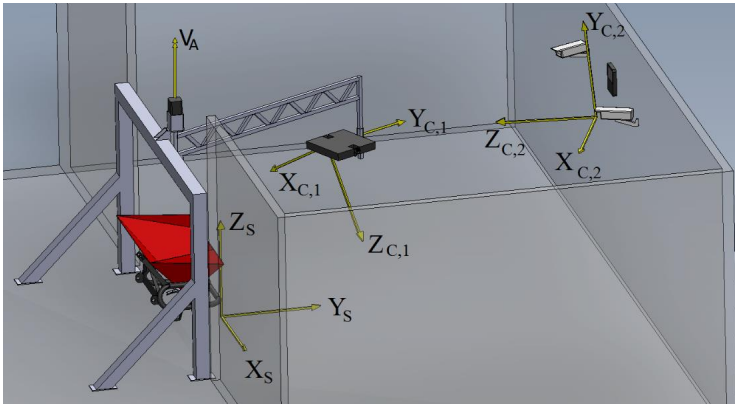
Figure 4.10. Particle dynamics were transformed from the first camera coordinate system ($X_{C,1}$, $Y_{C,1}$, $Z_{C,1}$) to the second camera system ($X_{C,2}$, $Y_{C,2}$, $Z_{C,2}$) and from there, to the spreader coordinate system (X_S, Y_S, Z_S). The rotation vector V_A of the rotating arm is indicated as well

The dynamic transformation matrix between the first and second camera system was determined in different steps. In a first step, the transformation matrix (homogeneous coordinates) between both coordinate systems was determined at one fixed arm position (θ_k) using camera calibration (M_{k-2}). A white plastic sphere[3] (120 mm diameter) was attached to the rotating arm to determine the position and direction of the rotation vector of the arm. For each arm position θ_i, the transformation matrix was calculated by determining this angle and transforming to the first coordinate system at angle θ_k.

---

[3] A sphere was used because it has a circular projection in all directions and the projection of the true centre should equal the centre point of the projection of the sphere on the images

To determine the rotation vector of the arm relative to the second camera system, images were taken with the arm at different positions (fixed intervals, 4° was used). For each image set, the sphere was segmented from the background, the centre point was determined and subsequently distortion-corrected (see 4.2.3). Using triangulation (see 4.2.4), the three dimensional position of the centre point at each position was calculated in the second camera system. Using the inverse of the transformation matrix M_{k-2}, the position of the centre points was calculated relative to the first camera system at position θ_k. From the set of centre points, the best fitting circle was determined and the centre point (C_A) and the normal vector (V_A) were determined. Based on this, the transformation matrix for the first camera system from position θ_k to θ_i (M_{k-i}) was determined as (Murray, 2013):

$$M_{k-i} = \begin{bmatrix} u^2+(v^2+w^2)c_1 & uvc_2-ws_1 & uw(1-\cos\theta)+vs_1 & \left(a(v^2+w^2)-u(bv+cw)\right)c_2+(bw-cv)s_1 \\ uvc_2+ws_1 & v^2+(u^2+w^2)c_1 & vw(1-\cos\theta)-us_1 & \left(b(u^2+w^2)-u(au+cw)\right)c_2+(cu-aw)s_1 \\ uwc_2-vs_1 & vwc_2+us_1 & w^2+(u^2+v^2)c_1 & \left(c(u^2+v^2)-w(au+bv)\right)c_2+(av-bu)s_1 \\ 0 & 0 & 0 & 1 \end{bmatrix}$$

(4.14)

with: u, v, w the vector coordinates of V_A and a, b, c the coordinates of C_A both expressed in the first camera system at θ_k. $c_1 = \cos(\theta_k - \theta_i)$, $c_2 = 1 - \cos(\theta_k - \theta_i)$, $s_1 = \sin(\theta_k - \theta_i)$)

The transformation matrix to transform from the first camera system at position θ_i to the second camera system was determined as:

$$M_{i-2} = (M_{k-i} M^{-1}{}_{k-2})^{-1} \qquad\qquad (4.15)$$

The orientation of the ground plane relative to the second camera system was determined based on a number of images of the (large) calibration pattern on the ground in view of both cameras (see Figure 4.11).
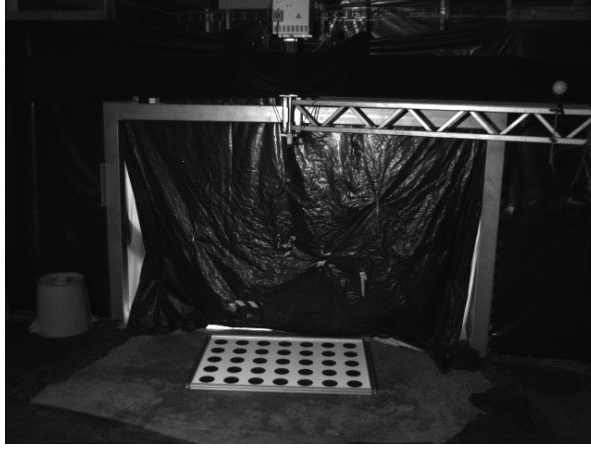
Figure 4.11. Calibration pattern placed on the ground viewed by one of the cameras of the second camera coordinate system to determine the orientation of the ground plane

The centres of the circular markers were determined and were matched between the images of the two cameras. After distortion-correcting these points (see 4.2.3) their position was calculated relative to the second camera system (see 4.2.4). The best fitting plane through these points was determined using least squares (average distance to the plane was approximately 0.47 mm). The unit vector, normal to the plane was determined (N_{gnd}). From this, the projection of the centre point of the calibration pattern in the last image onto the ground plane was calculated (P_{proj}).

To determine the transformation from the second camera coordinate system to a coordinate system parallel to the ground, firstly a translation was performed from the optical centre to P_{proj}:

$$T_1 = \begin{bmatrix} 1 & 0 & 0 & -P_{i,x} \\ 0 & 1 & 0 & -P_{i,y} \\ 0 & 0 & 1 & -P_{i,z} \\ 0 & 0 & 0 & 1 \end{bmatrix} \qquad (4.16)$$

Next, a rotation was performed for the angle between the z-vector of the second camera system and the normal vector of the ground plane:

$\boldsymbol{R_1}$

$$= \begin{bmatrix} cos(\theta_1) + u_x^2(1 - cos\,\theta_1) & u_x u_y(1 - cos\,\theta_1) - u_z sin\theta_1 & u_x u_z(1 - cos\,\theta_1) + u_y sin\theta_1 & 0 \\ u_y u_x(1 - cos\,\theta_1) + u_z sin\theta_1 & cos\,\theta_1 + u_y^2(1 - cos\,\theta_1) & u_y u_z(1 - cos\,\theta_1) - u_x sin\theta_1 & 0 \\ u_z u_x(1 - cos\,\theta_1) - u_y sin\theta_1 & u_z u_y(1 - cos\theta_1) + u_x sin\theta_1 & cos\,\theta_1 + u_z^2(1 - cos\,\theta_1) & 0 \\ 0 & 0 & 0 & 1 \end{bmatrix} \quad (4.17)$$

with: $\boldsymbol{u} = [0\ 0\ 1] \times \boldsymbol{N_{gnd}}$ and $\theta_1 = cos^{-1}([0\ 0\ 1] \cdot \boldsymbol{N_{gnd}})$

Next, a second translation was performed to correct for the height of the calibration plate above ground (27 mm).

$$\boldsymbol{T_2} = \begin{bmatrix} 1 & 0 & 0 & 0 \\ 0 & 1 & 0 & 0 \\ 0 & 0 & 1 & h_{cal} \\ 0 & 0 & 0 & 1 \end{bmatrix} \quad (4.18)$$

Finally, the transformation matrix from the second camera coordinate system to the ground coordinate system (**M**2-G) was calculated as:

$$\boldsymbol{M_{C2-G}} = \boldsymbol{T_2 R_1 T_1} \quad (4.19)$$

The spread pattern needs to be determined relative to the spreader, however the spreader orientation is not fixed. The position and horizontal orientation of the spreader relative to the ground coordinate system was automatically determined before each spread test by attaching two circular markers (140 mm in diameter; black on white background) to the back of the spreader, with equal distance to the centreline of the spreader (see Figure 4.12).

Figure 4.12. Circular markers attached to an Amazone fertilizer spreader placed in the measurement system

After segmenting the circles from the background, their position was calculated in the second camera system (C_A and C_B). By taking the geometric mid-point between these two points, the centre of the spreader (C_C) was determined. The projection of these points on the ground surface was found by:

$$C_{A,proj} = T_{C2-G}[C_A \; 1]^T$$
$$C_{B,proj} = T_{C2-G}[C_B \; 1]^T \qquad (5.20)$$
$$C_{C,proj} = T_{C2-G}[C_C \; 1]^T$$

The ground coordinate system was translated to the projection of the centre point on the ground surface:

$$T_3 = \begin{bmatrix} 1 & 0 & 0 & -C_{C,proj,x} \\ 0 & 1 & 0 & -C_{C,proj,y} \\ 0 & 0 & 1 & 0 \\ 0 & 0 & 0 & 1 \end{bmatrix} \qquad (5.21)$$

Next, a rotation in the horizontal plane was performed to align the translated ground coordinate system with the back of the spreader. The horizontal spreader orientation relative to the ground coordinate system was determined by using the position of the line connecting C_A and C_B.

$$T_3 = \begin{bmatrix} \cos\theta_2 & \sin\theta_2 & 0 & 0 \\ -\sin\theta_2 & \cos\theta_2 & 0 & 0 \\ 0 & 0 & 1 & 0 \\ 0 & 0 & 0 & 1 \end{bmatrix} \qquad (5.22)$$

with:

$$\theta_2 = \tan^{-1}(\frac{C_{A,proj,y} - C_{B,proj,y}}{C_{A,proj,x} - C_{B,proj,x}}) \qquad (5.23)$$

The transformation matrix from the ground coordinate system to the spreader coordinate system was calculated as:

$$M_{G-S} = R_2 T_3 \qquad (5.24)$$

Finally, the transformation matrix from the second camera system to spreader coordinates was calculated as:

$$M_{C2-S} = M_{G-S} M_{C2-G} \qquad (4.25)$$

4.3.3.3. Determining particle parameters for the first disc

<u>General</u>

The next step consisted of determining the parameters of the fertilizer particles that have left the spreading vanes using image processing algorithms. Stereovision was used to extract three-dimensional information from the images. The particle dynamics (position and velocity) were determined relative to the spreader coordinate system. Furthermore, the particle size was determined which was used to determine the projected area and volume. Together with the true density, this allows to calculate the ballistic flight of the particles and subsequently determine their landing position.

Multi-exposure technique

As mentioned before, particles move at high velocity and high framerates would be necessary to determine the particle velocity by determining two subsequent positions. Instead of using high speed cameras, the multi-exposure technique was used to retrieve similar high speed information with standard cameras at a much lower cost. The LED illumination system developed in Chapter 4 was mounted in between the cameras of the first camera system and was synchronized with the image acquisition of both cameras. During the exposure of each image, the system flashed two times, with a specific time delay t_{delay} (cf. infra) in between (determined based on preliminary spreading tests to achieve an optimal disparity on the images). Because of the dark environment, only the objects that are in the field of view of the camera at the time of the flashes were acquired on the images. Because two flashes were used for each camera exposure, moving fertilizer particles were projected two times on each image (see Figure 4.13).

(a)   (b)
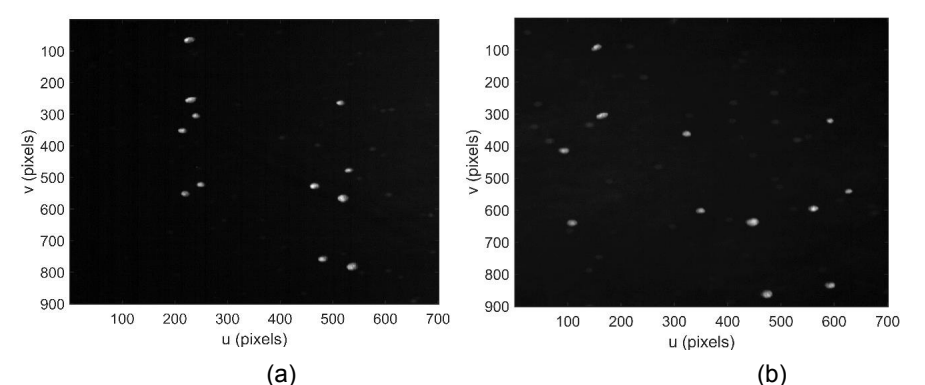
Figure 4.13. Raw image taken by both cameras of the first camera system using the multi-exposure technique: (a) camera 1 and (b) camera 2. Moving particles are projected two times on the image. Only a part of the total image is shown for clarity

The delay time between both flashes, combined with the velocity of each particle, determines the disparity (difference in position) between both particle positions. Because the cameras are hardware-synchronized, meaning that images are taken at the same time, the illumination technique ensures that projections of particles are perfectly synchronized which is necessary for accurate stereovision.

Pre-processing

The first image processing step was applying a median filter to reduce noise. The effect of the filter is shown in Figure 4.14.

(a)   (b)
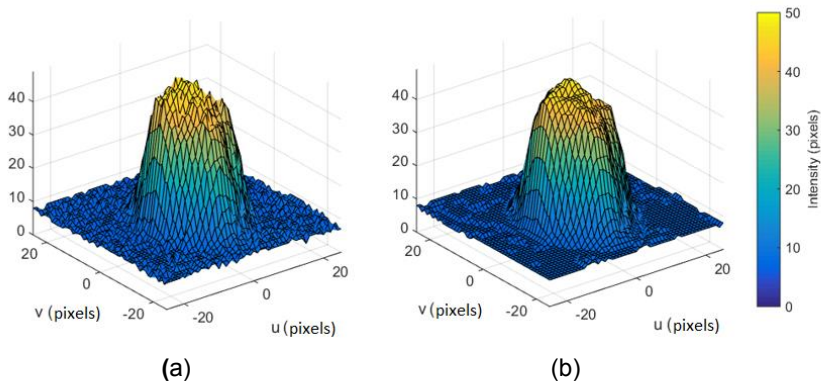
Figure 4.14. Visualization of the projection of a single fertilizer particle on the image: (a) raw image, (b) image filtered with median filter (3x3 kernel)

On the filtered image, a global thresholding operation was used to segment particles from background (see Figure 4.15a). This was possible due to the controlled environment, the uniformity of the illumination and the black background. A binary image was generated from the thresholding operation and previous image was multiplied with this mask (see Figure 4.15b).

(a)   (b)
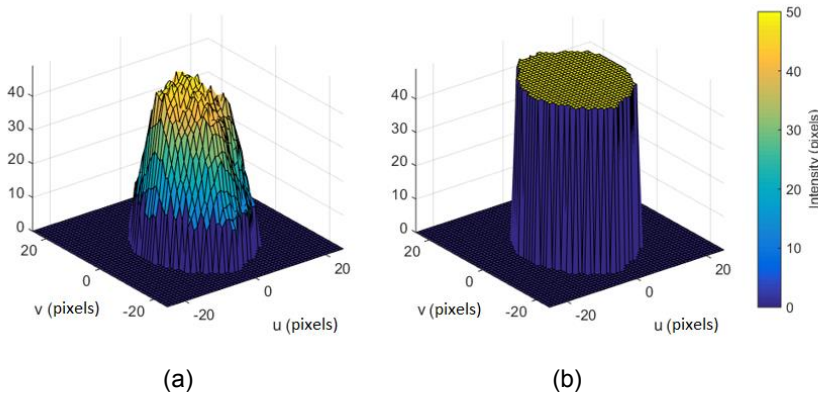
Figure 4.15. Visualization of the projection of a single fertilizer particle on the image:
(a) thresholded image (b) binarized image (relative to the maximal value)

The contours of the connected components were determined using the algorithm of Suzuki et al. (1985) for further processing. The pixels within connected components (regions) were localized for further processing. The perimeter and area of the regions were determined to calculate their convexity γ (-):

$$\gamma = \frac{A_p}{A_{hull}}$$ (4.26)

with: A the area of the blob (pixels)

Ahull the area of the convex hull (pixels)

and circularity η (-):

$$\eta = \frac{4\,\pi\,A_p}{P_p^2}$$ (4.27)

With: P_p the perimeter of the contour (pixels)

The three descriptors: area, convexity and circularity were used for particle segmentation. Empirically following intervals were determined: [Amin, Amax],[γmin, γmax] and [ηmin, ηmax] (cf. infra). Each blob whose features fall in all three ranges was accepted as a particle. For each particle, the image moments were determined (m=[0,1], n=[0,1]) .

$$m_{n,m} = \sum_x \sum_y x^n y^m I_{x,y} \qquad (4.28)$$

with: $I_{x,y}$ the pixel value at position x,y

From this, the centre was calculated as follows:

$$\left[\frac{m_{10}}{m_{00}}, \frac{m_{01}}{m_{00}}\right] \qquad (4.29)$$

with: m_{00}, m_{01} and m_{10} the image moments of the particle (pixels)

The particle centres were distortion-corrected by using the internal camera parameters, determined by calibration. For each particle i in the first image (camera 1), the epipolar line (the line in the second image on which the centre of the particle geometrically should be residing) in the second image (camera 2) was calculated using the external camera parameters. Each line was encoded by three parameters (a_i, b_i, c_i):

$$a_i x_j + b_i y_j + c_i = 0 \qquad (4.30)$$

Determining particle position

The 3D position was determined based on the position of the particle on the images of both cameras and on the intrinsic and extrinsic parameters of the camera system using triangulation (see Section 4.2.4). To determine the 3D position of the particles relative to the first camera coordinate system, the position in both camera images needs to be known. The matching between particles on both camera images, a process called stereo-matching (see Figure 4.16), was done by using a custom-designed algorithm (see Figure 4.17).

For each particle projection i in the first image, the corresponding projection j in the second image was searched. The distance to the epipolar line (δ) was determined as:

$$\delta = \left| \frac{a_i x_j + b_i\, y_j + c_i}{\sqrt{a_i{}^2 + b_i{}^2}} \right| \qquad (4.31)$$

with: (a_i, b_i, c_i) the parameters of the epipolar line of particle i in the second image
x_j, y_j the position of particle j in the second image
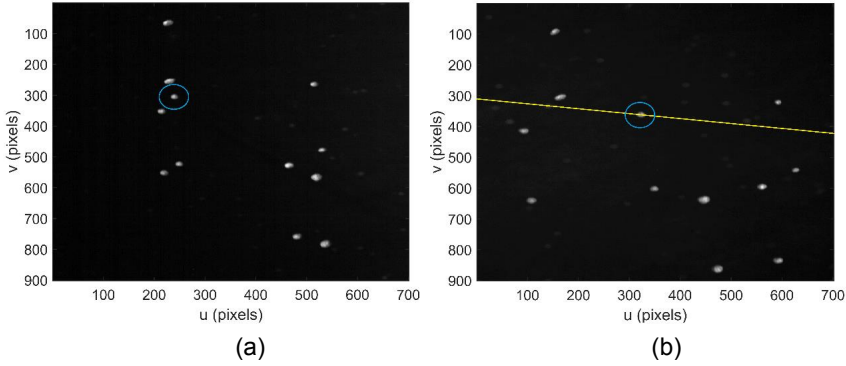
Figure 4.16. The process of stereo matching. For each particle projection in the left image (a), the corresponding projection in the second image (b) was searched. The matched projections are indicated with a blue circle. The epipolar line is given in yellow. Only a part of the total image is shown for clarity

In the ideal case, the distance from the particle to the epipolar line of its match would be very low (subpixel) and the matching process would be simple. However, because of the different viewpoint of the cameras and the fact that particles are not perfectly spherical or due to illumination variability, there can be a deviation between the geometric centre of the projection of the particle and the projection of the true particle centre. Therefore, all particle projections with an epipolar distance smaller than a pre-set value ($\delta_{max,}$ cf. infra) were considered as possible matches and their 3D position was determined in the camera coordinate system of the first camera (C_0) and from this set of candidates, the true match was searched. Using the transformation matrix between the first and second camera coordinate system ($M_{C_1-C_3}$), the position of the particle in the second camera coordinate system (C_2) was determined.

The position in the spreader coordinate system (P_S) was determined based on the transformation matrix between the first camera coordinate system and the spreader coordinate system M_{C_0-S}

$$P_S = M_{C_1-S}\, P_{C_0} \tag{4.32}$$

START

j=0

Consider match j in second image

Already matched — y

Determine δ — n

$\delta < \delta_{max}$ — n / y

Determine 3D in SCS

$z \in [z_{min}, z_{max}]$ — n / y

Determine ε_{stereo}

$\varepsilon_{stereo} < \varepsilon_{stereo,min}$ — n / y

Store best match as j
$\varepsilon_{stereo,min} = \varepsilon_{stereo}$

j=j+1

$j = m$ — n / y

Report best match as j

STOP
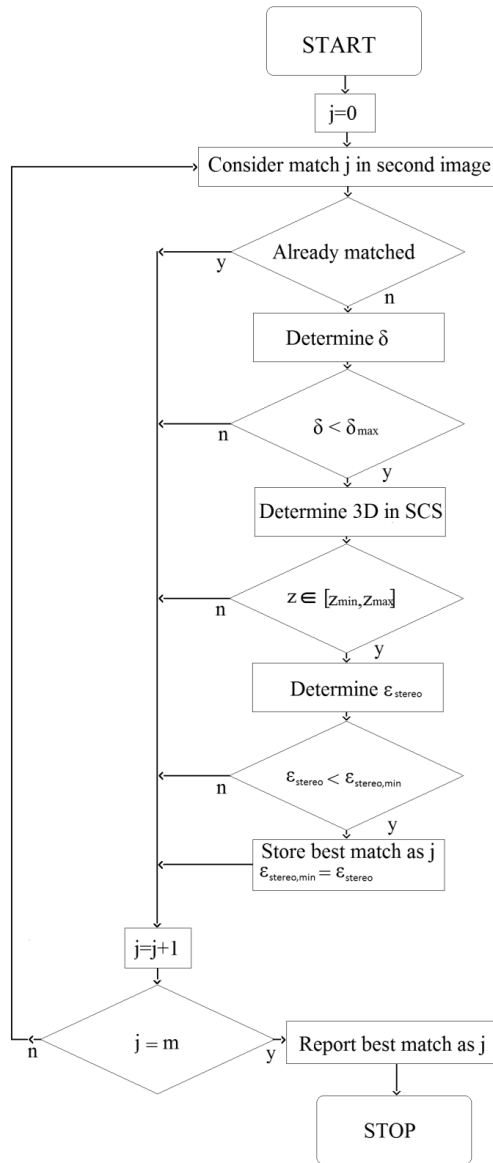
Figure 4.17. Flowchart of the stereo matching algorithm. For each particle projection i in the first camera image, the match j was searched in the second camera image. With m the total number of particles, δ the distance to the epipolar line, ε_{stereo} the stereo matching coefficient

Fertilizer particles thrown by a spreader move at a certain height above the ground. When the z-coordinate of the particle in the spreader coordinate system was part of the interval [h_{min},h_{max}] (cf. infra), the match was approved and the stereo matching coefficient was calculated:

$$\varepsilon_{stereo} = \quad k_{w1}\frac{|P_{S,z} - h_{mean}|}{h_{mean}} + k_{w2}\frac{|\eta_i - \eta_j|}{\dfrac{\eta_i + \eta_j}{2}}$$
$$+ k_{w3}\frac{|D_i - D_j|}{\dfrac{D_i + D_j}{2}} \tag{4.33}$$

with: k_{w1}, k_{w2} and k_{w3} weighting coefficients, determined empirically, cf. infra (-)

when D_i is the diameter of the particle based on the particle area in the first image (A_i):

$$D_i = \quad 2\sqrt{\frac{A_i}{\pi}\frac{P_{C_1,z}}{f_1}} \tag{4.34}$$

and D_j the diameter of the particle based on the area of the particle's match in the second image (A_j)

$$D_j = \quad 2\sqrt{\frac{A_j}{\pi}\frac{P_{C_2,z}}{f_2}} \tag{4.35}$$

The match with the smallest value for ε_{stereo} was considered as the best match. The 3D position in the spreader coordinate system (P_{SCS}) was approved. The particle diameter was calculated as the average value between D_i and D_j.

To verify the calculation of the particle diameter using image processing, an experiment with plastic spheres with known diameter (5.96 mm +- 0.005) was conducted. The spheres were launched one by one (50 in total) with an average velocity of approximately 25 m/s using an air pressure device which was mounted horizontally at 90 cm above ground. The average absolute difference between the true diameter and the measured diameter was calculated.

Determining particle velocity

To determine the velocity of the particles, the two projections of each particle on the multi-exposure (two flashes) images must be found. In the previous step, the 3D position of each particle position was found. After matching the two positions for each particle, i.e. time-matching, the velocity in 3D can be determined. Compared to the stereo-matching process, the number of possible matches is significantly bigger. Particles were not matched using traditional feature descriptors and matchers because different particles can geometrically be very similar and only two-dimensional information is used in those cases. Furthermore, due to particle spin, their two-dimensional projection (associated with each flash) can change. The time-matching algorithm presented here is based on four factors. Three are image related: the particle shape, particle area and the direction of motion. The fourth matching factor is the 3D position relative to the spreader coordinate system. Figure 4.18 illustrates the time-matching process.
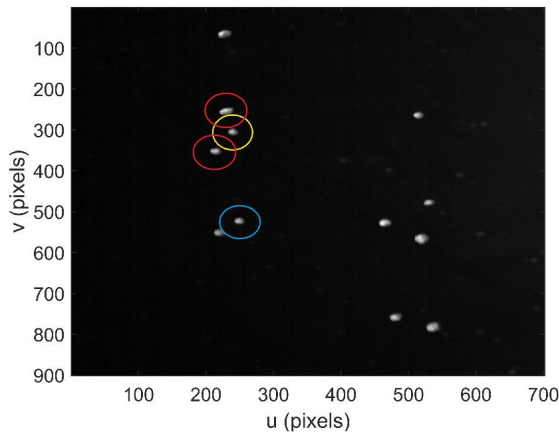
Figure 4.18. The process of time-matching, based on the multi-exposure technique. For each particle projection (blue circle), its corresponding projection (yellow circle) was determined. The red circles indicate other particle projections that were possible matches but resulted in a lower matching coefficient and therefore were considered as projections of other particles. Only part of the total image is shown for clarity

For each particle, all candidate matches were determined. A particle was considered a candidate match when the disparity (difference in 2D position) and direction of motion fall within a certain range and when the difference in height above ground between the

two positions did not exceed a maximal value. For each match, a matching coefficient (ε_{time}) was calculated as follows:

$$\varepsilon_{time} = k_{w4}\left(1 - \frac{|A_p - A_q|}{\frac{A_p + A_q}{2}}\right) + k_{w5}\left(1 - \frac{|\eta_p - \eta_q|}{\frac{\eta_p + \eta_q}{2}}\right) \quad (4.36)$$

with: A_p, A_q, η_p, η_q the particle area (pixels) and circularity (-) of two particles p and q
k_{w4}, k_{w5} weighting coefficients, determined empirically (-)

After calculating the matching coefficients, the matches were further analysed. For each particle that was not matched already, the number of possible matches was checked. When there was only one candidate, the candidate matches of this candidate were checked. If here was only one match (the particle) or the particle was the best match (largest matching coefficient) of the candidate, the match was approved. In case there were multiple candidates, and the candidate had the particle as best match, the match was added to a vector of possible matches. The vector of possible matches was then checked and from this vector, the candidate with the highest matching coefficient was approved as best match. After approving each match, both particles were removed from the stack of particles that still needed to be matched.

After matching, the particle diameter was calculated as the average diameter between the two positions.

The 3D velocity ($\boldsymbol{v}_{p,SCS}$) was determined based on the 3D position at both particle instances (t and t+Δt) and the time between the two subsequent flashes of the illumination system (Δt):

$$\boldsymbol{v}_{p,S} = \frac{\boldsymbol{P}_S(t + \Delta t) - \boldsymbol{P}_S(t)}{\Delta t} \quad (4.37)$$

with: $\boldsymbol{P}_S$ the 3D position of the particle instances (m) in the spreader coordinate system
Δt the time between two subsequent flashes (s)

The particle positions and velocity vectors were expressed relative to the spreader coordinate system, associated with the fertilizer spreader, which was static during the test, but moving while spreading in the field. Therefore, vectors in the spreader coordinate system needed to be transformed to a static world coordinate system (W) to account for the tractor driving speed (v_t):

$$\boldsymbol{v}_{p,W} = \boldsymbol{v}_{p,S} + \boldsymbol{v}_{t,S} \qquad (4.38)$$

4.3.3.4. Simulating particle parameters for the second disc

For clarity, only the spread pattern of the left disc was measured. This was done by closing the orifice feeding the right spreading vane. In practice, however, both discs are used. This can be done by mirroring the spread pattern of the spreader (Piron et al., 2010). However this way, the effect of wind cannot be calculated. Therefore, the spread pattern of the right disc was obtained here by mirroring the particle position and velocity vectors with respect to the spreader centreline (the y axis of the spreader coordinate system). Because the spreader coordinate system was situated at the spreader centre, this was done relative to position x=0. The spread pattern of both discs was then obtained by simple superposition of the left and right spreading patterns assuming no interaction, e.g. collision, between particles from the different discs.

4.3.3.5. Spread pattern calculation and comparison

Based on the particle dynamics and the particle size, which were determined using image processing (see previous sections), the true density of the fertilizer type and the drag coefficient, the landing position of the particles were calculated with the ballistic model from Chapter 2 (see section 2.2.1). The tractor velocity and direction and velocity of wind, were taken into account as well. Based on the landing position of all fertilizer particles and their respective weight, the two-dimensional spread pattern was calculated by transforming to a grid (resolution 1 m², 51 x 51 cells). The total mass in each grid cell (x=i,y=j) was calculated based on the summed masses of all individual particles landing in that cell ($S_{i,j}$).

To compare two different spread patterns (α, β), the Pearson coefficient of correlation was used:

$$\rho_{p} = \frac{Cov_{\alpha,\beta}}{\sigma_{\alpha}\sigma_{\beta}} \qquad (4.39)$$

with σ the standard deviation:

$$\sigma = \sqrt{\frac{1}{n-1}\sum_{i=1}^{n_x}\sum_{j=1}^{n_y}\left(S_{i,j} - \bar{S}\right)^2} \qquad (4.40)$$

With $\bar{S}$ the average mass per grid cell (kg), n_x and n_y the number of cells in the x and y direction respectively.

$\text{Cov}_{\alpha,\beta}$ is the covariance between the two spread patterns:

$$\text{Cov}_{\alpha,\beta} = \frac{1}{n-1} \sum_{i=1}^{n_x} \sum_{j=1}^{n_y} \left(S_{\alpha_{i,j}} - \bar{S}_\alpha \right) \left(S_{\beta_{i,j}} - \bar{S}_\beta \right) \qquad (4.41)$$

The two-dimensional spread patterns were transformed to transverse spread patterns to enable comparison with transverse spread patterns obtained in the field which are measured perpendicular to the driving direction. However, because much more particles are being spread than being captured on the images due to the small field of view of the cameras, the absolute application rate cannot directly be determined from this. To determine the transverse spread pattern, firstly, the sum of the mass of all the cells in the driving direction was taken. Next, the total transverse spread pattern, i.e. the transverse spread pattern of the spreader taking into account multiple swaths, was calculated based on overlapping the spread pattern of three subsequent swaths (ASAE 341.2, 1988) at the working width specified by the manufacturer. The values were rescaled to obtain an average application rate after overlap equal to the theoretical value. The latter was calculated based on the mass flow rate of one disc Q_m (kg/s), the working width W (m) and the velocity of the tractor $v_{tractor}$ (m/s):

$$\bar{T}_{theo} = 2 \frac{Q_m}{W\, v_{tractor}}\, 10\,000 \qquad (4.42)$$

With: $\bar{T}_{theo}$ the theoretical application rate (kg/ha)

Because fertilizer particles can bounce in or out of the collection trays, despite the trays being subdivided (Parish, 1991a), only the relative spatial distribution can be determined using collection trays (see section 1.3.2.1). To directly compare the measured transverse spread patterns with the predicted transverse spread patterns, the measured spread patterns were multiplied with a correction factor, relating the measured application rate after overlap with the theoretical value.

The coefficient of variation (CV, %) was calculated based on the data from the centre point of the first swath to the centreline of the third swath:

$$CV = \frac{\sigma_t}{\mu_t} 100 \qquad (4.43)$$

with: μ_t and σ_t the mean and standard deviation (kg/ha)

The min-to-max ratio (-) was defined as:

$$\frac{\min(S_{t,i})}{\max(S_{t,i})} \qquad (4.44)$$

with: $S_{t,i}$ the mass of fertilizer at x=i

4.4. Experimental procedures

To evaluate the developed system, spreading experiments were conducted with a commercially available fertilizer spreader. The physical properties of the fertilizer used during the experiments were determined in Chapter 2 and are summarized in Table 4.2. The particle size distribution measured by sieving (according to standard EN1235/A1 (2003)) was used to verify the values measured by the system developed in this research. The spreader used in the experiments was a new Vicon RO-XL (VN236), as illustrated in Figure 4.19.

Figure 4.19. Twin-disc Vicon RO-XL fertilizer spreader used for the experiments

The spreader was equipped with two spreading discs containing six longer vanes (285 mm long, 60 mm high) and two shorter vanes (80 mm long, 60 mm high) at the standard configuration provided by the manufacturer. The vanes were straight and mounted on a flat disc. The spreader was set according to the manufacturer spreading charts. Two different configurations were used, as illustrated in Table 4.2. For each experiment with the measurement setup (see Figure 4.20), two scanning rotations were performed for

each experiment, meaning that the rotating arm moved twice in a continuous way from its begin to end position during one experiment. Each scan took 60 seconds, and 1500 images were taken (25 fps). Two experiments (a total of four scanning rotations) were performed for each spreader configuration. Because the spreader fill level can have an effect on the spreading process (see section 1.2.3.2), the spreader was filled to the same level before each experiment (300 kg fertilizer as six separate bags of 50 kg).

Figure 4.20. Vicon spreader placed under the measurement system for predicting the spread pattern

Table 4.2. List of settings used in this study for the Vicon RO-XL (VN236) spreader. In all cases, the spreader was placed horizontally with discs 750 mm above ground. The position of the orifice was set at N (manufacturer-specific scale). Two different disc rotational velocities (ω) were used. The dosage setting indicated the size of the orifice. The application rate was 116 kg/ha

Configuration	Working width (m)	ω (rpm)	Dosage setting (-)
A	12	540	38
B	18	750	44

The parameters used for fine-tuning the image processing algorithms are given in Table 4.3. These parameters were found after executing many spreading tests, executed with a custom made single-disc experimental spreader with a flat disc and an Amazone ZAM spreader with different conical discs (OM 12-16, OM 18-24, OM 24-36).

Table 4.3. Image processing algorithm parameters used during the experiments

Parameter	Unit	Value
$[A_{min}, A_{max}]$	pixels	[50, 1200]
$[h_{min}, h_{max}]$	m	[0.6, 1.2]
$[k_{w1}, k_{w2}, k_{w3}, k_{w4}, k_{w5}]$	-	[0.33, 0.33, 0.33, 0.5, 0.5]
t_{delay}	μs	1700 (configuration A) 1250 (configuration B)
δ_{max}	pixels	2
$[\gamma_{min}, \gamma_{max}]$	-	[0.91, 1]
$[\eta_{min}, \eta_{max}]$	-	[0.55, 1]

Field experiments on a flat field were conducted to compare the obtained transverse spread pattern at the same spreader configurations (see Figure 4.21). A total of 100 collection trays (0.5 m x 0.5 m) were placed on one row of ladders, perpendicular to the driving direction of the tractor. Trays were removed at the positions of the tractor wheels. Results were transformed to a resolution of 1 m x 1 m to compare with the transverse spread patterns obtained with the camera system.

Figure 4.21. Field experiments to determine the transverse spread pattern using collection trays at the ILVO test site

During the field experiments, the average wind velocity and direction were measured using a local weather station at 5 minute intervals (05103-L sensor on a CR1000 data logger, Campbell Scientific, Logan, USA). The tractor driving direction was determined

by measuring two points of the trajectory with a GNSS receiver (Stonex S10, Stonex, Lissone, Italy) using the Flemish Positioning Service (FLEPOS) correction signals. Based on this, the wind velocity vector was calculated in the spreader coordinate system (see Table 4.4) and used for calculating the spread pattern with the camera system. The air density and dynamic viscosity was not measured, a value of 1.225 kg/m³ and 1.8 * 1e-5 kg/(m s) was assumed for the simulations.

Table 4.4. Wind velocity expressed in the spreader coordinate system ($v_{wind,x}$, $v_{wind,x}$). The resulting wind velocity is given as well ($v_{wind,tot}$)

Configuration	Wind velocity (m/s)		
	$v_{wind,x}$	$v_{wind,y}$	$v_{wind,tot}$
A	-1.93	-1.00	2.17
B	-2.10	-1.40	2.52

Using the results of the experiments, simulations were performed to investigate the effect of wind, spreader height and velocity of the tractor on the shape of the spread pattern. The different settings were compared to the base case, for which the settings recommended by the manufacturer were used. Simulations were performed assuming that particle dynamics do not change compared to the base case, which is true for spreader height and fairly true for tractor velocity and wind given the limited trajectory that particles travel until measured. The effect of front, back and side wind[4] was investigated. For the simulations, data from both replicates was combined. The parameters for the simulations are given in Table 4.5.

Table 4.5. Simulation parameters to determine the effect of spreader height, tractor velocity and wind on the spread pattern

Parameter	Base case	Cases	Unit
Spreader height	750	1000	mm
Tractor velocity	2.22	5.56	m/s
Front or back wind	0	[5, 10, 15]	m/s
Side wind	0	[5, 10, 15]	m/s

[4] Front, back and side wind is used as terminology instead of head-, tail- and crosswind in chapter 2 to indicate that the wind direction is expressed relative to the driving direction of the tractor.

4.5. Results and discussion

4.5.1. Spread tests

The physical properties of the fertilizer particles are given in Table 4.6.

Table 4.6. List of fertilizer physical properties for CAN fertilizer* (Ammonium nitrate 27% N + 4% MgO, Scoriethom) used in this experiment. True density was determined using gas pycnometry. For density, two replicates were used. Both the bulk and true density were determined

Parameter	Specification	Value
Density (kg m^{-3})	Bulk	1035, 1033
	True	1780, 1790
Sieve fraction** (%)	0-1.4 mm	0.16
	1.4-2 mm	0.21
	2-2.5 mm	1.33
	2.5-3.15 mm	15.98
	3.15-3.55 mm	21.96
	3.55-4 mm	30.80
	4-4.5 mm	18.23
	>4.5 mm	11.33
Median diameter (mm)***		3.70
Sphericity (-)		0.9655

* Supplier: Aveve Dirk Notebaert, Scheldewindeke, Oost-Vlaanderen, Belgium

** Mass fraction

*** Determined based on linear interpolation of sieve test results

Table 4.7 gives the median distance to the epipolar line for particles from both replicates for spreader configuration A and B. The 10th and 90th percentile are given as well. Generally, it can be seen that the median distance lies below 0.47 pixels and that the value was slightly smaller for configuration B. This indicates that the stereo-matching algorithm performed well since this value is very small. The 10th and 90th percentile illustrate the differences between different particles. This can have multiple causes. Particles in the first camera image can be matched incorrectly to other particles with similar shape and size that are coincidentally on the epipolar line of the other camera image. However because also the calculated 3D position was also taken into account for the matching process, this is unlikely to happen. Another cause can be the non-sphericity of the particles and the fact that the cameras use two different

viewpoints and therefore, the particle centres on both images do not represent exactly the same 3D point.

Table 4.7. Median distance of particle centre to epipolar line in pixels (between brackets, the 10th and 90th percentile are given)

Configuration	Test 1	Test 2
A	0.4645 (0.0856, 1.2269)	0.3998 (0.0719, 1.1329)
B	0.3391 (0.0617, 0.9821)	0.3292 (0.0608, 0.9539)

Figure 4.22 illustrates the positions of the individual particles in the air, expressed in the spreader coordinate system. In this case, the positions of 5270 particles were determined. The particle positions are situated around a circle segment, because they are acquired by cameras that are mounted on a rotating arm and particles are only registered when they pass below this camera setup. The figure does not represent a single throw, but a collection of particles that were captured on image.
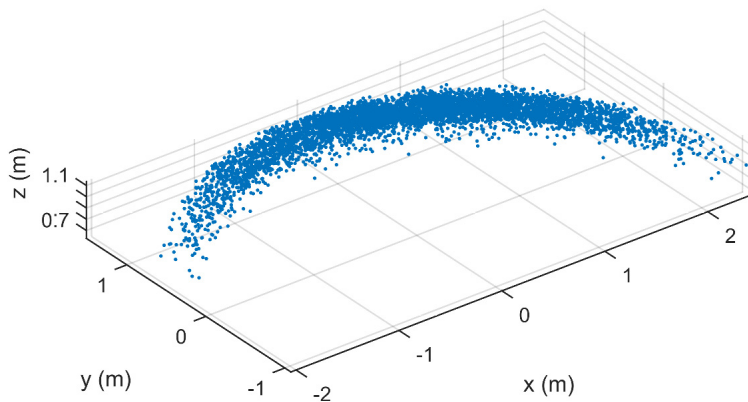
Figure 4.22. Particle 3D positions in spreader coordinate system. The spreader was set at configuration B

Table 4.8 and Figure 4.23 illustrate the measured particle size distribution. In Figure 4.23, also the results from the sieve test in chapter 2 are given. To verify the calculation of the particle diameter, an experiment with moving plastic spheres with known diameter was conducted. The average absolute difference between the true diameter and the measured diameter was 0.0671 mm (σ = 0.0422 mm) indicating a very high accuracy of the system.

Table 4.8. Particle size distribution for two tests at each spreader configuration (mass based). The 10th, 50th and 90th percentile are given (all in mm)

Configuration	Test	D10	D50	D90
A	1	3.03	3.67	4.39
	2	2.99	3.61	4.36
B	1	3.07	3.73	4.53
	2	3.00	3.63	4.30
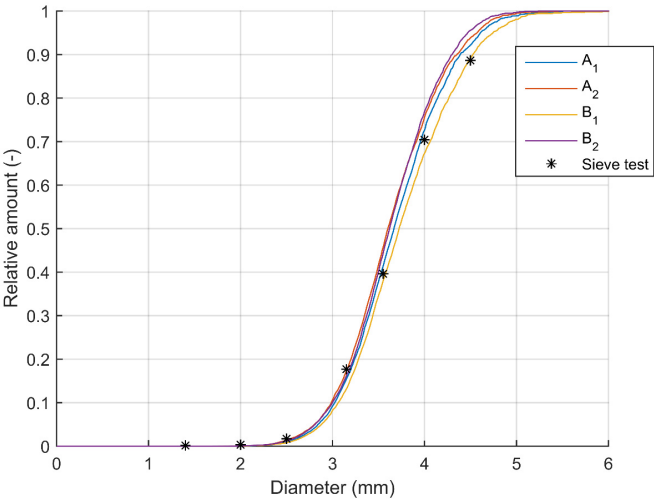
Figure 4.23. Cumulative particle size distribution (mass based). Results from image processing are given (two tests of configuration A and B), as well as the results of the sieve test

From Table 4.8 and Figure 4.23, it can be seen that the size distribution of the fertilizer particles is similar between the replicates of each spread test. The size distribution for the first test at configuration B is slightly larger compared to the second test. This can be caused by the fact that, although the same fertilizer type (from the same manufacturer) was used between tests, small differences between different batches can be found (measurements were performed using multiple separate bags of 50 kg). Furthermore, it is possible that the ambient light level was slightly different. Although a plastic cover was used to create a dark environment for the measurements, external light could enter the measurement zone through gaps, especially at the sides of and underneath the spreader. From Figure 4.14, it can be seen that although particle edges are steep, they are still several pixels wide. This can be caused by the fact that the

edges reflect less light, originating from the illumination system towards the camera sensor compared to the centre of the particles. Apart from increasing the amount of noise in the images (which can affect also further steps in the algorithm), an increase in ambient light intensity level increases the global intensity level of the particles on the images. Because of the gradual edges, and the fact that a fixed, global threshold was used for segmenting the particles, this can cause an increase in the area of their projection on the images and therefore cause a minor over-estimation of the particle diameter. Furthermore, despite the short duration of the flashes of the illumination system (30 μs), motion blur can still occur, especially in the case of faster moving particles (particles ejected with the longer vanes at configuration B). This can cause a slight increase in the size of the cross-section in the direction of motion which can increase the predicted particle size. The amount of external light however was difficult to quantify and the quantitative effect on the particle size is unsure.

Figure 4.23 shows that the particle size distribution is also comparable between the two spreader configurations even though at configuration B, a higher disc rotational velocity was used. This suggests that in this case, there is no increase in the breaking of particles due to a larger impact with the vanes. Lawrence et al. (2007) found a difference between the particle diameter pre- and post-spreading, indicating mechanical breaking of particles. The fact that this is not the case here could be attributed to the quality of the fertilizer (high particle strength), but also to the design of the spreader, which uses a centred feeding in contrast to most other spreader manufacturers on the market (reducing the impact force of the particles with the vanes). When we compare the results from Table 4.8 with the particle sizes determined with micro-CT (see Table 2.9) for CAN fertilizer, it can be seen that, although in the latter case a small sample was used, results are very similar, the difference between the median diameter is generally smaller than 0.2 mm. Figure 4.23 shows that the particle size distribution is also comparable to the distribution measured in the sieve test. In three of the four tests, a slightly smaller amount of large particles (>4.5 mm) was found compared to the sieve test. Hofstee (1992) found an increase in particle strength with an increase in diameter for CAN fertilizers, indicating that this finding does not relate to a higher breaking percentage of larger particles. As mentioned before, small differences between different batches of the same fertilizer can exist which could be the reason for this small difference. Furthermore, during sieving, particles fall through the sieve if their size in either orientation is smaller than the mesh size. It is therefore possible that the sieve test underestimates the true particle. In case particle spin occurs, the camera system determines the diameter of each particle based on four different projections (two positions for each camera) and can therefore be more accurate.

The velocity of the particles was determined based on two subsequent 3D positions using the multi-exposure technique. For each particle, a 3D velocity vector was determined based on the time matching algorithm explained in the materials and methods section. Figure 4.24 shows the velocity vector for a small amount of particles (10% of the total). Figure 4.25 represents the 3D velocity components for all the particles at configuration B (first replicate). It should be noted that the points thus do not represent particle positions. Two groups of velocities can be identified. These represent particles that are thrown with the small and large vanes of the spreader respectively. The groups appear to be situated around circle segments, indicating a similar resulting velocity. It can be seen that some particles have slightly different velocity components, this can be caused by impact of particles with e.g. the camera frame, by rebounding particles or by a wrong match by the time-matching algorithm. Particles are not perfectly spherical and can spin during the ballistic flight (Cool et al., 2014). Therefore, the shape of the 2D projection between the two subsequent positions can change, which can have an effect on the matching process. This is why, in contrast to Hijazi et al. (2014), no fixed window-based correlation methods were used for the matching process. Generally, it can be seen that the number of particles with abnormal velocity components is very limited indicating a good performance in the prediction of the velocity vectors.
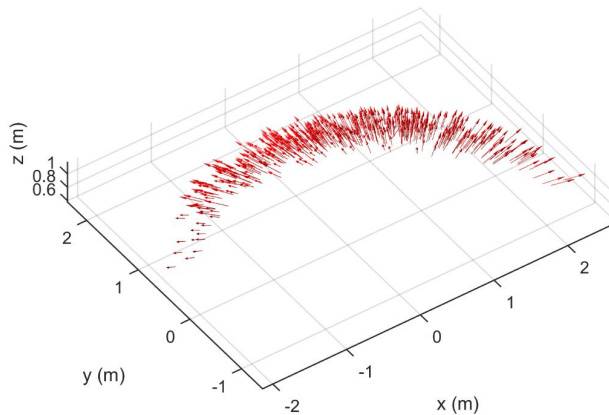
Figure 4.24. Velocity vector plot of particles expressed in spreader coordinate system. The spreader was set at configuration B. For reasons of clarity, only 10% of the particles are shown
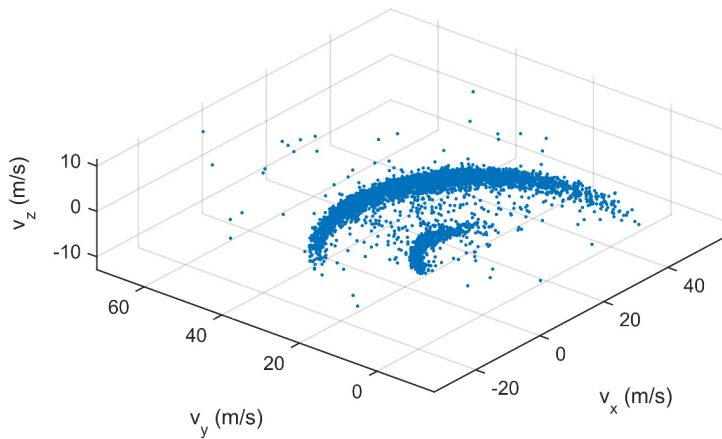
Figure 4.25. Particle 3D velocity components expressed in spreader coordinate system. The spreader was set at configuration B

In Figure 4.26, histograms of the resulting velocity are shown for both replicates of configuration A and B. Each histogram shows two peaks, related to the two groups of velocities that were found on Figure 4.25 (the resulting velocity is the magnitude of the vector). The reason for these two peaks is that two types of vanes were used on the spreading disc: six long ones and two short ones. The two short vanes are responsible for the small peak in the histograms (at lower velocities) while the six longer vanes are responsible for the large peak in the histograms (at higher velocities). Histograms for both replicates are very similar, indicating a high repeatability of the measurements. Minor differences can be caused by the spreader, e.g. small changes in the mass flow rate.
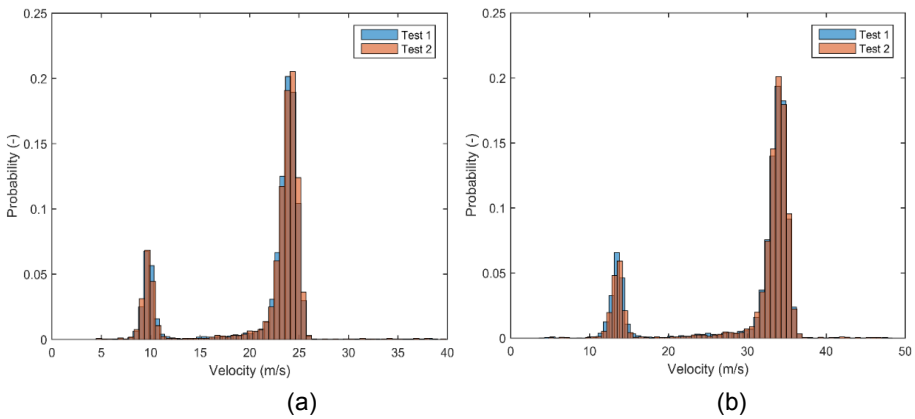
Figure 4.26. Histograms of resulting velocities for configuration A (a) and B (b). The overlap between the two replicates is given in brown

The static spread patterns for both tests for both spreader configurations are given in Figures 4.27 and 4.28. As mentioned before, only the left spreading disc was used during the experiments. Therefore, the resulting spread pattern was asymmetric around the centre point. The applied dosages of fertilizers in the figures are relatively low. This can be explained by the fact that the static spread patterns are determined based on the weights of the particles that have been identified on the images. Because of the small field of view of the cameras attached to the rotating arm, much more fertilizer particles are being spread during experiments than being captured on images (see section 4.3.3.5).

The area covered by the spread pattern clearly increased because of the larger disc rotational speed, which is necessary to obtain a larger working width. Each spread pattern has two c-shaped parts, the smallest part is caused by slower moving particles, ejected by the two smaller vanes. The larger part is caused by particles that are ejected by the longer vanes, giving the particles more radial and tangential velocity (Cunningham, 1967). The correlation coefficients between the two replicates for both configurations are given in Table 4.9. The results indicate a high repeatability. The correlation coefficient is slightly smaller for configuration B, which can be attributed to the larger spreading area and the increased sensitivity of the spread pattern for errors due to the larger working width.

Table 4.9. Correlation coefficients between two replicates of the static spread pattern as calculated by Equation 4.39. A grid resolution of 1m x 1 m was used (51x35 cells)

Configuration	Correlation coefficient (-)
A	0.9806
B	0.9505

(a)   (b)
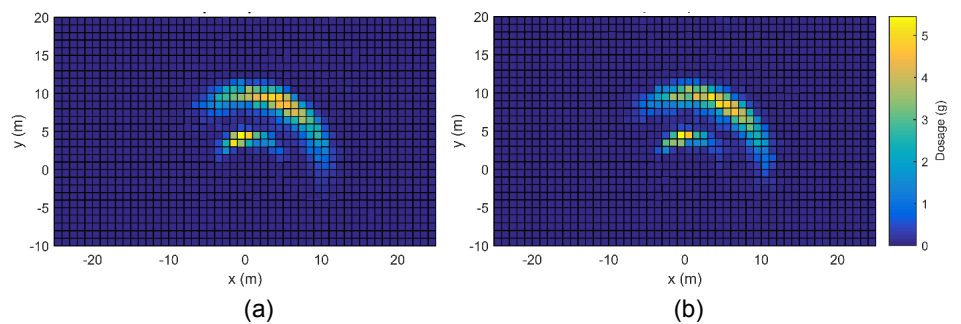
Figure 4.27. Spread pattern for the measured spreading disc, configuration A, test 1 (a) and test 2 (b).

(a)   (b)
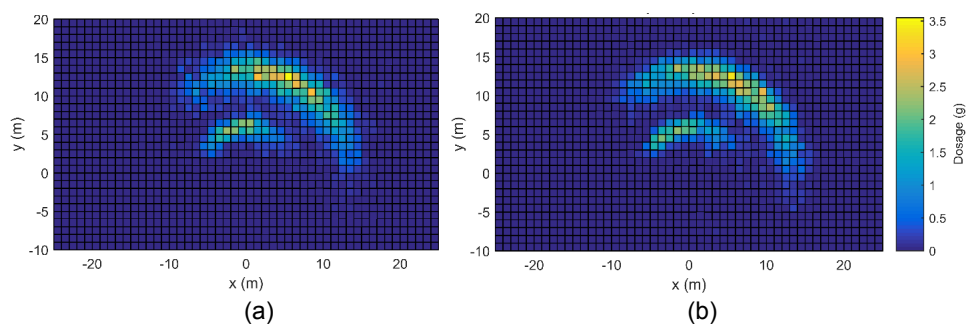
Figure 4.28. Spread pattern for the measured spreading disc, configuration B, test 1 (a) and test 2 (b)

The transverse spread patterns measured in the field and predicted with the system are given in Figures 4.29 and 4.30. Table 4.10 gives the correlation coefficients for the transverse spread patterns. It can be seen that the correlation coefficient for the two replicates with the measurement system were larger compared to the field measurements, for both spreader configurations. The repeatability for the camera system is thus higher compared to the repeatability of the field measurements. The variability between the replicates of the field measurements are in line with results

reported by Cool et al. (2016b). This was expected because more external factors can influence the spreading process. Generally, high correlations were found between the field measurements and the simulated spread patterns. Small deviations between both can have multiple causes. As mentioned before, the density of air during the field test was assumed 1.225 kg/m³. Based on data from the local weather station (air temperature and humidity) and historical data (air pressure), a value of 1.253 was calculated afterwards. From this, it can be seen that for the simulated spread patterns, the air density was under-estimated, which can lead to an over-estimation of the individual particle trajectories. Simulations in chapter 2 however showed a low absolute sensitivity to this parameter (see Figure 2.29). Considering the worst case scenario of a particle moving at 40 m/s for a flat disc (α=0°) and CAN fertilizer, this would result in an error of only 0.067 m which is negligible. From Table 2.9, it can be seen that the sphericity can vary between particles from the same batch, while for the simulated trajectories, a fixed value was used (see Table 4.6). For some particles, this will result in an under-estimation of the travelled distance, while for others the travelled distance will be over-estimated. The effect on the spread pattern will be a combination of the effect for all individual particle trajectories. To simulate this however, the sphericity of each particle measured with the camera system would need to be known. In future research, this could be done by linking the 2D shape of the particles on the images to the 3D sphericity. The unevenness of the terrain can cause vibrations of the spreader, which can influence the behaviour of the particles on the disc and the mass flow rate at a certain moment. Furthermore, the velocity of the particles relative to the ground can change because the spreader can slightly be pivoted in different directions due to surface irregularities on the field. These effects were not taken into account for the simulated spread patterns since the spreader remains static during these experiment and simulating these effects would be too difficult. Although the wind velocity and direction were measured, short term fluctuations can occur which affect the trajectory of particles in the air (see chapter 2). Because of the grass in the field, particles are expected to bounce less compared to measurements on a solid surface such as concrete. Despite the anti-reflection grids in the collection trays, particles can bounce out of the collection trays (Cool et al., 2016b, Parish, 1991a).

From the simulations in chapter 2, it was seen that for single particles, the absolute sensitivity of the travelled distance for some parameters (e.g. particle diameter, true density, sphericity) increases with the particle velocity and cone angle, which are associated with larger working widths. Based on this, it can be expected that for similar measurement errors, the predicted spread pattern would be less accurate for larger working widths. In Table 4.10 however, similar correlation values were found for both

spreader configurations, although for configuration B, higher particle velocities were reached (see Figure 4.26).

Table 4.10. Correlation coefficients between transverse spread patterns for configuration A and B measured with the measurement system and with collection trays on the field. A grid resolution of 1 m x 1 m was used (51 cells)

Configuration	Comparison	Correlation coefficient (-)
A	System rep. 1- system rep. 2	0.9944
	Field rep. 1 - field rep. 2	0.9893
	System rep. 1 - field rep. 1	0.9759
	System rep. 1 - field rep. 2	0.9829
	System rep. 2- field rep. 1	0.9754
	System rep. 2 - field rep. 2	0.9795
B	System rep. 1 - system rep. 2	0.9920
	Field rep. 1 - field rep. 2	0.9861
	System rep. 1- field rep. 1	0.9790
	System rep. 1 - field rep. 2	0.9851
	System rep. 2- field rep. 1	0.9768
	System rep. 2 - field rep. 2	0.9777
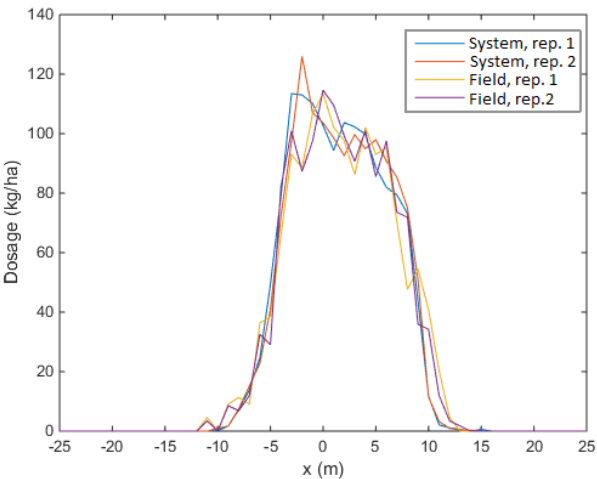
Figure 4.29. Transverse spread pattern for the measured spreading disc for configuration A. Two replicates were measured with the camera system (system) and in the field using collection trays (field)
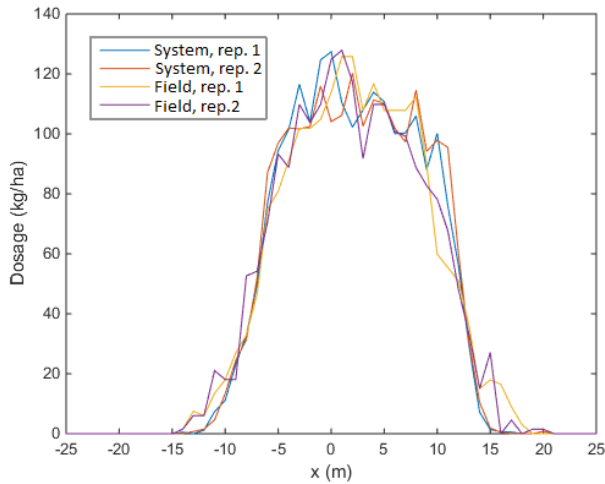
Figure 4.30. Transverse spread pattern for the measured spreading disc for configuration B. Two replicates were measured with the camera system (system) and in the field using collection trays (field).

Figure 4.31 gives the combined static spread pattern after overlap for both discs for configuration A. Table 4.11 gives the min-to-max ratio and Coefficient of Variation for the total transverse spread pattern after overlapping subsequent swaths. Results are given for both spreader configurations, measured with the camera system and with the collection trays on the field.
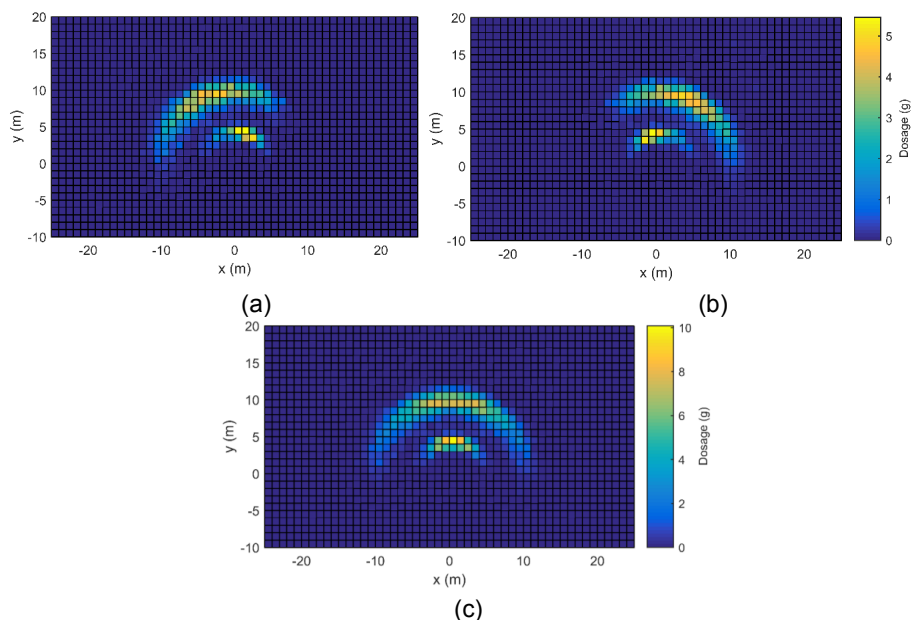
Figure 4.31. Measured spread pattern for the right (a) and the left (b) spreading disc and for both discs combined (c), in case of configuration A

Table 4.11. Minimum to maximum ratio and Coefficient of Variation (CV) for the total transverse spread pattern at working width specified by the manufacturer (12 m for configuration A, 18 m for configuration B). Transverse distributions for both replicates with the collection trays on the field and with the system developed in this work were used. The tractor was driven at 3 km/h during tests

Spreader configuration	Measurement system	Replicate	Min-to-max (-)	CV (%)
A	Field	1	0.80	5.86
		2	0.76	8.82
	System	1	0.77	8.73
		2	0.76	7.45
B	Field	1	0.91	3.20
		2	0.80	5.56
	System	1	0.74	7.45
		2	0.72	8.85

Figure 4.32 illustrates the total transverse spread pattern for one measurement with the camera system at spreader configuration B. It can be seen that the transverse spread pattern for a single swath is not symmetrical. This is caused by the wind, that was simulated, which had a component in the transverse direction (see Table 4.4).
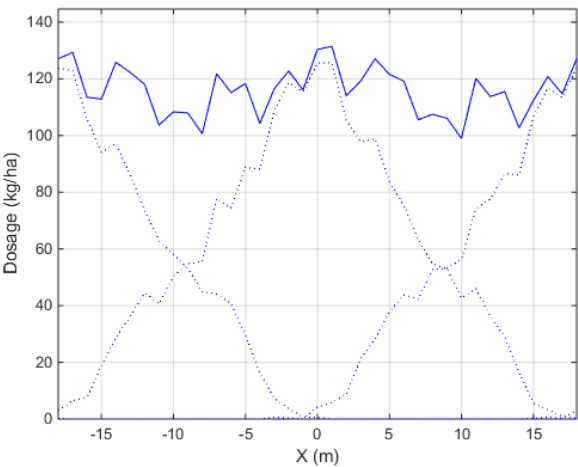
Figure 4.32. Predicted total transverse spread pattern (solid line) with overlap between spread patterns of subsequent swaths (dashed line). The spread pattern was measured by the camera system at configuration B (18 m working width, first replicate). A CV value of 7.52% was found

It can be seen that generally, the spreader performs well, since all CV values are far below 15% which is considered as the acceptable limit for centrifugal spreaders in the field (see section 1.2.3). The obtained values were very similar between both replicates with the measurement system (less than 1.5% difference in the calculated CV and less than 2% difference for the min-to-max ratio). For the field experiments, the repeatability was lower (less than 3% difference in CV and less than 15% for the min-to-max ratio). This was expected because the correlation between spread patterns was lower compared to the measurement system (see Table 4.10). The average difference between the CV obtained with both approaches was 0.75% for the first spreader configuration and 3.77% for the second spreader configuration. For the min-to-max ratio, this was 1.5% and 12.5% respectively. Based on these findings, it could be concluded that the resulting spread patterns were comparable with spread patterns obtained in the field.

The measurement system developed in this work assumes that the behaviour of the particles on the disc and the mass flow rate remains constant during an experiment. A relatively large heterogeneity in particle size distribution can cause particles to segregate during filling (Miserque & Pirard, 2004) or transport (Tissot et al., 1999). This phenomenon can cause differences in the particle size of particles being spread, which can indirectly affect the velocity of the particles (Reumers et al., 2003a) but also change the mass flow rate. When the mass flow fluctuates during an experiment, at certain arm positions more or less particles will be found than others, which will distort the spread pattern. Experiments by Parish (1999) showed that the spreader fill level had an effect on the mass flow rate. One spreading experiment however takes only 60 seconds, thus little variation in the mass flow rate or particle size distribution should be expected. Performing multiple measurements and combining the results increases the reliability of the results. The possible effects of segregation or variation in mass flow rate remain however important. Similarly to traditional transverse collection tests, the spread pattern that is determined should be representative for the whole spreading process. Protocols for transverse spread pattern testing could be used to ensure that a representative measurement is performed. The developed measurement system can be used for further investigating these effects in the future.

4.5.2. Simulations

The effect of wind, spreader height and tractor velocity was simulated based on the measured particle parameters. Figure 4.33 illustrates the simulated spread patterns and the difference with the reference case and Figure 4.34 shows the corresponding transverse spread patterns. It can be seen that front wind increases the area over which particles are dispersed while for back wind, the opposite is true. The width of the transverse spread pattern for back wind is slightly smaller compared to the reference. For front wind, the opposite is true. Side wind clearly shifts the spread pattern to one side, causing an asymmetric distribution around the spreader centre. The higher the wind velocity, the larger the shift and the more the spread pattern becomes skewed (see Figure 4.35). It is clear that side wind has a large effect on the transverse distribution. This however does not directly imply a large effect on the distribution homogeneity after overlap, because when the wind conditions remain similar, the shift will be in the same direction for subsequent swaths. In case of boundary spreading however, the effect will clearly be large. When the wind is directed towards the boundary, a large amount of particles can end up over the field boundary resulting in losses for the farmer but also in eutrophication in case the field is adjacent to a watercourse. When the wind is directed in the opposite way, the section next to the boundary might be under-fertilized, resulting in yield losses.

Increasing the tractor velocity decreases the relative velocity of the particles to the ground and therefore the travelled distance, however this has little effect on the transverse spread pattern. Increasing the spreader height increased the travelled distance of the particles and increased the width of the transverse spread pattern. Compared to the effect of wind however, the effect of increasing the spreader height was relatively small, although the height was increased with 250 mm for this simulation. This is in accordance with the findings in chapter 2 for single particle simulations (see section 2.3.3).
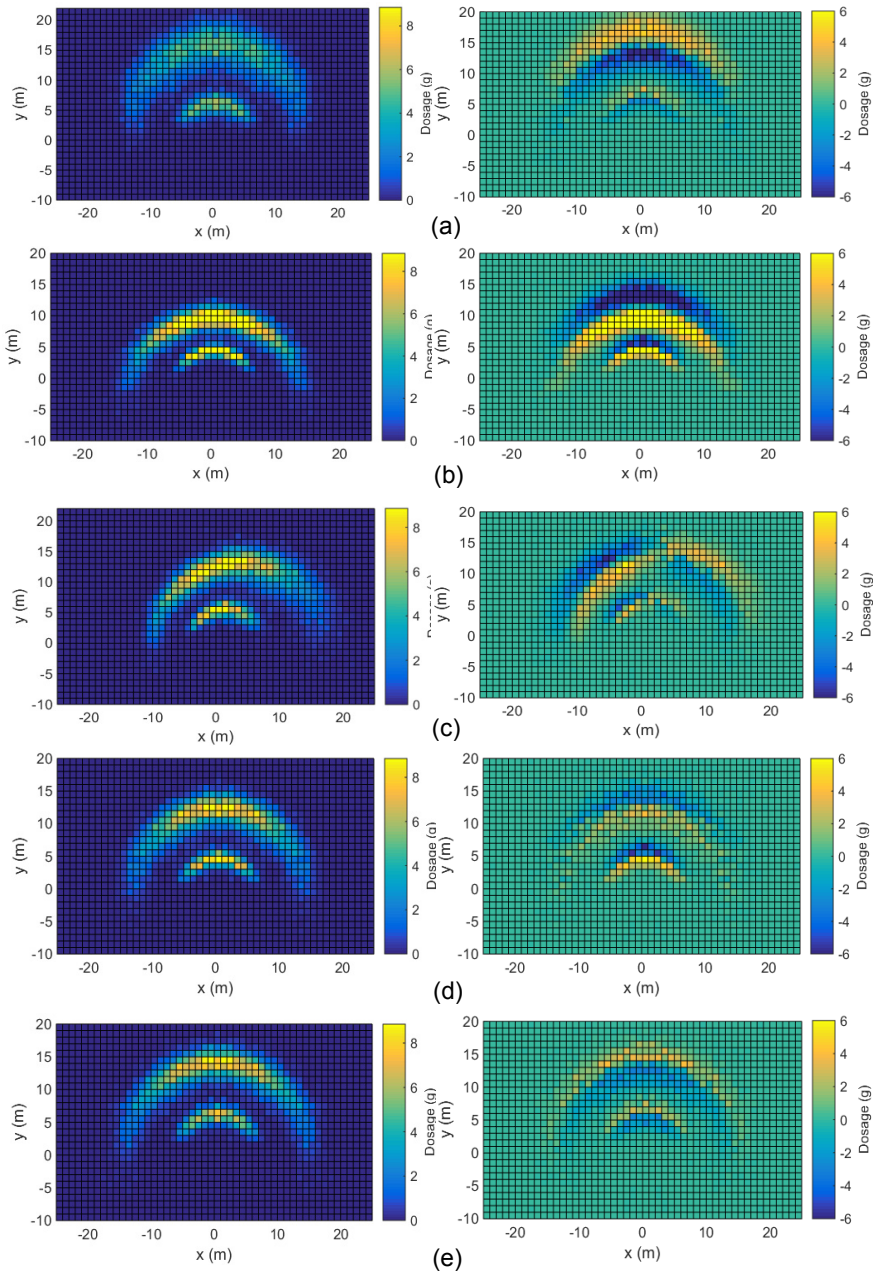
Figure 4.33. Predicted spread pattern (left) and difference with the base case (right) for front wind (10 m/s) (a), back wind (10 m/s) (b), side wind (10 m/s) (c), increased tractor velocity (20 km/h) (d) and spreader height (1m) (e). Data for both replicates combined. Spreader configuration B was used
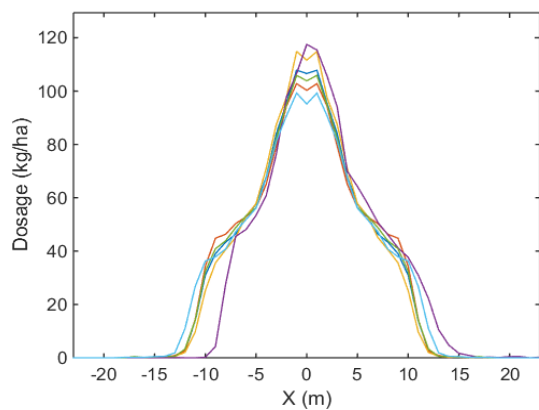
(a)
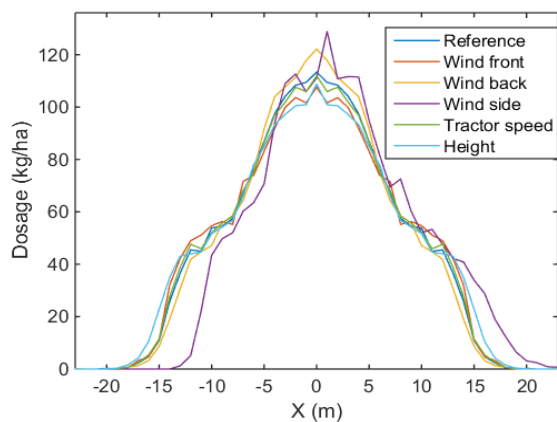
(b)

Figure 4.34. Transverse spread pattern (both discs combined) for configuration A (a) and B (b) for different cases (wind of 10 m/s)
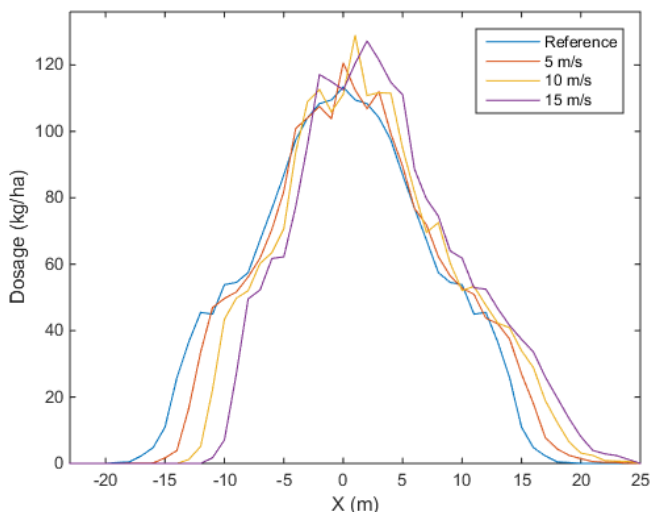
Figure 4.35. Transverse spread pattern (both discs combined) for different wind conditions. A side wind of 5, 10 and 15 m/s was applied. Data for both replicates of configuration B combined

Tables 4.12 and 4.13 show the min-to-max ratio and CV for the transverse distribution after overlapping for subsequent swaths for both configurations respectively. Generally, increasing wind velocities decreased the distribution uniformity. Wind in the longitudinal direction (frond and back wind) had less effect compared to side wind. Side wind velocities of 10 and 15 m/s clearly decreased the min-to-max ratio and increased the CV, indicating a low distribution homogeneity on the field. This finding is in accordance with field experiments by Grafton et al. (2015a; 2015b). For side wind of 15 m/s, the CV exceeds the allowable limit of 15% for both spreader configurations, the large effect on the transverse distribution after overlap is illustrated in Figure 4.36. The tractor velocity had little effect on the spreading homogeneity, even though a velocity of 20 km/h (5.56 m/s) was assumed, which is more than double the velocity used for the base case. Also, the effect of increasing the height of the spreader was rather low.

Table 4.12. Minimum to maximum ratio and Coefficient of Variation (CV) for the total transverse spread pattern (data from both replicates was combined) for different cases (wind, tractor speed and spreader height). In all cases, one parameter was changed relative to the base case (settings according to manufacturer for **configuration A**, $v_{tractor}$=8 km/h, v_{wind}=0)

Case	Parameter	Min-to-max (-)	CV (%)
Base case		0.822	7.36
Front and back wind (m/s)	5	0.782	7.89
	10	0.764	9.00
	15	0.749	9.89
Side wind (m/s)	5	0.770	8.36
	10	0.703	12.89
	15	0.583	17.27
Tractor speed (m/s)	5.56	0.826	7.16
Spreader height (mm)	1000	0.810	8.43

Table 4.13. Minimum to maximum ratio and Coefficient of Variation (CV) for the total transverse spread pattern (data from both replicates was combined) for different cases (wind, tractor speed and spreader height). In all cases, one parameter was changed relative to the base case (settings according to manufacturer for **configuration B**, $v_{tractor}$=8 km/h, v_{wind}=0)

Case	Parameter	Min-to-max (-)	CV (%)
Base case		0.883	4.42
Front and back wind (m/s)	5	0.819	5.60
	10	0.752	7.75
	15	0.715	9.78
Side wind (m/s)	5	0.749	7.90
	10	0.611	13.26
	15	0.540	17.24
Tractor speed (m/s)	5.56	0.868	5.16
Spreader height (mm)	1000	0.820	7.10
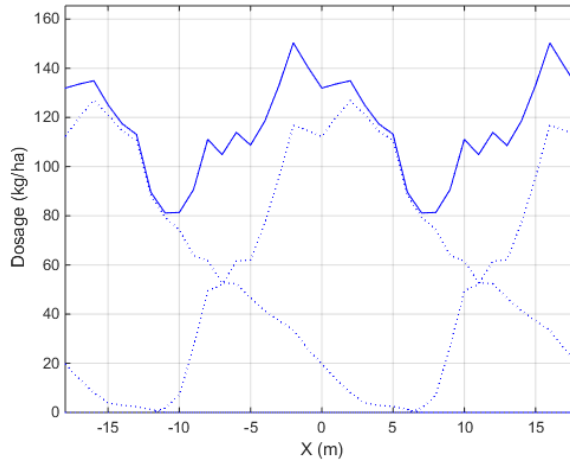
Figure 4.36. Predicted total transverse spread pattern (solid line) with overlap between spread patterns of subsequent swaths (dashed line). Data for both replicates of configuration B combined. Simulation for side wind of 15 m/s. A min-to-max value of 0.54 and a CV value of 17.24% was found for this case

4.5.3. Comparison to previous approaches

Compared to previous approaches that were developed to predict spread patterns, significant improvements were made. In contrast to most previous studies (Grift & Hofstee (1997), Reumers et al. (2003a; 2003b), Cointault et al. (2003), Villette et al. (2006), Vangeyte (2013)), the position and the velocity of the particles was determined in three spatial dimensions. This eliminates the need for a cylindrical collector like the one used by Reumers et al. (2003a; 2003b) and Vangeyte (2013) to determine the vertical outlet angle of the particles and allows to determine the spread pattern for both flat and conical disc spreaders. Compared to the approach of Villette et al. (2008), the 3D velocity of the particles can be determined without depending on parameters related to the spreader configuration, meaning that the same methodology can be applied for each centrifugal spreader type and configuration. By implementing the multi-exposure technique, the use of expensive high speed cameras was avoided and high resolution cameras could be used at a relatively low cost (cameras + lenses: 5496 €) . Compared to Cointault et al (2003) and Hijazi et al. (2014), a small field of view was used to achieve a high particle resolution on the images. The illumination system developed Compared to Vangeyte (2013), the illumination system used for multi-exposure developed in this work provided a more homogeneous and higher illumination intensity level, which allowed to decrease the length of the flashes,

decreasing the amount of motion blur. In contrast to other hybrid approaches in literature using cameras, the particle size was determined using image processing during each spreading experiment and not through sieving before the tests. This is important because particle size can change during due to mechanical impact with the vanes and during spreading because segregation can occur in the hopper (Miserque & Pirard, 2004). By simultaneously measuring the size and the dynamics of the particles, possible interactions between the particle size and the particle velocity (Reumers et al., 2003) can be taken into account. Until now, only spread patterns from custom-designed experimental spreaders were reported in literature. The measurement system developed in this work on the other hand was evaluated using a commercially available fertilizer spreader at realistic settings. In literature, no "predict rather than collect" approach has yet succeeded in accurately determining the spread pattern of a centrifugal spreader. Results from experiments conducted in this work indicated a high similarity with field experiments using a transverse row of collection trays. Although more experiments will be necessary to test and improve the robustness of the technique for other fertilizer types and spreaders, the system shows promising results. The absolute application rate (related to the mass flow rate) cannot be determined using the system, since much more particles are being spread than being captured on the images due to the small field of view of the cameras. However, mass flow rate can easily be determined using other sensors that are specifically designed for this (load cells, torque sensors), see section 1.2.2.

4.5.4. Possible applications

Spreader assessment in practice

Because of the cost and the space of the system, it is unlikely that farmers will be interested to purchase the system for individual use. To achieve this, the system would have to be down scaled and mounted directly on the spreader, which will require adaptations. The system in its current state however can be used for spreader assessment in practice by service providers or control bodies, e.g. on demand of the farmer, for certification programs, etc. In case the test indicates unsatisfactory results, spreader parameters can be adjusted to correct the spreading process to ensure a more homogeneous distribution in the field. Also for new or unknown fertilizers, the spread pattern can be determined fast and accurately, for example in case of spreading organomineral fertilizers (Antille et al., 2013a) and organic fertilizers, for which no spreading charts exist.

<u>Industry</u>

The system can be of interest for spreader manufacturers as a tool for spreader design and to create spreading charts, but also for manufacturers of organic or inorganic fertilizer, e.g. for optimizing the spreadability of their product. The prototype developed in this study requires much less space (10 m x 5 m) compared to traditional testing facilities and the test bench by Piron et al. (2010) and the size of the measurement zone can be even more reduced. This means reduced costs for building test facilities and reduced running costs (heating, cleaning, air conditioning). The technique provides much more insight in the spreading process and allows to study the quantitative effect of different input parameters on the shape of the spread pattern without having to perform extra experiments. Similar to this work, simulations can be performed to determine the effect of parameters which would be difficult to measure using traditional approaches (e.g. the effect of wind).

4.6. Conclusions

Because of the large environmental impact of fertilizers, it is important that they are correctly distributed on the field. For granular fertilizer, mostly centrifugal fertilizer spreaders are used. Although simple in working principle, their spread pattern is prone to errors, which are often caused by lack of calibration for the specific fertilizer used. At farm level, spread patterns are traditionally measured using collection trays, which is a laborious and time consuming work. Measurements can be executed under controlled conditions using automated weighing systems, however these require large testing facilities which are very expensive. Different "predict rather than collect" approaches have been developed in literature, being faster and requiring less space, however until now, none of these approaches could predict the spread pattern in an accurate way.

In this chapter, an innovative multi-camera system was developed to predict the spread pattern in a fast, accurate, cost- and space-efficient way. Using a first set of cameras and corresponding image processing algorithms, the positions and velocities of the particles being ejected by the spreader were determined in three spatial dimensions. The multi-exposure technique was implemented to achieve high speed and high resolution information at a relative low cost (cameras + lenses: 5496 €). Furthermore, also the size of the individual particles was determined using image processing. The particle dynamics were expressed relative to a coordinate system associated with the spreader, which was automatically determined using a second set of cameras. By

using this information as input for the ballistic model developed in chapter 2, landing positions of individual fertilizer particles were simulated and the spread pattern was determined.

Experiments were conducted with a commercially available spreader in combination with a commonly used fertilizer type. Two configurations, each with two replicates, were evaluated, corresponding to a lower and higher disc rotational velocity. The measurement system showed a high repeatability in determination of the particle size distribution, as the results were similar between all experiments. An experiment with ideal spheres showed a very accurate calculation of the particle size. This was confirmed by the fact that the calculated size distributions for fertilizer particles were similar to sieve test results. The predicted particle velocities and resulting two-dimensional spread patterns were highly repeatable between replicates. The spread patterns were transformed to transverse spread patterns to compare the results with spread patterns obtained in the field using a transverse row of collection trays. The spread patterns showed a good correlation (97.5% to 98.5% over all experiments). The calculated min-to-max ratios and CV values after overlap for subsequent swaths were calculated. The values were very similar between both replicates with the measurement system (less than 1.4% difference in the calculated CV and less than 2% difference for the min-to-max ratio). For the field experiments, the repeatability was lower (less than 3% difference in CV and less than 15% for the min-to-max ratio). Overall, the CV and min-to-max ratio were similar between the field experiments and the experiments with the measurement system. The average difference between the CV obtained with both approaches was 0.75% for the first spreader configuration and 3.77% for the second spreader configuration. For the min-to-max ratio, the differences were 1.5% and 12.5% respectively. Based on these findings, it could be concluded that the resulting spread patterns were comparable with spread patterns obtained in the field.

Because spread patterns are predicted by simulating individual particle trajectories based on particle parameters that are measured after ejection by the spreader, simulations can be performed to study the effect of different parameters on the spread pattern without having to perform extra measurements. By using the data from the spread tests above, the effect of the tractor velocity, the spreader height and wind on the spread pattern was simulated. Wind had a relatively larger impact compared to an increase in tractor velocity and spreader height. Side wind shifted the two-dimensional and transverse spread pattern to one side, causing an asymmetric distribution around the spreader centre. Especially in case of boundary spreading, this is important, since it can imply that a large amount of particles can end up over the field boundary. The

effect of wind on the spread pattern after overlapping subsequent swaths was clearly depending on the wind velocity and the direction. Compared to the base case, side wind increased the CV from 7.36% and 4.42% to 17.27% and 17.24% (for the highest wind velocity considered) for spreader configuration A and B respectively. The min-to-max ratio dropped from 82.2% to 58.3% for configuration A and 88.3% to 54% for configuration B. For front- and backwind and spreader height and tractor velocity, the CV and min-to-max ratio were generally less affected. The results indicate that wind is an important parameter to consider when spreading fertilizer with a centrifugal fertilizer spreader but more research is necessary to evaluate this for other settings, particle types and spreaders.

Compared to previous approaches that were developed to predict spread patterns, significant improvements were made. By using stereovision, not only the particle positions and velocities in 3D can be determined, but also the size of the particles. By implementing the multi-exposure technique, high resolution images were obtained and the use of expensive high speed cameras was avoided. Compared to traditional techniques using collection trays, the measurement system is much more space efficient. The total surface area of the measurement system is 10 m x 5 m, and this can be further reduced. The system developed in this study can be used for assessment of spreader performance in practice and to calibrate spreaders. The system can be of interest for spreader manufacturers to design spreading charts without the need for large spread halls while offering more insight in the spreading process compared to traditional approaches. Simulations can be performed to quantify the effect of different parameters such as wind, spreader height and tractor velocity on the spread pattern, without having to perform extra experiments. By fertilizer producers, the system can be used for performing experiments and simulations, e.g. to improve the spreadability of their product.

CHAPTER

5

GENERAL CONCLUSIONS AND FUTURE WORK

5.1. General conclusions

Distributing the correct fertilizer quantity at the right place requires correct spreader settings, especially in the case of centrifugal spreaders. To assess the performance of these spreaders and perform corrections if necessary to assure a correct and precise application of fertilizer, the spread pattern must be determined. Measuring the spread pattern at farm level using collection trays on the field is very labour-intensive and time-consuming and therefore rarely done in practice. Alternatively, measurements can be executed under controlled conditions using automated weighing systems, however these require large testing facilities which are very expensive. Different "predict rather than collect" methods have been developed, determining the spread pattern by simulating individual particle trajectories and calculating their landing position. Compared to the traditional approach, they are much faster and require less space. Furthermore, they provide more insight in the spreading process and could be used as control system for online corrections, e.g. in the case of variable rate fertilization. However until now, none of these approaches could predict the spread pattern in an accurate way. Furthermore, no test results were reported on real, commercially available spreaders.

The aim of this PhD research was to develop and evaluate an automated system, capable of determining spread patterns of centrifugal spreaders in a fast, accurate and cost- and space-efficient way. Based on a literature review, the most promising method to fulfil these requirements was to predict the spread pattern using the hybrid approach, i.e. by simulating the spread pattern based on measurements of particle parameters after leaving the discs and then predicting their trajectories and subsequent landing positions using a ballistic model. From all hybrid techniques, image processing approaches are most promising because they allow to determine the parameters of multiple particles without interfering with the fertilizer flow. To avoid the use of expensive high speed cameras to retrieve three-dimensional information, stereovision with multi-exposure was used to determine the particle positions and the velocities in three dimensions and the particle sizes.

The first objective of this work was to develop a three-dimensional ballistic model capable of calculating the trajectories of fertilizer particles and their subsequent landing positions. The model incorporated the effect of gravitation and drag but also wind. The drag coefficient was calculated based on the Reynolds number, which possibly changes during the trajectory and the particle sphericity. Because the equations of motion could not be solved in an analytic way, a numerical solver was used. By

performing simulations, the effect of different step sizes on the accuracy of the landing position was investigated. Generally, increasing the step size caused an over-estimation of the travelled distance. Decreasing the step size and interpolation of the landing position increased the accuracy. Results indicated that a step size of 1e-3 s resulted in errors less than 10 mm for the travelled distance, which is more than sufficient for predicting fertilizer landing positions.

The second objective of this thesis was to determine the physical properties of different fertilizer types and use these in preliminary simulations to quantify their effect. Eight commonly used fertilizer types were selected based on their different physical properties. Their particle size distribution was determined using sieving and gas-pycnometry was used to determine the true density. Micro-CT was used to determine the three-dimensional shape of the particles and based on this, the sphericity distribution was calculated. Based on the sphericity and the Reynolds number, the drag coefficient was determined using an equation from literature. Although direct comparisons are not possible because the particle types were not identical, comparisons with experimental results from literature were made. For CAN and NPK fertilizer, results were very similar, for KCL however, the drag coefficient was over-estimated. This can be caused by a more irregular shape in our case or by the equation that was used to calculate the drag coefficient. Clearly, more research is necessary on the drag coefficient of irregular fertilizer particles. Based on the measurement results, single-trajectory simulations were performed to determine the travelled distance for the different fertilizer types. Different cases were considered: particles leaving a flat and a conical disc with different velocities. The travelled distance between different particle types was clearly different and depending on the disc and particle velocity. The difference between particle types was generally higher for the conical compared to the flat disc case and increased clearly with the particle velocity. Because of their different aerodynamic behaviour, it is clear that some fertilizer types should not be blended together to be spread simultaneously on the field. Simulations were performed to determine the quantitative effect of different particle- and environmental parameters involved in predicting the landing position of fertilizer particles. Results indicated that an increase in particle velocity, vertical outlet angle, initial height, tail wind, particle size, true density and sphericity increased the travelled distance, while for increasing the air density and head-wind, the opposite was true. The sensitivity was clearly affected by the particle type, velocity and vertical outlet angle. To compare the effect of the different parameters, the relative sensitivity was calculated. Generally, it was found that the landing position was most sensitive for the vertical velocity component and particle diameter and least for the initial height and the density of air. The effect of wind on the individual particle trajectories was relatively large. The effect on the spread

pattern, generated by superimposing multiple particle trajectories however remains unclear and should be further investigated. Based on our findings, it can be concluded that hybrid methods predicting spread patterns based on individual particle trajectories should measure particle velocities in three spatial dimensions and particle sizes should be determined accurately.

The third objective of this thesis was to develop an illumination system for acquiring multi-exposure images of fast-moving fertilizer particles. To achieve a high accuracy for measuring the particle parameters from the images, a high irradiance level was necessary without compromising the uniformity of light distribution. In a first step, the optimal type of LED was selected from a range of commercially available power LEDs taking into account spectral distribution of the LEDs and the camera sensitivity. Next, the optimal configuration of LEDs was determined using a multiple objective genetic algorithm. Both the irradiance level and homogeneity of the light distribution were considered, in contrast to other approaches in literature. The angular distribution pattern from the manufacturer was used to simulate light distribution patterns for multiple LEDs. Comparing simulation results for three types of lenses, the narrow angle lens was found optimal for this application. Multiple Pareto optimal solutions were found for different numbers of LEDs and from this set, the best configuration was selected. The optimal configuration resulted in a high irradiance and a coefficient of variation below 2%.

The fourth objective of this thesis was to design a system for predicting spread patterns based on individual particle trajectories. A multi-camera system was developed to predict the spread pattern of commercial centrifugal spreaders in a fast, accurate, cost- and space-efficient way. Using a first set of cameras and corresponding image processing algorithms, the positions and velocities (particle dynamics) of the particles being ejected by the spreader were determined in three spatial dimensions. The illumination system developed before was implemented for multi-exposure to achieve high speed and high resolution information at a relative low cost. Next to the particle dynamics, also the size of the individual particles was determined using image processing. The particle dynamics were expressed relative to a coordinate system associated with the spreader, which was automatically determined using a second set of cameras. The landing positions of the individual particles were predicted using the ballistic model developed earlier and subsequently, the spread pattern was calculated.

The final objective of this work was to evaluate the system by performing experiments with a commercially available fertilizer spreader at realistic settings and compare the

results with field tests. Spreading experiments were conducted with a Vicon spreader in combination with a commonly used fertilizer type (CAN). Two configurations were evaluated, corresponding to a lower and higher disc rotational velocity. The measurement system showed a high repeatability and accuracy in determination of the particle size distribution, as the results were similar between all experiments and the particle size distributions corresponded well with sieve test results. The predicted particle velocities and resulting two-dimensional spread patterns were highly repeatable between replicates. The spread patterns were transformed to transverse spread patterns to compare the results with spread patterns obtained in the field using a transverse row of collection trays. Generally, the spreader performed well, since the CV after overlapping subsequent swaths was below 15% for all experiments. The predicted spread patterns showed a high correlation (97.5% to 98.5% over all experiments) with the spread patterns obtained in the field. The calculated homogeneity of distribution, quantified by the CV after overlapping subsequent swaths was also similar. The average difference between the CV obtained with both approaches was 0.75% for the first spreader configuration and 3.77% for the second spreader configuration. Based on these findings, it could be concluded that the resulting spread patterns were comparable with spread patterns obtained in the field.

Compared to previous approaches that were developed to predict spread patterns, significant improvements were made. Generally, the requirements set for this work were successfully achieved:

- The system can determine the spread pattern of commercially available centrifugal fertilizer spreaders in a fully autonomous way.
- By implementing the multi-exposure technique, high speed information and high resolution images were obtained at a relatively low cost (cameras + lenses = 5496 €).
- The system works fast: one scanning rotation takes only 60 seconds and the image processing takes approximately 4-6 minutes and can be further optimized.
- The measurement system is space-efficient: only a surface area of 5 m x 10 m was used and this can be further reduced.
- Spread tests were conducted with a commercially available spreader and a commonly used fertilizer type. Predicted particle size distributions corresponded well with sieve test results and the predicted spread pattern was comparable with spread patterns obtained in the field.

Based on the data from the measurements, simulations were performed to study the effect of wind, tractor velocity and spreader height on the spread pattern. The effect of wind was larger compared to an increase in tractor velocity and spreader height, especially in the case of side-wind. Side wind shifted the two-dimensional and transverse spread pattern to one side, causing an asymmetric distribution around the spreader centre. This is important in the case of boundary spreading, since it can imply that a large amount of particles can end up over the field boundary. The effect of wind on the spread pattern after overlapping subsequent swaths was clearly depending on the wind velocity and the direction. Compared to the base case, side wind increased the CV from 7.36% and 4.42% to 17.27% and 17.24% for both spreader configuration A and B respectively. The min-to-max ratio dropped from 82.2% to 58.3% for configuration A and 88.3% to 54% for configuration B. For front- and backwind and spreader height and tractor velocity, the CV and min-to-max ratio were generally less affected. The results indicate that wind is an important parameter to consider when spreading fertilizer with a centrifugal fertilizer spreader but more research is necessary to evaluate this for other settings, particle types and spreaders. In a similar way, the effect of other parameters on the spread pattern can be determined. Although it should be noted that these parameters may also influence the behaviour of the particles on the disc and therefore change the particle dynamics of the particles being ejected by the spreader.

Compared to previous approaches that were developed to predict spread patterns, significant improvements were made. By using stereovision, not only the particle positions and velocities in 3D can be determined relative to the spreader, but also the size of the particles. By implementing the multi-exposure technique, high resolution images were obtained and the use of expensive high speed cameras was avoided. Compared to traditional techniques using collection trays, the measurement system is much more space efficient.

The measurement system developed in this study can be used for assessment of spreader performance in practice and to calibrate spreaders, e.g. by service providers or control bodies (since the system will be expensive for individual farmers). The system can be used by manufacturers of spreaders to design spreading charts without the need for large spread halls while offering more insight in the spreading process compared to traditional approaches. Simulations can be performed to quantify the effect of different parameters such as wind, spreader height and tractor velocity on the spread pattern, without having to perform extra experiments. Furthermore, fertilizer manufacturers can use the system, e.g. to improve the spreadability of their product.

5.2. Future work

5.2.1. Additional tests and simulations

5.2.1.1. Spread tests

Although for the development of our method different types of spreaders were used for fine-tuning the algorithms, the spread pattern was only validated for one spreader (Vicon RO-XL) at two different settings for one specific type of fertilizer. Similarly, experiments should be conducted to evaluate the performance of the measurement system for other fertilizer types (mineral, but also organic particles) and other spreaders at different settings (different rates, working widths, boundary spreading,...). Fertilizer types have different colours (see Figure 2.3) which can influence the segmentation process and different physical properties (see section 2.3.3) which can potentially affect the accuracy of the measured 3D positions, velocities and particle sizes. Together with inaccuracies in the drag coefficient, these can cause errors in the predicted landing positions and the subsequent spread pattern. In a similar way as in this work, the predicted particle size distribution can be compared to the distribution measured using sieving. Experiments can be conducted to measure the accuracy of the predicted particle velocities. This can most easily be done for single particles, which can be ejected using a particle accelerator like the one developed by Grift & Hofstee (1997a). The velocity of these particles should then be simultaneously measured with an alternative measurement system. The image processing algorithms can be further fine-tuned or improved based on these findings. To validate the predicted spread patterns, transverse spread patterns can be measured in the field to compare the spread pattern in one spatial dimension, similar to this work. Alternatively, spreading experiments can be conducted in spread halls to exclude the effect of external conditions like wind or field irregularities. Furthermore, by measuring the spread pattern with a system like the CEMIB, the spread pattern could be compared in two spatial dimensions.

5.2.1.2. Simulations

Many parameters can affect the spread pattern of centrifugal fertilizer spreaders. Simulations offer the possibility to study these effects. In contrast to field experiments, the effect of parameters can be determined independent from other factors or perturbations that occur during practical experiments. Data obtained with the measurement system can be used to study the quantitative effect of the different input parameters (e.g. particle size, density or shape) on the spread pattern and gain more insight in the spreading process. These results could be interesting for spreader

manufacturers, but also for manufacturers of fertilizer for example to improve the spreadability of their product. In this work, the effect of wind, tractor velocity and height of the spreader was simulated for one specific case. Similar experiments can be conducted for other spreaders and fertilizer types (see above).

5.2.2. Optimizations

5.2.2.1. General improvements

Some general improvements can be made for the measurement system. To reduce reflection of light from the background to the cameras visualizing the particles, black cloths were placed on the ground. During spreading experiments however, dust and particles accumulate on the cloths increasing the amount of background noise on the images. Therefore, after each test, the cloths need to be wiped clean before continuing other experiments. It should be investigated how this problem can be solved. One possibility could be placing a gridded collection system with relatively high edges on the ground. Because the cameras are inclined relative to the ground, these edges could occlude dust and fertilizer particles lying on the ground. Care should be taken that the gridded system can be easily segmented from the images.

Although the measurement system is very small in size (10 m x 5 m) compared to other approaches, its size can still be reduced. After particles have been acquired on image, they are no longer required. The measurement zone can therefore be reduced to the circumference of the rotating arm. The particles however must be discharged without bouncing back. This could be done by using a catchment system, based on the cylindrical collector systems developed in Reumers et al. (2003b). This way, not only the size of the measurement system can be reduced, but also the collection of particles can be done more efficiently reducing the amount of time needed for cleaning. The collected particles could be funnelled to a weighing system to simultaneously measure the mass flow rate during the spread tests.

It was observed that fertilizer particles, due to their hygroscopic properties, absorb water from the air, causing them to liquefy. This makes the cleaning afterwards more complicated and causes, in the case of ammonium holding fertilizers, the formation of ammonia gas. Keeping the relative humidity of the air low by using a climate-control system will prevent this process and keeps the particles from liquefying, making it possible to reuse them.

It is important for the accuracy of the measurements, that spreading experiments are performed at conditions that are similar to those during calibration. The room temperature must not deviate too much, because the material of the frame holding the cameras can thermally expand due to temperature. For the same reason, the temperature of the cameras and optics must be kept as constant as possible. This is why before each calibration or experiment, the cameras were warmed up. Keeping the temperature of the measurement system constant would reduce the need for frequent recalibrations. No experiments were performed to quantify the effect of thermal expansion on the measurement accuracy. Using the climate-control system, it would be possible to change the temperature and quantify the effect on the accuracy of the measurement system. Algorithms or procedures should be further refined to check the accuracy of the measurement system in its current state and assess the need for recalibration before performing spreading experiments. When a certain level of accuracy is no longer guaranteed, the user should be recommended to recalibrate the measurement system. By checking the accuracy before performing spreader experiments, unwanted errors, for example because a person or tractor touched the cameras causing their relative orientation to change, could be identified as well.

5.2.2.2. Drag coefficient of fertilizer particles

In this work, micro-CT scans were performed to determine 3D models of fertilizer particles. Based on their sphericity, the drag coefficient was calculated using a general equation from literature. Compared to experimental results obtained by Grift et al. (1997), the drag coefficient for CAN and NPK fertilizer was very similar, however for KCL fertilizer, the parameter was over-estimated. Clearly, more research is necessary to link the shape of fertilizer particles to the drag coefficient. The 3D models of the particles that were determined in this study could be used for further investigation. Computational Fluid Dynamics (CFD) software could be used to simulate the flow of air around these particles at realistic conditions. Based on the integration of local pressures on the particle surface and the dimensions of the particles, this should allow to determine the drag coefficient of the particles. These findings should be validated with well-designed experiments. Only a few particle types were scanned with micro-CT. Many other fertilizer types exist, and their properties can change with the manufacturing process or due to transport and handling. Using micro-CT and CFD simulations before performing each spread test for a specific type of fertilizer is too difficult and requires specific (and expensive) machinery and software. Nevertheless, these or similar experiments could be done by fertilizer manufacturers, and indicated as "spreadability parameter" on the label of their product. Alternatively, simple methods to measure the drag coefficient of unknown particle types could be developed. The

two-dimensional shape of the particles on the images of the measurement system could be linked with the drag coefficient for certain groups of fertilizers. In this way, the drag coefficient could be determined for individual particles after leaving the spreading discs which could improve the accuracy, because the shape of the particles can change due to mechanical breakage.

5.2.2.3. Procedures

Finally, procedures should be developed for executing spread tests in the future. Research should be conducted to study the influence of different measurement parameters such as the time of measurement, number of repetitions, resolution of the grid, etc. on the measurement results.

5.2.3. Towards an online feedback sensor
5.2.3.1. General

The measurement system can be used as the basis for developing a feedback sensor which can be mounted on spreaders. Using this sensor, feedback on the produced spread pattern could be provided during spreading on the field. At the moment, the measurement system takes 60 s to perform one scanning rotation. Unless this can be reduced to a large extent, measurements should be performed with a moving tractor to avoid over-applications when standing still. By measuring the spread pattern during spreading on the field, alterations in the spreading performance could immediately be detected and reported or corrected by automatically changing the spreader settings. Finding the optimal settings can be done by iteratively changing the settings and subsequently measuring the spread pattern until the result is satisfactory. The major influences of the different settings on the spread pattern should be known for this. Alternatively, the approach suggested by Grift & Kweon (2006) could be used for spreaders of which the position of the orifice can be rotated around the disc centre. By measuring the two-dimensional spread pattern at one orifice position and simulating the spread patterns for other positions, the optimal setting can be found by analysing the quality of the simulated spread patterns. Although the system can automatically measure the particle dynamics and particle size, also the drag coefficient and particle true density should be known to calculate the particle trajectories and their subsequent landing positions. As mentioned before, the two-dimensional shape of the particles on the images could be linked to the drag coefficient in further research. The true density is however a parameter that is more difficult to determine, either automatically, either by the farmer before spreading. One possibility is that fertilizer manufacturers pre-

determine this parameter and mention it on the label of their product. This is also possible for the particle shape or the drag coefficient (see 5.2.1.3). To reduce the effect of unwanted disturbances, e.g. caused by driving over a clot or a stone during measuring, it is expected that some level of data filtering will be necessary to improve the robustness of the technique on the field.

5.2.3.2. Required adaptations

Adaptations of the measurement system would be necessary to use it as feedback sensor on spreaders. The multi-exposure technique is a good alternative for high speed cameras, and was used successfully in this research in a protected (dark) environment. It is however uncertain if the technique can be used in a similar way for outdoor applications. The ambient light intensity will be higher and more variable (also depending on the weather conditions). To shield the particles under the measurement system from direct sunlight, a protective cover could be used. Nevertheless, because of the sensor exposure between both flashes using the multi-exposure approach, the background will be much more visible on the images compared to the static application in dark environment, and possible over-exposed. Because soil, plants, shadows, etc. will be visible on the images, the particles will be much more difficult to segment from the background. This could be solved using a retractable cover underneath the measurement zone, to exclude the background from the images. In this case however, it is likely that dust and particles accumulate on the cover, causing noise in the images. To limit the size of the screen, it would have to be placed relatively close to the cameras, which would further increase the signal to noise ratio. Nevertheless, a relative high ambient light level would be present. Because of the high velocity of the particles and the sensor exposure in between the two flashes, motion blur of the particles would occur on the images. Adaptations of the illumination system, the lenses (e.g. spectral filters) and camera settings will be necessary to visualise the particles with sufficient contrast on multi-exposure images.

Alternatively to multi-exposure with a two-camera stereo-system, a four-camera stereo-system could be used, consisting of two systems of two cameras, possibly placed at different radial distances on the rotating arm. The relative extrinsics of all cameras can be determined using camera calibration. By subsequently triggering the two camera systems, concurrently with the flashes of the illumination system, the particles will be visible on both sets of images at subsequent time intervals. Using the transformation matrix between both camera systems, and the time between the trigger-signals, the velocity of the particles can be calculated. This would increase the contrast

of the particles with the background to a large extent and completely remove motion blur.

In this study, an arm was used to move the camera system around the measurement zone over which particles were dispersed. The arm had a considerable length to reduce overlap of particles and assure that particles could be individually identified. For an online feedback sensor, this is too long for practical and safety reasons. Further research will be necessary to reduce the length of the arm. Instead of mounting the cameras on a rotating arm, multiple sets of cameras could be statically mounted to the spreader. This would further improve the safety of the system, although it would increase the cost because multiple sets of cameras would be required to provide enough resolution for the particles on the images and cover the whole area over which particles are dispersed.

With the static measurement system, a second set of cameras was used to determine the position of the spreader and the ground plane relative to the measurement setup and from this, transform the particle dynamics measured with the first camera system to the spreader coordinate system. When the sensor is mounted on the spreader, this set of cameras will no longer be required. However, a calibration procedure will still be necessary to transform the measured particle positions and velocities to a coordinate system associated with the spreader and relative to which the spread pattern will be calculated. Nevertheless, the position and orientation of the spreader relative to the ground plane should still be known. This could be measured in real time using an Inertial Measurement Unit (IMU) and ultrasonic or laser sensors respectively, which can be attached to the frame of the spreader.

Other important factors to consider are corrosion resistance and mechanical vibrations, caused by the spreading process and the tractor and the surface irregularities on the field. The sensor should be vibration-resistant and the measurement accuracy should remain unchanged. As discussed earlier, a warning signal could be given when the accuracy is no longer sufficient and recalibration is necessary.

5.2.3.3. Possibilities with the online feedback sensor
Determining optimal spreader settings

An online feedback sensor would avoid the need for manually adjusting the settings according to the spreading charts before spreading, increasing the ease of use for the farmer and reducing errors due to incorrect settings. During spreading, the spread

pattern could be checked at regular intervals to correct for possible deviations in the spreading process, for example caused by changes in particle size distribution or behaviour of the particles on the disc.

Surface irregularities

When spreading in the field, the spreader is subjected to vibrations due to surface irregularities in the field. Experiments conducted by Parish (1991b) with manually pushed lawn-type spreaders, operated over a surface with steel rods indicated a large effect on the spread pattern. Not only can the particle behaviour on the disc change (e.g. due to bouncing), affecting the particle dynamics relative to the spreader, also the velocity relative to the ground surface can alter because the spreader can be pivoted in different directions. Simulations for single-particle trajectories in Chapter 2 indicated that the landing position was highly sensitive to the vertical velocity component, therefore a large effect can be expected, especially for spreaders with large working widths. Inducing these vibrations while measuring the spread pattern with the static measurement system to determine the effect of these irregularities on the spread pattern can be challenging. Using the feedback sensor which is mounted to the spreader and continuously measuring the orientation of the spreader relative to the ground, this effect could be taken into account.

Spreading on slopes

Using the static measurement system developed in this work, it is possible to simulate the effect of changing the orientation of the ground plane or to apply Digital Elevation Models (DEMs) and calculate landing positions of the particles when the simulated trajectories intersect these surfaces. This way, using GPS-tracking data, as-applied maps could be created. However, in most cases, while spreading on a slope, the spreader will be inclined relative to the ground surface. This will affect the behaviour of the particles on the disc, e.g. by changing the position of the drop point relative to the disc centre, affecting the outlet position, the outlet angle and the velocity of the particles. The effect of slope can thus only be truly determined when placing the spreader out of level while performing spreading experiments with the measurement setup developed in this work. This would only be possible to a limited extent with the measurement system developed in this work, because inclination of the spreader relative to the static frame would cause a different distance of the particles to the camera system across the different arm positions, causing some particles to be out of

focus. Mounting the sensor on the spreader could resolve this problem and would enable to determine the spread pattern on slopes or inclined fields.

Wind

In Chapter 2, a relatively large effect was found for wind on the individual trajectories of fertilizer particles, especially in the case of high particle velocities and conical discs. In Chapter 4, it was shown that wind can affect the two-dimensional spread pattern and the homogeneity of the distribution perpendicular to the driving direction. Also, a large effect is expected for boundary spreading in the case of crosswind. Using an anemometer while spreading, wind conditions could be measured and the effect on the spread pattern could be determined in real-time.

Section control and variable rate technology

Some more advanced fertilizer spreaders have section control, this means that the spreading width can be adjusted during spreading, e.g. to account for wedge-shaped fields. To keep the application rate constant, the mass flow rate to the spreading discs must be changed accordingly. Traditionally, to evaluate these section control systems, the spread pattern must be determined for each individual spreader configuration. With variable rate technology, the dosage must be changed automatically during spreading through changing the size of the orifice. This can be done in an offline approach using prescription maps and GPS technology or online using sensors technology and decision models to determine the application rate (Van Liedekerke et al., 2006a). Simulations and experimental results from literature (see Figure 1.9) however showed that changing the dosage by altering the mass flow rate to the spreading can also influence the shape of the spread pattern which should be taken into account. Furthermore, for centrifugal fertilizer spreaders, the spread pattern is curve-shaped and lies at a considerable distance behind the spreader. Using the feedback system, the spread pattern can be determined for each different setting of the spreader at realistic field conditions, taking into account the tractor velocity and wind. Based on this, the relative position of all parts of the spread pattern relative to the GPS antenna can be taken into account by the VRT controller. Despite the fact that the spatial distribution of fertilizer can be simulated, and as-applied maps can be created after spreading based on the tracked GPS trajectories, performing online corrections fast enough remains challenging and requires prior knowledge about the behaviour of the spreading process for the specific type of fertilizer used.

5.2.4. Precision spreading

The centrifugal fertilizer spreader is a broadcast spreader designed to achieve large working widths while having a relatively small size. Due to the fact that particles describe a considerable trajectory in the air before reaching the ground, this type of spreaders is very sensitive to errors. As mentioned before, there is a positioning offset between the spread pattern and the spreader and the spread pattern is curve-shaped, making precise applications very difficult. Therefore, it can be argued whether equipping this type of spreader with various sensors to control the application rate is the best way to go. For precise applications, pneumatic spreaders are more promising because they are less prone to errors and have a line-shaped spread pattern. By controlling the rate for different sections of the spreading boom, it is possible to respond to much shorter range variabilities and work according to description maps at higher resolution. Furthermore, because the spread pattern has steep edges, it is more suited for boundary spreading. This does increase the sensitivity for driving errors compared to centrifugal spreaders, however with the increasingly used Real Time Kinematic (RTK) GPS systems, this can easily be overcome. Although calibration is still necessary, the spreading process is less affected by the fertilizer physical properties. Compared to broadcast spreaders, all types of fertilizer (also small or less dense fertilizers) can be distributed at large working widths with this type of spreader. At the moment, pneumatic spreaders are much more expensive, reducing their use in practice. Unless new fertilizer application technology is designed, the price of pneumatic spreaders decreases or other incentives (e.g. policies for environmental reasons) favouring pneumatic spreaders are applied, the centrifugal spreader is expected to remain the most commonly used spreader in practice. With the use of sensor technology, the spreading process can be better controlled, minimizing application errors and allowing a more precise application of fertilizer.

REFERENCE LIST

Abbou-ou-cherif, E., M., Prion, E., Chateauneuf, A., Miclet, D., Lenain, R., Koko, J. (2017). On-the-field simulation of fertilizer spreading: Part 2- Uniformity investigation. Computers and Electronics in Agriculture 141, 118-130.

Antille, D. L., Gallar, L., Miller, P., Godwin, R. J. (2015). An investigation into the fertilizer particle dynamics off-the-disc. Applied Engineering in Agriculture 31(1), 49-60.

Antille, D. L., & Godwin, R. J. (2013a). Determining the particle size range of organomineral fertilisers based on the spreading characteristics of the material. In 2013 Kansas City, Missouri, July 21-July 24, 2013 (p. 1). American Society of Agricultural and Biological Engineers.

Antille, D. L., Sakrabani, R., Tyrrel, S. F., Le, M. S., & Godwin, R. J. (2013b). Characterisation of organomineral fertilisers derived from nutrient-enriched biosolids granules. Applied and Environmental Soil Science, 2013.

Aphale, A., Bolander, N., Park, J., Shaw, L., Svec, J., & Wassgren, C. (2003). Granular fertiliser particle dynamics on and off a spinner spreader. Biosystems Engineering 85(3), 319-329.

ASAE 341.2 (1988). Procedure for measuring distribution uniformity and calibrating granular broadcast spreaders.

Brabant, L., Vlassenbroeck, J., De Witte, Y., Cnudde, V., Boone, M. N., Dewanckele, J., & Van Hoorebeke, L. (2011). Three-dimensional analysis of high-resolution X-ray computed tomography data with Morpho+. Microscopy and Microanalysis 17(02), 252-263.

Bradsky, G. & Kaehler, A.(2008). Computer vision with the OpenCV Library.

Cheng, L., Nong, L., & JianXin, C. (2012). The research of LED arrays for uniform illumination. Adv. Inf. Syst. Sci 4, 174-184.

Chien, S. F. (1994). Settling velocity of irregularly shaped particles. SPE Drilling & Completion 9(4), 281-289.

Cointault, F., Sarrazin, P., Paindavoine, M. (2002). Fast imaging system for particle projection analysis: application to fertilizer centrifugal spreading, Measurement Science and Technology. 13, 1087-1093.

Cointault, F., Sarrazin, P., Paindavoine, M. (2003). Measurement of the motion of fertilizer particles leaving a centrifugal spreader using a fast imaging system. Precision Agriculture 4, 279-295.

Cointault, F.; Vangeyte, J., (2005). Photographic Imaging Systems to Measure Fertilizer Granule Velocity during Spreading. In Proceedings of the International Fertilizer Society, London, UK, 27 October 2005.

Cointault, F., Vangeyte, J., Dubois, J., Baert, J., & Clerc, C. (2008). New high speed imaging system for fertilizer granule characteriastion at the ejection. In International Conference on Agricultural Engineering & Industry Exhibition, pp. OP-1555. European Society of Agricultural Engineers (AgEng).

Cool, S., Pieters, J. G., Mertens, K. C., Hijazi, B., Vangeyte, J. (2014). A simulation of the influence of spinning on the ballistic flight of spherical fertilizer grains. Computers and Electronics in Agriculture 105, 121-131.

Cool, S., Pieters, J. G., Mertens, K., Mora, S., Cointault, F., Dubois, J., Van De Gucht, T., Vangeyte, J. (2015). Development of a high irradiance LED configuration for small field of view motion estimation of fertilizer particles. Sensors 15, 28627-28645

Cool, S., Pieters, J., Van Acker, J., Van Den Bulcke, J., Mertens, K.C., Nuyttens, D., Van De Gucht, T.& Vangeyte, J. (2016a). Determining the effect of wind on the ballistic flight of fertilizer particles. Biosystems Engineering 151, 425-434.

Cool, S., Vangeyte, J., Mertens, K.C., Nuyttens, D., Sonck, B., Van De Gucht, T. & Pieters, J.G.(2016b). Comparing different methods of using collection trays to determine the spatial distribution of fertilizer particles Biosystems Engineering 150, 142-150.

Cunningham, F. M., & Chao, E. Y. (1967), Design relationships for centrifugal fertilizer distributors. Transactions of the ASAE 10, 91-95.

Deb, K., Pratap, A., Agarwal, S. & Meyarivan, T. (2002). A fast and elitist multiobjective genetic algorithm: NSGA-II. IEEE Transactions on Evolutionary Computation 6, 182-197.

Dierick, M., Van Loo, D., Masschaele, B., Van den Bulcke, J., Van Acker, J., Cnudde, V., Van Hoorebeke, L. (2014). Recent micro-CT scanner developments at UGCT. Nuclear Instruments and Methods in Physics Research Section B: Beam Interactions with Materials and Atoms 324, 35–40.

Dintwa, E., Tijskens, E., Olieslagers, R., De Baerdemaeker, J., & Ramon, H. (2004b). Calibration of a spinning disc spreader simulation model for accurate site-specific fertiliser application. Biosystems Engineering 88(1), 49-62.

Dintwa, E., Van Liedekerke, P., Olieslagers, R., Tijskens, E., & Ramon, H. (2004a). Model for simulation of particle flow on a centrifugal fertiliser spreader. Biosystems Engineering 87, 407-415.

EN1235/A1 (2003). European Standard. Vaste meststoffen – zeefanalyse.

EN1236 (1992). European Standard. Fertilizers – Determination of bulk density (loose) (ISO 3944 :1992 modified).

References

EN1237 (1992) European Standard. Fertilizers – Determination of bulk density ()t (ISO 5311: 1992 modified).

EN12047 (1995). European Standard. Vaste meststoffen – bepalen van de statische storthoek.

EN13739(2011). European Standard. Landbouwmachines - Breedwerpige strooiers en strooiapparatuur over de gehele breedte voor vaste meststoffen - Milieubescherming - Deel 1: Eisen, Deel 2: Beproevingsmethoden.

FAO (2017). World fertilizer trends and outlook to 2020. Food and Agriculture Organization of the United Nations, summary report, Rome.

Fulton, J. P., Shearer, S. A., Stombaugh, T. S., & Higgins, S. F. Comparison of variable-rate granular application equipment (2003). ASAE Annual Meeting (p. 1). American Society of Agricultural and Biological Engineers.

García-Ramos, F. J., Boné, A., Serreta, A., & Vidal, M. (2012). Application of a 3-D laser scanner for characterising centrifugal fertiliser spreaders. Biosystems Engineering 113(1), 33-41.

Gindert-Kele, A.B., 2005. Physical Properties of Fertiliser Particles and Their Movement Analysis. Doctoral Thesis of the University of Debrecen, Hungary, 24p.

Goldberg, D.E., Holland, J.H.(1988). Genetic algorithms and machine learning. Machine learning 3, 95-99.

Goucher, L., Bruce, R., Cameron, D. D., Koh, S. L., & Horton, P. (2017). The environmental impact of fertilizer embodied in a wheat-to-bread supply chain. Nature Plants 3, 17012.

Grafton, M.C.E., Izquierdo A., D., Yule, I.J. Willis, L.A. (2016). Measuring the Spread Patterns of Spreaders Under Normal Field Conditions Compared to test Conditions. In: Integrated nutrient and water management for sustainable farming. (Eds. L.D. Currie and R. Singh) http://flrc.massey.ac.nz/publications.html. Occasional Report No. 29. Fertilizer and Lime Research Centre, Massey University, Palmerston North, New Zealand. 11 pages.

Grafton, M. C., Izquierdo, D. A., Yule, I. J., Willis, L. A., & Manning, M. J. (2015a). The Effect of Field Conditions on In-Field Spread Patterns from Twin Disc Spreaders. In 2015 ASABE Annual International Meeting (p. 1). American Society of Agricultural and Biological Engineers.

Grafton, M., Yule, I., & Rendle, B. (2011). A review of technologies for improved fertiliser application accuracy. Adding to the knowledge base for the nutrient manager.

Grafton, M. C., Yule, I. J., Robertson, B. G., Chok, S. M., & Manning, M. J. (2015b). Ballistic modeling and pattern testing to prevent separation of New Zealand fertilizer products. Applied Engineering in Agriculture 31, 405-413.

Griepentrog, H. W., & Kyhn, M. (2000). Strategies for site specific fertilization in a highly productive agricultural region. In Proceedings of the 5th International Conference on Precision Agriculture, July 2000.

Griepentrog, H. W., & Persson, K. (2001). A model to determine the positional lag for fertiliser spreaders. In Proceedings of the 3rd European conference on precision agriculture, Montpellier. Agro Montpellier, June 2001, Ecole Nationale Superieure Agronomique (pp. 671-676).

Griffis, C., Ritter, D., Matthews, E. (1983). Simulation of rotary spreader distribution patterns. Transactions of the ASAE 26, 33–37.

Grift, T. E. (2000). Spread pattern analysis tool (SPAT): I. Development and theoretical examples. Transactions of the ASAE 43(6), 1341.

Grift, T. E., & Hofstee, J. W. (1997a). Development of a fertilizer particle accelerator. Journal of Agricultural Engineering Research, 66(3), 229-233.

Grift, T. E., & Hofstee, J. W. (1997b). Measurement of velocity and diameter of individual fertilizer particles by an optical method. Journal of Agricultural Engineering Research 66(3), 235-238.

Grift, T.E., Hofstee, J.W. (2002). Testing an online spread pattern determination sensor on a broadcast fertiliser spreader. Transactions of the ASAE 45, 561–567.

Grift, T. E., & Kweon, G. (2006). Development of a uniformity controlled granular fertilizer spreader. In 2006 ASAE Annual Meeting (p. 1). American Society of Agricultural and Biological Engineers.

Grift, T. E., Kweon, G., Hofstee, J. W., Piron, E., & Villette, S. (2006). Dynamic friction coefficient measurement of granular fertiliser particles. Biosystems Engineering 95(4), 507-515.

Grift, T. E., Walker, J. T., & Hofstee, J. W. (1997). Aerodynamic properties of individual fertilizer particles. Transactions of the ASAE 40(1), 13-20.

Hartley, R., Gupta, R., & Chang, T. (1992). Stereo from uncalibrated cameras. In Computer Vision and Pattern Recognition. Proceedings CVPR'92., IEEE Computer Society Conference (pp. 761-764).

Hartley, R. I., & Sturm, P. (1997). Triangulation. Computer Vision and Image Understanding 68, 146-157.

Hensel O (2003). A new methodology for mapping fertilizer distribution. Presentation at the 2003 ASAE Annual International Meeting, Las Vegas, USA.

Hijazi, B., Cointault, F., Dubois, J., Coudert, S., Vangeyte, J., Pieters, J., Paindavoine, M. (2010). Multi-phase cross-correlation method for motion estimation of fertilizer granules during centrifugal spreading. Precision Agriculture 11, 684–702.

Hijazi, B., Cointault, F., Dubois, J., Villette, S., Vangeyte, J., Yang, F., & Paindavoine, M. (2009). New high speed image acquisition system and image processing

techniques for fertilizer granule trajectory determination. In E. J. van Henten, D. Goense & C. Lokhorst (Eds.), Precision agriculture '09 proceedings of the 7th European conference on precision agriculture (pp. 639–647). Wageningen, The Netherlands: Wageningen Academic Publishers.

Hijazi, B., Cointault, F., Yang, F., & Paindavoine, M. (2008). High speed motion estimation of fertilizer granules with Gabor filters. Proc. of SPIE 7126, pp. 712616-1).

Hijazi, B., Cool, S., Vangeyte, J., Mertens, K., C., Cointault, F., Paindavoine, M., Pieters, J. G. (2014). High speed stereovision setup for position and motion estimation of fertilizer particles leaving a centrifugal spreader. Sensors 14, 21466-21482

Hijazi, B., Vangeyte, J., Cointault, F., Dubois, J., Coudert, S., Paindavoine, M. & Pieters, J. (2011). Two-step cross-correlation-based algorithm for motion estimation applied to fertiliser granules' motion during centrifugal spreading. Optical Engineering 50, 639–647.

Hofstee, J. W. & Huisman, W. (1990). Handling and spreading of fertilizers Part 1: Physical properties of fertilizer in relation to particle motion. Journal of Agricultural Engineering Research 47, 213-234.

Hofstee, J. W., Speelman, L., Scheufler, B. (1999). Part 1.4 Fertilizer Distributors. B.A. Stout and B. Cheze, eds. CIGR Handbook of Agricultural Engineering, Volume III: Plant Production Engineering. St. Joseph, Michigan, USA: American Society of Agricultral Engineers, pp. 240-268.

Hofstee, J. W. (1992). Handling and spreading of fertilizers: Part 2, physical properties of fertilizer, measuring methods and data. Journal of Agricultural Engineering Research 53, 141-162.

Hofstee, J. W.(1994). Handling and spreading of fertilizers: part 3, measurement of particle velocities and directions with ultrasonic transducers, theory, measurement system, and experimental arrangements. Journal of Agricultural Research 58, 1-16

Hofstee, J. W. (1995) Handling and spreading of fertilizers: part 5, the spinning disc type fertilizer spreader. Journal of Agricultural Research 62, 143-162.

IFA (2017). Fertilizer outlook 2017 -2021. International Fertilizer Association Annual Conference, 22-24 May, Marrakech.

Inns, F. M., and A. R. Reece. (1962). The theory of the centrifugal distributor: II. Motion on the disc, off–center feed. Journal of Agricultural Research 7, 345–353.

Isherwood, K. F. (2000). Mineral fertilizer use and the environment by International Fertilizer Industry Association. Revised Edition, Paris.

ISO5690/1 (1985). International standard. Equipment for distributing fertilisers - test methods - Part 1: Full width fertiliser distributors.

Jones, J. R., Lawrence, H. G., & Yule, I. J. (2008). A statistical comparison of international fertiliser spreader test methods - Confidence in bout width calculations. Powder Technology 184(3), 337-351.

Kweon, G., & Grift, T. E. (2006). Feed gate adaptation of a spinner spreader for uniformity control. Biosystems Engineering 95(1), 19-34.

Kweon, G., Grift, T. E., & Miclet, D. (2007). A spinning-tube device for dynamic friction coefficient measurement of granular fertiliser particles. Biosystems Engineering 97(2), 145-152.

Lawrence, H.G. (2007). Adoption of precision agriculture technologies for fertiliser placement in New Zealand. PhD thesis. Massey University.

Lawrence H.G., Yule I.J., and Coetzee M.G. (2007). Development of an image-processing method to assess spreader performance. Transactions of the ASABE 50, 397-407.

Lawrence, H. G., & Yule, I. J. (2005). Accessing Spreader Performance for Variable Rate Fertiliser Application. In 2005 ASAE Annual Meeting (p. 1). American Society of Agricultural and Biological Engineers.

Lawrence, H. G., Yule, I. J., & Jones, J. R. (2006). A statistical analysis of international test methods used for analysing spreader performance. New Zealand Journal of Agricultural Research 49(4), 451-463.

Lei, P., Wang, Q., Zou, H. (2014). Designing LED array for uniform illumination based on local search algorithm. Journal of the European Optical Society rapid publications 14, 14014.

Mueller, N. D., Gerber, J. S., Johnston, M., Ray, D. K., Ramankutty, N., & Foley, J. A. (2012). Closing yield gaps through nutrient and water management. Nature 490(7419), 254.

Murray, G. (2013). Rotation about an arbitrary axis in 3 dimensions. Online http://inside. mines.edu.

Miserque, O., & Pirard, E. (2004). Segregation of the bulk blend fertilizers. Chemometrics and intelligent laboratory systems 74(1), 215-224.

Miserque, O., Pirard, E., Schenkel, Y., Mostade, O., & Huyghebaert, B. (2008). Spreading segregation of blended fertilizers: influence of the particles properties. Applied Engineering in Agriculture 24(2), 137-144.

Miserque, O., Pirard, E. & Tissot S. (2001). Caractérisation des particules d'engrais: corréation entre les propriéte´s physiques et morphométriques, Visualisation-Image-Modélisation 15 (Nancy).

Moreno, I., Avendano-Alejo, M., Tzonchev, R. I. (2006). Designing light-emitting diode arrays for uniform near-field irradiance. Applied Optics 46, 2265-2272.

Moreno, I., Sun, C.C. LED array: where does far-field begin. In proceedings of International Conference on Solid State lighting (7058), San Diego, USA, 16 December 2010.

Olieslagers, R., Ramon, H., & De Baerdemaeker, J. (1996). Calculation of fertilizer distribution patterns from a spinning disc spreader by means of a simulation model. Journal of Agricultural Engineering Research 63, 137-152.

Padfield, E. (2011). Searching for the best fertilizer spreader. Farmers weekly. http://www.fwi.co.uk/machinery/searching-for-the-best-fertiliser-spreader.htm

Parish, R. L. (1986). Comparison of spreader pattern evaluation methods. Applied Engineering in Agriculture 14, 35.

Parish, R. L. (1991a). Effect of material bouncing into and out of collection pans on observed spreader distribution pattern. Applied Engineering in Agriculture 7, 311e315.

Parish, R.L. (1991b). Effect of rough operating surface on rotary spreader distribution pattern.

Applied Engineering in Agriculture 7, 61-63.

Parish, R. L. (2002). Rate setting effects on fertilizer spreader distribution patterns. Applied Engineering in Agriculture 18(3), 301.

Parish, R. L. (2003). Effect of impeller angle on pattern uniformity. Applied Engineering in Agriculture 19(5), 531.

Parkin, C. S., Basford, B., & Miller, P. C. H. (2005). Spreading accuracy of solid urea fertilisers. Report for DEFRA Project NT2610. London, U.K.: Department of Environment, Food and Rural Affairs.

Patterson, D. E & A. R. Reece. (1962). The theory of the centrifugal distributor: I. Motion on the disc, near–center feed. Journal of Agricultural Engineering Research 7, 232–240.

Pelz, J. (1993). The Focal Encyclopedia of Photography (Leslie D. Stroebel, Richard D. Zakia, ed.). Focal Press. p. 467. ISBN 0-240-51417-3.

Piron E & Miclet, D. (2006), Spatial distribution measurement: a new method for the evaluation and testing of centrifugal fertilizer spreaders, 2nd International Symposium on Centrifugal Fertilizer Spreading, 24 –25 septembre, Montoldre, France.

Piron, E., Miclet, D., & Villette, S. (2010). CEMIB: And innovative bench for spreader eco-design. AgEng, International Conference on Agricultural Engineering.

Press, W., Teukolsky, S., Vetterling, W., & Flannery, B. (1992). Numerical Recipes in Fortran 77: The Art of Scientific Computing, 933 pp.

Reumers, J., Tijskens, E., & Ramon, H. (2003a). Experimental characterisation of the tangential and cylindrical fertiliser distribution pattern from a spinning disc: a parameter study. Biosystems Engineering 86(3), 327-337.

Reumers, J., Tijskens, E., & Ramon, H. (2003b). Experimental characterisation of the cylindrical distribution pattern of centrifugal fertiliser spreaders: towards an alternative for spreading hall measurements. Biosystems Engineering 86(4), 431-439.

Schaffer, J. Multiple objective optimization with vector evaluated genetic algorithms. In Proceedings of an international conference on genetic algorithms and their applications, Pittsburgh, USA, 24 July 1985.

Scharf, P.C. (2010). Streaky nitrogen applications, why they happen and what you can do about them. Integrated pest and crop management 20(4), 27-27.

Søgaard, H. T. & Kierkegaard P. (1994) Yield reduction resulting from uneven fertilizer distribution. Transactions of the ASAE 37(6), 1749-1752.

Suzuki, S. (1985). Topological structural analysis of digitized binary images by border following. Computer Vision Graphics and Image Processing 30, 32-46.

Tijskens, B., van Liedekerke, P., & Ramon, H. (2005). Modelling to aid assessment of fertiliser handling and spreading characteristics. International Fertiliser Society

Tilman, D., Balzer, C., Hill, J. & Befort, B. L. (2011). Global food demand and the sustainable intensification of agriculture. Proceedings of the National Academy of Sciences 108, 20260–20264.

Tissot, S., Miserque, O., Mostade, O., Huyghebaert, B., & Destain, J. P. (2002). Uniformity of N-fertiliser spreading and risk of ground water contamination. Irrigation and drainage 51(1), 17-24.

Tissot, S., Miserque, O., & Quenon, G. (1999). Chemical distribution patterns for blended fertilizers in the field. Journal of Agricultural Engineering Research 74(4), 339-346.

Vangeyte, J. & Sonck, B. (2005). Image analysis of particle trajectories. In B. Tijskens, & H. Ramon (Eds.), Proceedings of the 1st international symposium on centrifugal fertiliser spreading. KULeuven: Leuven, Belgium.

Vangeyte, J. (2013). Development and Validation of a Low Cost Technique to Predict Spread Patterns of Centrifugal Spreaders. Doctoral Thesis of the University of Leuven, Belgium, 146p.

Van Liedekerke, P. (2008). Study of the granular fertilizers and the centrifugal spreader using Discrete Element Method (DEM) simulations. IAgrE Landwards e-Xtra 63.

Van Liedekerke, P., De Baerdemaeker, J., & Ramon, H. (2006a). Fertilizer application control. CIGR Handbook of Agricultural Engineering, 273-278.

Van Liedekerke, P., Tijskens, E., Dintwa, E., Anthonis, J. & Ramon, H. (2006b). A discrete element model for simulation of a spinning disc fertiliser spreader I. Single particle simulations. Powder Technology 170, 71–85.

Van Liedekerke, P., Tijskens, E., Dintwa, E., Rioual, F., Vangeyte, J., & Ramon, H. (2009a). DEM simulations of the particle flow on a centrifugal fertilizer spreader. Powder Technology, 190(3), 348-360.

Van Liedekerke, P., Tijskens, E., & Ramon, H. (2005). DEM modeling of centrifugal fertilizer spreading. In First International Symposium on Centrifugal Fertiliser Spreading, 25-32.

Van Liedekerke, P., Tijskens, E., & Ramon, H. (2009b). Discrete element simulations of the influence of fertiliser physical properties on the spread pattern from spinning disc spreaders. Biosystems engineering 102(4), 392-405.

Villette, S., Cointault, F., Chopinet, B., & Paindavoine, M. (2006). Optimizing Hough transform for fertilizer spreading optical control. Optical Engineering 45, 027006-027006.

Villette, S., Cointault, F., Piron, E., & Chopinet, B. (2005). Centrifugal spreading: an analytical model for the motion of fertiliser particles on a spinning disc. Biosystems Engineering 92, 157-164.

Villette, S., Gée, C., Piron, E., Martin, R., Miclet, D., & Paindavoine, M. (2010). Centrifugal fertiliser spreading: velocity and mass flow distribution measurement by image processing. In AgEng: International Conference on Agricultural Engineering (pp. 10-p).

Villette, S.; Piron, E.; Cointault, F.; Chopinet, B. (2008). Centrifugal spreading of fertilizer: Deducing three-dimensional velocities from horizontal outlet angles using computer vision. Biosystems Engineering 99, 496–507.

Villette, S., Piron, E., & Miclet, D. (2017). Hybrid centrifugal spreading model to study the fertiliser spatial distribution and its assessment using the transverse coefficient of variation. Computers and Electronics in Agriculture 137, 115-129.

Villette, S., Piron, E., Martin, R., Miclet, D., Jones, G., Paoli, J. N., & Gée, C. (2013). Estimation of two-dimensional fertiliser mass flow distributions by recording granule impacts. Biosystems Engineering 115(4), 463-473.

Virk, S. S., Fulton, J. P., Fasina, O. O., & McDonald, T. P. (2013). Influence of Broiler Litter Bulk Density on Metering and Distribution for a Spinner-Disc Spreader. Applied Egineering in Agriculture 29(4), 473-482.

Vlassenbroeck, J., Dierick, M., Masschaele, B., Cnudde, V., Van Hoorebeke, L., Jacobs, P. (2007). Software tools for quantification of X-ray microtomography at the UGCT. Nuclear Instruments and Methods in Physics Research, Section A: Accelerators, Spectrometers, Detectors and Associated Equipment 580, 442–445.

Walker, J.T., Grift, T.E., Hofstee, J.W. (1997). Determining effects of fertilizer particle shape on aerodynamic properties, Transactions of the ASAE 40, 21-27.

Wang, K, Wu, D., Qin, Z., Chen, F., Luo, X., Liu, S. (2011). New reversing design method for LED uniform illumination. Optics Express 19, 830-840.

Whang, A. J. W, Che n, Y., Teng, Y. (2009). Designing uniform illumination systems by surface-tailored lens and configurations of LED arrays. Journal of Display Technology 5, 94-103.

Yang, H., Bergmans, J., Schenk, T., Linnartz, J.P., Rietman, R. (2009). Uniform illumination rendering using an array of LEDs: a signal processing perspective. IEEE T. Signal Processing 57, 1044-1057.

Yildirim, Y. (2006a). Effect of cone angle and revolution speed of disc on fertilizer distribution uniformity in single-disc rotary fertilizer spreaders. J. Applied Sci 6(14), 2875-2881.

Yildirim, Y. (2006b). Effect of vane number on distribution uniformity in single-disc rotary fertilizer spreaders. Applied Engineering in Agriculture 22(5), 659-663.

Yildirim, Y. (2008). Effect of side to side spreader angle on pattern uniformity in single- and twin-disc rotary fertilizer spreaders. Applied engineering in Agriculture 24(2), 173-179.

Yildirim, Y., & Kara, M. (2003). Effect of vane height on distribution uniformity in rotary fertilizer spreaders with different flow rates. Applied engineering in Agriculture 19(1), 19.

Yule, I. (1996). The effect of fertilizer particle size on spread distribution. NZ Centre for Precision Agriculture, Massey University, Palmerston North, New Zealand, 1-9.

Yule, I. J., & Grafton, M. C. E. (2013). New spreading technologies for improved accuracy and environmental compliance. Accurate and efficient use of nutrients on farms.

Yule, I. J., & Lawrence, H. G. (2008). Accuracy and Confidence Issues Around Broadcast Spreaders Transverse Pattern Testing Methods. In 2008 Providence, Rhode Island, June 29–July 2, 2008 (p. 1). American Society of Agricultural and Biological Engineers.

Zhang, X., Davidson, E. A., Mauzerall, D. L., Searchinger, T. D., Dumas, P., & Shen, Y. (2015). Managing nitrogen for sustainable development. Nature 528, 51-59.

CURRICULUM VITAE

Simon Cool werd op 12 juli 1990 geboren in Roeselare. Na zijn studies latijn-wiskunde aan het Sint-Aloysiuscollege van Diksmuide begon hij in 2008 aan zijn opleiding Bio-ingenieur aan de Universiteit Gent. Na het afwerken van zijn masterproef, in samenwerking met het Instituut voor Landbouw-, Visserij- en Voedingsonderzoek (ILVO) behaalde hij in 2013 met grootste onderscheiding zijn masterdiploma in de Bio-ingenieurswetenschappen afstudeerrichting landbouwkunde. In september 2013 begon Simon aan zijn doctoraatsonderzoek "Development of an imaged based 3D technique to determine spread patterns of centrifugal fertilizer spreaders", een samenwerking tussen het ILVO en de vakgroep Biosysteemtechniek van de Universiteit Gent. In 2015 heeft hij tijdens een stage van drie maanden in Winterthur (Zwitserland), gefinancierd door FWO, expertise opgedaan over camera kalibraties. Simon heeft tijdens zijn onderzoek meerdere wetenschappelijke publicaties geschreven en op verschillende internationale congressen zijn onderzoek toegelicht.

Simon Cool was born in Roeselare on the 12th of July 1990. After his studies at the Sint-Aloysius college of Diksmuide, he began his studies at the faculty of Bioscience Engineering of Ghent University in 2008. After finishing his master's thesis in cooperation with the Research Institute for Agriculture, Fisheries and Food (ILVO), he achieved summa cum laude his master's degree in the Bioscience Engineering, Agriculture. On the first of September 2013, Simon started his PhD research: "Development of an imaged based 3D technique to determine spread patterns of centrifugal fertilizer spreaders", a collaboration between ILVO and the department of Biosystems Engineering of Ghent University. In 2015, he performed an internship in Winterthur (Switzerland) about camera calibrations, funded by FWO. During his research, Simon has written multiple scientific publications and presented his research results on different international scientific conferences.

LIST OF PUBLICATIONS

International publications (A1)

1. Cool, S., Pieters, J.G., Mertens, K.C., Hijazi, B. & Vangeyte, J. (2014). A simulation of the influence of spinning on the ballistic flight of spherical fertiliser grains. Computers and Electronics in Agriculture 105, 121–131.

2. Cool, S., Pieters, J.G., Mertens, K.C., Mora ,S., Cointault, F., Dubois, J., Van De Gucht, T. & Vangeyte, J. (2015). Development of a high irradiance LED configuration for small field of view motion estimation of fertilizer particles. Sensors 15(11), 28627–28645.

3. Cool, S. R., Pieters, J.G., Seatovic, D., Mertens, K.C., Nuyttens, D., Van De Gucht, T.. & Vangeyte, J. (2017). Development of a Stereovision-Based Technique to Measure the Spread Patterns of Granular Fertilizer Spreaders. Sensors 17, 1396.

4. Cool, S. R., Pieters, J.G., Van Acker, J., Van Den Bulcke, J., Mertens, K. C., Nuyttens, D. R. E., Van De Gucht, T. C. & Vangeyte, J. (2016). Determining the effect of wind on the ballistic flight of fertiliser particles. Biosystems Engineering 151, 425-434.

5. Cool, S., Vangeyte, J., Mertens, K.C., Nuyttens, D.R.E., Sonck, B. R., Van De Gucht, T., Pieters, J.G. (2016). Comparing different methods of using collection trays to determine the spatial distribution of fertilizer particles. Biosystems Engineering 150, 142-150.

6. Hijazi, B., Cool, S., Vangeyte, J, Mertens, K.C., Cointault, F., Paindavoine, M., & Pieters, J.G. (2014). High speed stereovision setup for position and motion estimation of fertilizer particles leaving a centrifugal spreader. Sensors 14(11), 21466–21482.

Conference presentations

1. Cool, S., Mertens, K.C., Van De Gucht, T., Vangeyte, J., Pieters, J.G. (2014). Determining the drag coefficient of fertilizer grains using stereovision. International conference of Agricultural Engineering (Ageng 2014 Zürich).

2. Cool, S., Pieters, J. G., Mertens, K. C., Nuyttens, D., Hijazi, B., Dubois, J., Cointault, F. & Vangeyte, J. (2016). Characterization of centrifugal spreaders. International Conference of Agricultural Engineering (CIGR-Ageng).

3. Cool, S., Vangeyte, J., Mertens, K.C., Nuyttens, D., Pieters, J.G. (2016). Precisiestrooien als onderdeel van precisielandbouw. Poster presentation. Studiedag Starters in het natuur- en bosonderzoek (Brussel).

4. Cool, S., Vangeyte, J., Nuyttens, D., Mertens, K., Van De Gucht, T., Mora , S., Sonck, B., Seatovic , D., Pieters , J.G. (2015). Measuring the dynamic mass flow rate of a centrifugal fertilizer spreader. 10th European conference on Precision Agriculture.

5. Cool, S., Vangeyte, J., Pieters , J. G., Nuyttens, D., Sonck, B., Van Damme , J., Van De Gucht, T., Mertens, K.C. (2015). Comparison of different spread pattern determination techniques (2015). 10th European conference on Precision Agriculture.

6. Hijazi, B., Vangeyte, J., Cool, S., Mertens, K., Nuyttens, D., Dubois, J., Cointault, F., Pieters, J. (2014). Predicting spread patterns of centrifugal fertiliser spreaders. International conference of Agricultural Engineering (Ageng Zürich).

7. Van De Gucht, T., Blanckaert, T., Goemaere, J., Naessens, C., Cool, S., Mertens, K., Van Nuffel, A., Vangeyte, J. (2014). Development of an open-source, low-cost and adaptable 3D accelerometer for monitoring animal motion. International conference of Agricultural Engineering (Ageng Zürich).

Conference proceedings

1. Cool, S., Pieters, J. G., Mertens, K. C., Nuyttens, D., Hijazi, B., Dubois, J., Cointault, F. & Vangeyte, J. (2015). Image based techniques for determining spread patterns of centrifugal fertilizer spreaders. Agriculture and Agricultural Science Procedia, 7, 59-63.